

ISSN 2542-2049

Saint-Petersburg State University

16 International School-Conference

Magnetic resonance and its applications

proceedings



Spinus

31 March — 5 April 2019

Saint-Petersburg, Russia

SAINT PETERSBURG STATE UNIVERSITY
Department of Nuclear Physics Research Methods

16th International School-Conference

MAGNETIC RESONANCE AND ITS APPLICATIONS

Proceedings

an AMPERE event

March 31 — April 5, 2019
Saint Petersburg, Russia

Magnetic Resonance and its Applications. Spinus-2019.
Proceedings. Saint Petersburg State University, 2019. 304 pp.
ISSN 2542-2049

Schola **Spinus**



16th International School-Conference
MAGNETIC RESONANCE AND ITS APPLICATIONS
SPINUS-2019

ORGANIZING COMMITTEE

Chairman	Dr. Sci. Denis Markelov, professor, SPSU
Vice-chairman	M. Sc. Alexander Ievlev, researcher, SPSU
Committee members	Dr. Andrey Egorov, associate professor, SPSU Dr. Marina Shelyapina, associate professor, SPSU Dr. Pavel Kupriyanov, engineer, SPSU Dr. Konstantin Tyutyukin, senior teacher, SPSU M. Sc. Timofey Popov, SPSU
Layout of proceedings	Aleksandr Levantovskii

CONTACTS

1, Ulyanovskay st., Peterhof, 198504, St. Petersburg, Russia
Department of Nuclear Physics Research Methods
St. Petersburg State University

Tel.	+7-953-350-0640
Fax	+7-812-428-7240
E-mail	spinus@spinus.spb.ru
Website	http://spinus.spb.ru/

The SPINUS-2019 was financially supported by the Russian Foundation for Basic Research, project No. 19-02-20041.

PROGRAM COMMITTEE

SCIENTIFIC ADVISER OF THE SCHOOL-CONFERENCE

Vladimir Chizhik Honored scientist of Russia,
Professor Emeritus, SPSU

ADVISORY BOARD

Balevicius V. Professor, Vilnius, Lithuania

Cabal C. Professor, Havana University, Cuba

Chizhik V. I. Professor, St. Petersburg State University, Russia

Dvinskikh S. V. Professor, Royal Institute of Technology, Stockholm,
Sweden

Fraissard J. Professor, University Pierre and Marie Curie, Paris,
France

Grunin L. Yu. Associate Professor, CEO, Resonance Systems, Russia

Lahderanta E. Professor, Lappeenranta Technical University, Finland

Michel D. Professor, Leipzig University, Germany

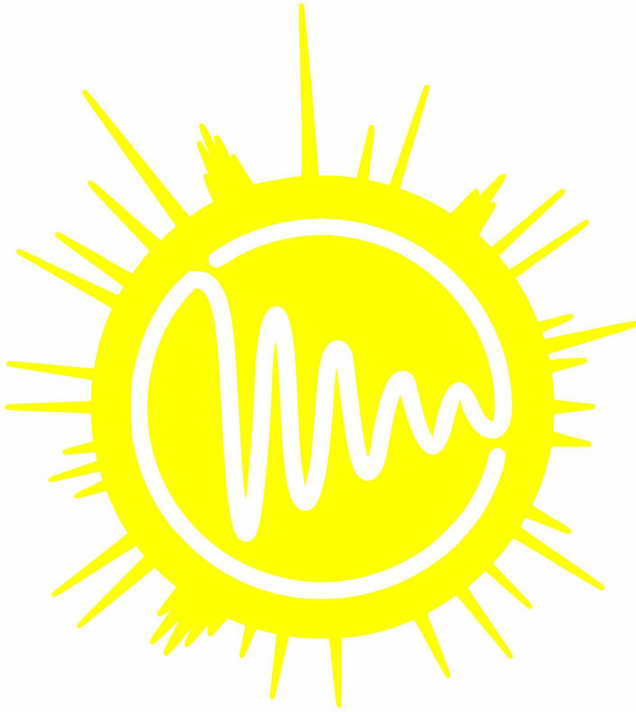
Rameev B. Professor, Gebze Technical University, Turkey

Skrynnikov N. R. Professor, St. Petersburg University, Russia, Purdue
University, USA

Tagirov M. S. Professor, Kazan Federal University, Russia

Varela L. M. Professor, University Santiago de Compostela, Spain

Vasiliev S. Professor, University of Turku, Finland



Spinus



Bruker Corporation
bruker.com



rfbr.ru



Mestrelab Research
chemistry software solutions
mestrelab.com



RESONANCE
SYSTEMS

Resonance systems Ltd.
nmr-design.com



LUT
University

Lappeenranta-Lahti University of Technology
www.lut.fi



Magicplot Systems, LLC
magicplot.com



SciJob.ru

Careers in
Science &
Technology

Contents

SCHEDULE	21
WELCOME TO THE SCHOOL-CONFERENCE "SPINUS".....	35
LECTURES	37
<i>E. V. Charnaya, S. V. Baryshnikov</i>	
NMR studies of bulk and nanostructured ferroelectrics.....	38
<i>Yury Bunkov</i>	
Supermagnonics at room temperature.....	40
<i>Carlos Cabal Mirabal</i>	
MRI Synopsis of the Physical and Hardware bases.....	41
<i>Uwe Eichhoff</i>	
The human brain: development and aging explored by MRI	43
<i>Jacques Fraissard</i>	
Xe NMR technique: various applications.....	44
<i>Vladimir I. Chizhik, Pavel A. Kupriyanov</i>	
Peculiarities, possibilities, and areas of applications of quantitative analysis by NMR in magnetic field of the Earth.....	45
<i>Dieter Michel, Marko Bertmer, and Jürgen Haase</i>	
EPR and NMR study of nitric oxide – an interesting molecule for bio-medical applications.....	46
<i>Vladimir V. Matveev, Alexandr V. Ievlev, Konstantin V. Tyutyukin, Luis M. Varela</i>	
Comparison of ionic liquids and highly concentrated electrolyte solutions: similarity and differences in structure and in dynamics	47
<i>T. Meersmann</i>	
Hyperpolarized (hp) ^{83}Kr and hp ^{129}Xe as MRI contrast agents.....	48
<i>G. V. Mozzhukhin, G. S. Kupriyanova, S. Sh. Mamadazizov, B. Z. Rameev</i>	
Low field ^{14}N NMR as a tool for estimation of quadrupole coupling constants and correlation times in liquids.....	50
<i>A. F. Privalov, L. B. Gulina, M. Weigler, M. Vogel, I. V. Murin</i>	
Fluorine dynamics in nanosized superionic conductors as seen by NMR diffusometry	53

<i>O. N. Rogacheva, S. A. Izmailov, D. A. Luzik, S. O. Rabdano, I. S. Podkorytov, L. V. Slipchenko, M. A. Indeykina, T. F. Cunningham, Z. Hasanbasri, S. Saxena, N. R. Skrynnikov</i> When Molecular Dynamics met NMR (and various other experimental methods)	56
<i>Anna Semisalova, Craig Barton, Rantej Bali, Aisuloo Aitkulova, Kay Potzger, Roman Böttger, Kilian Lenz, Jürgen Fassbender, Thomas Thomson, Jürgen Lindner</i> From ESR to FMR – a powerful tool to investigate novel ferromagnets, illustrated with the study of tunable magnetic properties of thin metallic FeRh films	57
<i>E. Yu. Tupikina, P. M. Tolstoy, V. V. Mulloyarova, I. S. Giba, G. S. Denisov</i> How to estimate hydrogen bond energies from NMR spectra	60
ORAL REPORTS	63
<i>Ramadan Atta, Andrey A. Zolotarev, Maria E. Dmitrenko, Anastasia V. Penkova</i> Preparation and pervaporation performance of polyphenylene isophthalamide membranes modified by fullerene derivatives	64
<i>Dahiana Avila, Dmitrii Bogdanov, Delia Brauer</i> Mechanism of hydrolysis of cobalt oxide-doped bioactive phosphate glasses: ^{31}P MAS NMR, ^{31}P NMR and ESR.....	65
<i>Valeriia Baranauskaitė, Olga Pestova</i> Dynamical characteristics of the ternary systems (Chlorides of Li, Mg, and Cs) in wide temperature and concentration ranges by NMR method	67
<i>Manuel Becher, Elisa Steinrücken, Michael Vogel</i> Dynamics of Room Temperature Ionic Liquids: Structural Relaxation Probed by ^1H and ^{19}F NMR	68
<i>Sergei Bystrov, V. I. Chizhik</i> Molecular mobility in a set of imidazolium-based ionic liquids.....	70
<i>Jing Dai, Boris B. Kharkov, Sergey V. Dvinskikh</i> Multinuclear dipolar NMR spectroscopy in ionic liquid crystals.....	72
<i>S. V. Efimov, Yu. O. Zgadzay, A. V. Slivka, S. Darwish, P. P. Kobchikova</i> Various NMR approaches in studies of polypeptides: Application to insulins and cyclosporins	73
<i>Viacheslav Frolov, Konstantin Tyutyukin</i> Magnetic Resonance Imaging in Low Magnetic Field.....	76

<i>Leonid Grunin</i> Up-to-Date Industrial Applications of Time-Domain NMR.....	77
<i>Maria S. Ivanova, Leonid Yu. Grunin</i> Development of a technique for determination of total fat content in food products by NMR-relaxation	78
<i>Jarno Järvinen, Denis Zvezdov, Janne Ahokas, Sergey Vasiliev, Yutaka Fujii and Leonid Vlasenko</i> Dynamic nuclear polarization of doped silicon at high fields and low temperatures	80
<i>Alexandr A. Khrapichev</i> LiverMultiScan – a diagnostic aid for liver disease	81
<i>Andrei V. Komolkin, Irina A. Silanteva</i> Visualization of the DNA environment from the molecular dynamics simulation.....	82
<i>Lidia V. Konopleva, Oleg V. Nedopekin, Marco Reisert, Kamil A. Il'yasov</i> Optimization of based on DW MRI fiber tracking results. Simulated phantom results	85
<i>Denis D. Kosenkov, Yuriy I. Neronov, Aleksey N. Zolotov</i> Registration of NMR signals in magnetic fields of 0.13 and 2.1 T for estimation of the age-related changes in living tissues	88
<i>Benjamin Kresse, Mark Höfler, Alexei F. Privalov, and Michael Vogel</i> Spatially Resolved NMR with Micrometer Resolution in Static Field Gradients.....	91
<i>Tatiana P. Kulagina, Grigorii E. Karnaukh, Irina Yu. Golubeva</i> Evolution of polarization of three spin groups and their contribution to line shape and solid-echo NMR.....	93
<i>Galina S. Kupriyanova, George Mozhukhin, Sultonazar Mamadazizov</i> ¹⁴ N NQR relaxation in 5 aminotetrazole.....	96
<i>Manuel Arsenio Lores Guevara, Carlos Alberto Cabal Mirabal, Robert Muller, Sophie Laurent, Yulianela Mengana Torres, Juan Carlos García Naranjo</i> NMRD study of the Bound water rotational correlation time in protein solutions	98

<i>Irina Lushpinskaya, Marina Shelyapina, Sergei Kurnosenko, Oleg Silyukov, Irina Zvereva</i> Multinuclear NMR study of hybrid organic-inorganic composites: layer perovskite-like oxides $H_2La_2Ti_3O_{1.0}$ with methanol, methylamine and butylamine molecules	99
<i>Yuliana Mengana Torres, Manuel Arsenio Lores Guevara, Juan C. García Naranjo, Beatriz T. Ricardo Ferro, Edalis Guerrero Piña, Carlos Alberto Cabal Mirabal, Lidia C. Suárez Beyrio, María A. Marichal Felue, Teresa Simón Brada, Inocente C. Rodríguez Reyes, Jan Philippé</i> Evaluation of protein viscosity in Sickle Cell Disease	100
<i>G. S. Musabirova, A. V. Aganov, I. A. Latfullin, V. V. Klochkov</i> Interaction of statins with cell membrane by NMR spectroscopy	101
<i>C. Okay, A. Maraşlı, G. Mozzhukhin, B. Rameev</i> 1H NMR relaxation times of alcohol-water mixtures	103
<i>Yanina A. Pankratova, Alexander A. Pavlov</i> Application of paramagnetic NMR to the magnetic properties investigation of cobalt(II) pseudotetrahedral single-molecule magnet	106
<i>Alexander A. Pavlov and Valentin V. Novikov</i> NMR spectroscopy of paramagnetic transition metal complexes: theory and application examples	109
<i>Melanie Reuhl, Max Weigler, Nail Karabas and Michael Vogel</i> Broadband dielectric and nuclear magnetic resonance spectroscopy study on dynamics of water DMSO mixtures, glycerol, and ethylene glycol in mesoporous silica	111
<i>Ago Samoson</i> H-MAS	113
<i>Sarah Schneider, Christoph Säckel, Michael Vogel</i> Ion and molecule transport in aqueous salt solutions in bulk and in nanopores – a NMR study	114
<i>Daria Shurtakova, B. Yavkin, M. Gafurov, G. Mamin, S. Orlinskii, L. Kuznetsova, S. Bakhteev, I. Ignatyev, I. Smirnov, A. Fedotov, V. Komlev</i> Study of calcium phosphate by EPR methods	115
<i>Alexey V. Soloninin, Alexander V. Skripov, Roman V. Skoryunov, Olga A. Babanova, Jacob Grinderslev, Torben R. Jensen</i> Atomic motion in the bimetallic borohydrides $LiLa(BH_4)_3X$, $X=Cl, Br, I$: NMR study	117

<i>Vadim Zorin, Leandro Gil-Silva, Maruxa Sordo Touza, Esther Vaz, Felipe Seoane, Irakusne Lopez, Armando Navarro-Vázquez, Roberto R. Gil, Carlos Cobas</i> StereoFitter and 3D Computer-Assisted Structure Elucidation.....	120
POSTER SESSION	123
<i>Ilgiz Abdullin, Alexandr Voronin, Konstantin Tyutyukin, Andrei Komolkin, Viacheslav Frolov</i> Progressive saturation technique in ultralow field.....	125
<i>Dmitry Aleshin, Yulia V. Nelyubina, Igor Nikovskiy, Alexander V. Polezhaev, Nikolay N. Efimov, Alexander A. Pavlov</i> Spin state of 2,6-di(pyrazol-3-yl)pyridine complexes of iron(II) and cobalt(II) in solution by paramagnetic NMR method	127
<i>N. A. Antonova, A. M. Ryzhkov, A. V. Komolkin</i> Computer simulation of micelle formation in magnesium hexanoate solution	130
<i>Irina A. Avilova, Ekaterina A. Dolgikh, Olga A. Kraevaya, Aleksandr V. Zhilenkov, George A. Saratov, Yuliia V. Soldatova, Raisa A. Kotelnikova, Pavel A. Troshin, Vitaliy I. Volkov</i> Interaction of fullerene derivative with biomembranes – studied by pulsed field gradient NMR technique.....	133
<i>O. Bavrina, M. Shelyapina, K. Klyukin, A. Livshits</i> Hydrogen solubility and diffusion in V-Pd substitution alloys studied by DFT	136
<i>Yu. V. Bogachev, A. V. Nikitina</i> Simulation and optimization of pulse RF sequences for contrast enhancement of MR images in the presence of magnetic nanoparticles	139
<i>Dmitrii Bogdanov, Stanislav Sukharzhevskii, Marina Shelyapina, Yurii Zhukov, Inocente Rodriguez-Iznaga, Vitalii Petranovskii</i> EPR study of copper complexes in mordenite channels	142
<i>Inna G. Borodkina, Gennadii S. Borodkin, Igor S. Vasilchenko, Pavel B. Chepurnoy, Natalya V. Stankevich</i> Multinuclear NMR investigation of structure of coupling products of salicylaldehydes and 2-aminobenzamid	144
<i>Armando Consiglio, Andrei V. Komolkin, Tobias Cramer</i> Computer Simulations of PEDOT:PSS/solid interface	147
<i>S. Darwish, S. V. Efimov, A. A. Balandina, V. V. Klochkov</i> Behavior of cyclosporine C in solvents of different polarity	150

<i>Nina Djapic</i> Free colours tetrapyrroles: yellow.....	153
<i>Mariia E. Dmitrenko, Ramadan R. Atta, Anastasia V. Penkova</i> Development and study of novel pervaporation membranes based on polyphenylene isophthalamide, modified by Pluronic F127.....	155
<i>Alexander K. Dmitriev, Anton K. Vershovskii</i> Two-quantum optically detected resonances in NV centers in diamond in zero magnetic field.....	156
<i>Aleksandra A. Efimova, Anton S. Mazur, Lyudmila Y. Yakovleva, Peter M. Tolstoy</i> MRI study of magnetic field distortions generated by cellulose microbeads labelled with iron oxide nanoparticles in phantom samples	159
<i>Maria I. Egorova, Andrei V. Egorov, Vladimir I. Chizhik</i> Fluctuations of local electric fields at Li^+ , Cl^- , and NO_3^- ions in aqueous solution studied by Car-Parrinello molecular dynamics simulations.....	161
<i>Verena Fella, Yang Yao, George Floudas, Michael Vogel</i> Crystallisation and Dynamics of Water Confined to MCM-41	162
<i>V. V. Frolov, P. A. Kupriyanov, A. E. Shilov</i> Zonal harmonics calculation to compensate the magnetic field heterogeneity in a magnet gap	164
<i>Elena Galitskaya, Alexei Privalov, Max Weigler, Michael Vogel, Alexei Kashin, Ivan Ryzhkin, Vitaly Sinitsyn</i> NMR studies of various perfluorosulfonated membranes in wide temperature range	167
<i>Irina Yu. Golubeva, Grigorii E. Karnaukh, Tatiana P. Kulagina</i> Solid-echo signal in a three-spin system with arbitrary dipole-dipole interaction constants	170
<i>Stanislav O. Garkavyi, Ecaterina V. Schmidt, Vadim L. Matukhin, Rustem R. Khusnutdinov, Georgy V. Mozzhukhin, Nicolay K. Andreev</i> Spin lattice relaxation of nuclei in magnetic semiconductor compound CuFeS_2	173
<i>Roman V. Haponchik, Alexey B. Ustinov</i> Investigation of the nonlinear frequency shift of a ferromagnetic film resonator	176

<i>Viacheslav A. Ivanov, Anna A. Hurshkainen, Georgiy A. Solomakha, Mikhail A. Zubkov</i> Adjustable tuning range RF-coil for heteronuclear MRI.....	179
<i>O. Karatas, S. Güler, C. Okay, S. Kazan, R. Khaibullin, B. Rameev</i> Textured growth of magnetic nanoparticles in implanted TiO ₂ and ZnO single crystals as revealed by FMR	181
<i>K. Kass, A. V. Ievlev, E. Sorokina</i> The study of ionic liquids using NMR.....	184
<i>Dilorom N. Khamidova, Emil I. Fatullaev, Sofia E. Mikhtaniuk, Igor M. Neelov</i> Interaction of dendrigraft of second generation with molecules of LVFFAE peptide. Molecular dynamics simulation.....	185
<i>M. A. Khasanov, A. V. Ievlev</i> Temperature dependences of NMR spectra of ionic liquid EAN with addition of inorganic nitrates	188
<i>Rustem R. Khusnutdinov, Vasily V. Ogloblichev, Vadim L. Matukhin, Irina Yu. Arapova, Stanislav V. Shmidt</i> Nuclear spin-lattice relaxation ⁶³ Cu in semiconductor compound CuAlO ₂	190
<i>Naira R. Khusnutdinova, Aidar R. Yulmetov</i> Modeling of dynamics and calculation of relaxation parameters for monomer of bovine insulin	192
<i>I. A. Kiselev, V. A. Ryzhov, V. V. Deriglazov</i> Magnetic resonance study of the peculiarities of the paramagnetic-ferromagnetic transition in manganites on the example of La _{0.78} Ca _{0.22} MnO ₃	195
<i>V. V. Klochkov</i> Investigation of the spatial structure of different drugs, proteins & oligopeptides, and their complexes with models of cell membrane in solution by modern NMR spectroscopy.....	196
<i>Edda Klotz, Stefan Spannenberger, Marc Duchardt, Bernhard Roling, and Michael Vogel</i> NMR studies on ion dynamics in solid electrolytes for batteries	198
<i>P. P. Kobchikova, S. V. Efimov, I. A. Khodov, V. V. Klochkov</i> Studying of Cyclosporin D by High Resolution NMR: Obtaining Information on the Spatial Structure	199

<i>V. A. Konovalov, A. V. Egorov, V. I. Chizhik</i> Microstructure and dynamics of ions in mixtures of imidazolium-based ionic liquids with water. A molecular dynamics simulation study	202
<i>Pavel Kupriyanov, Vladimir I. Chizhik</i> Influence of fast fluctuation of Earth magnetic field on NMR-spectra .	203
<i>Anna I. Kuzminova, Anastasia V. Penkova, Maria E. Dmitrenko</i> Development and investigation of mixed-matrix membranes based on PVA modified by various organic nanoparticles	204
<i>Nikolai A. Kuznetsov, Alexey B. Ustinov</i> Investigation of a nonlinear phase shifter based on spin waves	205
<i>Thai Ly, Richard Yong, John E. Daniels, David Miljak</i> Single Pulse NQR for Broad Resonance Lines.....	208
<i>Veronika V. Mamontova, Andrei V. Komolkin, Irina A. Silanteva</i> Micelle formation of azobenzene-containing surfactant: investigation by molecular dynamics method	211
<i>S. E. Miktaniuk, V. V. Bezrodnyi, E. I. Fatullaev, A. A. Marchenko, E. I. Bychkova, I. M. Neelov</i> Investigation of complex of lysine dendrimer of 2nd generation with 8 molecules of therapeutic vezugen peptide by computer simulation.	213
<i>Anastasia V. Nam, Alina S. Koneva, Peter M. Tolstoy</i> Partitioning of solutes between micelles and water studied by diffusion NMR and micellar liquid chromatography	216
<i>A. S. Ostras, P. M. Tolstoy</i> Phosphine oxides as probes in study of halogen bonds: quantum chemistry approach	218
<i>Vladislav Panov, Oleg Dmitriev, Konstantin Tyutyukin, Viacheslav Frolov</i> Projection reconstruction in ultralow field MRI.....	220
<i>Vladimir I. Petrov, Anatoly S. Pazgalev and Anton K. Vershovskii</i> Isotopic shift of Xe nuclei precession frequencies caused by spatial inhomogeneity of optically oriented alkali atoms.....	222
<i>Evgeny Pestov, Dmitry Pestov, Alla Besedina, Sergei Ermak and Roman Lozov</i> On the realization of an extremely small TFC value at a magnetic resonance frequency 6.834 GHz in rubidium atomic clocks on ⁸⁷ Rb absorption cell with two anti-relaxation components (coating + buffer gas)	224

<i>Alina A. Pichugina, Larisa V. Tsyro</i> Electronic spin resonance in the study of the processes of association of gallstones	227
<i>Yu. A. Popova, S. L. Shestakov, A. Yu. Kozhevnikov, D. S. Kosyakov, A. V. Faleva</i> Application of solid-state NMR to the study of water sorption with hydrolysis lignin	230
<i>E. A. Razina, A. S. Ovsyannikov, S. E. Solovieva, I. S. Antipin, A. I. Konovalov, G. V. Mamin, M. R. Gafurov, M. S. Tagirov, S. B. Orlinskii</i> EPR of calixarenes doped by Lu^{3+} , La^{3+} , Tb^{3+} , Gd^{3+} , Yb^{3+} , Er^{3+} , Dy^{3+} ions	234
<i>A. M. Ryzhkov, N. A. Antonova, A. V. Komolkin</i> Analyzing the parameters of atom-atom interactions for Molecular dynamics simulations of micelle formation	237
<i>V. A. Salikov, I. S. Podkorytov, B. B. Kharkov and N. R. Skrynnikov</i> Protein unfolding (denaturation) as monitored by PFG NMR measurements of translational diffusion.....	241
<i>A. A. Selivanov, A. V. Ievlev</i> Temperature dependence of NMR-relaxation rate in IL BmimAc	242
<i>Oleg V. Shavykin, Valeriy V. Bezrodniy, Sofia E. Miktaniuk, Igor M. Neelov, Denis A. Markelov</i> Computer simulation of orientational dynamics in alpha- and epsilon-lysine peptides	245
<i>Oleg V. Shavykin, Maxim Yu. Ilyash, Emil I. Fatullaev, Igor M. Neelov, Denis A. Markelov</i> Molecular dynamics simulation of global and local dynamics in dendrigraft of second generation	248
<i>M. G. Shelyapina, E. A. Krylova, Yu. Zhelezniak, V. Petranovskii, R. Yocupicio-Gaxiola, J. Antunez-Garcia, S. Fuentes</i> Multinuclear NMR for structural study of lamellar mordenite and ZSM-5 zeolites	251
<i>V. Ya. Shifrin, D. I. Belyakov, D. D. Kosenkov, and A. E. Shilov</i> Precise definition of γ ^{133}Cs with resolved structure in magnetic fields higher than 0.8 mT	252
<i>S. A. Shubin, V. V. Frolov, K. V. Tyutyukin</i> Experimental results of an impact of the spin echo pulse sequence on a J-coupled two-spin system	255

<i>P. I. Simeshchenko, V. M. Cheremisin, I. G. Kamyshanskaya, M. Yu. Podgorniyak, V. V. Prits</i> Multiparameter MRI protocol for evaluating the results of surgical treatment of brain gliomas	258
<i>A. Sklyarova, V. I. Popkov, I. V. Pleshakov, V. V. Matveev, and H. Štěpánková</i> Influence of morphology on the magnetic behavior in nano-EuFeO ₃ : NMR study.....	261
<i>A. V. Slivka, S. V. Efimov, O. V. Aganova, V. V. Klochkov</i> NMR characterization of structure of cyclosporin B.....	262
<i>Janez Stepišnik, Carlos Mattea, Siegfried Stapf and Aleš Mohorič</i> Measurements of molecular velocity auto-correlation of water in mixtures with glycerol by NMR MGSE method	265
<i>K. T. Smolyarov, A. N. Matsulev, A. A. Kondrasenko</i> Investigation of Re-Pt vinylidene complex Cp(CO) ₂ RePt(μ-C=CHPh)(PPh ₃) ₂ by solid-state NMR	268
<i>Larisa V. Tsyro, Alina A. Pichugina</i> Analysis of the kerns of the Yuzhno-Cheremshansky field by the method of electron spin resonance	271
<i>Milosh Ubovich, Sergei A. Izmailov, Andrei V. Egorov</i> Conformational dynamics of the two-domain Pax5 protein in aqueous solution. A molecular dynamics simulation study	274
<i>E. I. Uskova, I. H. Fatkhutdinov, M. M. Dorogynitskii, V. D. Skirda</i> NMR method for assessing the inhibitory properties of drilling fluids .	276
<i>N. I. Uskova, D. Yu. Podorozhkin, E. V. Charnaya, D. Yu. Nefedov, S. V. Baryshnikov</i> NMR studies of nanocomposite based on the organic ferroelectric DIPAB.....	279
<i>S. Vasiliev, J. Ahokas, J. Järvinen, S. Sheludiakov, V. V. Khmelenko and D. M. Lee</i> Magnetic resonance studies of atomic hydrogen in porous Ne at ultra-low temperatures	281
<i>Siqi Wang, Alexander S. Filatov, Alexander V. Stepakov, Stanislav I. Selivanov</i> Synthesis and NMR study of adducts of ninhydrin-derived azomethine ylide with cyclopropenes	282

*Radik R. Zaynullin, Stanislav O. Garkavyi, Ekaterina V. Shmidt,
Stanislav V. Shmidt, Vadim L. Matukhin, Nikolay K. Andreev,
Erika Dutkova*
NMR and EPR in mechanochemically synthesized chalcopyrite
nanocrystals.....285

Aleksey N. Zolotov, Yuriy I. Neronov, Denis D. Kosenkov
Some capabilities of the NMR relaxometer for evaluation of the age-
related changes in muscle tissue289

POEMS ABOUT SCHOOL 293

AUTHOR INDEX..... 297

Schedule of Spinus-2019

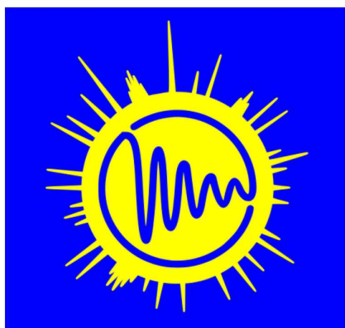
	31.03.19 Sunday	01.04.19 Monday	02.04.19 Tuesday	03.04.19 Wednesday	04.04.19 Thursday	05.04.19 Friday	06.04.19 Saturday
08:45 – 10:00		BREAKFAST				9:10-10:30 BREAKFAST	BREAKFAST
10:00 – 11:30		Registration 30 Opening 10 Chizhik 30 GROUP PHOTO 20	Tolstoy 40 Zorin 20 Järvinen 15 Baranauskaite 15	Excursion Day	Cabal 40 Lores I 20 Lores II 15 Musabirova 15	Matveev 30 Bystrov 15 Khrapichev 15	Departure
11:30 – 12:00		COFFEE BREAK			COFFEE BREAK		
12:00 – 14:00		Privalov 40 Schneider 15 Kresse 15 Reuhl 15 Lushpinskaya 15 Soloninin 20	Fraissard 40 Meersmann 40 Samoson 20 Dvinskikh 20		Eichhoff 40 Efimov 15 Skrynnikov 40 Komolkin 25	Michel 40 Semisalova 40 Shurtakova 15 Avila 15 Neronov 15	
14:00 – 15:30		LUNCH			LUNCH		
15:30 – 17:00		Charnaya 40 Pavlov 20 Pankratova 15 Lahderanta 15	Atta 15 Oral blitz reports of young scientists (5min x 15)		Konopleva 15 Oral blitz reports of young scientists (5min x 15)	Bunkov 40 Kupriyanova 20 Mozzhukhin 40	
17:00 – 17:30	Registration of participants	COFFEE BREAK			COFFEE BREAK		
17:30 – 19:00		Becher 15 Kulagina 20 Rameev 20 Ivanova 15 Grunin 20	POSTER SESSION I		POSTER SESSION II	Awarding Closing	
19:00 – 20:00		DINNER				DINNER	
20.00	Welcome	Cultural and sporting activities			CONFERENCE DINNER		

Schedule

16-th International School-Conference «Magnetic Resonance and its Applications. Spinus-2019»

March 31 – April 05, 2019

St. Petersburg



SUNDAY – 31 March 2019	
14:00 – 15:30	LUNCH
15:30 – 19:00	REGISTRATION OF PARTICIPANTS
19:00 –	WELCOME PARTY «EVENING IN KARELIA»

MONDAY – 01 April 2019	
08:45 – 10:00	BREAKFAST
10:00 – 10:30	Registration
10:30 – 10:40	Opening
10:40 – 11:10	Vladimir I. Chizhik (Saint-Petersburg, Russia) Lecture: Possibilities, Peculiarities and Areas of Applications of Quantitative Analysis by NMR in Magnetic Field of the Earth
11:10 – 11:30	GROUP PHOTO
11:30 – 12:00	COFFEE BREAK
12:00 – 12:40	Alexei Privalov (Darmstadt Germany) Lecture: Fluorine dynamics in nanosized superionic conductors as seen by NMR diffusometry
12:40 – 12:55	Sarah Schneider (Darmstadt, Germany) Oral report: Ion and Molecule Transport in Aqueous Salt Solutions in Bulk and in Nanopores - a NMR study
12:55 – 13:10	Benjamin Kresse (Darmstadt, Germany) Oral report: Spatially Resolved NMR with Micrometer Resolution in Static Field Gradients
13:10 – 13:25	Melanie Pia Reuhl (Darmstadt, Germany) Oral report: Broadband Dielectric and Nuclear Magnetic Resonance Spectroscopy Study on Dynamics of Water DMSO Mixtures, Glycerol, and Ethylene Glycol in Mesoporous Silica
13:25 – 13:40	Irina Lushpinskaya (Saint-Petersburg, Russia) Oral report: Multinuclear NMR study of hybrid organic-inorganic composites: layer perovskite-like oxides $H_2La_2Ti_3O_{10}$ with methanol, methylamine and butylamine molecules
13:40 – 14:00	Alexey Soloninin (Ekaterinburg, Russia) Oral report: Atomic Motion in the Bimetallic Borohydrides $LiLa(BH_4)_3X$ X=Cl, Br, I: NMR Study
14:00 – 15:30	LUNCH
15:30 – 16:10	Elena Charnaya (Saint-Petersburg, Russia) Lecture: NMR studies of bulk and nanostructured ferroelectrics
16:10– 16:30	Alexander Pavlov (Moscow, Russia) Oral report: NMR Spectroscopy of Paramagnetic Transition Metal Complexes: Theory and Application Examples
16:30– 16:45	Yanina Pankratova (Moscow, Russia) Oral report: Application of Paramagnetic NMR to the Magnetic Properties Investigation of Cobalt(II) Pseudotetrahedral Single-Molecule Magnet
16:45– 17:00	Erkki Lahderanta (Lappeenranta, Finland) Oral report: Masters Degree Programme in Lappeenranta

17:00 – 17:30	COFFEE BREAK
17:30 – 17:45	Manuel Becher (Darmstadt, Germany) Oral report: Dynamics of Room Temperature Ionic Liquids: Structural Relaxation Probed by ^1H and ^{19}F NMR
17:45 – 18:05	Tatiana Kulagina (Chernogolovka, Russia) Oral report: Evolution of polarization of three spin groups and their contribution to line shape and solid-echo NMR
18:05 – 18:25	Rameev (Gebze, Turkey) ^1H NMR relaxation times of alcohol-water mixtures
18:25 – 18:40	Maria Ivanova (Yoshkar-Ola, Russia) Oral report: Development of a technique for determination of total fat content in food products by NMR-relaxation
18:40 – 19:00	Leonid Grunin (Yoshkar-Ola, Russia) Oral report: Up-to-Date Industrial Applications of Time-Domain NMR
19:05 – 20:00	DINNER
20:00 –	CULTURAL AND SPORTING ACTIVITIES

TUESDAY – 02 April 2019	
08:45 – 09:45	BREAKFAST
10:00 – 10:40	Petr Tolstoy (Saint-Petersburg, Russia) Lecture: How to estimate hydrogen bond energies from NMR spectra
10:40 – 11:00	Vadim Zorin (Santiago de Compostela, Spain) Oral report: StereoFitter and 3D Computer-Assisted Structure Elucidation
11:00 – 11:15	Jarno Järvinen (Turku, Finland) Oral report: Dynamic Nuclear Polarization of Doped Silicon at High Fields and Low Temperatures
11:15 – 11:30	Valeriia Baranaukaite (Saint-Petersburg, Russia) Oral report: Dynamical Characteristics of the Ternary Systems (Chlorides of Li, Mg, and Cs) in Wide Temperature and Concentration Ranges by NMR Method.
11:30 – 12:00	COFFEE BREAK
12:00 – 12:40	Jacques Friassard (Paris, France) Lecture: Xe NMR Technique: Various Applications
12:40 – 13:20	Thomas Meersmann (Nottingham, United Kingdom) Lecture: Hyperpolarized (hp) ^{83}Kr and hp ^{129}Xe as MRI Contrast Agents
13:20 – 13:40	Ago Samoson (Tallinn, Estonia) Oral report: H-MAS
13:40 – 14:00	Sergey Dvinskikh (Stockholm, Sweden) Oral report: Multinuclear Dipolar NMR Spectroscopy in Ionic Liquid Crystals
14:00 – 15:30	LUNCH
15:30 – 15:45	Ramadan Atta (Damietta, Egypt) Oral report: Preparation and Pervaporation Performance of Polyphenylene Isophthalamide Membranes Modified by Fullerene Derivatives
15:45–17:00	Oral blitz reports of young scientists (5min × 15); see speakers below in the list of POSTER SESSION I
17:00 – 17:30	COFFEE BREAK
17:30 – 19:00	POSTER SESSION I
19:00 – 20:00	DINNER
20:00 –	CULTURAL AND SPORTING ACTIVITIES

	WEDNESDAY - 03 April 2019
08:45 - 09:45	BREAKFAST
	EXCURSION DAY
19:00 - 20:00	DINNER
20:00 -	

THURSDAY – 04 April 2019	
08:45 – 09:45	BREAKFAST
10:00 – 10:40	C. Cabal Mirabal (Havana, Cuba) Lecture: MRI Synopsis of the Physical and Hardware bases.
10:40 – 11:00	Guzel Musabirova (Kazan, Russia) Oral report: Interaction of Statins with Cell Membrane by NMR Spectroscopy
11:00 – 11:15	Manuel Arsenio Lores Guevara (Santiago de Cuba, Cuba) Oral report: Evaluation of Protein Viscosity in Sickle Cell Disease
11:15 – 11:30	Manuel Arsenio Lores Guevara (Santiago de Cuba, Cuba) Oral report: NMRD study of the Bound water rotational correlation time in protein solutions
11:30 – 12:00	COFFEE BREAK
12:00 – 12:40	Uwe Eichhoff (Rheinstetten, Germany) Lecture: The human brain: development and aging explored by MRI.
12:40 – 12:55	Sergey Efimov (Kazan, Russia) Oral report: Various NMR Approaches in Studies of Polypeptides: Application to Insulins and Cyclosporins
12:55 – 13:35	Nikolai R. Skrynnikov (West Lafayette, USA) Lecture: When Molecular Dynamics met NMR (and various other experimental methods)
13:35 – 14:00	Andrei Komolkin (Saint-Petersburg, Russia) Oral report: Visualization of the DNA Environment from the Molecular Dynamics Simulation
14:00 – 15:30	LUNCH
15:30 – 15:50	Lidia Konopleva (Kazan, Russia) Oral report: Optimization of based on DW MRI fiber tracking results. Simulated phantom results
15:50 – 17:00	Oral blitz reports of young scientists (5min × 14); see speakers below in the list of POSTER SESSION II
17:00 – 17:30	COFFEE BREAK
17:30 – 19:00	POSTER SESSION II
20:00 –	CONFERENCE DINNER
	FRIDAY – 05 April 2019

09:10 – 10:30	BREAKFAST
10:30 – 11:00	Vladimir Matveev (Saint-Petersburg, Russia) Lecture: Comparison of Ionic Liquids and Highly Concentrated Electrolyte Solutions: Similarity and Differences in Structure and in Dynamics
11:00 – 11:15	Sergei Bystrov (Saint-Petersburg, Russia) Oral report: Molecular Mobility in a Set of Imidazolium-based Ionic Liquids
11:15 – 11:30	Alexandr Khrapichev (Oxford, United Kingdom) Oral report: LiverMultiScan – a diagnostic aid for liver disease
11:30 – 12:00	COFFEE BREAK
12:00 – 12:40	Dieter Michel (Leipzig, Germany) Lecture: EPR and NMR Study of Nitric Oxide - an Interesting Molecule for Bio-Medical Applications
12:40 – 13:20	Anna Semisalova (Dresden, Germany) Lecture: From ESR to FMR – a Powerful Tool to Investigate Novel Ferromagnets, Illustrated with the Study of Tunable Magnetic Properties of Thin Metallic FeRh Films
13:20 – 13:35	Daria Shurtakova (Kazan, Russia) Oral report: Study of Calcium Phosphate by EPR Methods
13:35 – 13:50	Dahiana Avila (Jena, Germany) Oral report: Mechanism of Hydrolysis of Cobalt Oxide-Doped Bioactive Phosphate Glasses: P-31 MAS NMR, P-31 NMR and ESR
13:50 – 14:05	Yuriy Neronov (Saint-Petersburg, Russia) Registration of NMR Signals in Magnetic Fields of 0.13 and 2.1 T for Estimation of the Age-Related Changes in Living Tissues
14:05 – 15:30	LUNCH
15:30 – 16:10	Yury Bunkov (Kazan, Russia) Lecture: Spin Superfluidity at room temperature
16:10 – 16:30	Galina Kupriyanova (Kaliningrad, Russia) Oral report: ^{14}N NQR relaxation in 5 Aminotetrazole
16:30 – 17:10	Georgy Mozzhukhin (Gebze, Turkey) Lecture: Low field ^{14}N NMR as a tool for estimation of quadrupole coupling constants and correlation times in liquids
17:10 – 17:30	COFFEE BREAK
17:30 – 18:00	AWARDING CLOSING
19:00 – 20:00	DINNER

	SATURDAY - 06 April 2019
08:45 - 09:45	BREAKFAST
	DEPARTURE

POSTER SESSION I (Tuesday, 17:30 – 19:00)		
1	Vladimir Petrov	Isotopic shift of Xe nuclei precession frequencies caused by spatial inhomogeneity of optically oriented alkali atoms.
2	Milosh Ubovich	Conformational dynamics of the two-domain Pax5 protein in aqueous solution. A molecular dynamics simulation study.
3	Alina Pichugina	Electron spin resonance in the study of association processes of gallstones
4	Viacheslav Frolov	Zonal harmonics calculation to compensate a magnetic field heterogeneity in a magnet gap
5	Dmitrii Bogdanov	EPR study of copper complexes in mordenite channels
6	Polina Kobchikova	Studying of Cyclosporin D by High Resolution NMR: Obtaining Information on the Spatial Structure
7	Irina Avilova	Interaction of fullerene derivative with biomembranes - studied by pulsed field gradient NMR technique
8	Mariia Dmitrenko	Development and study of novel pervaporation membranes based on polyphenylene isophthalamide, modified by Pluronic F127
9	Thai Ly	Single Pulse NQR for Broad Resonance Lines
10	Ksenia Kass	The study of ionic liquids using NMR.
11	Elena Razina	EPR of Calixarenes Doped by Lu, La, Tb, Gd, Yb, Er, Dy Ions
12	Markus Rosenstihl	DAMARIS – An open source NMR instrumentation software
13	Verena Fella	Crystallisation and Dynamics of Water Confined to Mesoporous Silica
14	Edda Klotz	NMR studies on ion dynamics in solid electrolytes for Li-ion batteries
15	Siqi Wang	Synthesis and NMR study of adducts of ninhydrin-derived azomethine ylide with cyclopropenes.
16	Armando Consiglio	Computer Simulations of PEDOT:PSS/solid interface
17	Anton Ryzhkov	Analyzing the parameters of atom-atom interactions for Molecular dynamics simulations of micelle formation.
18	Alexander Selivanov	NMR Relaxation in ionic liquid Bmim-AC, comparison on different frequency
19	Alexandra Slivka	NMR characterization of structure of cyclosporin B
20	Shaza Darwish	Behavior of cyclosporine C in solvents of different polarity
21	Irina Golubeva	Solid-echo signal in a three-spin system with arbitrary dipole-dipole interaction constants
22	Natalya Uskova	NMR studies of nanocomposite based on the organic ferroelectric DIPAB

23	Anna Kuzminova	Development and investigation of mixed-matrix membranes based on PVA modified by various organic nanoparticles
24	Elena Galitskaya	NMR STUDIES OF VARIOUS PERFLUOROSULFONATED MEMBRANES IN WIDE TEMPERATURE RANGE
25	Elena Uskova	NMR method for assessing the inhibitory properties of drilling fluids
26	Nadezhda Antonova	Computer simulation of micelle formation in magnesium hexanoate solution
27	Roman Haponchik	Investigation of the nonlinear frequency shift of a ferromagnetic film resonator
28	Nikolay Kuznetsov	Investigation of a nonlinear phase shifter based on spin waves
29	Magomed Khasanov	Temperature dependences of NMR spectra of ionic liquid EAN with addition of inorganic nitrates
30	Julia Popova Anna Faleva	Application of solid-state NMR to the study of water sorption with hydrolysis lignin
31	Ozgul Karatas	Textured growth of magnetic nanoparticles in implanted TiO ₂ and ZnO single crystals as revealed by FMR
32	Ilgiz Abdullin	Progressive saturation technique in ultralow field

POSTER SESSION II (Thursday, 17:30 – 19:00)		
1	Veronika Mamontova	Micelle formation of azobenzene-containing surfactant: investigation by molecular dynamics method
2	Pavel Kupriyanov	Influence of fast fluctuation of Earth magnetic field on NMR-spectra
3	Nina Djapic	Free colours tetrapyrroles: yellow
4	Igor kiselev	Magnetic resonance study of the peculiarities of the paramagnetic-ferromagnetic transition in manganites on the example of La _{0.78} Ca _{0.22} MnO ₃
5	Anastasia Kozlenko	Study of a new salt spiropyran structure containing carbomethoxy group in the 6'-position of 2H-chromene moiety
6	Konstantin Smolyarov	Investigation of Re-Pt vinylidene complex Cp(CO) ₂ RePt(μ-C=CHPh)(PPh ₃) ₂ by solid-state NMR
7	Anastasia Nikitina	Simulation and optimization of pulse RF sequences for contrast enhancement of MR images in the presence of magnetic nanoparticles
8	Olga Bavrina	Hydrogen solubility and diffusion in V-Pd substitution alloys studied by DFT
9	Dmitry Aleshin	Spin state of 2,6-di(pyrazol-3-yl)pyridine complexes of iron(II) and cobalt(II) in solution by paramagnetic NMR method
10	Aleksandra Efimova	MRI study of magnetic field distortions generated by cellulose microbeads labelled with iron oxide nanoparticles in phantom samples
11	Oleg Shavykin	Computer simulation of orientational dynamics in alpha- and epsilon-lysine peptides
12	Alina Pichugina	Analysis of the kerns of the Yuzhno-Cheremshansky field by the method of electron spin resonance
13	Ekaterina Krylova	Multinuclear NMR for structural study of lamellar mordenite and ZSM-5 zeolites
14	Alexander Dmitriev	Two-quantum optically detected resonances in NV centers in diamond in zero magnetic field.
15	Roman Lozov	On the realization of the extremely small value of a TFC at the frequency 6.834 GHz of atomic magnetic resonance in quantum frequency standards on 87Rb-absorption cells containing two anti-relaxation components (coating + inert gas)
16	Oleg Shavykin	Molecular dynamics simulation of global and local dynamics in dendrigraft of second generation
17	Emil Fatullaev	Interaction of dendrigraft of second generation with molecules of LVFFAE peptide. Molecular dynamics simulation

18	Sofia Mikhtaniuk	Investigation of complex of lysine dendrimer of 2nd generation with 8 molecules of therapeutic vezugen peptide by computer simulation
19	Alexey Ostras	Phosphine Oxides as Probes In Study of Halogen Bonds: Quantum Chemistry Approach
20	Maria Egorova	Fluctuations of local electric fields at Li+, Cl-, and NO3- ions in aqueous solution studied by Car-Parrinello molecular dynamics simulations
21	Anastasia Nam	Partitioning of solutes between micelles and water studied by diffusion NMR and micellar liquid chromatography
22	Radik Zaynullin	NMR and EPR in mechanochemically synthesized chalcopyrite nanocrystals
23	Vladislav Konovalov	Microstructure and dynamics of ions in mixtures of imidazolium-based ionic liquids with water. A molecular dynamics simulation study.
24	Stanislav Garkavyi	Nuclear spin-lattice relaxation ⁶³ Cu in semiconductor compound CuAlO ₂
25	Pavel Simeshchenko	Multiparameter MRI protocol for evaluating the results of surgical treatment of brain gliomas
26	Rustem Khusnutdinov	Spin-Lattice Relaxation of nuclear spins in magnetic semiconductor CuFeS ₂
27	Viacheslav Ivanov	Adjustable tuning range RF-coil for heteronuclear MRI
28	Naira Khusnutdinova	Modeling of dynamics and calculation of relaxation parameters for monomer of bovine insulin
29	Vladislav Salikov	Protein unfolding (denaturation) as monitored by PFG NMR measurements of translational diffusion
30	Sergey Shubin	Experimental results of an impact of the spin echo pulse sequence on a J-coupled two-spin system
31	Vladislav Panov	MRI projection technique in low magnetic field
32	Anastasia Sklyarova	Influence of morphology on the magnetic behavior in nano-EuFeO ₃ : NMR study



Spinus

Welcome to the School-Conference “Spinus” of Saint Petersburg State University

The St. Petersburg State University (SPSU) holds International School-Conference “Magnetic resonance and its application” Spinus-2019 in the 16th time. “Spinus” is organized in according to the subjects of researches and master’s degree programs, which are developed and implemented in the SPSU. In modern physics, the term “magnetic resonance” refers to a set of phenomena accompanied with the emission or absorption of electromagnetic waves of the radiofrequency diapason by quantum systems (nuclei, electrons, atoms, molecules, etc.). These phenomena, the physical nature of which is of independent interest, provided the basis of radiospectroscopic methods for studying the structure of matter and physical-chemical processes in it. They are also used for the creation of quantum generators, amplifiers, and magnetometers. For the development of ideas and applications of magnetic resonance six Nobel Prizes were awarded in the areas of physics, chemistry, biology, physiology and medicine (the latter was in 2003).

Primarily, magnetic resonance methods are:

- Nuclear Magnetic Resonance (NMR)
- Electron Paramagnetic Resonance (EPR)
- Nuclear Quadrupole Resonance (NQR)

These methods, being contactless, do not destroy an object under a study, that makes them unique and in demand not only in physics and chemistry, but also in medicine, geology, biology, archeology. Now, any medical center with high reputation has a magnetic resonance imaging (MRI). In Russia, NMR is used in oil well logging, laboratory analysis of the productivity of oil-bearing reservoirs, analysis of oil content and moisture of seeds; EPR technique is used for geological research, non-destructive control of precious stones, as well as for the dating of paleontological artifacts; there are NQR applications for remote detection of solid explosives and narcotics. Magnetometry methods based on magnetic resonance are indispensable for carrying out archaeological researches.

The designation “school-conference” means that, on the one hand, the organizers include in the program the lectures, which reflect the basics of magnetic resonance and current state of knowledge and experience in this field, and, on the other hand, as well as at any conference it is expected to discuss new results, obtained by young scientists, using magnetic resonance techniques. It should be emphasized that our school-conference aims not only to researchers specializing in the field of magnetic resonance, but also to representatives of other sciences, where these methods can be successfully applied.

Earlier the school organizers worked at the Department of quantum magnetic phenomena (QMPH) of the St. Petersburg State University, which was founded in 1993 on the initiative of Professor V. I. Chizhik on the basis of the laboratory, created in the 50s of the last century by F. I. Skripov at the Department of Radio Physics (the branch “Quantum Radiophysics”). On January 1, 2014, the Department of QMPH joined the united Department of nuclear-physics research methods (Head of the Department is Corresponding Member of the Russian Academy of Sciences, Professor Mikhail Kovalchuk). The QMPH collective has a number of priority works in the field of nuclear magnetic resonance. One of the most significant achievements was the first in the world implementation (in 1958) of the Fourier transform of a free induction signal in order to obtain a NMR spectrum. Concurrently with the research activity, the staff of the department are actively involved in the development of practical applications of magnetic resonance. The department graduates work not only in Russia and the CIS, but also in Sweden, USA, New Zealand, England, Cuba, Germany, France, Italy, occupying positions from a highly advanced operator of radiospectrometers to a professor.

The main research areas developing in the team of quantum magnetic phenomena:

- Nuclear magnetic relaxation in liquids;
- Nuclear magnetic resonance in solids, including magnetically ordered materials;
- NMR in liquid crystals;
- NMR in heterogeneous systems;
- MRI in weak magnetic fields;
- Electron paramagnetic resonance;
- Nuclear magnetic resonance in the magnetic field of the Earth;
- The quantum magnetometry in archeology.

It is evident from the above that the scope of our research interests is quite wide. We are always open for the collaboration with researchers from various fields of science.

Our team has published a series of monographs, textbooks and training manuals on Magnetic Resonance. For example:

1. Vladimir I. Chizhik, Yuri S. Chernyshev, Alexey V. Donets, Viatcheslav Frolov, Andrei Komolkin, Marina G. Shelyapina. Magnetic Resonance and Its Applications. 2014, Springer-Verlag. 782 pp. (*Now about 27800 downloads*).
2. Квантовая радиофизика: магнитный резонанс и его приложения. Учеб. пособие. 2-е изд., перераб. Под ред. В. И. Чижика. – СПб.: Изд-во С.-Петерб. ун-та, 2009. 700 с.
3. В. И. Чижик. Ядерная магнитная релаксация. Учеб. пособие. 3-е изд. – СПб.: Изд-во С.-Петерб. ун-та, 2004. 388 с.
4. Практикум по магнитному резонансу. Учебное пособие. Под ред. В. И. Чижика. – СПб.: Изд-во С.-Петерб. ун-та, 2003. 184 с.



*Dr. Sci., Professor, SPSU, Denis A. Markelov
Chairman of Organizing committee of the 16th School-conference
“Magnetic resonance and its applications” Spinus-2019*

Lectures

NMR studies of bulk and nanostructured ferroelectrics

E. V. Charnaya¹, S. V. Baryshnikov²

¹*St. Petersburg State University, St. Petersburg, 198504 Russia*

²*Blagoveschensk State Pedagogical University, Blagoveschensk, 675002 Russia*

E-mail: charnaya@mail.ru

Introduction

We present in this lecture a short review of our last studies of ferroelectric materials using Nuclear magnetic resonance (NMR). The main attention is focused on the impact of size reduction on the temperatures of structural phase transitions in ferroelectric nanoparticles embedded into nanoporous matrices (porous glasses, molecular sieves, porous alumina, and opals). Recent results on new organic bulk and nanostructured ferroelectrics are also reported.

Samples and experiment

The samples under study are the sodium nitrite (NaNO_2) nanoparticles embedded into mesoporous sieves and porous alumina as well as those of its alloys, the Rochelle salt nanoparticles confined to the similar porous matrices, bulk and nanostructured KDP and DKDP (with two different levels of deuteration, 80% and more than 95%), and newly discovered organic ferroelectrics diisopropylammonium chloride (DIPAC), diisopropylammonium bromide (DIPAB), and their nanoparticles within silica opal matrices.

The measurements were performed using pulse Bruker Avance 400 NMR spectrometers in the temperature ranges which covered the ferroelectric phase transitions. The temperature variations of the NMR lineshape, line positions (chemical shifts), and nuclear spin-lattice relaxation rate were observed. The structural phase transitions were detected by alterations in the NMR characteristics mentioned above. For the organic ferroelectric materials we used a standard ^{13}C cross-polarization MAS pulse sequence.

Results

It was shown that confined NaNO_2 and $\text{NaNO}_2\text{-KNO}_3$ mixtures within the MCM-4a molecular sieves below the bulk melting point consisted of two parts with relaxation times which differ by two orders in magnitude [1]. A fraction under confinement exhibited bulk-like properties with the ferroelectric phase transition temperature slightly lower than the bulk transition temperature. This fraction prevailed below and near the ferroelectric phase transition and its amount decreased strongly when increasing temperature. Fast nuclear relaxation in another fraction revealed very high molecular mobility. It dominates above 510 K. It was suggested that fast relaxation corresponds to melted or pre-melted state caused by confinement. The correlation time of electric field gradient fluctuations was found for this part to be similar to those in viscous liquids and the activation energy was evaluated. The similarity of ferroelectric properties in confined and bulk was discussed and ascribed to the influence of long-distance interparticle electric coupling. In contrast, the ferroelectric phase transition temperature for NaNO_2 embedded into porous alumina increased compared to bulk [2].

^{23}Na MAS and MQ MAS NMR spectra revealed a complex structure of Rochelle salt within molecular sieves [3]. The major part of particles within molecular sieves had a structure similar to that of bulk Rochelle salt with phase transitions slightly shifted to low temperatures. The lower transition temperature increased for Rochelle salt embedded into porous alumina. The upper phase transition within porous alumina shifted to high temperatures above the decomposition range.

The ferroelectric phase transition in bulk KDP was found to correlate with the step-like changes in the chemical shift and lineshape [4]. No changes corresponded to the ferroelectric

transition were seen for KDP within porous glasses [5]. Similar results were obtained for the bulk deuterated samples.

The changes of ^{31}P NMR line shape and line position due to the ferroelectric phase transition were observed for two kinds of deuterated nanoparticles embedded into opals. The parameters of the chemical shift tensors were calculated on the basis of the obtained results. The phase transition temperatures were found to decrease compared to bulk (Fig. 1).

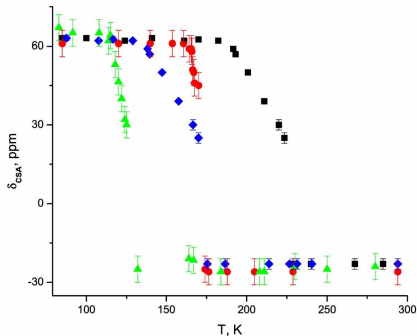


Figure 1. Temperature dependence of the ^{31}P chemical shift anisotropy for two deuterated DKDP samples, bulk and embedded into opals

The ^{13}C CP-MAS NMR spectra of DIPAC, bulk and embedded into opal matrices demonstrated signals from five nonequivalent carbon positions below the phase transition and three nonequivalent carbon positions above the phase transition. The clear shift of the phase transition temperature in the nanocomposite compared to bulk was not detected. However, the results showed that structural changes in bulk and nanoconfined DIPAC are more complicated than previously thought.

The NMR studies revealed complex spectra of DIPAB due to the coexistence of two different crystalline structures at room temperature. Only two lines were observed above the temperature of the ferroelectric phase transition for both samples which correspond to two nonequivalent carbon groups.

In conclusion, our studies demonstrated that NMR is a powerful probe to get information on nanostructured ferroelectric materials and to reveal changes compared to bulk induced by size reduction and influence of confinement.

References

1. C. Tien, E.V. Charnaya, M.K. Lee, et al. Coexistence of melted and ferroelectric states in sodium nitrite within mesoporous sieves. – *Phys. Rev. B* **72**, 104105 (2005).
2. C. Tien, E.V. Charnaya, D.Y. Podorozhkin, et al. Ferroelectricity and gradual melting in NaNO_2 particles confined within porous alumina. – *Phys. Status Solidi b* **246**, 2346-2351 (2009).
3. C. Tien, E.V. Charnaya, M.K. Lee, et al. NMR studies of structure and ferroelectricity for Rochelle salt nanoparticles embedded into mesoporous sieves. – *J. Phys.: Cond. Matter* **20**, 215205 (2008).
4. N.I. Uskova, D.Y. Podorozhkin, E.V. Charnaya, et al. Nuclear magnetic resonance study of potassium dihydrophosphate. – *Phys. Solid State* **58**, 685–688 (2016).
5. N.I. Uskova, D.Y. Podorozhkin, E.V. Charnaya, et al. NMR and dielectric studies of ferroelectric nanocomposites with KDP. – *Ferroelectrics* **514**, 50–60 (2017).

Supermagnonics at room temperature

Yury Bunkov

Russian Quantum Center, Moscow, Russia

Institut Neel, Grenoble, France

E-mail: Yury.bunkov@neel.cnrs.fr

The Electronics is the field of science which describes the non-linear behavior of electric current. It was developed for a century. Later there was observed the phenomenon of supercurrent – the coherent transport of electrons without friction. This effect forms the basis of new types of electronics – Superelectronics. The main element of Superelectronics is the Josephson connection – the interference between the coherent wave function of electrons on a two sides of weak connection. This effect leads to a construction of SQUID, the supersensitive devise which can measure of a quant of magnetic field. The circuits with SQUID may be used as an element of quantum memory.

Later the new types of non-linear phenomena were developed – Spintronics and Magnonics. In the first case the magnetic moment of electrons takes in to account. Indeed, the Superspintronics does not exist because the electron Cooper pairs has a zero magnetic moment. The Magnonics case refers to information transport and signals processing by spin waves. A magnon current has advantages as compared to a conventional spin-polarized electron current. It does not involve the motion of electrons and, thus, it is free of Joule heat dissipation. In low-damping magnetic dielectrics (for example, yttrium-iron-garnet, YIG) magnons can propagate over millimeters distances whereas an electron-carried spin current is limited by the spin diffusing length, which does not exceed one micrometre.

Indeed the coherent magnon transport was observed about 30 years ago in Kapitza Institut. In different with a simple magnonics, the magnetization transport by Supermagnonics described by a coherent state of magnons – the magnons Bose Condensate. Its gradient leads to a Spin Supercurrent. There was observed the Josephson Effect, the main nonlinear effect of Supermagnonics. The Supermagnonics was observed in superfluid $^3\text{He-B}$. Magnetic superfluid $^3\text{He-B}$ is a 3 sublattice antiferromagnetic. The other examples, where the magnons BEC was observed are superfluid $^3\text{He-A}$, nuclear-electron precession in antiferromagnets (MnCO_3 , CsMnF_3). Recently the conventional magnon BEC of magnons with $k=0$ was observed in YIG at room temperature. The phenomenon of Supermagnonics and Josephson Effect in YIG will be presented in the lecture.

References

1. *Yu. M. Bunkov, G. E. Volovik* “Spin superfluidity and magnon BEC”
2. Chapter IV of the book “Novel Superfluids”, eds. K. H. Bennemann and J. B. Ketterson, Oxford University press, (2013) *arXiv:1003.4889v3*
3. Yury Bunkov, “Magnon BEC Versus Atomic BEC” *J. Low Temp. Phys.*, 183, DOI 10.1007/s 10909-016-1583-z (2016)

MRI Synopsis of the Physical and Hardware bases

Carlos Cabal Mirabal

Physics Faculty Havana University, Cuba

E-mail: carlos.cabal@fisica.uh.cu

A didactic general overview of the Magnetic Resonance Imaging (MRI) is presented. The role of different electromagnetic fields in the images formation. Similarly, the relationship between these fields are discussed [1-8]:

- Intensity, stability and homogeneous of external homogeneous Magnetic field (B_0),
- The pulse shape, stability and intensity of Gradient of the Magnetic Field
- The intensity, modulation's law and pulse duration of Radiofrequency field (RFB1)

The requirements and characteristics of these fields in order to make possible the MR imaging are emphasizing. Phase and frequency codification as a base of the Fourier images are presented. The Phase space are defined. The 2D and 3D Spin Echo (SE) and Gradient Echo (GE) pulse sequences are deliberated [1-8].

The connection between the Gradients characteristics, Field of View (FOV), Spatial and Spectral resolutions, the matrix dimension and Images Time is considerate.

The Phase space characteristics for different pulse sequences and its connection with the image's characteristics are discussed. The relationship between the Images Contrast, Contrast Noise ratio, Signal Noise ratio and Images Time of the images are briefly evaluated. Similarly, the image's distortions and artifacts evaluate [1-8].

The possibilities and challenges of the MRI focusing in the physical and technological opportunities and restrictions, are presented. Undesirable situations related to fields interactions and eddy currents it is examined. Some methods to overcome these unwanted conditions are deliberated.

Different alternatives to decrease the Images Time keeping and even improving the images characteristics are exposed: diverse pulse sequences, the array of RF coils and the parallel imaging including the use of localized gradients by no linear gradients [3-9].

The original, simple and useful case of the Single-side NMR is concisely commented [10].

Cuban's experiences concerning to the calculation, design, construction and validation Magnetic Resonance (MR) technology and introduction in the clinical practice are mention. Cuban MR Technology includes MR relaxometer, Magnetometers and MRI whole body machines.

Acknowledgements

The author express gratitude to Prof. Dr. V.I. Chizhik and to the collective of Medical Biophysics Centre of University of Oriente, Cuba.

References

1. R.W. Brown, Yu-Chung N. Cheng, E. Mark Haacke, M. R. Thomson, R. Venkatesan, "Magnetic Resonance Imaging Physical Principles and Sequence Design" Second edition, Willey Blackwell, 2014.
2. C.N Chen and D.I. Hoult "Biomedical Magnetic Resonance Technology". Adam Hilger, NY, 1989.
3. M. A. Bernstein, K.F. King X.J. Zhou, "Handbook of MRI Pulse sequences". Elsevier, Academic Press, 2004.
4. J. T. Vaughan, J. R. Griffiths "RF Coils for MRI" John Willey and Sons, 2012.

5. J. Mispelier, M. Lapu, A. Briguet “NMR Probe heads for Biophysical and Biomedical Experiments. Theoretical Principles and Practical Guidelines” Imperial Collage Press, 2009.
6. A. G. Webb “*Magnetic Resonance Technology. Hardware and System component design*” The Royal Society of Chemistry, 2016.
7. J. Jin, *Electromagnetic Analysis and Design in MRI*» CRC Press, 1999.
8. Zhi Pei Liang, P: Lauterburg “*Principles of Magnetic Resonance Imaging. A signal Processing Perspective*”, IEEE Press, NY 2000.
9. G. Shultz, “*Magnetic Resonance Imaging with Nonlinear Gradient Fields. Signal encoding and Images Reconstruction*” Springer Spectrum, 2013.
10. F. Casanova, J. Perlo, B. Blümich “*Single-Sided NMR*” Springer, 2011.

The human brain: development and aging explored by MRI

Uwe Eichhoff

Bruker BioSpin GmbH (retired)

E-mail: barbara.uwe@t-online.de

Continuous hardware development and new advanced MRI methods play an important role in exploring finest anatomical details as well as organization of the human brain and contribute to the understanding of mental processes. The formation and development of the brain in early childhood can be followed as well as the decline of cognitive abilities in age.

The whole entity of MRI contrast mechanisms like spin density, T₁, T₂, T₂^{*}, magnetic susceptibility, structural anisotropy allow segmentation of brain images into the particular brain anatomical substructures. Based on this segmentation Diffusion Tensor Imaging (DTI), MR tractography and resting state functional MRI (rs-fMRI) allow to elucidate structural (DTI) and functional connectivities (fMRI) between the various brain areas and complement anatomical findings.

These methods visualize functional connectivities through in the Blood Oxygen Level Dependent (BOLD MRI signal). Even in complete rest the brain is active and oxygen is extracted from blood and fresh blood is supplied. The detection of the small signal changes needs highest sensitivity and the MRI scans must be repeated as fast as possible. Statistical evaluation and cross-correlation of the signals in all voxels show synchrony of signal level fluctuations even in remote brain areas. This allows to establish functional networks in the brain.

The most important networks are the Default Mode Network (DMN), the Salience Network (SN) and the Central Executive Network (CEN). Anatomical locations within the brain sharing two or three of these networks determine our relation to external stimuli, our emotional reaction and activities. Applications to autism beginning in early childhood and decline of cognitive abilities in age, such as mild cognitive impairment, Alzheimer disease will be discussed.

Deep Brain Stimulation (DBS) has become now a well accepted therapy in Parkinson disease. Its application in Alzheimer and depression is still controversial Functional MRI allows to visualize the areas of stimulation and to find the optimal location for the stimulation electrodes.

Xe NMR technique: various applications

Jacques Fraissard

Sorbonne Universities, 4 Place Jussieu, Paris
ESPCI, LPEM, 10 rue Vauquelin, Paris

The ^{129}Xe NMR technique was initially introduced in 1980 [1] for the characterization of the free space of zeolites. The adsorbed ^{129}Xe detected by NMR is an excellent probe to determine microporous solid properties difficult to detect by classical physico-chemical techniques. Indeed the very large and extremely polarisable electron cloud of xenon makes this atom particularly sensitive to its immediate environment. Small variations in the physical interactions with the latter cause marked perturbations of the electron cloud which are transmitted directly to the xenon nucleus and greatly affect the NMR chemical shift.

Since 2000, this technique has taken a new turn with the advent of hyperpolarized xenon [2] (HP-Xe) in the characterization of materials and organisms. The use of HP-Xe increases the sensitivity for the detection of xenon by several orders of magnitude. The range of its applications becomes wider each day.

This technique allows the determination of pore size, location and charge of compensating cations, structural defects, distribution of adsorbed species, etc. It is applied now for the characterization of a lot of solids: mesoporous silica, clays, liquid crystals, metal-organic framework compounds (mainly their elasticity), carbons, solid polymers, diffusion in porous structures and even in archaeology.

Encaged in a cryptophane cage bearing a ligand, xenon is a very sensitive sensor for detecting bio-medically relevant protein targets or metal cations involved in many pathological and physiological processes. Medical applications increase each day, such as: xenon dissolved in the blood for the measurement of the rate of blood in arteries and veins, xenon imaging in brain or human lungs collected *in vivo* [3].

We will give some applications of this universal probe in the domains of materials, biology and medicine.

References

1. Ito, T.; Fraissard, J. In: *Proc of the 5th Int Zeolite Conf*, ed. Rees L.V., Heyden and son, London, GB, 1980, pp 510-515.
2. Raftery, D.; Long, H.; Meersmann, T.; Grandinetti, P.J.; Reven, L.; Pines, A. *Phys Rev Lett*, 1991, 66(5), pp 584-587.
3. *Hyperpolarized Xenon-129 Magnetic Resonance*, Royal Society 2013, Ed: T. Meersmann and E. Brunner.

Peculiarities, possibilities, and areas of applications of quantitative analysis by NMR in magnetic field of the Earth

Vladimir I. Chizhik, Pavel A. Kupriyanov

Faculty of Physics, Saint-Petersburg State University, Ulianovskaya 1, 198504,

Saint-Petersburg, Russia

E-mail: v.chizhik@spbu.ru

In the Saint-Petersburg State University, the fundamental researches in the area of nuclear magnetic resonance (NMR) have been carrying out since the beginning of the 50-ies of the last century. Basing on them, a number of practical applications have been developed (see, for example [1]), and in the report the results, obtaining in the area of NMR in the magnetic field of the Earth, are presented. The NMR sensitivity strongly depends on the magnitude of a static magnetic field B_0 , but the experience shows that the registration of NMR signals is possible even in the Earth magnetic field ($\sim 0,5 \cdot 10^{-4}$ Tl).

First, the general problems of quantitative analysis using NMR (advantages and disadvantages) are briefly described. Then, the new original developments of NMR in the magnetic field of the Earth are presented:

(i) The pre-polarization of nuclei using the alternating magnetic field of low frequency can provide the increase in sensitivity of the method and/or decrease in power consumption of a spectrometer. The description of the process can be carried out on the basis of the Bloch equation using the “swinging” coordinate system.

(ii) The neutralization of the effect of fluctuations of the Earth's magnetic field gives the possibility to realize necessary accumulation of NMR signals for the detection of weak satellites in spectra.

The method considered allows the analysis of liquids enclosed in sealed containers (including bottles) of various volumes and shapes. Besides, it is possible to analyze liquids in containers (cans), the shells of which are made from thin non-magnetic metals but in this case the thickness of shell walls must be much less than a skin-layer for electromagnetic waves in a metal. The NMR frequency for ^1H nuclei in the Earth's magnetic field is about 2 kHz and the skin-layer for copper and aluminum is approximately of 2 mm.

References

1. Vladimir Chizhik, Some Problems of Quantitative Analysis by NMR Method // Magnetic Resonance and its application, 2018, Issue 15, p. 39.

EPR and NMR study of nitric oxide – an interesting molecule for bio-medical applications

Dieter Michel, Marko Bertmer, and Jürgen Haase

*Leipzig University, Faculty of Physics and Earth Sciences,
Linné-Strasse 5, D-04103 Leipzig*

NO molecules are of particular interest because of their broad biological-medical applications. From the physical point of view, NO molecules are very interesting because they possess an unpaired electron, and they reveal interesting coupling phenomena between the electron spin, the orbital angular momentum, and the angular momentum due to the free rotation of the NO molecules. In the liquid phase the NO molecules show the tendency to form NO-NO dimers.

The interesting properties of NO molecules are accessible on the basis of EPR und NMR studies. Detailed studies of the behaviour of NO molecules above the boiling point are carried out by means of EPR measurements which are run over a broad range of temperatures. ^{15}N NMR measurements of highly ^{15}N enriched NO molecules can be only carried out in the liquid phase of NO (and, in principle, also for solid NO) and they are very suitable to understand the equilibrium between NO and dimers of NO in the liquid phase. Moreover, the adsorption behaviour of NO molecules in porous media (mainly in zeolites of type NaA) was investigated. At low temperatures the NO molecules were found to be coordinated to the sodium ion (in the zeolite framework) in a bent complex structure. The EPR spectra are subjected to motional averaging by a two-site jump process between two chemically identical complex structures at $T > 30$ K. Desorption processes of the NO molecules from the Lewis acid centres manifest themselves in homogeneous line broadening effects in the EPR spectra for Na^+ -NO adsorption complex at higher temperatures. In this model, the homogeneous linewidths are determined by the lifetime of the adsorption complex and provide a direct measure of the adsorption energy of NO at the sodium cation sites. Furthermore, desorption of the nitric oxide from the zeolite can be monitored simultaneously by the EPR signal because free NO molecules in the gas phase lead to quite typical EPR spectra.

The authors are very grateful to Dr. Thomas Rudolf Results of EPR and ^{15}N NMR measurements will be presented for NO molecules in the gaseous, liquid and adsorbed state for its valuable contributions by means of EPR spectroscopy and to Arafat Kahn for its NMR work. Moreover, the permanent support of Prof. Andreas Poepl is greatly acknowledged.

Comparison of ionic liquids and highly concentrated electrolyte solutions: similarity and differences in structure and in dynamics

Vladimir V. Matveev¹, Alexandr V. Ievlev¹, Konstantin V. Tyutyukin¹, Luis M. Varela²

¹*Department of Nuclear Physics Research Methods, Saint Petersburg State University, 199034, 7/9 Universitetskaya nab., Saint Petersburg, Russia*

²*Grupo de Nanomateriais e Materia Branda, Departamento de Física da Materia Condensada, Universidade de Santiago de Compostela, Campus Vida s/n E-15782, Santiago de Compostela, Spain*

E-mail: v.matveev@spbu.ru

Ionic liquids (IL), i.e. salts with an organic cation and a low melting point, are in recent decades the most actual liquid systems. This is due to their unique physicochemical properties and application prospects in various fields of science and technology. ILs are widely studied using various experimental techniques and computer simulation methods.

Nuclear magnetic resonance (NMR) is one of the most effective methods of studying liquid systems. Ionic liquids represent a favorable target of all three of the main varieties of NMR technique -- spectra, relaxation, diffusometry – to obtain extensive and, in many cases, unique information both on the local structure and on the translational and orientation dynamics in these systems.

In the first part of the report the main results reached by NMR for ILs of various types are briefly analyzed. The additional opportunities of the technique in such systems are demonstrated in comparison with normal liquids and solutions of inorganic salts. Characteristic examples of temperature dependences of spin-lattice NMR relaxation of ¹³C and ¹H nuclei for some imidazolium-based ILs are shown. These dependences allow one to obtain information concerning the orientation mobility of the cation functional groups as well as of ions mobility as a whole [1, 2]. Also we demonstrate some errors in interpretation of the experimental relaxation data which were used in earlier published articles.

Besides we considered achievements of NMR spectroscopy in the testing of electrolytes, which are promising for use in supercapacitors and other electrochemical devices of new generations. For example, solutions of inorganic salts in so-called “protic” ILs show the effectiveness of the use of NMR to study their local composition and structure [3].

In the second part of the report current ideas are discussed about the heterogeneous structure of some ionic liquids and IL-based liquid systems. We have analyzed the existing data on possible heterogeneity which were obtained by various techniques, including NMR.

Acknowledgements

The work was partly supported by RFBR, grant #17-03-00057. The NMR measurements have been carried out partially in the Center for Magnetic Resonance of Research Park of St. Petersburg State University.

References

1. V.V. Matveev *et al.* PCCP. 2014, **16**. 10480-10484.
2. V.V. Matveev *et al.* Magn. Reson. Chem., 2018, **56**. 140-143.
3. V.V. Matveev *et al.*, J. Mol. Liq., Vol. 278, 2019, pp. 239-246.

Hyperpolarized (hp) ^{83}Kr and hp ^{129}Xe as MRI contrast agents

T. Meersmann

Sir Peter Mansfield Imaging Centre, Division of Respiratory Medicine, School of Medicine, University of Nottingham, Nottingham, NG7 2RD, United Kingdom

Department of Electrical and Electronic Engineering, University of Nottingham, Ningbo, PR China

The development of magnetic resonance imaging (MRI) with hyperpolarized noble gases has resulted in a number of excellent protocols to probe different structural and functional aspects of lungs in health and disease. Technological improvements have enabled pulmonary hyperpolarized (hp) ^{129}Xe MRI at high spatial resolution, in particular to provide functional maps of lung ventilation. Furthermore, tissue solubility, large chemical shift range, and interaction with specific sensor molecules allows for a variety of biomedical hp ^{129}Xe application and some recent developments will be discussed [1, 2].

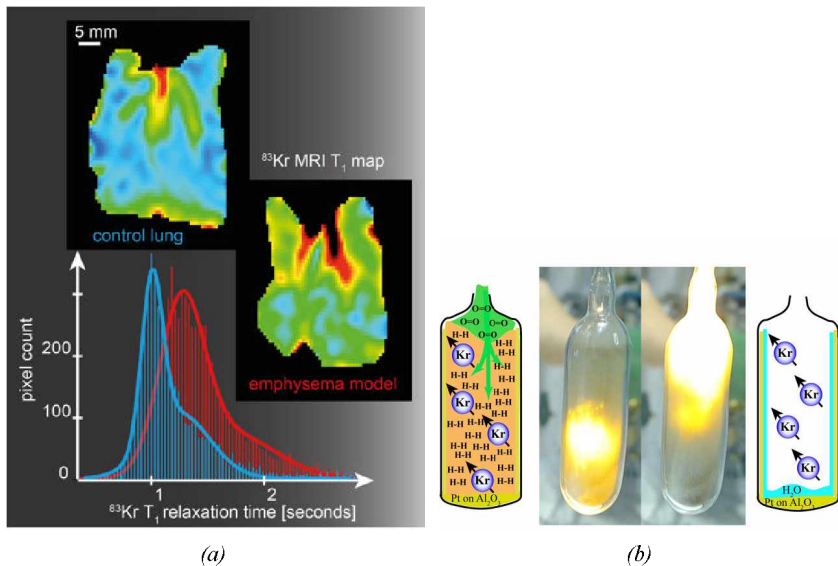


Figure 1. (a) ^{83}Kr surface quadrupolar relaxation (SQUARE) T_1 map of a control rat lung (left) and of an emphysema model lung (right). The blue color indicates fast relaxation (about 1 – 1.2 s) while green color indicates slower relaxation due to reduced surface to volume ratios in the emphysema model. The histograms (below) show the magnitude of the effect. (b) Catalytic combustion of the H_2 buffer gas in the presence of O_2 leaving pure Hp Kr gas. The major combustion event is largely completed within the short time span of 10 ms and leaves the hyperpolarized state fully preserved

Successful implementation of hp MRI typically requires great care to reduce relaxation of the precious hyperpolarized spin state and the associated signal loss. However, our group has made significant progress with hp ^{83}Kr , a stable, nuclear spin $I = 9/2$ isotope that according to ‘common wisdom’ was an unlikely candidate for hp MRI applications because of its fast quadrupolar relaxation. The apparent disadvantage can be turned into a useful probe for

surfaces, as quadrupolar relaxation requires the presence of fluctuating electric field gradients (EFGs) that are predominately generated during adsorption on surfaces. We have demonstrated ^{83}Kr surface quadrupolar relaxation (SQUARE) T_1 maps of an emphysema model in excised rodent lungs [3] – see Fig. 1a.

However, the distinct physical properties of ^{83}Kr that enable unique MRI contrast also complicate the production of hp ^{83}Kr . By altering the buffer gas, used in spin exchange optical pumping (SEOP), from molecular nitrogen to molecular hydrogen, we present a radically new approach for the production of hyperpolarized contrast agents [4]. This allows for the first time, the production of highly concentrated hyperpolarized ^{83}Kr through the use of catalytic combustion to reactively purify the noble gas (see Fig. 1b).

References

1. F. Zamberlan, C. Lesbats, N. J. Rogers, J. L. Krupa, G. E. Pavlovskaya, N. R. Thomas, H. M. Faas, and T. Meersmann, *Chemphyschem* **16**, 2294 (2015).
2. F. H.M., K. J.A., T. A.J., Z. F., W. H.E.L., J. S.J., G. E. Pavlovskaya, T. N.R., and T. Meersmann, *Contrast Media Mol I* **in press**.
3. D. M. L. Lilburn et al., *J R Soc Interface* **12** (2015).
4. N. J. Rogers, F. Hill-Casey, K. F. Stupic, J. S. Six, C. Lesbats, S. P. Rigby, J. Fraissard, G. E. Pavlovskaya, and T. Meersmann, *P Natl Acad Sci USA* **113**, 3164 (2016).

Low field ^{14}N NMR as a tool for estimation of quadrupole coupling constants and correlation times in liquids

G. V. Mozzhukhin¹, G. S. Kupriyanova², S. Sh. Mamadazizov^{1,2}, B. Z. Rameev^{1,3}

¹Department of Physics, Gebze Technical University, 41400 Gebze/Kocaeli, Turkey

²I. Kant Baltic Federal University, 236041 Kaliningrad, Russian Federation

³E. Zavoisky Physical-Technical Institute, FRC Kazan Scientific Center of RAS, 420029 Kazan/Tatarstan, Russian Federation

E-mail: mgeorge@yandex.ru

Introduction

It is well known that a number of energetic and explosive liquid substances contain nitrogen in their structure. For this reason, the detection of ^{14}N NMR signal has been proposed by P. Prado *et al.* as an important criteria of their discrimination [1, 2]. An advantage of ^{14}N NMR is a fast detection procedure due to rather short relaxation times. Besides, already the fact of detection of ^{14}N NMR signal alarms a security threat. However, the ^{14}N NMR detection of energetic substances is a challenging technical task due to a very small SNR for nitrogen NMR signal. In this work, the correlation times of the molecular motion versus the nuclear quadrupole coupling constants of a number of nitrogen-containing substances were estimated from experimental data.

Experimental details and samples

Three groups of nitrogen liquids were studied by low field ^{14}N NMR. The first group was the liquids with nitro (NO_2) group: nitromethane, nitroethane, nitrobenzene and sodium nitrite water solutions. The second group were nitrates with the NO_3 group: water solutions of nitric acid, ammonium nitrate, potassium nitrate, lead nitrate, and magnesium nitrate hexahydrate. The third group were some toxic and flammable materials: acetonitrile, triethanolamine, dimethylformamide and dimethylacetamide.

Low field ^{14}N NMR setup was assembled for the studies of these substances, consisting of the permanent magnet system with a magnetic field of 0.575 T, a home-made RF probe, Tecmag Apollo NMR console and 500 W Tomco power amplifier. The results of the measurements of relaxation parameters of these substances and discussion of the received results in relation to the prospects of ^{14}N NMR for the detection of dangerous substances have been already presented in [3]. In this work, we presents the calculations of quadrupole coupling constant values of these substances as well as compared the different methods of their calculations.

Calculation of quadrupole coupling constants

For nuclei with spin $I > 1/2$, the main interaction is the quadrupole interaction, i.e. the interaction of nucleus quadrupole moment with the electric field gradient (EFG) of surrounding electrons. In liquids, the components of the quadrupole interaction tensor fluctuate randomly with time providing the quadrupole mechanism as the main relaxation mechanism [4]. The parameters of spin lattice (longitudinal) and spin-spin (transverse) relaxation in this case are following:

$$\left(\frac{1}{T_1}\right)_Q = \left(\frac{1}{T_2}\right)_Q = \frac{3}{8} \left(1 + \frac{\eta^2}{3}\right) \left(\frac{e^2 Q q_z}{\hbar}\right)^2 \tau_c, \quad (1)$$

where $(T_1)_Q$ and $(T_2)_Q$ are longitudinal and transverse relaxation times correspondently, eq_z is the principal component of electric field gradient (EFG) tensor, $\eta = (V_{xx} - V_{yy})/V_{zz}$ is asymmetry parameter EFG, V_{ii} are the principal components of EFG tensor, Q is quadrupole moment of nuclear, and \hbar is Planck constant.

Using the longitudinal relaxation times given in [3] and accepting quadrupole mechanism as dominating channel in the relaxation, it is possible to estimate the correlation time of molecular motion, if the quadrupole coupling constant (QCC):

$$C_q = \frac{e^2 Qq_{zz}}{h} \quad (2)$$

and asymmetry parameter η are known. On the other hand, it is possible to extract information on the quadrupole constant if the correlation time of molecular motion is known. It is easy to show that the effect of the asymmetry parameter in the Eq. 1 is very small (neglecting η results in 3% error in calculations at most) for all studied compounds, thereby we excluded it from the further consideration.

Using Debye model [5] the correlation time of rotational motion of spheroid molecules in solution in diffusion limit is defined by molecular volume V_{mol} , viscosity and temperature of solution as follows:

$$\tau_c = \frac{4\pi a^3}{3kT} \sigma = \frac{V_{mol}}{kT} \sigma, \quad (3)$$

where a is radius of spheroid molecule of volume V_{mol} , σ is a viscosity, k is a Boltzmann constant, T is a temperature. It is supposed that a molecular motion is an isotropic molecular motion. Therefore, using our T_1 relaxation data and Eq. 1 we can calculate correlation times as a function of inverse product of square QCC value with T_1 for the measured compounds and compare them with the literature data [6-8]. It should be noted that the QCC values, obtained in different works, reveals essential spread. Therefore, our estimations can also contribute to clarifying the C_q values.

The calculations of correlation times for planar molecules were carried out based on two approaches. The first model assumes that the molecules have a solid sphere under the reorientation in a viscous media and the correlation time is determined using of the Stokes-Debye formula [5]. Viscosity coefficients are taken near room temperature from literature. The dimensions of molecules were estimated in the approximation of hexagonal close packed solid sphere [8],

$$0.74V_{mol} = \frac{4\pi a^3}{3N_0}, \quad (4)$$

where V_{mol} is a molar volume, N_0 is Avogadro's number.

The second approach takes into account that the investigated molecules can be considered as planar ones. In this case, the Lamb model can be used for calculating the effective molecular volume [9]. Lamb showed that (edge-to-edge) the motion of an infinitely thin circular disk of radius z through a viscous fluid collide with the same frictional resistance as the sphere of radius r given by the formula $r = 0.566 z$. The effective volume is following:

$$V_Q = \frac{4\pi r^3}{3} = 0.76z^3 \quad (5)$$

Effective molecular volumes and the correlation times for sodium nitrite, nitromethane and nitroethane were estimated by the formulas (3) and (5). Comparative data on the correlation times obtained using the above-mentioned approaches are presented in the Fig. 1 (a, b). It can be seen that the results obtained using the Lamb model are close to the correlation times obtained from the experimental relaxation time T_1 , whereas the correlation times calculated from the Debye model differ from the experimental ones by several times.

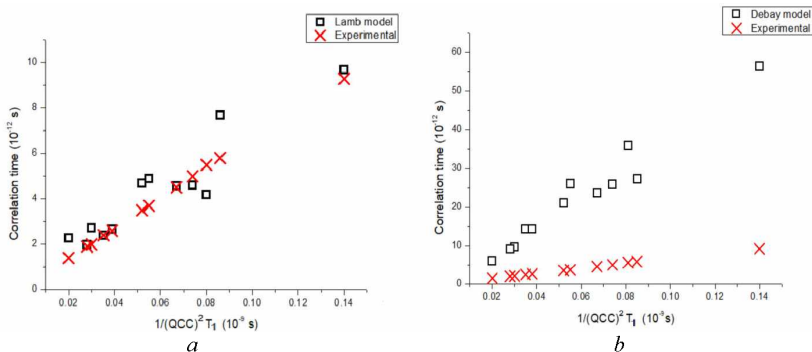


Figure 1. The dependences of the correlation times from $(1/(T_1 C_q^2))$ calculated by the use of Lamb (left) and Debye (right) models and experimental data

Conclusions

The obtained experimental data [3] made possible estimation of the correlation times of the molecular motion (or vice versa, the quadrupole coupling constants if the correlation time is known). The results received for the correlation times as a function of $(1/(T_1 C_q^2))$ were compared with previous works and revealed satisfactory correlation with the Lamb model. The received data allowed us to estimate the quadrupole constant for previously unexplored compounds, such as: $C_q(\text{Pb}(\text{NO}_3)_2) = 0.84$ MHz and $C_q(\text{Mg}(\text{NO}_3)_2 \cdot 6\text{H}_2\text{O}) = 0.56$ MHz.

Acknowledgements

The work was supported by NATO Science for Peace and Security Programme (NATO SPS grant No. 985005 [G5005]). Authors also acknowledge a partial support by TUBITAK grant under the Programme 2221 for Visiting Scientist (G. S. Kupriyanova) and by Research Fund of Gebze Technical University (grants No. BAP 2017-A-105-44).

References

1. P. Prado, Detecting Hazardous materials in containers utilizing nuclear magnetic resonance based measurements. Patent US 2014/0225614 A1, Aug. 14, 2014.
2. P. Prado, Bottled Liquid Scanner for Security Checkpoints, in NATO book "Magnetic Resonance Detection of Explosives and Illicit Materials", NATO Science for Peace and Security Series - B: Physics and Biophysics, Eds: Tomaz Apih, Bulat Rameev, Georgy Mozzhukhin, and Jamie Barras, Springer (2013) 89-98.
3. G.V. Mozzhukhin, G.V. Kupriyanova, S.Sh. Mamadazizov, A. Marařli, B.Z. Rameev, Low-field ^{14}N nuclear magnetic resonance for detection of dangerous liquids, Chemical Physics, Volume 513(2018)129-134.
4. M. Witanski, Nitrogen NMR. Spectroscopy, Pure and Applied Chemistry 37 (1974) 225-233.
5. A. Abragam, The Principles of Nuclear Magnetism, The Clarendon Press, Oxford, (1961) 314 p.
6. G.J. Jenks, NMR Investigation of the Nitrogen Quadrupole Coupling Constant in Liquid Samples, J. Chem. Phys. 54(2) (1971) 658-663.
7. A. Loewenstein. Nuclear quadrupole coupling constants in the liquid phase, Adv. in Nuclear quadrupole. Resonance 5 (1983) 53-82.
8. W.B. Moniz and H.S. Gutowsky, Nuclear Relaxation of N-14 by Quadrupole Interactions in Molecular Liquids, J. Chem. Phys. 38 (1963) 1155-1162.
9. H. Lamb, Hydrodynamics, Dover, New York (1932) 605 p.

Fluorine dynamics in nanosized superionic conductors as seen by NMR diffusometry

A. F. Privalov¹, L. B. Gulina², M. Weigler¹, M. Vogel¹, I. V. Murin²

¹*Institut für Festkörperphysik, TU Darmstadt, Hochschulstr. 6. 64289 Darmstadt Germany*

²*Institute of Chemistry, Saint Petersburg State University, Universitetskaya nab. 7/9. 199034, St. Petersburg, Russia*

E-mail: alexei.privalov@physik.tu-darmstadt.de

Introduction

It is known that dynamics in the solid state can be significantly changed if the size of particles tends in to the nano range. We investigated the influence of the size of nano-particles on the mobility of the fluorine ions in the superionic conductor LaF_3 using ^{19}F NMR diffusometry in a temperature range up to 800 K.

Sample preparation

The samples have been prepared using novel synthesis at the gas-solution interface, developed in recent years [1]. This method allows for the synthesis of nano-structures with non-trivial morphology like 1D or 2D materials. In our case by processing a solution of lanthanum salt with gaseous HF, a thin layer of lanthanum fluoride is formed on the surface [2]. This layer consists of 2D nano-crystals oriented perpendicular to the layer surface as shown in Fig. 1. The dimension surface size of the crystals is in μm range while the thickness is in nm range.

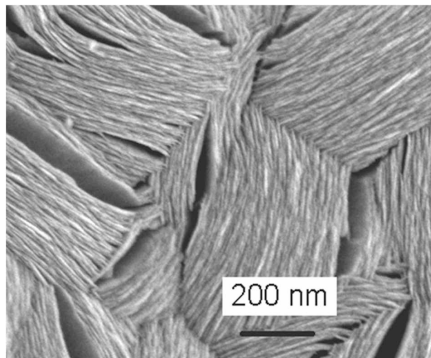


Figure 1. SEM image of 2D LaF_3 crystals

The advantage of this method is the possibility to vary the thickness of the nano-crystals by the concentration and pH of the reagent solution. In this way we have succeeded to prepare several nanosized samples with nano-crystals thickness from 6 nm to 18 nm.

Method: NMR diffusometry

In order to quantify the influence of the nano-sheet thickness on the dynamic properties, the self-diffusion coefficients of the fluorine ions were measured using ^{19}F Static Field Gradient NMR diffusometry [3]. For these measurements the three pulse stimulated echo sequence was used which provides an echo amplitude decay that is mainly governed by spin relaxation and ionic diffusion. To eliminate the decay due to spin relaxation, we perform identical measurements at two different magnetic field gradients, $g_1=107$ T/m and $g_2=64$ T/m, but at the same resonance frequency and divide the results. Since the relaxation effects are independent

of the field gradient, they cancel out and, thus, the decay of the divided data reflects only diffusion in an effective magnetic field gradient ($g_1^2 - g_2^2$):

$$\frac{S(t_m, \tau, g_1)}{S(t_m, \tau, g_2)} = S_0 \cdot \exp \left[-(\gamma\tau)^2 (g_1^2 - g_2^2) \cdot \left(\frac{2}{3} \tau + t_m \right) D \right], \quad (2)$$

where D is the self-diffusion coefficient, γ is the ^{19}F gyromagnetic ratio, τ is an interval between the first two RF pulses in stimulated-echo sequence and t_m is the interval between the second and the third pulses in this sequence.

Such measurements can be performed only when using a magnetic system with an anti-Helmholtz arrangement of superconducting coils, where up to 4 positions with the same Larmor frequency, but two different gradients are available by properly adjusting the probe head location along the magnet axis.

Results and conclusion: Influence of morphology on dynamic properties

The results are presented in Fig. 2. Data for bulk LaF_3 are included for comparison.

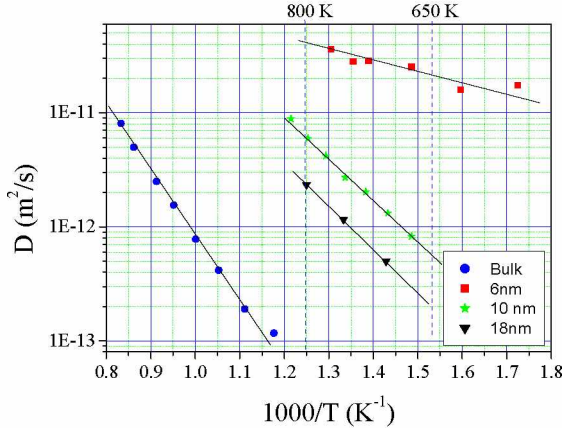


Figure 2. Diffusion coefficients in nano-crystalline LaF_3 samples with the indicated nano-sheet thicknesses

The temperature dependence of the diffusion coefficient can be described by the Arrhenius model for all considered samples. The fluorine diffusion in 2D materials is significantly faster as compared to that in bulk LaF_3 and is strongly dependent on the nano-crystalline sheet thickness. A decrease from 18 nm to 6 nm leads to an increase of mobility by almost two orders of magnitude, especially at low temperatures, resulting in an overall mobility enhancement of more than three orders of magnitude compared to mono-crystalline LaF_3 . Moreover, the activation energy is reduced from 1.2 eV for mono-crystals to 0.23 eV for 6 nm thin nano-crystals.

Thus our study confirms the strong influence of particle size on ionic dynamics if the particle size is in nm range [4].

Acknowledgements

The reported study was supported by a grant of the Russian Science Foundation, research project No 16-13-10223.

References

1. V.P. Tolstoy, L.B. Gulina, *J. Nano-Electron. Phys.* **5**, 01003-1-3, 2013.
2. L.B. Gulina, V.P. Tolstoy, *Russ. J. Gen. Chem.* **84**, 1472-1475, 2014.
3. I. Chang, F. Fujara, B. Geil, G. Hinze, H. Sillescu, A. Tölle, *J. Non-Cryst. Solid* **172-174**, 674, 1994.
4. L. B. Gulina, M. Schikora, A. F. Privalov, M. Weigler, V. P. Tolstoy, I. V. Murin, M. Vogel. *Appl. Magn. Reson.* 2018. <https://doi.org/10.1007/s00723-018-1077-z>

When Molecular Dynamics met NMR (and various other experimental methods)

O. N. Rogacheva¹, S. A. Izmailov¹, D. A. Luzik¹, S. O. Rabdano¹, I. S. Podkorytov¹,
L. V. Slipchenko², M. A. Indeykina³, T. F. Cunningham⁴, Z. Hasanbasri⁴, S. Saxena⁴,
N. R. Skrynnikov^{1,2}

¹Laboratory of Biomolecular NMR, St. Petersburg State University, St. Petersburg 199034, Russia.

²Department of Chemistry, Purdue University, West Lafayette, Indiana 47907, USA.

³Emanuel Institute for Biochemical Physics, Russian Academy of Sciences, Moscow 119334, Russia.

⁴Department of Chemistry, University of Pittsburgh, Pittsburgh, Pennsylvania 15260, USA.
E-mail: nikolai@purdue.edu

In this report, we provide an overview of several projects exploiting the synergy between, on the one hand, MD modeling and quantum-chemical computations and, on the other hand, magnetic resonance (NMR and ESR) experiments as well as structural information from the Protein Databank. In the first project, we have identified a recurring structural motif that appears in thousands of protein structures. This motif involves carbonyl oxygen in linear arrangement with lysine side-chain ϵ -ammonium group. Of interest, such linear interaction involving conserved lysine is consistently found in the P-loop of numerous NTPase domains, including the notorious oncogene product Ras. We have comprehensively characterized this interaction by means of PDB analyses and DFT calculations. In the second project, we investigated the formation of covalent complex between the activated Sos1-derived peptide and N-terminal SH3-domain of adapter protein Grb2. The peptide has been modified by adding to its sequence a non-native reactive residue (chloroacetyl lysine). The peptide initially binds to its target non-covalently before reacting with the proximal cysteine on the surface of the protein. The formation of covalent complex has been confirmed using SDS-PAGE, heteronuclear 2D/3D NMR spectroscopy and LC-MS/MS. The collected data allowed us to determine the rate constant of the reaction and its pH dependence. We have further designed and implemented an MD-based algorithm to model formation of Sos1-Grb2-SH3 covalent complex *in silico*. The resulting high-resolution model of the complex has been validated via the comparison of the predicted and experimental chemical shifts. Finally, in the third project we have focused on the use of the ESR spin label (2,2,5,5-tetramethyl-1-oxyl-3-methyl methanethiosulfonate, MTSL) as a probe of local protein environment and dynamics. Toward this end, we have recorded six 20- μ s-long MD trajectories of different MTSL-labeled variants of the B1 domain of staphylococcal protein G (GB1). Based on the MD trajectories, respective ESR spectra were simulated using two methods: (i) direct propagation method based on numerical integration of the Liouville – von Neumann equation and (ii) Redfield-theory treatment. We have also manufactured six recombinant samples of single-cysteine mutants of GB1 and recorded their ESR spectra. The experimental spectra proved to be excellent agreement with the MD-based predictions. Further analyses led us to conclude that the shape of ESR spectra is dictated by the degree of steric confinement experienced by an MTSL tag in the protein molecule.

Acknowledgment

This work was supported by the RSF grant 15-14-20038.

From ESR to FMR – a powerful tool to investigate novel ferromagnets, illustrated with the study of tunable magnetic properties of thin metallic FeRh films

Anna Semisalova^{1,5}, Craig Barton², Rantej Bali¹, Aisuluu Aitkulova³, Kay Potzger¹, Roman Böttger¹, Kilian Lenz¹, Jürgen Fassbender¹, Thomas Thomsen², Jürgen Lindner¹

¹*Helmholtz-Zentrum Dresden – Rossendorf, Institute of Ion Beam Physics and Materials Research, Dresden, Germany*

²*School of Computer Science, The University of Manchester, Manchester, UK*

³*Moscow Institute of Physics and Technology, Dolgoprudny, Moscow, Russia*

E-mail: anna.semisalova@uni-duisburg-essen.de

⁵*Present address: University of Duisburg-Essen, Faculty of Physics, Lotharstrasse 1, 47057, Duisburg, Germany*

Introduction

Ferromagnetic resonance (FMR) is a powerful technique to characterize magnetic properties via detecting the magnetization precession in a ferromagnetic sample. FMR is related to the electron paramagnetic resonance (EPR, or electron spin resonance ESR) phenomena, with the difference that the first one occurs in the systems exhibiting magnetic coupling. In both techniques, the microwave absorption is measured, and the resonance field/frequency is detected. Since the resonance conditions in ferromagnetic materials are determined by effective magnetic field, which includes demagnetizing field and magnetocrystalline anisotropy field in addition to applied DC and RF microwave fields, FMR spectroscopy allows for identification of the magnetic anisotropy contributions along with g-factor [1]. Moreover, the linewidth of FMR signal can be used for studying the relaxation processes in ferromagnets, giving an access to the value of Gilbert damping constant. The application of FMR technique for investigation of new magnetic materials will be illustrated with the study of disorder-induced magnetization in binary FeRh metallic films irradiated with Ne ions.

Structurally B2-ordered equiatomic FeRh thin films are known for unique properties such as a temperature, magnetic field, and spin polarized current driven phase transition from the antiferro- to the ferromagnetic state. The strain and structural disorder also influence the magnetic properties of FeRh, which opens a new way for controllable modification of properties at the micro- and nanoscale. Namely, structural modification by ion beam irradiation was shown to be an effective tool for tuning the phase transition temperature in FeRh as well as the saturation magnetization [2-4].

Here, we investigated the disorder-induced ferromagnetism in epitaxial FeRh thin films irradiated with Ne ions. We show the shift of phase transition temperature towards lower values for ion fluence below 1×10^{14} ions/cm² and transformation of FeRh into a ferromagnet with tunable saturation magnetization and low Gilbert damping at higher fluence.

Materials and Methods

The thin FeRh films of 40 nm thickness have been grown epitaxial on MgO(100) substrates using magnetron sputtering of alloyed target. The films have been post-annealed at 750°C to stabilize structurally ordered B2 phase and then cooled down in vacuum. The ion irradiation was performed at Ion Beam Center, HZDR, Dresden. The energy of Ne⁺ ion beam was 25 keV; fluence was varied from 1×10^{13} to 4×10^{14} ions/cm².

The crystallinity of B2-ordered FeRh films was investigated with X-ray diffraction (XRD). The degree of long-range chemical order, or S-parameter, in Ne-irradiated films was estimated from the intensity of superlattice (001) and fundamental (002) peaks. S-parameter

reflects the substitutional disorder and is determined as $S=r_{\alpha}+r_{\beta}-1$, where $r_{\alpha}(r_{\beta})$ is a fraction of Fe(Rh) atoms located on the Fe(Rh) site.

The transition from antiferromagnetic to ferromagnetic state confirming the chemical order in annealed FeRh thin films as well as the disorder-induced magnetization in irradiated films was investigated using SQUID magnetometry in the temperature range 50–400 K.

Ferromagnetic resonance (FMR) measurements have been performed using Vector Network Analyzer (VNA) setup. FeRh thin films were clamped onto a coplanar waveguide, Agilent microwave source was used to excite a ferromagnetic resonance in the frequency range 1–40 GHz. The transmission signal between the ports of VNA, a complex microwave scattering parameter S_{12} , was recorded as FMR signal while the external magnetic field was swept at fixed frequency of microwaves.

Results and Discussion

Fig. 1 presents the temperature dependence of magnetization of the B2-ordered sample before and after irradiation with fluence of 1×10^{13} and 2×10^{13} ions/cm². The annealed sample before ion bombardment exhibits a phase transition from antiferromagnetic to ferromagnetic state starting at temperatures close to 390 K (Fig. 1a). The minor temperature hysteresis loop has been recorded only, thus the complete transition was not observed. The annealed film has a residual magnetization of ~ 100 kA/m in nominally AFM state at room temperature which slightly increases when sample is cooled.

The irradiation with the lowest used Ne fluence of 1×10^{13} ion/cm² led to the formation of two magnetic phases with different temperatures of AFM-FM phase transition as can be seen from the overlapping thermal hysteresis loops (Fig. 1a). Similar was observed earlier in Ne irradiated MBE-grown FeRh films [2].

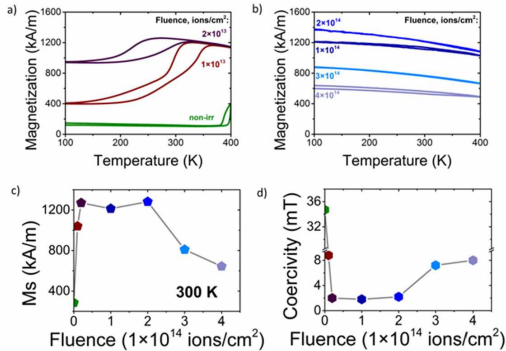


Figure 1. (a)–(b) Temperature dependence of magnetization of FeRh films irradiated with Ne ions with different fluence. The magnetic field 50 mT was applied in-plane. (c) Fluence dependence of saturation magnetization and (d) coercivity

Observed tunable shift of phase transition towards lower temperatures by ion irradiation is well known for FeRh system [3–5], it is attractive due to its reversibility by high-temperature annealing which resets the B2 order. Along with reported shift, the width of thermal hysteresis is increased with fluence while the magnitude of transition is decreased and residual FM signal is enhanced (see the plot for Ne fluence 2×10^{13} ions/cm², Fig. 1a) until the phase transition is finally erased (Ne fluence 1×10^{14} ions/cm² and higher, Fig. 1b) and disordered film exhibits a stable FM state in a temperature range 50–400 K.

Fig. 1c shows the fluence dependence of saturation magnetization M_s derived from the hysteresis loops measured at room temperature, demonstrating high tunability of magnetic

properties of irradiated FeRh. The rapid increase of M_s happens in the narrow fluence range up to 2×10^{13} ions/cm²; then the M_s value reaches its maximum and stays in the range 1210-1280 kA/m up to 2×10^{14} ions/cm², and third, the disorder-induced magnetization decays with further increase of ions dose. Similar but reversed trend is observed for coercivity (Fig. 1d) which drops to minimum value of 1.8-2.2 mT in the range 2×10^{13} - 2×10^{14} ions/cm².

Magnetic damping of material is another key property relevant to design of spintronics and magnonics devices. To investigate the magnetization dynamics and Gilbert damping in irradiated FeRh films, we performed broad-band ferromagnetic resonance measurements at room temperature in the frequency range up to 40 GHz, including polar and azimuthal angular dependences. Fig. 2 shows the summary of experimental analysis of damping – the Gilbert damping constant (Fig. 2a) and inhomogeneous broadening of the resonance line (Fig. 2b). Irradiated FeRh thin films exhibit a nearly independent on Ne fluence damping parameter which fluctuates in the range of 0.0030 – 0.0055.

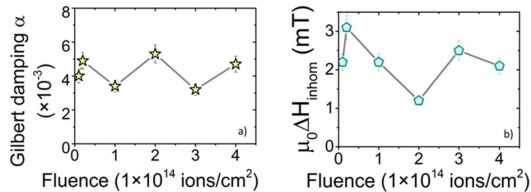


Figure 2. (a) Gilbert damping constant and (b) inhomogeneous broadening measured for Ne-irradiated FeRh thin films with different ion fluence

Such a low value of Gilbert damping in combination with relatively small inhomogeneous broadening of resonance linewidth is comparable with high-quality permalloy films and seems to be promising for a variety of magnonics applications.

Summarizing, we conclude the following:

- Tuning the AFM-FM phase transition temperature and residual FM at low temperatures in FeRh is possible by ion beam irradiation;
- Magnetostructural correlation in FeRh thin films opens a way to generate a disorder-induced ferromagnetism; saturation magnetization can be tuned in the range up to 1280 kA/m;
- The value of Gilbert damping remains as low as $\sim 4 \times 10^{-3}$ for the whole studied range of Ne ions/saturation magnetization;
- Combination of AFM-FM phase transition, tunable magnetization and low damping makes FeRh thin films promising for ion beam nanopatterning of thermally reversible planar magnonics and spintronics nanostructures and devices such as sensors and data storage elements.

Acknowledgements

The financial support of DFG (project AL 618/37-1) is gratefully acknowledged. Authors are thankful to Dr. R. Huebner (HZDR) for TEM analysis, Dr. J. Grenzer, Mrs. A. Scholz for (HZDR) and Dr. B. Abendroth (TU Freiberg) for their help with XRD analysis, and Prof. M. Farle (Univ. Duisburg-Essen) for fruitful discussions.

References

1. M. Farle, Rep Prog. Phys. 61 (1998) 755.
2. N. Fujita et al., J. Appl. Phys. 107 (2010) 09E302.
3. A. Heidarian et al., Nucl. Instr. Meth. B 358 (2015) 251-254.
4. S.P. Bennett et al., Mater. Res. Lett. 6 (2018) 106-112.
5. S. Cervera et al., Phys. Rev. Mater. 1 (2017) 065402.

How to estimate hydrogen bond energies from NMR spectra

E. Yu. Tupikina¹, P. M. Tolstoy², V. V. Mulloyarova², I. S. Giba¹, G. S. Denisov¹

¹*Department of Physics, St. Petersburg State University, St. Petersburg, Russia*

²*Institute of Chemistry, St. Petersburg State University, St. Petersburg, Russia*

E-mail: peter.tolstoy@spbu.ru

Introduction

Hydrogen bond energy estimation is a complicated task. In gas phase, the complexation enthalpy could be determined experimentally or calculated. In condensed phases – liquids, solutions, polymers, glasses, “soft matter”, heterogeneous systems – it gets trickier due to various solvation and packing effects. Moreover, for intramolecular bonds the H-bond energy requires an additional definition, which is often not obvious. As a result, the estimation of hydrogen bond energy by spectroscopic methods becomes especially useful.

Badger-Bauer rule and other IR diagnostic tools

The idea of a correlation between spectroscopically observable parameters and the H-bond energy originates from the papers of Badger and Bauer [1]. The linear proportionality between the H-bond energy and the stretching vibration frequency ν_{XH} is known as the Badger-Bauer rule:

$$\Delta E = k \cdot \nu_{\text{XH}}.$$

Eventually it was concluded, that the correlation coefficient k is not universal and should be defined for every homologous series of complexes individually. There were a number of attempts to find other measurable spectroscopic parameters that could serve as H-bond energy marker. For example, Iogansen proposed [2] to use intensification of the ν_{XH} band upon complexation

$$\Delta E \sim (\sqrt{A} - \sqrt{A_0}),$$

where A and A_0 are integral intensities of XH band for complex and free proton donor, respectively.

QTAIM parameters

In Bader's QTAIM approach (Quantum Theory of Atoms in Molecules [3]) the topological analysis of electron density for H-bonded complexes yields so called bond critical points (BCP). In many cases the local electronic kinetic (G) and potential (V) energy densities at BCP linearly correlate with the complexation energy [4,5] (V and G in kcal/mol/Å³, ΔE in kcal/mol):

$$\Delta E = 0.5 \cdot V,$$

$$\Delta E = 0.429 \cdot G.$$

Construction of such correlations is of particular value, as the electron density itself, G and V values can in principle be evaluated from experimental X-Ray data. Furthermore, QTAIM-based correlations could be applied equally for inter- and intramolecular hydrogen bonds.

NMR hydrogen bond correlations (quantum-chemical calculations)

F–H...F hydrogen bonds

We consider a set of 26 complexes with FHF hydrogen bonds formed by FH molecule as proton donor and various proton acceptors: fluoride anion, fluorinated alkyls, FH molecule, diatomic interhalogens, metal fluorides (alkali, alkaline earths and transition metals), covering

a wide H-bond energy range 0.2–47 kcal/mol. A couple of examples of equilibrium structures are shown in Fig. 1.

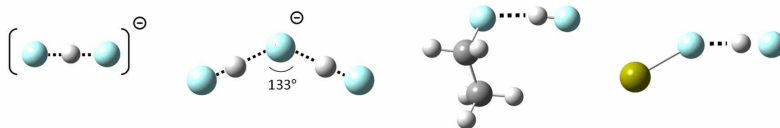


Figure 1. Structures of complexes formed by FH molecule and proton acceptors (from left to right): F^- , $(FHF)^-$, CH_3CH_2F , AlF

We show that that changes of parameters upon complexation, *i.e.* changes of the stretching frequency in local mode approximation $\Delta\nu_{LM}$, change of the proton chemical shift $\Delta\delta_H$ and change of the absolute value of spin-spin coupling constant $^1J_{FH}$ could be used for estimation of corresponding hydrogen bond strength. This work is published in [6].

N–H...N hydrogen bonds

We consider a set of 21 complexes with NHN hydrogen bond formed by aniline molecule (Fig. 2). This set features hydrogen bonds from weak to medium strong ones (2–21 kcal/mol), with neutral or anionic bases, with sp^3 and sp^2 hybridized nitrogen proton acceptor. For each complex apart of direct hydrogen bond energy calculation we have tested other ways to estimate the energy: a) using Badger-Bauer rule and b) using slightly modified abovementioned QTAIM correlations.

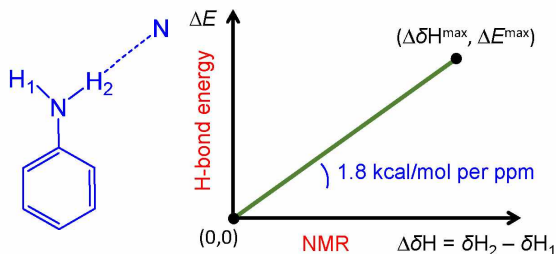


Figure 2. Schematic structure of studied complexes with NHN hydrogen bonds

We propose to use the NMR chemical shift difference of aniline's NH_2 protons, $\Delta\delta_H$, for the estimation of the H-bond energy and geometry ($N\dots H$ and $N\dots N$ distances). We conclude that

$$\frac{\Delta E^{\max}}{\Delta\delta H^{\max}}$$

ratio could serve as a conversion factor from proton chemical shifts to energy (ΔE^{\max} and $\Delta\delta H^{\max}$ are the energy and 1H NMR chemical shift values for the limiting case of a complex with central-symmetric $N\dots H\dots N$ hydrogen bond).

POO–H...O hydrogen bonds

We consider a series of cyclic dimers and trimers of phosphinic and phosphoric acids, in which a ring of two or three cooperatively coupled hydrogen bonds is being formed. We attempt to find out how to use ^{31}P NMR chemical shifts for the spectral diagnostics of H-bonds.

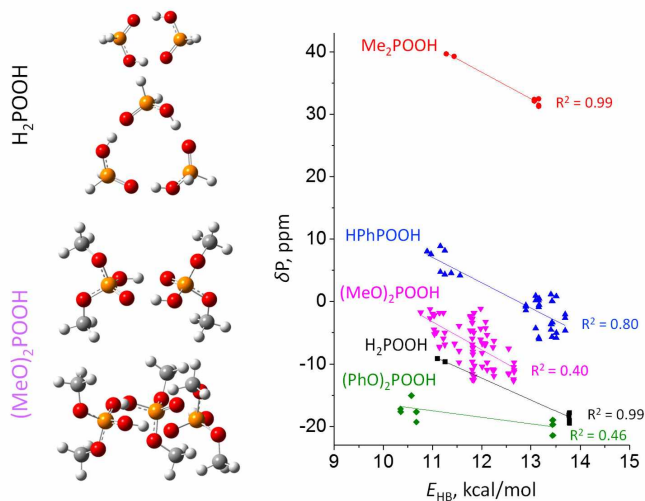


Figure 3. Left: equilibrium structures of some cyclic self-associates of phosphinic/phosphoric acids. Right: correlation between complexation energy (per one H-bond) and ³¹P NMR chemical shift for various conformers of cyclic self-associates of several acids

We show that the $\delta^{31}\text{P}$ values are very sensitive to the conformation of the complex, namely, to the angles and dihedral angles not only in the H-bond ring, but also in the substituents R (especially for phosphoric acids). Despite this sensitivity, we were able to propose a “rule of thumb” which states that the slope of δP dependence on H-bond energy for cyclic complexes of POOH acids is ca. 4 ppm per kcal/mol.

Acknowledgements

This work is supported by the RSF grant 18-13-00050.

References

1. R.M. Badger, The relation between the energy of a hydrogen bond and the frequencies of the O–H bands, *J. Chem. Phys.*, **1940**, 8(3), 288–289.
2. A.V. Iogansen, Direct proportionality of the hydrogen bonding energy and the intensification of the stretching $\nu(\text{XH})$ vibration in infrared spectra, *Spectrochim. Acta A*, **1999**, 55(7–8), 1585–1612.
3. R.F.W. Bader, Atoms in molecules, *Acc. Chem. Res.*, **1985**, 18(1), 9–15.
4. I. Mata, I. Alkorta, E. Espinosa, E. Molins, Relationships between interaction energy, intermolecular distance and electron density properties in hydrogen bonded complexes under external electric fields, *Chem. Phys. Lett.*, **2011**, 507(1-3), 185–189.
5. E. Espinosa, E. Molins, C. Lecomte, Hydrogen bond strengths revealed by topological analyses of experimentally observed electron densities. *Chem. Phys. Lett.* **1998**, 285, 170–173.
6. E.Yu. Tupikina, G.S. Denisov, S.M. Melikova, S.Yu. Kucherov, P.M. Tolstoy, New look at the Badger-Bauer rule: correlations of spectroscopic IR and NMR parameters with hydrogen bond energy and geometry. FHF complexes, *J. Mol. Struct.*, **2018**, 1164, 129–136.

Oral Reports

Preparation and pervaporation performance of polyphenylene isophthalamide membranes modified by fullerene derivatives

Ramadan Atta^{1,2}, Andrey A. Zolotarev¹, Maria E. Dmitrenko¹, Anastasia V. Penkova¹

¹*St. Petersburg State University, 7/9 Universitetskaya nab., St. Petersburg 199034, Russia*

²*Damietta University, Damietta, Egypt*

E-mail: ramadanatta75@du.edu.eg

Introduction

Polymers have specific structural features like chain flexibility, molecular weight, inter chain interactions, etc., which determine chemical, thermal, and mechanical properties of polymer membranes. In addition, the essential advantages of polymer membranes are easiness of preparation and good transport properties, which are necessary for membrane applications. Due to the aforementioned features, polymers are the most widely used materials in membrane technologies. Furthermore, pervaporation is one of the most promising fields of membrane technologies. It is a technology of separation of liquid mixtures by evaporation through membranes. It has shown its substantial importance in chemical, petrochemical, biochemical, and other industries because it is a low-power-consuming, effective, easy scale-up, ecologically clean, and wasteless technology that can be applied to separation of mixtures of closely boiling components, azeotropic mixtures, mixtures of isomers, and thermally unstable substances.

To improve the membrane quality, membranes with perfect properties are needed. Poly(phenylene isophthalamide) (PA) is applied in the production of dense (nonporous) membranes for the pervaporation processes due to its excellent chemical stability and mechanical properties. Fullerene and its derivatives are considered as promising additives for the development of membrane materials due to unique structural, physical, chemical, and electric properties. In the last few years, some kinds of membranes based on different polymers were modified by fullerene.

In the present work, novel polyphenylene isophthalamide pervaporation membranes modified with various fullerene derivatives were developed and investigated. Transport properties of fullerene-containing PA membranes were studied in pervaporation removal of methanol from its mixture with toluene (azeotropic 72 wt. % methanol - 28 wt. % toluene mixture). It was found that the modification of PA membranes by fullerene and its derivatives led to the improving of the permeation flux and the selectivity. The structural characteristics of the PA modified pervaporation membranes were characterized by scanning electron microscopy (SEM), Fourier Transform Infrared Spectrometry (FTIR), Nuclear Magnetic Resonance (NMR) spectroscopy, Small-angle X-ray scattering (SAXS), and sorption experiments. The evaluation of changes in surface characteristics of modified membrane was carried out by contact angles of water measurements.

Acknowledgements

Russian Science Foundation [grant No. 17-73-20060] supported this work. The experimental work was facilitated by equipment from Resource Centers: for Nano technology, Magnetic Resonance Research Centre, X-ray Diffraction Methods, Thermal Analysis and Calorimetry, Centre for Diagnostics of Functional Materials for Medicine, Pharmacology and Nanoelectronics, Chemical Analysis and Materials Research Centre and GEOMODEL at St. Petersburg State University.

Mechanism of hydrolysis of cobalt oxide-doped bioactive phosphate glasses: ^{31}P MAS NMR, ^{31}P NMR and ESR

Dahiana Avila¹, Dmitrii Bogdanov², Delia Brauer¹

¹*Otto Schott Institute of Materials Research, Friedrich Schiller University, Fraunhoferstr. 6, 07743 Jena, Germany*

²*Saint Petersburg State University, 7/9 Universitetskaya nab., St. Petersburg, Russia 199034*

E-mail: dahiana.avila@uni-jena.de

http://www.brauergroup.uni-jena.de/

The incorporation of CoO into the phosphate glass system $45\text{P}_2\text{O}_5-(30-x)\text{CaO}-25\text{Na}_2\text{O}-x\text{CoO}$ (x : 0.01 to 10 mol%) was found to tune the glass degradation rate, which is of interest for therapeutic applications where cobalt could be released locally such as in wound healing or as bactericide. In the present work, the paramagnetic nature of cobalt was used to study both the structure of the glass network and the structure of complexes of cobalt-phosphate fragments in solution via ^{31}P MAS NMR, ^{31}P NMR and ESR; seeking for insights regarding the mechanism of dissolution. According to MAS NMR, all glasses were composed of pyrophosphate Q^1 and metaphosphate Q^2 species with chains from 8 to 9 phosphate groups in length. Owing to paramagnetic effects, the intensity of both resonances decreased concomitantly with increasing CoO content, according to a model function [1]; until complete disappearance of the respective signals, indicating non-preferential bonding and a homogeneous doping scenario. ESR showed that cobalt existed in a +2 formal oxidation state with octahedral coordination (Fig. 1) in the glass network. The signal-to-noise ratio of ^{31}P NMR spectra allowed only the identification of fragments in solution comprised by up to three phosphate groups indicating fast hydrolysis of chains. The resonances corresponding to the trimetaphosphate ring and orthophosphate as predominant structures in solution, exhibited paramagnetic broadening evidencing that the phosphorus atom is bound within the second coordination sphere with the cobalt ion. Coordination of phosphate species by cobalt appears to play a catalytic role in the hydrolysis mechanism and may consist in turning phosphorus into a suitable electrophile, for a subsequent nucleophilic attack by water.

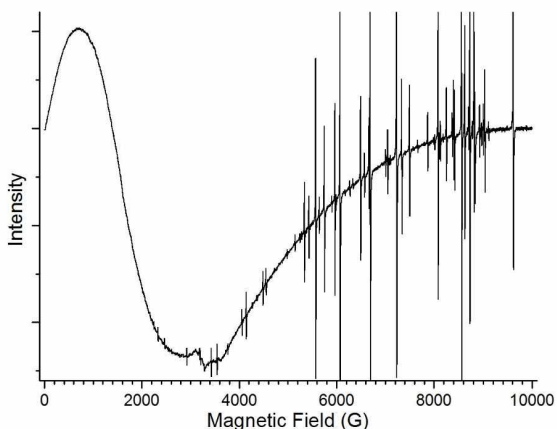


Figure 1. ESR spectrum of $45\text{P}_2\text{O}_5-(30-x)\text{CaO}-25\text{Na}_2\text{O}-x\text{CoO}$ with x : 10 mol%

Acknowledgements

The author would like to thank Peter Bellstedt from the NMR platform service facility at the Faculty of Chemistry and Earth Sciences of the FSU Jena, for carrying out the ^{31}P NMR measurements as well as the Center for Magnetic Resonance at St. Petersburg State University for performing the ESR experiments.

References

1. Li, W.; Celinski, V. R.; Weber, J.; Kunkel, N.; Kohlmann, H.; Schmedt auf der Günne, J. Homogeneity of Doping with Paramagnetic Ions by NMR. *Phys. Chem. Chem. Phys.* 2016.

Dynamical characteristics of the ternary systems (Chlorides of Li, Mg, and Cs) in wide temperature and concentration ranges by NMR method

Valeriia Baranauskaite¹, Olga Pestova¹

¹Institute of Chemistry, SPbSU, Saint-Petersburg, Russia

E-mail: valeriiabar@gmail.com

Introduction

Water-based electrolyte solutions are of special importance in many natural and technical processes. The structure of water-based solutions is still under debates and there are many theories and methods for explanation and direct or indirect definitions of the desired information. Still there are regularities allowing one to determine the structure of the concentrated aqueous solutions [1]. One of these methods is NMR, which is very sensitive to the nuclei surrounding.

A purpose of this investigation was to determine the dynamical characteristics of the particles (associates and nuclei) in the ternary water-based systems containing chlorides of Mg, Li and Cs. These particular cations are different by their nature: Mg²⁺ and Li⁺ are called “hydrophilic” or kosmotropic ions whereas Cs⁺ is “hydrophobic” or chaotropic. These terms stand for water retention in the closest surrounding of the ion, for Li and Mg it is greater than for Cs [2], [3]. Thus, it was very interesting to combine these ions together to see how they would influence the structure of the solution. The objects of this study were solutions in the wide ranges of concentrations and temperatures. The concentrations of components were kept at a constant rate and the temperatures were varied from room temperature (298 K) to the freezing point different for each sample. Using NMR method we have measured Self-Diffusion coefficients of several nuclei such as ¹H, ⁷Li, ¹³³Cs along with T₁ relaxation times.

We were able to measure Self-Diffusion coefficients dependencies on the wide temperature range and calculate the diffusion activation energies for ¹H, ⁷Li, ¹³³Cs nuclei. We compared this data with the relaxation activation energies and defined the correlation between nuclei translational movement, nuclei relaxation and possible surrounding of nuclei in the wide concentration ranges. The relative values of both relaxation and diffusional activation energies show the most thermodynamically profitable process. At the eutectic concentration the structure of solution is known to be chaotic and disordered, it reflects on the values of activation energies: potential barrier for diffusional process is lower than for relaxation process for ¹H. At the low-concentration range the activation energies show that there is no strong influence of ions on each other. At high concentration range the relaxation activation energy is considerably lower than diffusional activation energy due to huge increase of viscosity. Analogic dependencies and statements were made for other nuclei and solutions and the preferable ions surrounding was proposed. According to these statements we were able to estimate the structure of the solution at each concentration range and compare it with those of the binary systems.

Acknowledgements

Scientific research was performed at the Research park of St.Petersburg State University, Centre for Magnetic Resonance.

References

1. Ewine F. van Dishoeck, Edwin A. Bergin, Dariusz C. Lis, Jonathan I. Lunine, Water: from clouds to planets, - Protostars and Planets VI, University of Arizona Press, 2014.
2. Samojlov O.Ya. Struktura vodnyh rastvorov i gidratatsiya ionov. – M.: Izd-vo AN SSSR, 1957.
3. L. Lilich, M. Khripun Rastvory kak himicheskie sistemy. Donorno-akceptornye reakcii v rastvorah (In Russian), - SPbSU, SPb, 2010.

Dynamics of Room Temperature Ionic Liquids: Structural Relaxation Probed by ^1H and ^{19}F NMR

Manuel Becher, Elisa Steinrücken, Michael Vogel

Institute of Condensed Matter Physics, TU Darmstadt, Hochschulstrasse 6, 64283 Darmstadt

E-mail: mbecher@nmr.physik.tu-darmstadt.de

https://www.fkp.tu-darmstadt.de/groups/ag_vogel/

Introduction

Room Temperature Ionic Liquids (RTILs) are salts with a low melting point. They are usually glass-forming systems with complex and heterogeneous molecular dynamics. The combination of different cations and anions opens wide fields of chemical and physical applications, e.g., as solvents or fluid electrolytes, and their optimization. Hence, a fundamental understanding of the dependence of molecular dynamics on the liquid composition is of crucial importance. Here, we study imidazolium-based RTILs. To systematically vary the structural heterogeneity, we change the length of the alkyl chain at the cation [$\text{C}_n\text{-mim}$], while bis(trifluoromethane)sulfonamide [TFSI] is always used as the anion.

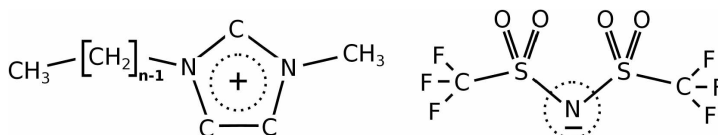


Figure 1. Cation and anion of the studied RTILs

Methods and results

To ascertain the dynamical behavior of these imidazolium based RTILs, we exploit that NMR provides access to glassy dynamics in wide ranges of time and length scales. Moreover, due to its isotope selectivity, the dynamical behaviors of different molecules/molecular groups can be separated. In conventional high field NMR we find T_1 minima strongly influenced by spin diffusion. A spectrally resolved evaluation reveals numerous internal motional processes of the cation. The structural relaxation can be identified using support from concomitant molecular dynamics simulations [1].

Applying Field-Gradient NMR, we measure the self-diffusion coefficient of the cations (^1H) and anions (^{19}F), revealing no hints to chain-length dependent clustering. Field-Cycling NMR provides frequency-dependent relaxation times $T_1(\omega)$, which, in turn, yield spectral densities of motional processes and, thus, translational and rotational correlation times.

Comparing long-range self diffusion with short-range structural relaxation, we analyze cation-anion couplings against the background of alkyl-chain length dependent structural heterogeneities. Increasing the chain length causes an overall slowdown of diffusion and a change in fragility. Over six orders of magnitude, rotational correlation times of cation and anion are shown and, at variance with previous publications, no decoupling due to structural changes is observed [2, 3].

The findings of our NMR experiments can be compared to results from dynamic light scattering. In more detail, high-temperature and low-temperature structural relaxation times measured using a Fabry-Perot-interferometer and photon correlation spectroscopy, respectively, are plotted together with the NMR data. The combination of both methods gives access to molecular dynamics over about 14 decades in time.

Acknowledgements

We thank F. Pabst and T. Blochowicz for providing us with dynamic light scattering data.

References

1. T. Pal, M. Vogel. Role of Dynamic Heterogeneities in Ionic Liquids: Insights from All-Atom and Coarse-Grained Molecular Dynamics Simulation Studies. - *Chem. Phys. Chem* (2017)
2. J. N. A. Canongia Lopes, A. A. H. Pádua. Nanostructural Organization in Ionic Liquids. - *J. Phys. Chem. B*, 110, 3330-3335 (2006)
3. A. Triolo, O. Russina, H.-J. Bleif, E. Di Cola. Nanoscale Segregation in Room Temperature Ionic Liquids. - *J. Phys. Chem. B*, 111, 4641-4644 (2007)

Molecular mobility in a set of imidazolium-based ionic liquids

Sergei Bystrov, V. I. Chizhik

Department of Nuclear-Physics Research Methods, Faculty of Physics, Saint-Petersburg State University

E-mail: barigapunk@gmail.com

Ionic liquids (ILs)/room temperature ionic liquids (RTILs), by the most widely accepted definition, are compounds consisting entirely of ions, but in contrast to ordinary salts they remain liquid at the room temperature or at temperatures below 100 °C. The first ILs were discovered more than 100 years ago but they have become the focus of intensive investigations only in the past few decades. The ILs are normally composed of asymmetric organic cation and anion of nearly any type. They possess unique properties such as low vapor pressure, high boiling point, high thermal stability, structural designability, and the ability to dissolve a wide range of chemical species [1]. These systems, neat and in solutions, may be considered as one of the most successful breakthroughs in creating smart multifunctional materials and compositions applied in “green chemistry”, in separation, purification and other technological processes [2]. The ILs have been suggested as non-aqueous electrolytes for electrochemical applications, energy storage and conversion, super- or ultra-capacitors, light-emitting and dye-sensitized solar cells. Beside physical and chemical properties, their biological activity, antimicrobial and cytotoxic properties and, thus, potential application in pharmaceuticals and medicine have been attracting significant interest of scientists working in the fields of life science, biochemistry, drug synthesis, etc [3, 4].

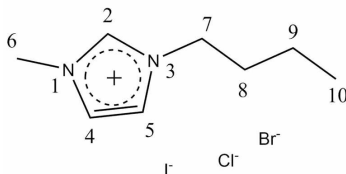


Figure 1. Ionic liquid of the [BMIM] type with numbering of the atoms within the cation

In this work the detailed investigation of the local mobility in a set of dried imidazolium-based ionic liquids (1-butyl-3-methylimidazolium) in a wide temperature range and varying anions (BF_4^- , I^- , Cl^- , Br^- , NO_3^- , TfO^-) is presented. Figure 1 shows the examples of such ionic liquids with the numbering of the atoms in the cation. The measurements of temperature dependencies of spin-lattice relaxation times of the ^1H and ^{13}C nuclei are motivated by the need to obtain a fundamental characterization of molecular mobility of the substances under study, namely, to estimate the correlation times, τ_c , for the motion of individual molecular groups. In particular, it follows from obtained results that the mobility of the hydrocarbon “tail” is higher (smaller τ_c) than the one of the imidazole ring, and it is important that this expected tendency is quantified. The effect of an anion type on the cation mobility is also analyzed.

Figure 2 shows the original ^{13}C relaxation data obtained for all the samples under the study. A specially designed computer algorithm allows one to calculate correlation times for each individual molecular group in case when a maximum on the relaxation curve exists in the temperature range under study. Figure 3 illustrates the results of such a technique.

Acknowledgements

The work is supported by the RFFI grant 17-03-00057.

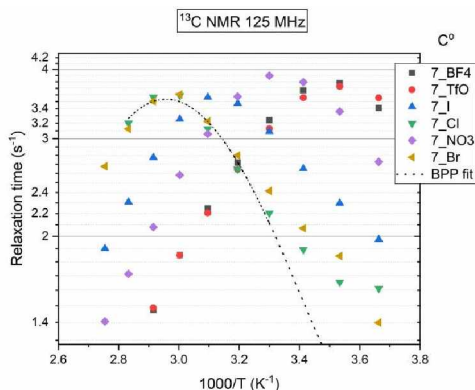


Figure 2. The temperature dependencies of the ^{13}C spin-lattice relaxation rates for the selected functional group (7) of the cation in the presence of different anions

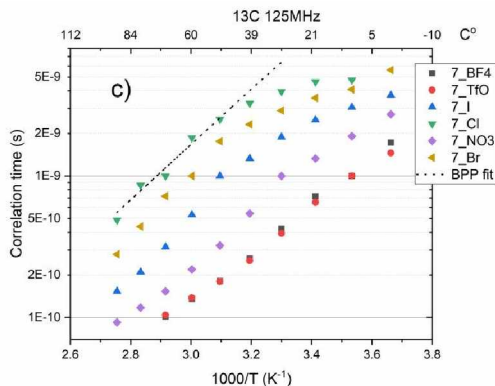


Figure 3. The temperature dependencies of the calculated correlation times for the selected functional group (7) of the cation in the presence of different anions

References

1. Ghandi, K. A Review of Ionic Liquids, Their Limits and Applications. *Green and Sustainable Chemistry* 2014, 04 (01), 44–53.
2. Fredlake, C. P.; Crosthwaite, J. M.; Hert, D. G.; Aki, S. N. V. K.; Brennecke, J. F. Thermophysical Properties of Imidazolium-Based Ionic Liquids. *Journal of Chemical & Engineering Data* 2004, 49 (4), 954–964.
3. Abe, H.; Kishimura, H.; Aono, M. Anomalous Phase Behavior of Excess Iodide in Room-Temperature Ionic Liquid: 1-Methyl-3-Propylimidazolium Iodide. *Chemical Physics* 2018, 502, 72–76.
4. Abe, H.; Takekiyo, T.; Shigemi, M.; Yoshimura, Y.; Tsuge, S.; Hanasaki, T.; Ohishi, K.; Takata, S.; Suzuki, J. Direct Evidence of Confined Water in Room-Temperature Ionic Liquids by Complementary Use of Small-Angle X-Ray and Neutron Scattering. *The Journal of Physical Chemistry Letters* 2014, 5 (7), 1175–1180.

Multinuclear dipolar NMR spectroscopy in ionic liquid crystals

Jing Dai¹, Boris B. Kharkov², Sergey V. Dvinskikh^{1,2}

¹Department of Chemistry, KTH Royal Institute of Technology, Stockholm, Sweden

²Laboratory of Biomolecular NMR, Saint Petersburg State University, Russia

E-mail: sergeid@kth.se

Ionic liquid crystals (ILC) belong to a class of materials that are ionic liquids capable of forming liquid crystalline phases on cooling from isotropic state [1]. ILC have the typical properties of ionic liquids, and, at the same time, an anisotropic nano-scale structure of liquid crystals. This results in unique combination of ionic conductivity displayed by ionic liquids, and anisotropic physico-chemical properties, revealed by liquid crystalline materials. The presence of the molecular orientational order in fluid ionic material leads to new dynamic properties exploited in modern technological applications.

NMR spectroscopy is a powerful experimental tool for investigating molecular conformation, orientational order and dynamics in liquid crystals. Structural and order parameters at the atomic and molecular levels can be obtained through the measurements of dipole-dipole spin couplings, which are orientation- and interatomic distances dependent. In contrast to isotropic phase, the motion of the individual molecules in a liquid crystalline phase is not fully isotropic. Thus, the residual dipolar coupling, left after the fast motions, is not averaged to any lower value.

We present number of experimental NMR approaches to measure dipolar couplings in mesophases of ILC samples with natural isotopic abundance. ¹³C-¹H and ¹⁵N-¹H heteronuclear dipolar couplings between abundant protons and rare isotopes are measured by separated local field spectroscopy method [2]. Homonuclear dipolar coupling between carbon-13 spin pairs at natural abundance of 0.012% are obtained in double-quantum correlation dipolar INADEQUATE experiment [3]. It is most challenging to experimentally detect ¹⁵N-¹³C dipolar spectra since the fraction of the molecules containing ¹⁵N-¹³C pairs is only 0.004%. Recent experimental strategies to record ¹⁵N-¹³C dipolar spectra in liquid crystalline samples with natural isotopic abundance will be presented [4, 5].

This work was supported by the Swedish Research Council VR and by the Russian Foundation for Basic Research (project no. 17-03-00057).

References

1. K. Goossens, K. Lava, C.W. Bielawski, K. Binnemans. – *Chem. Rev.* **116**, 4643 (2016).
2. S. V. Dvinskikh. In *Modern Methods in Solid-State NMR: A practitioners' Guide*, ed. by P. Hodgkinson. Abingdon: Royal Society of Chemistry (2018).
3. J. Dai, B. B. Kharkov, S. V. Dvinskikh. – *Crystals*, Submitted (2018).
4. M. Cifelli, V. Domenici, V. I. Chizhik, S. V. Dvinskikh. – *Appl. Magn. Reson.* **4**, 553 (2018).
5. L. Jackalin, B. B. Kharkov, A. V. Komolkin, S. V. Dvinskikh. – *Phys. Chem. Chem. Phys.*, **20**, 22187-22196 (2018)

Various NMR approaches in studies of polypeptides: Application to insulins and cyclosporins

S. V. Efimov, Yu. O. Zgadzay, A. V. Slivka, S. Darwish, P. P. Kobchikova

Institute of Physics, Kazan Federal University, Kazan, 420008 Russia

E-mail: Sergej.Efimov@kpfu.ru

Introduction

Development of biologically active molecules with new required properties can benefit from studies at the molecular level in conditions close to naturally occurring in a living organism. These conditions can be quite different, depending on the presence of other molecules or ions, polarity of the environment, etc. On the other hand, there are many NMR parameters which may be useful in every particular case, and specific experiments have been developed to gain corresponding information.

Here we describe investigations of biologically active peptides, namely, insulin and cyclosporins, which are conducted in the Laboratory of NMR at Kazan Federal University. The goal of this research is to establish properties of the compounds such as molecular structure, H-bond pattern, flexibility of the chain, and in the case of insulin – tendency to aggregation.

Object

Insulin is an irreplaceable preparation for people suffering from diabetes mellitus; that is why it is important to study its structure and interaction of insulin with different ligands. Conformation changes which accompany ligand binding are of fundamental interest. On the other hand, physicochemical properties such as solubility and stability are important in drug preparation and delivering [1].

Cyclosporins form a family of over 30 cyclic peptides found in nature as metabolites of soil fungi. Cyclosporin A (CsA) is widely used as an immunosuppressant. All cyclosporins have similar properties regarding their molecular weight and hydrophobicity, but different action on the organism. Variants A, C, and D show immunosuppressive properties, while CsB does not. Again, dynamical properties of the molecule are important in this case, as they were shown to be related with the ability to penetrate cell membranes and thus determine bioavailability [2]; on the other hand, coexistence of several conformations may decrease the activity of the drug if the active conformer has a small relative concentration [3].

We studied bovine insulin and cyclosporins A–D. Insulin molecule consists of two units called A and B and linked together with disulfide bonds. Bovine insulin differs from human insulin by three amino acid residues: Ala8A←Thr8A, Val10A←Ile10A, Ala30B←Thr30B (former residues belong to the bovine form; latter, human). This difference does not alter the most conservative and important segments of insulin, A1–A3, A12–A17, and B8–B25 [4].

Cyclosporin chain consists of 11 amino acid residues cycled from head to tail. Residue Bmt (4-methyl-4-[(E)-2-butenyl]-4,N-methyl threonine) or its derivatives is a unique feature of cyclosporins, it is usually considered as the first in the chain; D-Ala stands in the position 8; residue 2 is the most variable among the whole family of this peptides. Other differences between peptide variants may include alteration of amino acids, presence or absence of N-methylation of the amide group, and changes in the optical isomers of individual residues. The four studied variants differ in position 2: CsA has aminobutyric acid Abu at this site; CsB, alanine; CsC, threonine (polar amino acid); and CsD, valine.

Method

Bovine insulin extracted from pancreas was purchased from Sigma Aldrich. The sample was insulin dissolved in water (90% H₂O, 10% D₂O, concentration $c = 1.1$ mM); DSS was used

for referencing the chemical shift scale. Use of the acidic solution was needed due to a low solubility of insulin in neutral environment (HCl was added to achieve pH = 2.86).

Cyclosporins B, C and D were purchased from Bertin Bioreagent, AvaChem and Cayman Chemical, respectively. Solutions in deuterated chloroform with the concentration of 1.0–1.6 mM were prepared for investigation. TMS was used as an internal chemical shift standard.

All experiments were carried out on a Bruker Avance III HD 700 spectrometer (proton resonance frequency 700.13 MHz, ^{13}C resonance frequency 176.05 MHz). Temperature of the sample was stabilized with the accuracy of $\pm 0.1^\circ\text{C}$. Combination of DQF-COSY, TOCSY, ^1H , ^{13}C -HSQC and HMBC was used for signal assignment. Structural data were obtained using NOE spectroscopy (NOESY, ROESY); DOSY measurements were also performed in the case of insulin.

Results

Bovine insulin

Three helical regions were revealed in the bovine insulin molecule based on the backbone chemical shifts indices ($^1\text{H}\alpha$, $^{13}\text{C}\alpha$) and medium-range NOE contacts. They include residues A3–A7, A12–A18, and B8–B18. An additional series of TOCSY experiments with the sample dissolved in D_2O (with addition of HCl) was also made to observe proton–deuterium exchange. NH–H α cross-peaks of Cys6, Cys7, Ala8 in chain A and Leu6, Cys7, Arg22, Phe24 in chain B disappeared during the first few hours, while many signals in the mentioned helical regions were still visible in 11 hours after sample preparation. The helix 3A–7A turned out to be less stable and prone to chemical exchange with water. The bend at the C-terminal part of the B-chain showed a relatively slow exchange rate, though residues number 24, 26 are placed beyond the β -turn 20–23 which was reported for human insulin [5] and is expected to be found here.

We carried out DOSY measurements which allowed estimating the insulin self-diffusion coefficient $D_{\text{bi}} = 9.8 \cdot 10^{-11} \text{ m}^2/\text{s}$, while the internal standard (DSS) in the same solution had $D_{\text{DSS}} = 4.47 \cdot 10^{-10} \text{ m}^2/\text{s}$. Knowing the molecular weight of DSS, we can estimate roughly the MW of insulin, which is consistent with the range $M_{\text{bi}} = n \cdot 5733.5 \text{ Da}$, $n = 1, 2, 3$. To elucidate further the question of dynamical dimerization of protein molecules, we estimated also the correlation time τ_c from known interatomic distances in tyrosine ring and measured cross-relaxation rate. It was found to be $\tau_c \sim 2.9 \text{ ns}$, but decreased as the solution was diluted. Applying Stokes-Einstein formula to estimate the molecule size gives a result larger than expected for known insulin structures [6].

Cyclosporins

When dissolved in chloroform, all studied cyclosporins show similar spectra, which means that their spatial structure remains generally unaltered. However, there are some variations showing which segments of the peptide chain turn out to be most sensitive to amino acid replacement at position 2. Analysis of backbone atoms' chemical shifts (C α , H α , CO) reveals that in addition to amino acids 1 and 3 (which are neighbors of the altering site), more distant residues 5 and 8 experience noticeable changes. Positions of amide proton resonances are also similar, with the exception of Val5 NH whose chemical shift varies by 0.4 ppm among cyclosporins A–D. CsB and D were similar to CsA regarding their spectra, which does not correlate directly with their biological action. On the contrary, deviation between backbone chemical shifts of CsC and CsA was larger, while this peptide retains much of immunosuppressive activity.

Thus, biological action of a peptide may depend on specific sites, conformation of side chains, presence of certain hydrogen bonds, etc. In the case of cyclosporins, some unexpected

signals were observed in the region 3.8–4.1 ppm which were ascribed to Thr2 OH group in CsC and Bmt1 OH in CsD. No hydroxyl protons were observed in 1D spectra for cyclosporins A and B; however, they showed broad diagonal signals in the high-field region of 2D NOESY spectra which can be assigned to labile OH protons.

Another intriguing property of cyclosporins is their behavior in polar media such as water, DMSO, DMF, etc. A complex slow conformational exchange takes place in these solvents. Assignment of some peaks of NH protons of CsC in DMF was achieved at several temperatures from 14° to 40°C. Some of the signals (e.g., Thr2 NH) showed slow dependence of the chemical shift on the temperature which indicates the presence of an intramolecular H-bond; however, most of the signals changed their position rapidly towards the high fields as the temperature increased. This is in agreement with an idea that most intramolecular bonds in cyclic peptides are disrupted in polar media, which makes their structure flexible [7].

Conclusions

Overall sizes of structures of insulin molecules agree with the DOSY measurements assuming that the molecule exists in fast exchange between monomeric and oligomeric forms in solution with pH = 2.86. Indirect observations confirm this suggestion: molecular tumbling correlation time and peak width in the ¹H,¹³C-HSQC spectra were found to decrease as the insulin concentration decreased. This can be explained as the shift in the exchange equilibrium: the less concentrated the solution is, the larger the fraction of the monomeric form becomes.

Backbone and side chains chemical shifts of cyclosporins A–D were found to be similar, with small relative differences. We may expect that a decreased size of the residue 2 (alanine instead of aminobutyric acid) and a change in the H-bonding behavior of Bmt1 are responsible for the inactivation of the biological activity of CsB, since these residues belong to the cyclosporin/cyclophilin interaction interface.

Cyclosporin C in polar media behaves similarly to CsA and experiences a complex pattern of conformational changes. Few NH signals show a slow temperature dependence, which means that intramolecular hydrogen bonds of the peptide are mostly disrupted and directed into the solvent. The fraction of the molecules having an increased number of intramolecular H-bonds is small and corresponds to the minor NH signals.

References

1. M.A. Weiss. – *J. Health. Spec.*, **1**, 59-70 (2013).
2. C.K. Wang, J.E. Swedberg, P.J. Harvey et al. – *J. Phys. Chem. B*, **122**, 2261-2276 (2018).
3. G. Zeder-Lutz, M.H.V. Van Regenmortel, R. Wenger et al. – *J. Chromatogr. B*, **662**, 301-306 (1994).
4. J.P. Mayer, Z. Faming, R.D. DiMarchi. – *Pept. Sci.*, **88**, 687-713 (2007).
5. J.G. Menting, Y. Yang, S.J. Chan et al. – *Proc. Natl. Acad. Sci. USA*, **111**, E3395-E3404 (2014).
6. S.V. Efimov, Yu.O. Zgadzay, N.B. Tarasova et al. – *Eur. Biophys. J.*, **47**, 881-889 (2018).
7. K.A. Farley, Ye Che, A. Navarro-Vázquez et al. – *J. Org. Chem.*, <https://doi.org/10.1021/acs.joc.8b02811> (2019).

Magnetic Resonance Imaging in Low Magnetic Field

Viacheslav Frolov, Konstantin Tyutyukin

*St. Petersburg State University, 1, Ulyanovskaya str.,
St. Petersburg, 198504, Russian Federation
vfrolov@bk.ru*

In recent years there is a tendency in magnetic resonance imaging (MRI) to use an ever-increasing strong magnetic field. The trend is justified by the fact that MRI is characterized by low sensitivity, and this in turn leads to a long time of medical examination. Nevertheless, over the past decades, interest in obtaining an MRI in a weak magnetic field has not only not decreased but, on the contrary, has increased. This is primarily due to the economic factor: the creation of a magnetic field does not require superconducting magnets, and the equipment is several orders of magnitude cheaper.

However, in MRI in a weak magnetic field there are points of physical and practical interest. This is primarily a higher absolute resolution in a weak field with the same relative inhomogeneity of the magnetic field. Secondly, there is a dependence of nuclear magnetic relaxation times on the magnetic field level. This circumstance leads to the dependence of the contrast of relaxation-weighted images on the field level, which can be used in some cases for diagnosis. Another feature of an MRI in a weak field is the practical extinction of chemical shifts, so that there are no chemical shift artifacts on images. On the other hand, heteronuclear scalar interactions are well manifested in a weak field. This can be used, in particular, for indirect registration of nuclei other than protons.

To overcome the main difficulty of an MRI in a weak field - low sensitivity, various techniques are used. Firstly, careful optimization of receiving-transmitting hardware, the use of sensors with extremely high permissible quality are required. In addition, special techniques are used, among which, first of all, dynamic polarization should be mentioned. Also uses such exotic techniques as the registration of NMR using SQUID and the hyperpolarization.

References

1. Ю. В. Богачев, М. Н. Князев, Я. Ю. Марченко, А. Н. Наумова, К. В. Тютюкин, В. А. Фокин, В. В. Фролов, Ю. С. Черненко. Диагностический магнитный резонанс. СПб: Изд-во СПбГЭТУ "ЛЭТИ", 2013. 212 с.
2. Ю. В. Богачев, В. З. Драпкин, М. Н. Князев, Е. П. Попечителев, И. В. Разин, В. В. Фролов. Магнито-резонансная томография в слабом магнитном поле. СПб: Изд-во "ЛЭТИ", 2012. 260 с.
3. Н. К. Андреев. Методы и приборы низкочастотной релаксационной ЯМР-интроскопии. Казань: Казан. гос. энерг. ун-т., 2003. 208 с.

Up-to-Date Industrial Applications of Time-Domain NMR

Leonid Grunin^{1,2}

¹Resonance Systems GmbH, Seestrasse 28, D-73230, Kirchheim u. Teck, Germany

²Volga State University of Technology, Lenin sq. 3, Yoshkar-Ola, Russia

E-mail: mobilnmr@hotmail.com

<http://www.nmr-design.com>

Avalanche-like explosion of digitalization and cloud technologies of the Internet of Things (IoT) nowadays embrace nearly every branch of human activity starting from intelligent kitchenettes, amateur DIY by microcontrollers, wireless remote car maintenance and ending up at total automation of factory mass production, logistics and artificial intelligence in companies' boards of directors. According to forecasts of experts the market of sensors that are involved in digital life flow will be increased in a geometrical progression for the upcoming decade. This fact is bringing up new requirements for every analytical technique to migrate from stationary laboratory setups to inexpensive robust miniature modular sensors that can be immersed in standardized online solutions.

There is a good chance for the Time-Domain NMR (TD-NMR) to merge into this trend involving recent progress in permanent magnets, microelectronics and embedded software technologies. The presented talk is uncovering some aspects of the marked issue:

1. Development of miniaturized and cost effective hardware;
2. Easiness of installation;
3. Very robust, accurate and fast measurement techniques;
4. Reliable models of Sensor+Sample (development of *Digital Twins*)
5. Accessibility for online performance control and data analyzing/storing via Application Programming Interface (API) of IoT systems;

The following measurement techniques of TD-NMR will be discussed in details

- Solid Fat Content (SFC) – mostly in food products
- Total Fat Content (TFC) – mostly in food products
- Oil content – in food, seeds, artificial tissues (Spin Finish)
- Sugar content – in food and dairy products
- Moisture – in food, gun powders, sand, fuels (calorific value)...
- ¹H (proton) density – for fuels, polymers...
- Na, Fe, Al, P, Ca, F, N... content
- Droplet size distribution – oil and water droplet sizes in emulsions
- Specific Area – for particles dispersions and sorbents
- Particles size – for particles dispersions
- Pores volume – for adsorbent, construction materials
- Molecular weight and chain length – for medium size oligomers and fats
- Crystallinity – from sugars and celluloses to artificial polymers, their solubility and density
- Crosslinking – for elastic polymers network
- Purity of water and paramagnetic ions in trace concentrations for environmental research

Development of a technique for determination of total fat content in food products by NMR-relaxation

Maria S. Ivanova, Leonid Yu. Grunin

*Volga State University of Technology, Lenin sq. 3, Yoshkar-Ola, Russian Federation
E-mail: manyunya1107@gmail.com, mobilenmr@hotmail.com*

The vast majority of methods for determination of fat content are based on its extraction with organic solvents. Their main benefits are high accuracy and reproducible results. However, these methods have significant drawbacks – the duration of laboratory test takes more than 2 hours, the harmful reagents are used [1], and the experimenter need to be qualified as the analytical chemist, making it impossible to automate measurements. For these reasons, more and more efforts are now being made to intensively develop the most optimal methods for determination of fat content in food products.

Currently, express-methods for food quality control are mainly implemented on the basis of spectroscopic methods for analyzing substances which is associated with overcoming the deficiencies of reference methods and the absence of destructive effects. A significant number of methods for assessing the quality indicators of food products based on NMR-relaxation phenomena have been proposed for several decades [2]. The purpose of this research is to develop the universal technique for determination of total fat content (TFC) in any solid fat-containing food products based on nuclear magnetic resonance the advantages of which will be to reduce the duration of single measurement, the absence of weighing procedure for sample under study and the use of hazardous solvents, as well as the automation of measurements for process control.

Our proposed technique for TFC determination in samples under study is founded on separation the signal from fats and suppression the contribution of water. For this, model samples with various percentages of total fat (liquid and solid) and different protein-carbohydrate composition were maintained above temperature of transition of solid fats in the liquid state. All measurements were performed by the “Spin Track” NMR-analyzer [3] with the set of pulse sequence *Solid Echo – Hahn Echo* using the constant magnetic field gradient, the effect of which resulted in the signal from water molecules being almost completely suppressed. TFC in solid fat-containing foods is estimated by the ratio of amplitude of the spin echo to total amplitude of the signal recorded after applying the second 90° RF pulse of the Solid Echo sequence.

In Figure 1 we demonstrate the dependence of total fat content in model samples (TFC set value, %) established by reference methods (GOST 23042-2015, 31902-2012) on the ratio of spin echo amplitude to total amplitude of the NMR signal (NMR Data, a.u.).

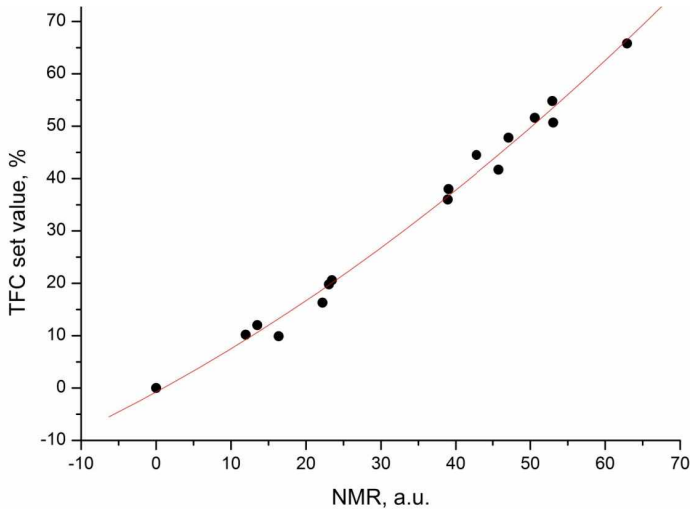


Figure 1. Approximation of experimental results

Experimental data were approximated by the second-order polynomial function. The non-linear nature of the dependence presented in Figure 1 can be explained by appearance of the interface layer at the section boundary “solid components–molten fat”. In the process of heating samples, the mutual penetration of molecules of one of the components of the interface layer into the other occurs, and therefore the movement of these molecules becomes quasi-limited which can lead to decrease in the intensity of their signal. This fact may be the main reason for the underestimated value of echo amplitude, while its overestimation is most likely due to the signal from water molecules that is not fully suppressed.

Results obtained by the proposed technique have a good correlation with values of total fat content in samples established by reference methods. Their errors may be due to incorrectly selected scan repetition time during signal accumulation, the not fully suppressed contribution of the water signal to the spin echo and the strong dependence of the transverse relaxation time of fats on temperature.

References

1. L.F. Ramazaeva. Methods for the Determination of Fat in Food Products: guidelines for laboratory work (in Russian). – Yuri Gagarin State Technical University of Saratov, Saratov, 2009.
2. G.H. Sorland, P.M. Larsen, F. Lundby, A. Rudi, T. Guiheneuf. – Meat Science, 66, 543-550 (2004).
3. <http://www.nmr-design.com>.

Dynamic nuclear polarization of doped silicon at high fields and low temperatures

Jarno Järvinen¹, Denis Zvezdov², Janne Ahokas¹, Sergey Vasiliev¹,
Yutaka Fujii³ and Leonid Vlasenko⁴

¹*Wihuri Physical Laboratory, Univ. of Turku, Turku, Finland*

E-mail: jaanja@utu.fi

²*Institute of Physics, Kazan Federal University, Kazan, Russian Federation*

³*Research Center for Development of Far-Infrared Region, Univ. of Fukui, Fukui, Japan*

⁴*Ioffe Physico-Technical Institute, St. Petersburg, Russian Federation*

Nuclear spins coupled to electrons is interesting system for future quantum architectures. Shallow donors in Si coupled to ²⁹Si nuclei is one such system. The coherence of ²⁹Si nuclei in the “frozen core” near the nuclei is protected by the donor electron leading to very long coherence times [1]. Here, we report on dynamic nuclear polarization (DNP) experiments of donor and ²⁹Si nuclear spins in silicon utilizing 130 GHz cryogenic electron spin resonance (ESR) spectrometer.

The Overhauser (OE) and solid effect (SE) methods of DNP provide almost full control of spin polarization of the donor and the nearby ²⁹Si nuclei [2]. In magnetic field of 4.6 T and below 1 K temperatures the donor electron spins are fully polarized and the nuclear relaxation times can be several days [3]. The DNP of nuclear spins is achieved by exciting allowed and forbidden ESR transitions. Spin polarization is observed directly from the ESR spectrum and the polarization is not disturbed during the measurement.

We have observed different polarization dynamics of ²⁹Si for OE and SE methods. Utilizing OE leads to preferential polarization of ²⁹Si nuclei with relatively weak hyperfine interaction with the donor electron. However, utilization of SE leads to preferential polarization of the strongly interacting spins and we demonstrate that the SE polarization method can create perfect polarization of the ²⁹Si with strong hyperfine interaction. We will also show that combining the OE and SE effect for ²⁹Si and donor nuclei it is possible to manipulate the spin polarization of ²⁹Si and isolate the ESR signal of the donors having a controlled number of ²⁹Si spins near the donor.

References

1. Gary Wolfowicz et al., *New J. Phys.* **18**, 023021 (2016)
2. J. Järvinen, *et al.*, *Phys. Rev. B* **92** (2015) 121202
3. J. Järvinen, *et al.*, *Appl. Magn. Reson.* **48** (2017) 473

LiverMultiScan – a diagnostic aid for liver disease

Alexandr A. Khrapichev

Perspectum Diagnostics, Oxford OX1 2ET United Kingdom

E-mail: alexandr.khrapichev@perspectum-diagnostics.com

http://www.perspectum-diagnostics.com

Introduction

Liver disease is a global epidemic affecting over 844 million people driven by a rising prevalence of non-alcoholic fatty liver disease (NAFLD) and its more severe subtype, non-alcoholic steatohepatitis (NASH). Global NASH prevalence is expected to increase by 63% between 2015 and 2030. Pharmaceutical companies are actively developing new treatments, with the NASH therapeutic market size projected to catapult from \$618M in 2016 to \$25.3B by 2026. Current gold standard for staging and diagnosis of NASH is liver biopsy, an invasive and often painful procedure with high-costs and risk of complications

Our Solution

New ways of accurately diagnosing liver disease early are essential if health care systems are to tackle this growing issue, which is predicted to lead to many more cases of serious liver damage and people needing liver transplants. Our work focuses on the detection and accurate, quantitative measurement of liver, gallbladder and pancreatic disease, including precancerous and cancerous states. We combine digital imaging and innovative software to provide non-invasive and accurate solutions for diagnosing liver disease, including NASH.

Our flagship product

LiverMultiScan™ is our flagship product, it uses cutting-edge multiparametric MRI techniques to non-invasively quantify liver health, by providing accurate measures of liver fat as well as correlates for iron and fibro-inflammatory disease. In addition to NASH, our work focuses on the detection and quantitative measurement of other liver, as well as gallbladder and pancreatic disease, including precancerous and cancerous states.

LiverMultiScan, is a diagnostic aid for liver disease. It is non-invasive and characterizes liver tissue by providing accurate and quantitative measures of liver fat and correlates of iron, fibrosis and inflammation levels (Figure 1) using multiparametric MRI. LiverMultiScan is suitable for clinical practice and clinical research; risk-stratification screening, enrichment and longitudinal monitoring. Our imaging solutions is empowering patients and the medical community through greater understanding of liver disease to enable diagnosis and targeted treatment.

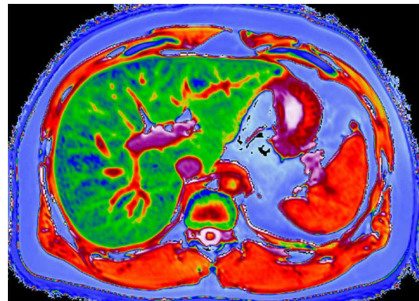


Figure 1. MR image of fibrosis and inflammation levels of a liver

References

1. R. Banerjee et al. Multiparametric magnetic resonance for the non-invasive diagnosis of liver disease. – *J Hepatol*, 60:69-77 (2014).
2. M. Pavlides et al. Multiparametric magnetic resonance imaging predicts clinical outcomes in patients with chronic liver disease. – *J Hepatol*, 64:308-315 (2016).

Visualization of the DNA environment from the molecular dynamics simulation

Andrei V. Komolkin, Irina A. Silanteva

Faculty of Physics, Saint Petersburg State University, 7-9 Universitetskaya emb., 199034, Saint Petersburg, Russian Federation

E-mail: a.komolkin@spbu.ru

Introduction

In the present study we investigated the local structure of DNA and its environment using a new visualization technique. The spiral staircase distribution function (SSDF) is determined as two-dimensional density distribution of atoms of water and ligands in local reference frames linked with each base pair of poly-DNA molecule, either GC or AT. This property of SSDF provides opportunity to study sequence-specific binding of ions, peptides and other agents derived from a molecular dynamics computer simulation.

Spiral staircase distribution function

In the report, the detailed algorithm of SSDF calculation will be described. Local reference frames are set for each of base pairs independently on other base pairs. The origin of the reference frame coincides with the center of mass of the heavy atoms (i. e. except hydrogen atoms) of the nucleobase pair and C1' carbons of deoxyriboses (Fig. 1). The axes of the frame are chosen as principal axes of the inertia tensor of the atoms mentioned above, the positive direction is chosen from the purine base (A or G) to the pyrimidine base (T or C).

Probability density of the water molecules, ions and other ligands around this base pair is calculated in the layer and is averaged in each voxel. The element of the layer is called voxel as it is named in magnetic resonance imaging (MRI) and in computed tomography (CT). We propose the voxel dimensions to be $0.1 \times 0.1 \times 2.8 \text{ \AA}^3$. The thickness of the layer is chosen to be less than the distance between base pairs which is equal to 3.4 \AA . The Z coordinates of the layer are between -1.4 and $+1.4 \text{ \AA}$. Between two layers there is a thin gap of 0.6 \AA . Two-dimensional SSDF can be plotted as a map in gray or color scale like in MRI or CT.

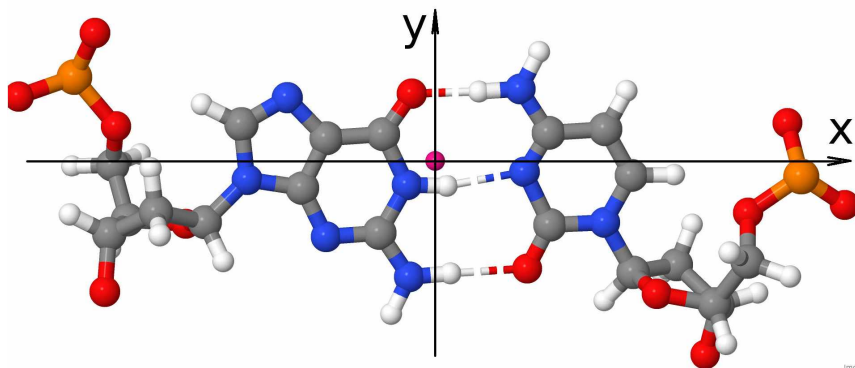


Figure 1. Local reference frame XY linked to GC base pair. Guanine is in the left, cytosine is in the right. H-bonds are shown with dashed lines. Magenta circle represents center of mass, Z-axis oriented perpendicular to the figure plane. Major groove is on the top of the figure

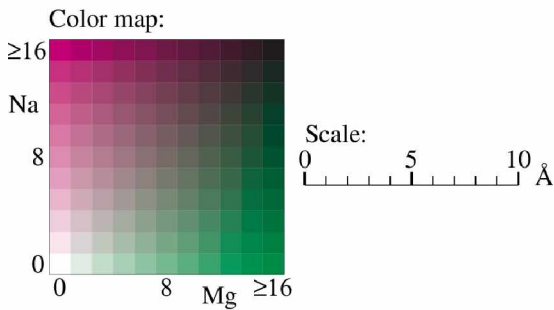
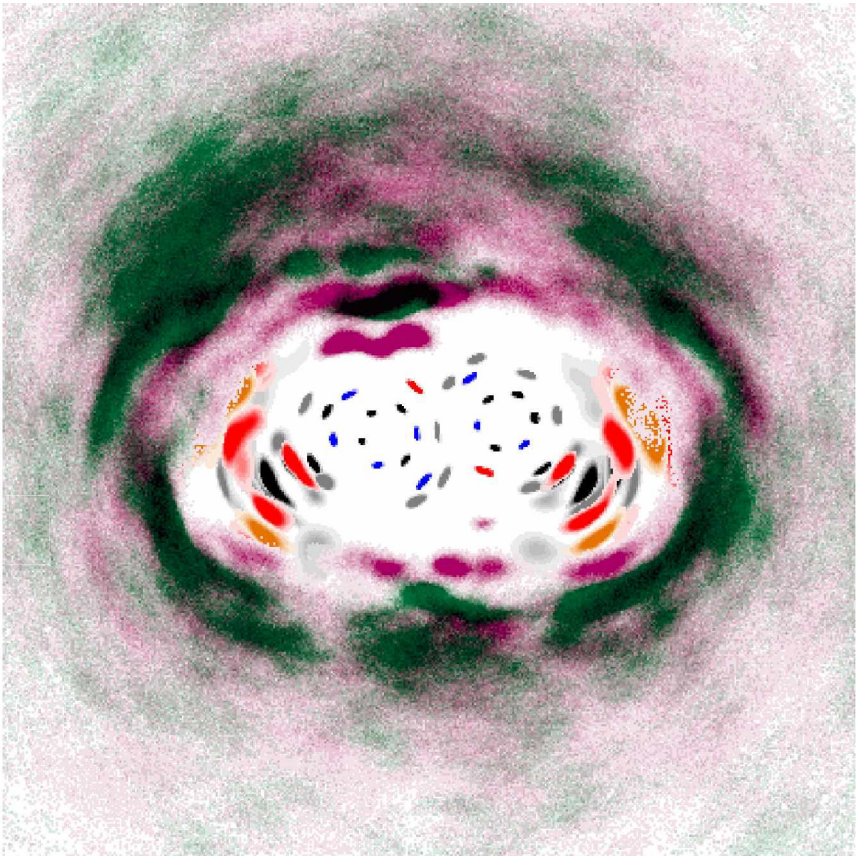


Figure 2. Distribution of sodium (magenta) and magnesium (green) ions around GC base pair, so called ionic atmosphere (upper plate). Two distributions are combined using secondary colors of light in additive color combination. Color map and linear scale (bottom plate)

Results

Double stranded DNA in water solution was investigated [1]. The DNA fragment used in the simulations consists of 18 base pairs: d(GCCCAGCATTTACCCAG), with the total charge of $-34|e|$. Two systems were simulated: (1) one DNA fragment in solution of 18983 water molecules and 34 Na^+ (molar concentration of sodium is about 0.1 M), (2) one DNA fragment in solution of 19000 water molecules and 17 Mg^{2+} (molar concentration is about 0.05 M). SSDFs for Mg^{2+} and Na^+ around GC base pairs are shown in Fig. 2. In this figure, the results (distributions) of two independent simulations are combined in one SSDF. So, reader should compare positions of Na^+ and Mg^{2+} with respect to DNA base pairs but not with respect to each other.

In the report, results of simulation of peptide/DNA system will be presented [2].

Conclusion

Newly introduced spiral staircase distribution function (SSDF) appears to be a suitable analysis tool for the investigation of interactions of active sites of double-stranded DNA (N7, N3 and O6 of purines and O2 and O4 of pyrimidines) with water, ions and biomolecules. The SSDF provides opportunities to study sequence-specific binding of ligands. The SSDF was designed to study mostly interactions of ligands with active sites of base pairs in major and minor grooves.

Acknowledgements

Research was carried out using computational resources provided by Resource Center "Computer Center of SPbU" (<http://www.cc.spbu.ru/en>).

References

1. I. Silanteva, A. V. Komolkin. – *J. Comput. Chem.*, **39**, 2300–2306 (2018). DOI: [10.1002/jcc.25549](https://doi.org/10.1002/jcc.25549)
2. I. A. Silanteva, A. V. Komolkin, E. A. Morozova, P. N. Vorontsov-Velyaminov, N. A. Kasyanenko. – *J. Phys. Chem. B* (2019). DOI: [10.1021/acs.jpcc.8b10359](https://doi.org/10.1021/acs.jpcc.8b10359).

Optimization of based on DW MRI fiber tracking results. Simulated phantom results

Lidia V. Konopleva¹, Oleg V. Nedopekin¹, Marco Reisert², Kamil A. Il'yasov^{1,3}

¹Institute of Physics, Kazan (Volga Region) Federal University, Russia

²Department of Radiology and Radiotherapy, University Medical Center Freiburg, Germany

³University Hospital "Kazan", Russia

E-mail: lidia.konopleva@gmail.com

Introduction

Diffusion-weighted magnetic resonance imaging (DW MRI) is a unique noninvasive method, that allows to investigate the structure of living tissue. Fiber tracking (FT) algorithms based on DW MRI use the local information about self-diffusion of water molecules to reconstruct fiber pathways in human brain. Over past decade, FT has become a very useful tool for solving a wide range of practical problems. Nevertheless, there are still many challenges in this area. According to [1] all connectomes built using FT algorithms are dominated by false positive connections. There are many factors that can affect FT results – insufficient in comparison with axon diameter spatial resolution, noise and artifact in data, inadequate models of local diffusion used for data reconstruction. So, there is need to optimize FT algorithms and FT reconstructions analysis methods to improve the reliability of obtained results. In this work we will demonstrate some approaches for improving the FT results using simulated phantom with known structure. Both methods were evaluated using simulated and *in vivo* data. We will demonstrate the results for simulated phantom, since there is known “ground truth” tracts and the results are more evident.

Simulated Phantom

The phantom with the ground-truth structure was simulated using the Phantomas software, 32 gradient encoding directions, $b = 1200 \text{ mm}^2/\text{s}^2$, resolution 1 mm isotropic, signal-to-noise ratio (SNR) 10, 30 and 50. Novel methods usually require data measured along many diffusion encoding directions, so we evaluated proposed methods on data simulated using common-used protocol for diffusion tensor imaging. The variation of “ball and stick” model was used to model diffusion in each voxel. “Tractometer” metrics were used to evaluate the proposed methods: valid tract – line that connect two correct area, invalid tract – line that build connection that doesn't exist in reality, bundle is a set of tracts that connect same areas.

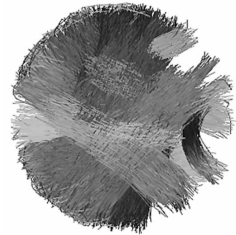


Figure 1. Reconstruction of simulated phantom

Modelfree objective for global tractography

The global FT algorithm proposed in [2] consider the whole dataset as integrated system, that has the internal and external energy. By minimizing the full energy of the system, the optimal configuration of axonal paths can be found. The external energy is defined by the relation of present system configuration to measured data, the internal energy is defined by interaction of fiber segments (small parts, that form chains). To calculate the system energy some assumptions about local diffusion model must be made. These assumptions can greatly influence the obtained results. It was found, that the energy objective without any assumptions about microparameters of local diffusion in voxel allows significantly improve the obtained results [3].

DW MRI signal can be modelled as convolution of model M with fiber orientation distribution function (FOD) F : $I = M \otimes F$. If we will find the optimal model M by minimizing

the quadratic objective $|I - M \otimes F|^2$ and insert it back, we will get the following expression for model-free external energy (in spherical harmonic expansion coefficients):

$$E_{ext}(F) = \sum_{l=0}^{l_{max}} \frac{\sum_b |\sum_{m=-l}^l F_{m,l} l_{l,m}^b|^2}{\sum_{m=-l}^l |F_{l,m}|^2}$$

here l_{max} denotes the maximal order of expansion, b is the b-factor value.

The method was compared with two alternative algorithms using simulated data and in vivo data with different acquisition schemes. It was found that the proposed method allows to reduce the number of false and broken tracts and to find tracts with more complex configuration. The example of results for phantom are shown in Fig. 1. It can be seen, that were always less invalid bundles in model-free Global Tactography (mfGT) results in comparison with other FT algorithms for all SNR levels. The method was compared with original Global Tracking and streamline algorithm iFOD2.

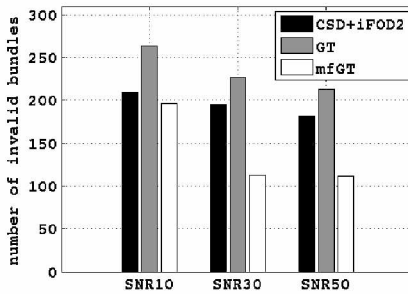


Figure 2. Number of invalid bundles for simulated phantom. Better results were obtained using the proposed method for all SNR levels

FT results filtering

Two parameters are used in this method to verify obtained FT results – the diffusion along selected direction and Shannon Entropy [4, 5]. The probability $p(\mathbf{r})$ can be calculated as follows:

$$p(\mathbf{r}) = \frac{D(\mathbf{r})^{a+2}\Omega}{\sum_j^{N_d} (D(\mathbf{r}_j)^{a+2}\Omega)}$$

where $D(\mathbf{r})$ is the diffusion coefficient in direction \mathbf{r} , a – is some parameter that affects the diffusion probability profile, Ω – is a small solid angle within which probability will be calculated.

Shannon entropy E :

$$E = \sum_j^{N_d} p(\mathbf{r}_j) \log_2 p(\mathbf{r}_j)$$

Using the values of these parameters along all obtained tracts we can filter results and find some false tracts. We use three metrics to filter results – part of segments with low diffusion probability in tract, peaks in change of Shannon entropy along tract and Shannon entropy at end points of tract. The method was evaluated using simulated and in vivo data with different acquisition schemes. It was found, that the diffusion probability characterizes the alignment of

found results to the measured data and Shannon entropy characterizes the diffusion anisotropy in voxel. Proposed filtering method allows to find false tracts and improve connectivity statistic. Fig. 3 shows obtained number of invalid bundles in FT results for phantom before and after filtering. It can be seen, that the number of invalid bundles was reduced after filtering.

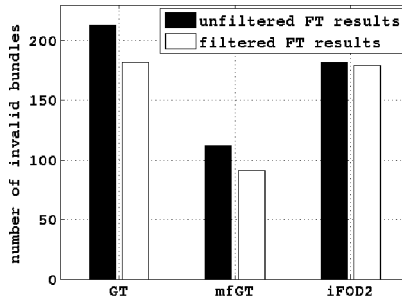


Figure 3. Number of invalid bundles in FT results before and after filtering

Conclusion

There are various ways to optimize FT results. In this work, two different approaches are considered – modification of FT algorithm and method for FT results filtering. Experiments with simulated and in vivo data have shown, that both methods were able to improve the reliability of obtained FT results.

References

1. K. H. Maier-Hein et al., “The challenge of mapping the human connectome based on diffusion tractography,” *Nat. Commun.*, vol. 8, no. 1, p. 1349, Dec. 2017.
2. M. Reisert, I. Mader, C. Anastasopoulos, M. Weigel, S. Schnell, and V. Kiselev, “Global fiber reconstruction becomes practical,” *Neuroimage*, vol. 54, no. 2, pp. 955–962, 2011.
3. L. Konopleva et al., “Model-free global tractography,” *Neuroimage*, vol. 174, pp. 576–586, Mar. 2018.
4. K. A. Il’yasov, L. V. Konopleva, and O. V. Nedopekin, “Validation of MRI-Based Fiber-Tracking Results,” *Appl. Magn. Reson.*, vol. 48, no. 3, pp. 241–254, 2017.
5. L. V. Konopleva, O. V. Nedopekin, and K. A. Il’yasov, “Verification of Diffusion MRI Fiber Tracking Results In Vivo,” *Appl. Magn. Reson.*, Jul. 2018.

Registration of NMR signals in magnetic fields of 0.13 and 2.1 T for estimation of the age-related changes in living tissues

Denis D. Kosenkov^{1,2}, Yuriy I. Neronov^{1,2}, Aleksey N. Zolotov^{1,2}

¹*Mendeleev Institute for metrology, St. Petersburg, Moskovskiy pr. 19, Russia*

²*Saint Petersburg National Research University of Information Technologies, Mechanics and Optics, St. Petersburg, Kronverkskiy pr. 49, Russia*

E-mail: wdenkosw@gmail.com, yineronov@mail.ru, alexzolotov2014@gmail.com

Introduction

Superconducting magnets designed for Magnetic Resonance Tomography are commonly used for the studying of living tissues by NMR spectroscopy. Moreover, as it turned out, such devices (MRI) are more effective for medical practice for imaging tissues of a patient. The reason for the lower efficiency of NMR spectroscopy of living tissues is that the NMR spectrum signals are, as a rule, too wide and overlap each other. This is due to the high intensity of metabolic processes, in which the studied environment is saturated with active metabolites and, as a result, the lifetime of molecular compounds is significantly limited.

In this paper, the goal was set to evaluate the capabilities of an NMR spectrometer with an electromagnet with a field of 2.1 T, in the study of age-related changes. Such a spectrometer is easier to maintain and is not associated with the need to periodically purchase liquid helium. The authors used a Bruker electromagnet with a gap between pole tips of 30 mm.

1. Description of the spectrometer and features of the NMR spectra

The authors manufactured a special NMR signal sensor for the 30 mm gap of electromagnet, which allows placing the palm of a participant in the magnet. In the center of the magnet there was a horizontally located resonant inductance, tuned to a frequency of 90.86 MHz. The inductance contained two ring turns with a gap of 2 mm. The participant of the experiment placed the palm between the poles of the magnet, and at the same time the thickened part corresponding to the center of the middle and distal parts of the two phalanges were in the center of the magnetic system.

Typical spectra obtained with such a spectrometer have the following features. In this case, the skin is thin and does not make a significant contribution to the intensity of the NMR signal. Bone tissue consists of the upper cortical layer, which contains little water and is shown on the NMR tomograms as dark stripes. Conversely, the central part of the bones usually appears on the tomograms in the form of bright areas, because it contains a spongy substance, saturated with bone marrow.

Figure 1 shows two spectra that were obtained during the registration of NMR signals from a student's (left spectrum) and teacher's (right spectrum) bone marrow. The red dots show the experimental data, the blue dots represent the calculated data. The excitation pulse had a duration of 30 μ s; 2048 points were used to digitize the free precession signal. The accumulation of the spectrum was performed in 30 seconds. The spectra display only the set of protons, which belongs to molecules that retain their structure for more than 0.01 s (the time of registration of the NMR signal exceeds 0.01 s). Both spectra contain two signals. It should be noted, that both signals are described quite well by the Lorenz contour (fig. 1) in a wide frequency range ($df > 200$ Hz).

A more intense signal corresponds to the water protons with a chemical shift of $\delta \approx 4.7$ ppm. A smaller signal with a chemical shift of $\delta \approx 2.9$ ppm is typical for lipid compounds in which the content of $-CH_2-$ molecular groups is high. The two spectra have little

differences on the presented scale. However, with careful mathematical processing of the corresponding numeric arrays (if use technique [1-3]), a number of differences can be identified.

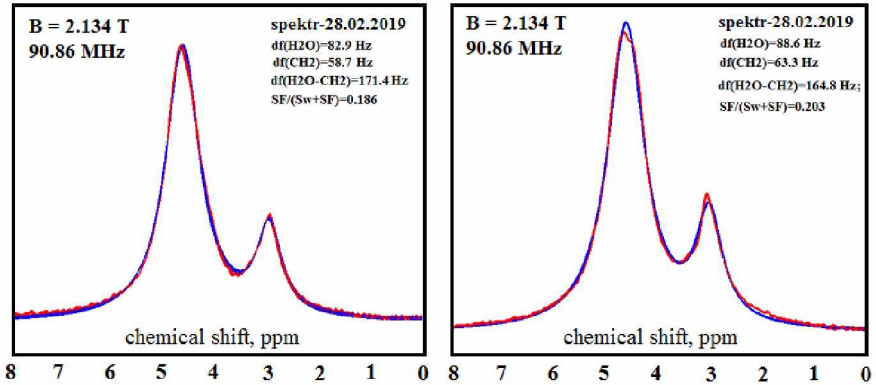


Figure 1. Spectrum for a man of 22 years on the left, spectrum for a man of 76 years on the right

To control the prevalence of fat cells, it is of interest to calculate the ratio of the areas of these two signals. The area of the signal described by the Lorentz contour is proportional to the product of the amplitude of the signal and its width. From the calculations, it follows that both signals (its real and imaginary parts) are described by two Lorentz contours with a standard deviation of 1%. With a similar error, one can estimate the ratio of the protons of the two states.

Table 1. Parameters of NMR signals obtained by processing spectral numerical arrays

Age 22 +/- 3 years			Age 75 +/- 4 years			Sf2 / Sf1
df(H2O)	df(CH2)	Sf/(Sw+Sf)	df(H2O)	df(CH2)	Sf/(Sw+Sf)	
83 Hz	59 Hz	0.186	88 Hz	63 Hz	0.203	1.09

The table uses the notation: df(H2O) - the width of the water signal; df(CH2)- the width of the signal of lipid compounds; Sw - area of the water signal; Sf - the area of the second signal. From the presented data it follows that the concentration of lipid compounds is 9 % higher for older experiment participants.

Then, the same experiment participants recorded a decrease in the NMR amplitudes of the echo signal using a relaxometer in a 0.13 T magnetic field. This device was described previously [4-7]. As before, the decrease in the amplitudes of the signals described by expression:

$$A(t) = A_o [w_a \times e^{\frac{-t}{T2a}} + w_b \times e^{\frac{-t}{T2b}}]$$

Moreover, the same tissue section was used, which was used to obtain spectra in a field of 2.1 T. The data obtained on this device are presented in table 2.

It is of interest to note that for bone marrow tissues a short relaxation time is 29 ms, while for muscle tissue, as a rule, it was 31 ms. This difference goes far beyond the typical error of the device and may indicate a higher saturation of the active metabolites of bone marrow tissues.

Table 2. The results of determining the parameters determining the decrease in the amplitudes of the spin echo signals for bone marrow tissues

Age 22 +/- 3 years			Age 75 +/- 4 years			$\frac{Wb2}{Wb1}$
T2a, ms	T2b, ms	Wb1, %	T2a, ms	T2b, ms	Wb2 %	
29.1(1)	128(1)	39(1)	29.0(3)	128(2)	44(1)	1.13

From the comparison of the data in Table 2, the following can be seen. The weight fraction of connective tissue (having a concentration of active metabolites four times lower: $128/29 \approx 4$) increased by 13 % for older experiment participants. Above, we noted that the increase in lipid concentration in the spectra was equal to 9 %. It can be assumed that the estimate of the increase in this tissue by 13 % is also correct, and the difference is due to the difference in the volume of research of the two devices.

References

1. Y. I. Neronov. «Reliability and accuracy in determining metabolite concentrations in brain tissue by in vivo NMR Spectrometry»; (2001) Measurement Techniques (*«Измерительная техника»*), 2001, Vol. 9, p. 63).
2. Y. I. Neronov, N. N. Seregin. «Precision determination of the difference in shielding by protons in water and hydrogen and an estimate of the absolute shielding by protons in water»; *Metrologia*. (2014), Vol. 51. p. 54-60.
3. Y. I. Neronov. «Determination of the temperature dependence of the shielding of water protons and a method for estimating the temperature of living tissues». *Measurement techniques*. (2017). Vol. 60. № 1. p. 96-102.
4. Y. I. Neronov, A. N. Seregin. «Mini-MRI scanner and some possibilities for its use for studying living tissues»; *Measurement techniques*, T. 54, № 1, 103-107 (2011).
5. A.N. Zolotov, Neronov Yu.I., Kosenkov D.D.; «An estimate of the change in the spin-spin relaxation time of protons of living tissue upon its cooling». In book: «*Magnetic resonance and its applications*». *Spinus - 2018*. Saint Petersburg State University, Department of Nuclear Physics Research Methods. (2018), p. 130-132.
6. D.D. Kosenkov, Neronov Yu.I., Zolotov A.N., Seregin N.N. «NMR relaxometer for the estimation of the spin-spin proton relaxation time of the living tissue». In book: «*Magnetic resonance and its applications*». *Spinus - 2018*. Saint Petersburg State University, Department of Nuclear Physics Research Methods. (2018), p. 77-79.
7. A.N. Zolotov, Neronov Yu.I., Kosenkov D.D.; «Some capabilities of the NMR relaxometer for evaluation of the age-related changes in muscle tissue. ». In book: «*Magnetic resonance and its applications*». *Spinus - 2019*, Saint Petersburg State University, Department of Nuclear Physics Research Methods. (2019), pp. 289-291.

Spatially Resolved NMR with Micrometer Resolution in Static Field Gradients

Benjamin Kresse, Mark Höfler, Alexei F. Privalov, and Michael Vogel

TU Darmstadt, Hochschulstr. 6, 64289 Darmstadt, Germany

E-mail: benjamin.kresse@physik.tu-darmstadt.de

https://www.fkp.tu-darmstadt.de/groups/ag_vogel

Introduction

For a better understanding of the interaction between transport and wetting processes, the knowledge of concentration gradients of mixtures near the contact line is essential. NMR is an established method for the investigation of chemical structures as well as molecular dynamics and spatially resolved measurements can be achieved by applying field gradients, as it is done for clinical applications called magnetic resonance imaging (MRI). However, the spatial resolution of standard MRI scanners has to be strongly increased to resolve potential concentration gradients near contact lines. Our approach is to increase the gradient by using a custom designed static field gradient (SFG) superconducting magnet to record one dimensional images.

Results

A new probe head was constructed which is specially designed for MRI with ultrahigh resolution in one dimension using a SFG magnet. In contrast to clinical MRI scanners with a spatial resolution of typically 0.1 to 1 mm a resolution of about $2\ \mu\text{m}$ is reached due to the high field gradient of 73 T/m, see Fig. 1. Systems with a rotational symmetry can be investigated by scanning the sample slice-wise. The key feature of the probe is a precise computer controlled adjustment of the sample position and orientation e.g. to adjust the sample axis parallel to the gradient of the magnetic field.

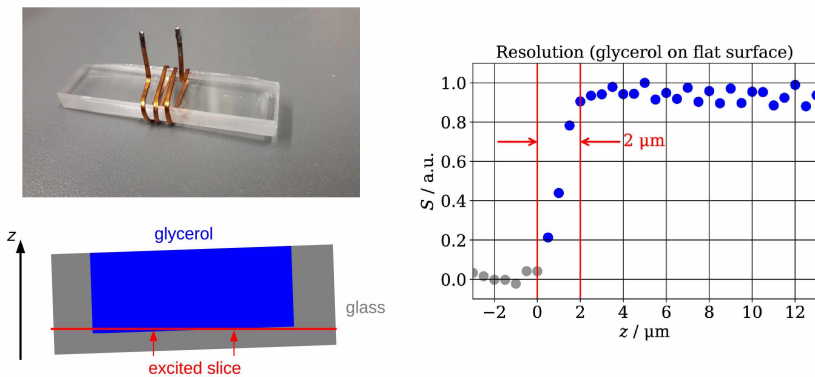


Figure 1. Proof of spatial resolution: Top left: Test sample, glycerol in flat cuvette.

Top bottom: Schematic picture of the setup.

Right: SFG NMR image, spatial resolution approx $2\ \mu\text{m}$

Wetting processes can be investigated. For example, droplets on surfaces can be studied in terms of density by inspecting the signal amplitude and in terms of molecular dynamics by measuring the relaxation time of the nuclear spins. Furthermore, concentration gradients of mixtures can be examined by measurements on different isotopes. It is also possible to

investigate biological objects with flat geometries like skin. In principle non-stationary processes like in microfluidics can be explored with an increased time resolution by a boosted signal-to-noise ratio using stripline designs.

Acknowledgements

We kindly acknowledge the financial support by the German Research Foundation (DFG) within the Collaborative Research Centre 1194 "Interaction between Transport and Wetting Processes", Project A08b.

Evolution of polarization of three spin groups and their contribution to line shape and solid-echo NMR

Tatiana P. Kulagina¹, Grigorii E. Karnaukh¹, Irina Yu. Golubeva^{1,2}

¹*Institute of Problems of Chemical Physics RAS, Semenov prospect 1t, Chernogolovka, Moscow region, 142432, Russia*

²*Moscow State University, Moscow*

E-mail: tan@icp.ac.ru

Introduction

NMR spectrum of an isolated group of spins can be complex and consist of a large number of discrete resonant lines [1, 2]. These spectra contain information about the structure and orientation of the group. In [1, 2] the eigenvalues and eigenvectors of the interaction Hamiltonian were obtained, but the analytical expression for the free induction decay (FID) and solid-echo (SE) are not given. This paper presents a method for calculating the FID, the line shape and SE in the three-spin system with arbitrary constants dipole-dipole interaction (DDI). The method involve the symmetry of rotation of all spins about the axis of the initial cross-polarization and allows significantly simplify the calculations. Influence of other spins of system was taken into account on the basis of a unified theory of NMR spin dynamics [3], which allows to simulate the FID and the line shape of a solid.

The theory of free induction decay in the group of three-spin

To calculate the FID was used the symmetry generated by the operation of all the spins rotate around the axis x. Taking into account this symmetry, the problem was reduced to the replacement of calculation on an eight-dimensional state space R to two calculations on four-dimensional state subspaces: $R = R_1 \oplus R_2$. Next, as in [1], all the eigenvalues and eigenvectors of the Hamiltonian's interaction have been found.

Hamiltonian of the interaction for three-spin group, consisting of nuclei with spins $1/2$, that connected by various constants of DDI b_{ij} ($i, j = 1, 2, 3$) has form:

$$\hat{H}_d^z = b_{12} \left(2\hat{S}_1^z \hat{S}_2^z - \hat{S}_1^x \hat{S}_2^x - \hat{S}_1^y \hat{S}_2^y \right) + b_{31} \left(2\hat{S}_3^z \hat{S}_1^z - \hat{S}_3^x \hat{S}_1^x - \hat{S}_3^y \hat{S}_1^y \right) + b_{23} \left(2\hat{S}_2^z \hat{S}_3^z - \hat{S}_2^x \hat{S}_3^x - \hat{S}_2^y \hat{S}_3^y \right), \quad (1)$$

where

$$b_{ij} = \frac{\gamma^2 \hbar^2 (3 \cos^2 \theta_{ij} - 1)}{2r_{ij}^3}, \quad (i, j = 1, 2, 3), \quad (2)$$

θ_{ij} – the angle between the vector \vec{r}_{ij} connecting the i -th and j -th spins and the direction of the magnetic field, r_{ij} – the length of the vector, S_i^k – the projection operators of moments of i -th nuclear spin on the axis x, y, z. The initial polarization is $\hat{S}^x = \hat{S}_1^x + \hat{S}_2^x + \hat{S}_3^x$. For simplification of further calculations were entered, the parameters depending on constants DDI:

$$\sigma_1 = b_{12} + b_{23} + b_{31}, \quad \sigma_2 = b_{12} b_{23} + b_{23} b_{31} + b_{31} b_{12}. \quad (3)$$

Hence, taking into account the eigenvalues of the Hamiltonian \hat{H}_d^z (3.4), we obtain the frequency of the transitions and the signal FID [4]:

$$\begin{aligned}
 G_3(t) &= \frac{\text{Tr} \left(\exp \left[-i\hat{H}_d^z t \right] \hat{S}^x \exp \left[i\hat{H}_d^z t \right] \hat{S}^x \right)}{\text{Tr} \left(\hat{S}^x \right)^2} = \\
 &= \frac{1}{8} \left(1 + 3 \cos^2 \beta \right) + \frac{3}{8} \sin^2 \beta \cos \left(\frac{1}{2} \sqrt{9\sigma_1^2 - 24\sigma_2} \right) t + \\
 &+ \frac{1}{2} \sin^2 \frac{\beta}{2} \cos \frac{1}{4} \left(3\sigma_1 - \sqrt{9\sigma_1^2 - 24\sigma_2} \right) t + \frac{1}{2} \cos^2 \frac{\beta}{2} \cos \frac{1}{4} \left(3\sigma_1 + \sqrt{9\sigma_1^2 - 24\sigma_2} \right) t
 \end{aligned} \tag{4}$$

where $\cos \beta = \frac{\sigma_1}{\sqrt{9\sigma_1^2 - 24\sigma_2}}$.

The resulting formula (4) for FID of the three-spin group allows us to analyze in detail the values of symmetric functions σ_1 and σ_2 , determine the orientation of the group to the direction of the magnetic field. Account of influence of other spins of the system on the shape of the NMR line conducted by a general kinetic equation for the partial densities of magnetic dipoles [3].

Proposed above theory can describe FID and the line shape in a solid which contains dedicated three-spin groups. Expression of FID for the whole spin system is as follows:

$$G(t) = G_3(t)G_r(t) \tag{5}$$

where $G_r(t)$ – signal of FID, that is associated with relaxation and diffusion processes of spin system and calculated from the general kinetic equation [3].

The line shape $F(\omega)$ is calculated by means of Fourier's transformation (5). In Fig. 1 represented $F(\omega)$ with the next parametres: $\sigma_1 = 0, \sigma_2 = -7 \cdot 10^9 \text{ s}^{-2}, \cos \beta = 0$.

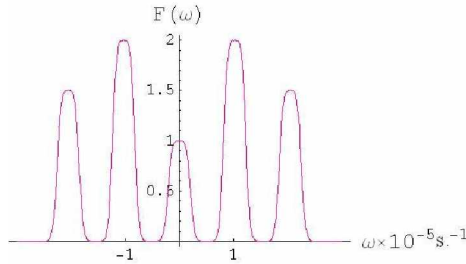


Figure 1. The line shape with weak influence of environment [4]

Solid-echo in three spin system

The space of all spin conditions of R breaks (is given) into two subspaces of states, even and odd, π impulse is relative. Also when calculating a signal the symmetry connected with spin exchange was used. The space of all spin conditions of R breaks into two subspaces of symmetric and anti-symmetric conditions of rather spin exchange [5].

$$R_s = \hat{P}_s R \text{ и } R_a = \hat{P}_a R, \text{ где } \hat{P}_s = \frac{1}{2}(\hat{E} + \hat{E}x), \hat{P}_a = \frac{1}{2}(\hat{E} - \hat{E}x).$$

Then the space of all spin conditions of R can be broken into four subspaces:

$$R = R_{ea} \oplus R_{oa} \oplus R_{es} \oplus R_{os}$$

$$R_{ea} = \hat{P}_e \hat{P}_a R, R_{oa} = \hat{P}_o \hat{P}_a R, R_{es} = \hat{P}_e \hat{P}_s R, R_{os} = \hat{P}_o \hat{P}_s R$$

It allows reduce calculation of a signal of SE in a three-spin system from a matrix of the 8-th order to calculation of a signal on two matrixes of the 1-st order and two matrixes of the 3-rd order.

The formula of a signal has a view:

$$A(t, \tau) = \frac{\text{Tr} \hat{S}^x(t) \hat{S}^x}{\text{Tr} (\hat{S}^x)^2} = \frac{\text{Tr} \hat{S}^x(t) \hat{S}^x}{\text{Tr} \sum_i^n (\hat{S}_i^x)^2} = \frac{\text{Tr} \hat{S}^x(t) \hat{S}^x}{n2^{n-2}} = \frac{\text{Tr} \hat{S}^x(t) \hat{S}^x}{6},$$

where $\hat{S}^x(t) = \hat{U}^{-1} \hat{S}^x \hat{U}$, $\hat{U} = e^{it\hat{H}_d^z} e^{i\frac{\pi}{2} \hat{S}^x} e^{i\tau \hat{H}_d^z}$.

Analytical expression for SE in three-spin systems is obtained [5].

In Fig. 2 the signal of solid echo after Fourier transformation with various constants DDI is given: $\tau = 10^{-5}$ s, $\sigma_1 = 0$, $\sigma_2 = -7 \cdot 10^9$ s⁻², $\cos \beta = 0$.

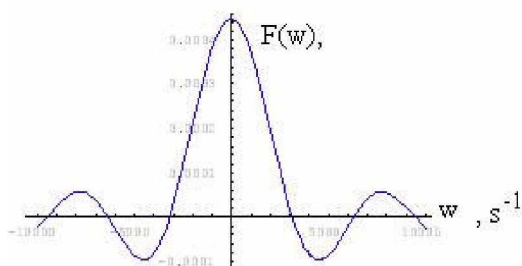


Figure 2. Solid-echo signal, calculated by formulas [5]

A theory of the line shape in a solid with dedicated three-spin groups is proposed and modeling of signals showed the influence of G3 (t) at FID signal, that allows to evaluate the constant dipole-dipole interactions, the comparison with the experiments and to extract information about the position (orientation) of three-spin groups in the substance.

Acknowledgements

This work was performed in accordance with the state task, state registration No. 0089-2014-0021.

References

1. E.R. Andrew, R. Bersohn. *J. Chem. Phys.*, **18**, 159-161 (1950).
2. Yu. N. Moskvich, N. A. Sergeev, G.I. Dotsenko. *Phys. Stat. Solid (a)*, 409-418 (1975).
3. B. N. Provotorov, T. P. Kulagina, G. E. Karnaukh. *J. Exp. Theor. Phys.*. **86**. 527-533 (1998).
4. T. P. Kulagina, G. E. Karnaukh, S. A. Andrianov. *Butlerov messages*, **35**, 1-9 (2013)
5. Yu. Golubeva, G. E. Karnaukh, T. P. Kulagina. *Structure and dynamics of molecular systems*, 161-165 (2018).

¹⁴N NQR relaxation in 5 aminotetrazole

Galina S. Kupriyanova¹, George Mozzhukhin², Sultonazar Mamadazizov²

¹*Institute of physics and mathematics, Immanuel Kant Baltic Federal University,*

²*Gebze Technical University, 41400 Gebze/Kocaeli, Turkey*

E-mail: galkupr@yandex.ru

Introduction

Interest in highly nitrogenous compounds, such as tetrazole derivatives (TZ), is caused by a wide range of their functional properties. TZ derivatives have applications in medicine, biochemistry, information recording system, in blended explosives, as well as isosteric substitutes for various functional groups in drugs that are resistant to biological degradation. An important advantage of tetrazoles is that they have a high thermal stability. Despite the growth of research of study of the structure, functional properties and applications, the dynamic and functional properties need additional studies. ¹⁴N Nuclear Quadrupole Resonance (¹⁴N NQR) is one of the most efficient techniques for the studies of the structure and dynamics of the quadrupole nuclei [1]. This approach is defined by dependence of NQR frequency from electric field gradient tensor around quadrupole nuclei. The advantage of ¹⁴N NQR method in TZ families is based on high concentration of ¹⁴N nuclei in studied molecule. That allows the detailed studies of the structural and dynamic processes of ring nitrogen and nitrogen in NH₂ groups [2].

In this paper, the ¹⁴N NQR spin-spin and the spin-lattice relaxation in 5 aminotetrazole monohydrate (ATZH) were studied using inverse Laplace transform in order to obtain more detailed information on the dynamics of nuclei.

Results and Discussion

¹⁴N NQR frequencies and the T₁, T₂ relaxation times in 5-aminotetrazole monohydrate (5ATZH) were measured by ¹⁴N NQR method with the use of the pulse NMR-NQR spectrometer Tecmag Apollo with use of TNMR software (Tecmag inc.). The Carr-Purcell-Meiboom-Gill (CPMG) sequence was used for T₂ measurements and inversion-recovery, saturation-recovery and Csaki-Bene sequences were also used for T₁ measurements [3]. The distribution of the spin-lattice relaxation times for all ¹⁴N nuclei at frequencies 3.7, 3.61, 3.14, 2.81 and 2.74 MHz was obtained by using the inverse Laplace transform.

The figure 1 shows that there are two regions for values of spin lattice relaxation times. We used two models for explanation of the experimental results. First of them is Bayer theory [4] that predicts two components relaxation for ring nitrogen nuclei if ¹⁴N (I=1). Additionally we takes into account that ring nitrogen nuclei have participation in hydrogen bonds. The estimation of the probabilities of the transitions in three levels system was carried out with use of the following equation [1]

$$\frac{W_1}{W_2} = 2\omega_p^2 \frac{\Delta\omega I_z}{(\omega_q - \omega_r)^2 kT},$$

where $\omega_{p,q,r}$ are NQR frequencies of ¹⁴N, I_z is moment of inertia corresponding Z axes of electric field gradient, T is a temperature.

The inertia moments were calculated with use the data from work [5]. The relaxation processes of ¹⁴N nuclei in NH₂ group differ from the relaxation of ring nuclei. This property is defined by the positions of ATZH molecules in unit cell [6]. The calculations show that nitrogen nuclei in NH₂ group in neighboring molecules in unit cell have the same resonance frequencies but their axes of electric field gradients are inverted [5]. The exchange interactions in this structure produce additional relaxation mechanism that also was taken into account in our

studies. The proposed models are based on Bayer's theory and later were developed by Osokin [1]. These models also take in attention the hydrogen bonds and exchange processes. Thus we mainly explain the relaxation behavior in ATZH without use of polymorphous form approach.

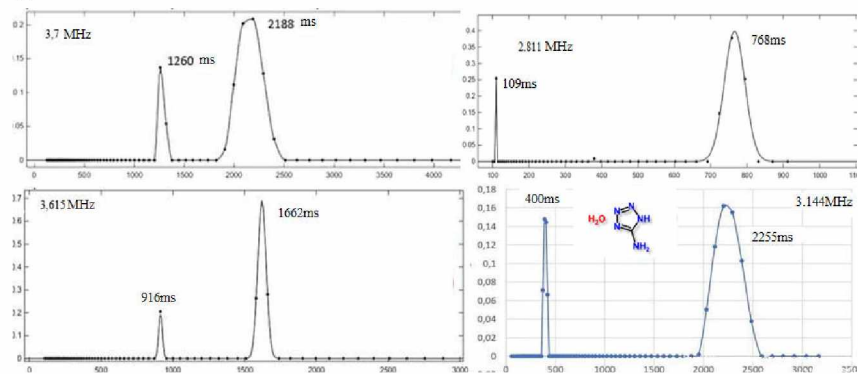


Figure 1. The plot for ^{14}N NQR spin relaxation times for aminotetrazole monohydrates

References

1. A.Safin, D.Ya. Osokin. Nuclear quadrupole resonance in nitrogen compounds. Moscow. 1977
2. J. Pirnat *et al.*, " ^{14}N NQR in the tetrazole family," *Chem. Phys.*, vol. 364, no. 1–3, pp. 98–104, 2009
3. S. Mamadazizov, A. Neniukhina, G.Kupriyanova. Multiexponential distribution of ^{14}N NQR relaxation times in tetrazole derivatives. Magnetic Resonance and its applications. Spinus. Saint- Petersburg, Russia. 1- 6 April 2018, p.88-89
4. H.Bayer, *Z. fur Phys.* 130, 227 (1951)
5. S.Mamadazizov, M.G.Shelyapina, G.S.Kupriyanova, G.V.Mozzhukhin. New assignment of ^{14}N NQR spectral lines for tetrazoles derivatives. *Chemical Physics*, (2018), 508, 27 pp. 52-60
6. Weihua Zhu • Heming Xiao. First-principles study of electronic structure, absorption spectra, and thermodynamic properties of crystalline ^1H -tetrazole and its substituted derivatives. *Struct. Chem* (2010) 21:847–854

NMRD study of the Bound water rotational correlation time in protein solutions

*Mamuel Arsenio Lores Guevara¹, Carlos Alberto Cabal Mirabal², Robert Muller³,
Sophie Laurent³, Yulianela Mengana Torres¹, Juan Carlos Garcia Naranjo¹*

¹*Centro de Biofísica Médica. Universidad de Oriente. Patricio Lumumba S/N. CP: 90500. Santiago de Cuba, Cuba.*

²*Facultad de Física, Universidad de la Habana, Cuba.*

³*Laboratoire de RMN et d'Imagerie Moléculaire. Département de Chimie Générale, Organique et Biomédicale. Faculté de Médecine et de Pharmacie. Université de Mons. Belgium.*

Key words: Dynamic viscosity, Correlation time, hemoglobin, Sickle Cell Disease.

Summary

The rotational correlation time (τ_R) of the water bound to the hemoglobin is determined in samples of hemoglobin A (HbA), and in samples of Hemoglobin S (HbS) before and after polymerization. Samples of whole blood from healthy patients were obtained from voluntary donors. Samples of whole blood from Sickle Cell Disease patients were obtained from residual samples at the ULB Brussels University Hospital after routine blood tests were finished. Hemoglobin samples were obtained starting from whole blood using classical methods. To evaluate the rotational correlation time the Cole-Cole model was applied to a Nuclear Magnetic Relaxation Dispersion (NMRD) profile obtained using a Fast Field Cycling Nuclear Magnetic Resonance relaxometer (STELAR FFC 2000 Spinmaster) in the frequency range between 20 KHz and 10 MHz. Additionally, spin lattice (T_1) and spin spin (T_2) relaxation times were measured at 20 MHz and 60 MHz using the Minispec units from Bruker: Mq 20 and Mq 60. The values of τ_R in HbA remain in the range from $(4.99 \pm 0.32) 10^{-8}$ s to $(7.91 \pm 0.47) 10^{-8}$ s and in the case of HbS this parameter vary from $(5.05 \pm 0.44) 10^{-8}$ s to $(6.21 \pm 0.33) 10^{-8}$ s. Both ranges are equivalent, which is coherent with the similarities between both proteins in diameter, protein concentration and dynamic viscosity according to the Debye model. The values of τ_R observed here match with the values of the protein rotational correlation time determined previously by our group using EPR, which agree with the tightly bound state of the associated water determining relaxation. Similar studies were done in Human serum albumin, which contributes to explain previous considerations already made during the development of a NMR method to evaluate dynamic viscosity in blood plasma.

Multinuclear NMR study of hybrid organic-inorganic composites: layer perovskite-like oxides $\text{H}_2\text{La}_2\text{Ti}_3\text{O}_{10}$ with methanol, methylamine and butylamine molecules

Irina Lushpinskaya, Marina Shelyapina, Sergei Kurnosenko, Oleg Silyukov, Irina Zvereva

Saint Petersburg State University, Department of Nuclear-Physics Research Methods

E-mail: irinapavlovna94@mail.ru

Hybrid organic–inorganic composites based on layered inorganic crystals are nowadays a rapidly developing area of functional materials applied in pharmaceuticals, catalysis, and optoelectronics. Ion-exchangeable layered perovskites exhibit remarkable electronic and photocatalytic properties. The protonated forms of Dion–Jacobson phases, to which $\text{H}_2\text{La}_2\text{Ti}_3\text{O}_{10}$ belongs, reveal ability to intercalate various organic molecules.

In this contribution we report on the result of the study of $\text{H}_2\text{La}_2\text{Ti}_3\text{O}_{10}$ layered perovskite like oxide with organic molecules: methanol, methylamine and butylamine. The research is mainly focused on the study of the spatial structure and mobility of organic molecules carried out by ^1H , ^{13}C and ^{14}N nuclear magnetic resonance under magic angle spinning (MAS NMR). The ^{13}C and ^{14}N NMR spectra of have been recorded in the cross-polarization mode. Basing on our previous ^1H NMR study of $\text{H}_2\text{La}_2\text{Ti}_3\text{O}_{10}$ with intercalated water molecules [1], it has been found that CH_3OH molecules are grafted onto the oxide layers, whereas the studied amines can be considered as intercalated: after being entered into the interlayer space they form $[-\text{NH}_3]^+$ cations by capturing the cage protons. For the sample with butylamine, the ^{13}C MAS NMR spectra have been recorded as a function of the contact pulse duration. That allowed us to estimate the characteristic relaxation times of different fragments of the organic molecules.

The research has been done at the Research Park of Saint Petersburg State University: Centre of Thermal Analysis and Calorimetry and Centre for Magnetic Resonance. The NMR spectra of ^1H , ^{13}C and ^{15}N have done by using primarily Bruker Avance III 400WB instrument (operating with Topspin version 3.2) using a double resonance 4 mm MAS probe. ^1H NMR experiments were done within 14 kHz MAS rotating rate. ^{13}C and ^{15}N cp-MAS experiments were done within 0–14 kHz rotating rate. The contact time was changed from 10 μs to 10000 μs . The work was supported by the Russian Foundation for Basic Research (Grant 18-03-00915).

Acknowledgements

The studies were carried out at the research park of Saint Petersburg state university, Center for Magnetic Resonance.

References

1. M.G. Shelyapina, D.Y. Nefedov, A.V. Kostromin, O.I. Silyukov, I.A. Zvereva. *Ceram. Int* 45 (2019) 5788–5795.

Evaluation of protein viscosity in Sickle Cell Disease

*Yulianela Mengana Torres¹, Manuel Arsenio Lores Guevara¹, Juan C. García Naranjo¹,
Beatriz T. Ricardo Ferro¹, Edalis Guerrero Piña², Carlos Alberto Cabal Mirabal³,
Lidia C. Suárez Beyrío⁴, María A. Marichal Felue⁴, Teresa Simón Brada⁴,
Inocente C. Rodríguez Reyes⁴, Jan Philippé⁵*

¹*Centro de Biofísica Médica, Universidad de Oriente, Patricio Lumumba S/N. CP: 90500. Santiago de Cuba. Cuba.*

²*Departamento Física, Facultad de Ciencias Naturales y Exactas, Universidad de Oriente, Patricio Lumumba S/N. CP: 90500. Santiago de Cuba. Cuba.*

³*Facultad de Física, Universidad de la Habana, Cuba.*

⁴*Hospital General "Dr. Juan Bruno Zayas Alfonso", Carretera del Caney S/N. Santiago de Cuba. Cuba.*

⁵*Department of Clinical Chemistry, Immunology and Microbiology, Ghent University, Ghent, Belgium.*

Key words: Dynamic viscosity, hemoglobin, plasma, Sickle Cell Disease.

Summary

The viscosity of proteins is a very important parameter used to evaluate the viscosity of whole blood, which strongly influence the hemodynamics of the human blood circulation. The classical viscometers (Capillary, Falling Body and rotational viscometers) are not adequate to do clinical measurement of dynamic viscosity because its require big amount of samples, are affected by turbidity and are dependent of the skill of the operator. A new magnetic resonance based method to evaluate dynamic viscosity of proteins is presented, which is based in the straight forward relation between dynamic viscosity and the proton relaxation rate in the solutions. A good agreement is obtained between the results obtained with the NMR based method and the gold standard used (Ostwald viscometer) for intracellular hemoglobin and Plasma. Was possible to evaluate the increasing of the dynamic viscosity in protein solutions (Plasma and hemoglobin) belong to the whole blood from sickle cell patients.

Interaction of statins with cell membrane by NMR spectroscopy

G. S. Musabirova, A. V. Aganov, I. A. Latfullin, V. V. Klochkov

Kazan (Volga region) Federal University, Kazan, Russia

E-mail: Guzel.musabirova@bk.ru

Statins are drug which reduce the amount of low-density lipoprotein (LDL) cholesterol by inhibiting hydroxyl-methyl-glutaryl-coenzyme A (HMG-CoA) reductase. Cholesterol is known as a well-established risk factor for atherosclerosis. Furthermore statins have an additional pharmacological properties which are called pleiotropic. Despite the fact that statins have a similar molecular structure their pleiotropic properties vary considerably. There is a hypothesis that this difference depend on location of statins in the cell membrane [1, 2], but to the present day there is a lack of information in literature on interactions of statins with the surface of the cellular membrane.

Micelle of dodecylphosphocholine (DPC) were used as a model cellular membranes system for investigating the interactions of atorvastatin, cerivastatin, fluvastatin, simvastatin and pravastatin. Investigation were carried out by NMR spectroscopy with Nuclear Overhauser Effect (NOESY and ROESY experiments). This method apply research intercellular interaction and obtain information about structure of molecular complex and also about parts of molecules which form binds.

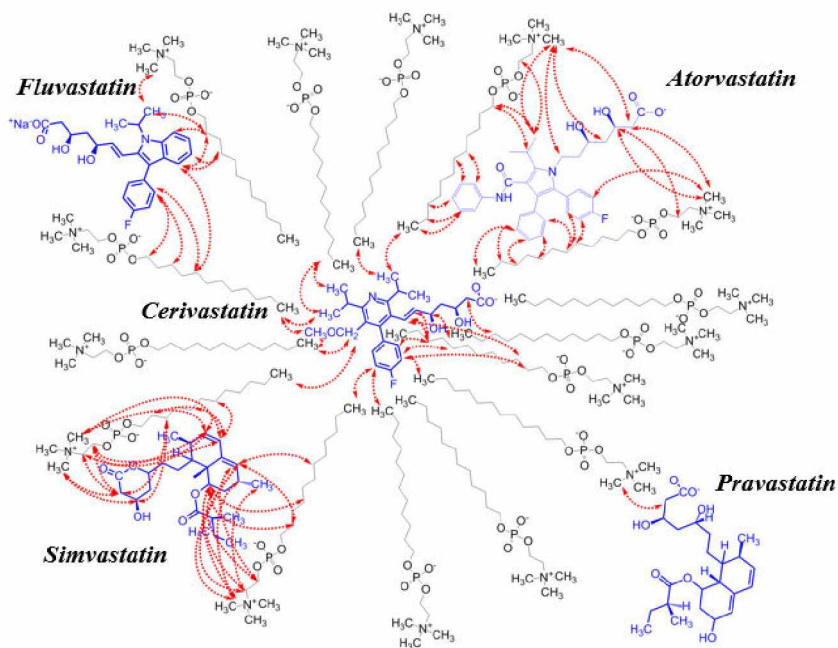


Figure 1. Schematic presentation of the NOEs (dashed arrows) observed in NMR spectra of different statins in D₂O + DPC micelles

The results of NMR experiments allowed determining average locations of different statins in model membranes. It was shown that in model systems cerivastatin has the deepest location in the membrane, pravastatin weakly or just partially interacts with membrane surface and other statins share intermediate locations in model membranes (fig. 1). Even minor differences in the structure of statins lead to different interactions with the model membrane, and these differences may explain the pharmacological properties of statins.

This work was funded by the subsidy of the Russian Government to support the Program of Competitive Growth of Kazan Federal University among World's Leading Academic Centers.

References

1. Galiullina, Leisan Interaction of different statins with model membranes by NMR data [text] /Leisan Galiullina, Oksana Aganova, Ildus Latfullin, Guzel Musabirova, Albert Aganov, Vladimir Klochkov//BBA - Biomembranes.- 2017.- V.1859, N 3.- P. 295-300. IF = 3.8.
2. Galiullina L.F., Spatial structure of atorvastatin and its complex with model membrane in solution studied by NMR and theoretical calculations [text] / L.F. Galiullina, G.S. Musabirova, I.A. Latfullin, A.V. Aganov, V.V. Klochkov //Journal of Molecular Structure. - 2018. - Vol.1167, Issue 4. - P. 69-77. IF = 2.01.

^1H NMR relaxation times of alcohol-water mixtures

C. Okay¹, A. Maraşlı², G. Mozhukhin², B. Rameev^{2,3}

¹*Department of Physics, Marmara University, 81040 Göztepe-Istanbul, Turkey*

²*Department of Physics, Gebze Technical University, 41400, Gebze-Kocaeli, Turkey*

³*Zavoitsky Physical-Technical Institute, FRC Kazan Scientific Center of RAS, 420029 Kazan/Tatarstan, Russian Federation*

E-mail: rameev@gyte.edu.tr or cokay@marmara.edu.tr

Introduction

Physical, chemical and biological properties of alcohol-water mixtures is the topic, which has been extensively studied for centuries. Methanol, ethanol, 1-propanol and 2-propanol are the most frequently used linear (alkyl) alcohols soluble in water in the whole concentration range. It is well known that aqueous solutions of short alcohols reveal heterogeneity due to formation of discreet water-water, alcohol-alcohol or alcohol-water clusters [1-6]. It has been established by a range of various techniques, including X-ray [1-3,7-9], neutron scattering [10], nuclear magnetic resonance (NMR) [11-14].

Taking into account that water-alcohols (especially ethanol-water) mixtures are very frequently met in typical security checkpoint situation, a very recent TD NMR study of short alcohol-water mixtures [15] looks especially interested. It is known that detection and discrimination of various liquid substances is very important problem both with respect security [16-20] and industrial applications [21]. TD-NMR is considered as one of very attractive techniques for detection of broad range of dangerous liquids because of its high selectivity as well as relatively low price and maintenance expenses. Thus, development of methods of effective screening of various liquids by their TD NMR parameters is very important issue.

In this study, spin-spin relaxation time (T_2) and spin lattice-relaxation time (T_1) in ^1H NMR of the methanol, ethanol and 1-(2-) propanol mixtures have been measured in a whole range of alcohol concentrations. Approaches for the quantitative characterization or discrimination of unknown liquid by NMR, including advanced processing algorithms (e.g. Inverse Laplace Transform and others) are discussed with respect of their possible implementation in TD NMR scanning protocols.

Experimental procedures

Two various ^1H low frequency NMR measurement devices have been used. The first one is Bruker Minispec mq series 20MHz TD NMR device, while the second one is Magritek Spinsolve 42MHz high-resolution (but low magnetic field) NMR. Prior to each measurement, all samples were kept for at least 10 min in the NMR device to attain the desired temperature. Carr-Purcell-Meiboom-Gill (CPMG) pulse sequence was applied to obtain T_2 relaxation times, while inversion/saturation recovery protocol was used to measure T_1 relaxation time. The Fourier transform spectra, received by Magritek Spinsolve, were integrated in whole (or predefined) spectrum region to plot the signal intensity as a function of time to obtain T_1 or T_2 parameters. It should be noted that various echo-times were tested to check the effect of self-diffusion. For minimization diffusion term, the echo-time were fixed to be 0.5ms.

Experimental results and their discussion

The results obtained by both devices (Bruker Minispec TD NMR and Magritek Spinsolve NMR) are very close to each other (maximal differences, observed at high alcohol concentrations, do not exceed 3%). Both T_1 and T_2 results are very close to literature data [11-15]. Spin-spin relaxation times (T_2), obtained in standard CPMG measurements with use of Bruker Minispec device, are given in Fig. 1.

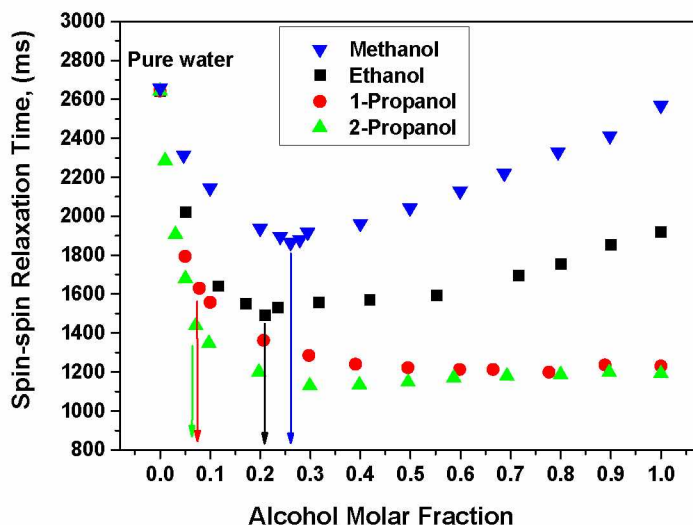


Figure 1. Spin-spin relaxation times for various alcohol-water solutions at 25°C obtained in measurements with use of Bruker Minispec mq20. Arrows are given as references to mark special volume concentrations: %46 (0.21 Molar) for ethanol, %42 (0.26 Molar) methanol, %24 (0.07 Molar) for 1-propanol and %24 (0.07 Molar) for 2-propanol

Taking into account that for unknown liquid, use of only T_1 and T_2 times does not provide non-ambiguous discrimination between various liquids, Inverse Laplace transform (ILT) was applied to obtain additional information on the tested materials. In contrast to the work [15], the results of Inverse Laplace transform (ILT) reveals bimodal distribution of relaxation times in alcohol-water mixtures. We also compared our results with those that obtained by dielectric spectroscopy. An important advantage of the later technique, which provides the complex dielectric constant in the broad range of microwave frequencies, is a possibility to use it in the combination with TD NMR.

Acknowledgements

The work was supported by NATO Science for Peace and Security Programme (NATO SPS grant No. 985005 [G5005]). Authors also acknowledge a partial support by East Marmara Development Agency (MARKA, project No. TR42/16/ÜRETİM/0013) and by Research Fund of Gebze Technical University (grants No. BAP 2017-A-105-44).

References

1. H. Hayashi, K. Nishikawa, T. Iijima, J. Phys. Chem. 94, 8334–8338, (1990).
2. K. Nishikawa, T. Iijima, Small-angle X-ray scattering study of fluctuations in ethanol and water mixtures, J. Phys. Chem. 97 (1993) 10824–10828, doi: 10.1021/j100143a049.
3. H. Tanaka, K. Nakanishi, H. Touhara, J. Chem. Phys. 82, 5184, (1985)
4. L.-J. Zhao, H.-S. Xiao, Aqueous solutions of lower alcohols investigated by pyrene fluorescence spectroscopy, Spectrochim. Acta A Mol. Biomol. Spectrosc. 88 (2012) 111–115, doi: 10.1016/j.saa.2011.12.009.
5. T. Takamuku, K. Saisho, S. Nozawa, T. Yamaguchi, J.Mol. Liq. 119,133–146, (2005).

6. N. Nishi, S. Takahashi, M. Matsumoto, A. Tanaka, K. Muraya, T. Takamuku, T. Yamaguchi, *J. Phys. Chem.* 99 462–468, (1995).
7. I. Akiyama, M. Ogawa, K. Takase, T. Takamuku, T. Yamaguchi, N. Ohtori, Liquid structure of 1-propanol by molecular dynamics simulations and X-ray scattering, *J. Solut. Chem.* 33 (2004) 797–809, doi: 10.1023/B:JOSL.0000043642.62263.69.
8. T. Takamuku, H. Maruyama, K. Watanabe, T. Yamaguchi, Structure of 1-propanol water mixtures investigated by large-angle X-ray scattering technique, *J. Solut. Chem.* 33 (2004) 641–660, doi: 10.1023/B:JOSL.0000043631.21673.8b.
9. H. Hayashi, Y. Udagawa, Mixing state of 1-propanol aqueous solutions studied by small-angle X-ray scattering: a new parameter reflecting the shape of SAXS curve, *Bull. Chem. Soc. Jpn.* 65 (1992) 155–159, doi: 10.1246/bcsj.65.155
10. A. Sahoo, S. Sarkar, V. Bhagat, R.N. Joarder, The probable molecular association in liquid D-1-propanol through neutron diffraction, *J. Phys. Chem. A* 113 (2009) 5160–5162, doi: 10.1021/jp8107717
11. K. Yoshida, A. Kitajo, T. Yamaguchi, *Mol. Liq.* 125, 158–163, (2006)
12. J. McGregor, R. Li, J.A. Zeitler, C. D'Agostino, J.H.P. Collins, M.D. Mantle, H. Manyar, J.D. Holbrey, M. Falkowska, T.G.A. Youngs, C. Hardacre, E.H. Stitt, L.F. Gladden, Structure and dynamics of aqueous 2-propanol: a THz-TDS, NMR and neutron diffraction study, *Phys. Chem. Chem. Phys.* 17 (2015) 30481–30491, doi: 10.1039/C5CP01132A.
13. K. Mizuno, Y. Miyashita, Y. Shindo, H. Ogawa, *J. Phys. Chem.* 99, 3225–3228, (1995).
14. M. Matsugami, R. Yamamoto, T. Kumai, M. Tanaka, T. Umecky, T. Takamuku, Hydrogen bonding in ethanol–water and trifluoroethanol–water mixtures studied by NMR and molecular dynamics simulation, *J. Mol. Liq.* 217 (2016) 3–11.
15. M.Z. Jora, M.V.C. Cardoso, E. Sabadini, Correlation between viscosity, diffusion coefficient and spin-spin relaxation rate in ¹H NMR of water-alcohols solutions, *J. Mol. Liq.* 238 (2017) 341–346; doi: 10.1016/j.molliq.2017.05.006
16. L. J. Burnett, *Liquid explosives detection*, SPIE Vol. 2092 Substance Detection Systems (1993) 208–216.
17. J. Fraissard, O. Lapina, eds.: *Explosives Detection using Magnetic and Nuclear Resonance Techniques*, NATO Science for Peace and Security Series B: Physics and Biophysics. Dordrecht, Netherlands: Springer, 2009.
18. B.Z. Rameev, G.V. Mozzhukhin, B. Aktas, eds.: *Magnetic Resonance Detection of Explosives and Illicit Materials*, *Appl. Magn. Reson.* 43, no. 4, 463–467 (2012).
19. T. Apih, B. Rameev, G. Mozzhukhin, J. Barras, eds.: *Explosives Detection using Magnetic and Nuclear Resonance Techniques*, NATO Science for Peace and Security Series B: Physics and Biophysics, Dordrecht, Netherlands: Springer, 2014.
20. S. Kumar, W.C. McMichael, Y.-W. Kim, A.G. Sheldon, E. E. Magnuson, L. Ficke, T. K. Chhoa, C. R. Moeller, G. A. Barrall, L. J. Burnett, P.V. Czipott, J. S. Pence, D. C. Skvoretz, Screening sealed bottles for liquid explosives, *Proceedings of SPIE Vol. 2934 (1997)* 126–137.
21. J. Mauler, E. Danieli, F. Casanova, B. Blimich, In: *Explosives Detection using Magnetic and Nuclear Resonance Techniques*. NATO Science for Peace and Security Series B: Physics and Biophysics. J. Fraissard; O. Lapina, (Eds.). Pp. 193–203 (2009).

Application of paramagnetic NMR to the magnetic properties investigation of cobalt(II) pseudotetrahedral single-molecule magnet

Yanina A. Pankratova^{1,2}, Alexander A. Pavlov²

¹Department of Chemistry, Moscow State University, Leninskie Gory, 119991 Moscow, Russia

²Nesmeyanov Institute of Organoelement Compounds, Russian Academy of Sciences, Vavilova str. 28, 119991 Moscow, Russia

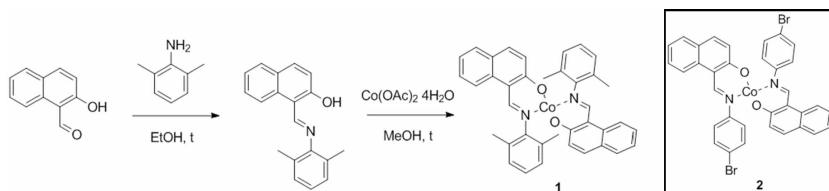
E-mail: yaninaalex916@gmail.com

Introduction

Single-molecule magnets (SMM) are compounds, usually organometallic and coordination complexes, that exhibit properties of a permanent magnet at a single-molecule level. It implies that the magnetization of every single molecule, acquired in an external magnetic field, is conserved for a limited period of time after the field is turned off [1]. There are few methods that can be used in order to determine the magnetic properties experimentally, for instance, ac-magnetometry and THz-EPR spectroscopy. However, these methods are relatively expensive and rare; as a result, a more accessible approach is needed. Here we apply an original NMR-based technique for investigation of cobalt (II) SMM.

Object of research

Here we report a pseudotetrahedral Co(II)-based single-molecule magnet **1**, which is analogous to previously reported complex **2** [2]. The synthesis was conducted through two steps, shown in Scheme 1 [3].



Scheme 1. Synthesis of studied complexes

Paramagnetic NMR spectroscopy

Energy levels of single-molecule magnets and magnetic anisotropy

The energy levels of SMM are generally determined by the following Hamiltonian [1]:

$$\hat{H}_0 = D \left[\hat{S}_z^2 - \frac{S^2}{3} \right] + g\mu_B B_z \hat{S}_z \quad (1)$$

where D – zero-field splitting; \hat{S} – spin operator; \hat{S}_z – operator of spin component along the z -axis; g – value of g -tensor; B_z – magnetic field component along the z -axis z .

Partial derivatives of energy E , determined by the Hamiltonian, with respect to the magnetic field components H_x , H_y and H_z , are components of magnetic susceptibility tensor:

$$\frac{d^2 E}{dH_i dH_j} = \chi_{ij}$$

Isotropic magnetic susceptibility, χ_{iso} , and axial magnetic anisotropy $\Delta\chi_{ax}$ are defined as:

$$\chi_{iso} = \frac{\chi_{xx} + \chi_{yy} + \chi_{zz}}{3}$$

$$\Delta\chi_{ax} = \chi_{zz} - \frac{\chi_{xx} + \chi_{yy}}{2}$$

NMR-based approach for zero-field parameter determination

NMR spectroscopy allows determination of isotropic magnetic susceptibility, χ_{iso} , by Evans method [4]. As for axial magnetic anisotropy $\Delta\chi_{ax}$, it can be obtained from dipolar chemical shift δ_{pcs} , which is expressed as:

$$\delta_{pcs} = \frac{1}{12\pi r^3} \Delta\chi_{ax} (3\cos^2\theta - 1) \quad (2)$$

where r and θ are polar coordinates of each nuclei.

Given all that, we can experimentally obtain the temperature dependence of χ_{iso} and $\Delta\chi_{ax}$, and fit these data by the Hamiltonian(1) to evaluate the value of zero-field parameter D .

Results

The temperature dependence of paramagnetic spectra of the studied complex is presented at Fig. 1.

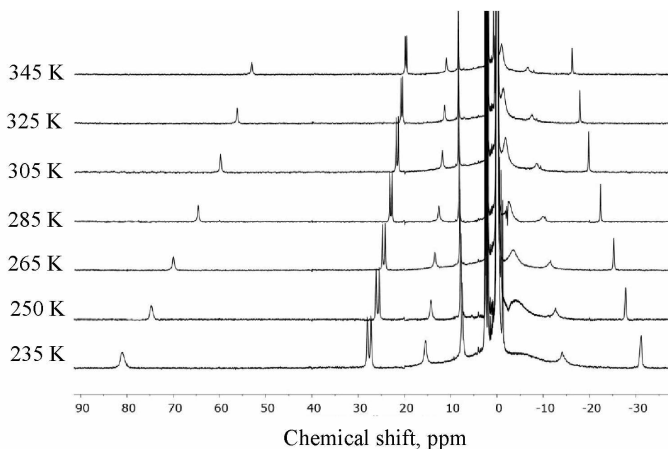


Figure 1. Temperature dependence of ^1H NMR spectra

Calculation of magnetic anisotropy for each temperature point was conducted, and the resulting $\Delta\chi_{ax}$ temperature dependence is shown in Fig. 2. Simulations of this data with Hamiltonian (1) resulted in zero-field parameter $D = -50,4 \text{ cm}^{-1}$ with $g_x = g_y = 2$, $g_z = 2.3$. According to previous magnetometry data, the value of D parameter for a similar compound **2**, which is approximately $27 \div 37 \text{ cm}^{-1}$ [2].

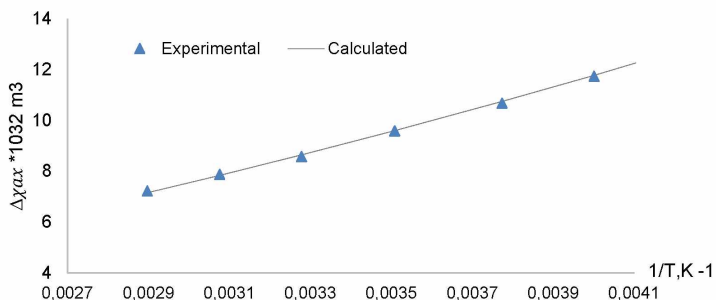


Figure 2. Axial magnetic anisotropy vs reverse temperature plot

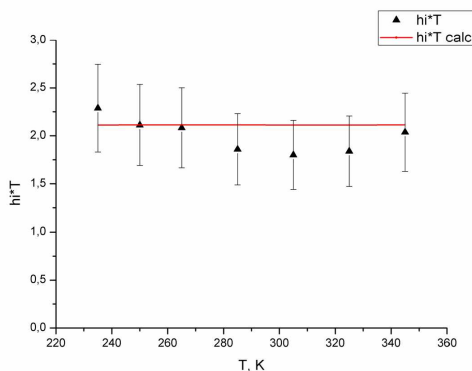


Figure 3. Calculated magnetic susceptibility (line) and Evans method data (triangles)

Simulation of isotropic magnetic susceptibility with the obtained value of D comes with the agreement with experimental Evans data (Fig. 3) (20 % error).

Conclusions

In conclusion, we have synthesized a new analogue of previously reported Co(II)-based SMM. In order to estimate the zero-field parameter for this compound, we employed the original NMR-based approach. The obtained value is close to previously reported magnetometry data for a similar compound; moreover, it comes in agreement with experimental data on isotropic magnetic susceptibility by Evans method.

Acknowledgements

This work is supported by Russian Science Foundation (project №18-73-00113).

References

1. D. Gatteschi, R. Sessoli, *Angew. Chem. Int. Ed.*, **2003**, *42*, 268-297.
2. Ziegenbalg S. et al. *Inorg. Chem.*, **2016**, *55*, 4047-4058.
3. Rauf A. et al. *Spectrochim., Acta A.*, **2015**, *138*, 58-66.
4. D.F. Evans, *J. Chem. Soc.*, **1959**, *0*, 2003-2005.

NMR spectroscopy of paramagnetic transition metal complexes: theory and application examples

Alexander A. Pavlov and Valentin V. Novikov

Nesmeyanov Institute of Organoelement Compounds of RAS

E-mail: pavlov@ineos.ac.ru

Introduction

Nuclear magnetic resonance (NMR) spectroscopy is a routine physical method of studying diamagnetic chemical compounds, while paramagnetic compounds are rarely investigated by NMR. The large chemical shifts (up to several thousand ppm) and line broadening (up to several thousand Hz) may be observed for them in NMR spectra giving information about geometry and electronic structure of a paramagnetic molecule. Unfortunately, there are some difficulties of acquisition and analysis of NMR data due to fast nuclear relaxation and complicated physical principles of observed spectral patterns.

In this lecture the general principles of paramagnetic NMR spectroscopy will be discussed as well as examples of its successful application [1].

Theoretical background of paramagnetic NMR

For paramagnetic compounds the chemical shift value has diamagnetic and paramagnetic parts (1).

$$\delta_{OBS} = \delta_{DIA} + \delta_{PARA} \quad (1)$$

The paramagnetic part arises from hyperfine interaction of a nucleus and unpaired electrons that is described by tensor \mathbf{A} (2).

$$\delta_{PARA} = \frac{S(S+1)\mu_B}{3kTg_N\mu_N} \cdot \mathbf{g} \cdot \mathbf{A} \quad (2)$$

The tensor of hyperfine interaction \mathbf{A} can be divided to isotropic and anisotropic parts (3) leading to contact and pseudocontact chemical shifts respectively. Isotropic (contact) paramagnetic contribution δ_{CS} , which arises from spin polarization through molecular orbitals follows the equation (4). The pseudocontact contribution δ_{PCS} , which arises from dipolar coupling between magnetic moments of a nucleus and of an unpaired electron, depends on nucleus coordinates (r, θ, φ) relative to localization center of unpaired electrons (5a). In case of axial symmetry of a molecule the equation (5) is simplified to (5b).

$$\mathbf{A} = A_{iso}\mathbf{1} + \mathbf{A}_{dip} \quad (3)$$

$$\delta_{CS} = \frac{S(S+1)\mu_B}{3kTg_N\mu_N} \cdot \mathbf{g}_{iso} \cdot A_{iso} \quad (4)$$

$$\delta_{PCS} = \frac{1}{12\pi r^3} \left[\Delta\chi_{ax}(3\cos^2\theta - 1) + \frac{3}{2}\Delta\chi_{rh}\sin^2\theta\cos 2\varphi \right] \quad (5a)$$

$$\delta_{PCS} = \frac{1}{12\pi r^3} \Delta\chi_{ax}(3\cos^2\theta - 1) \quad (5b)$$

where $\Delta\chi_{ax}$ and $\Delta\chi_{rh}$ – axial and rhombic anisotropy of magnetic susceptibility tensor determining magnitude of pseudocontact shifts of all nuclei in the molecule.

I. Application of paramagnetic NMR for spin-crossover compounds

Some 3d-metal complexes with electron configuration d_2-d_8 can be in the both low-spin (LS) and high-spin (HS) states. The spin-crossover (SCO) is a phenomenon of the spin state changes due to external stimuli such as a variation of temperature, pressure etc. Magnetic properties of a molecule in different spin states are also different, that is reflected in the NMR spectra. If the both spin states are populated in a solution, the observed chemical shift δ_{obs} is a weighted average of shifts for LS and HS species (η^{LS} and η^{HS} are their populations):

$$\delta_{obs} = \delta_{DIA} + (\delta_{CS}^{LS} + \delta_{PCS}^{LS}) * \eta^{LS} + (\delta_{CS}^{HS} + \delta_{PCS}^{HS}) * \eta^{HS} \quad (6)$$

For the i^{th} nuclei it thus becomes:

$$\delta_{obs}^i = \delta_{DIA}^i + \delta_{CS}^{i,LS} * (1 - \eta^{HS}) + \delta_{CS}^{i,HS} * \eta^{HS} + \frac{1}{12\pi r_i^3} \Delta\chi_{ax} (3\cos^2\theta_i - 1) \quad (7)$$

The diamagnetic part can be directly measured by NMR spectroscopy of a suitable diamagnetic analogue (such as an isostructural complex of a diamagnetic metal or a free ligand); the contact contributions $\delta_{CS}^{i,LS}$ and $\delta_{CS}^{i,HS}$ are accessible by DFT calculations, together with the geometrical parameters θ_i and r_i . The fitting experimental chemical shift values of all the nuclei simultaneously by the equation (7) can provide information about spin state populations η^{LS} and η^{HS} .

The proposed approach was tested on the various cobalt(II), iron(II) and iron(III) SCO complexes. The obtained results were compared with the well-known Evans method; advantages and disadvantages of this approach will be discussed during the lecture [2].

II. Application of paramagnetic NMR for single molecule magnets

Single molecule magnets (SMMs) are molecules able to retain their magnetization in the absence of an applied magnetic field. To keep molecules magnetized at higher temperatures, an intrinsic energy barrier to magnetization reversal should be enormous. For transition-metal-based SMMs the energy barrier to magnetization reversal is proportional to the zero-field splitting (ZFS) of the ground term. For SMMs zero-field interaction as well as electron Zeeman splitting make a major contribution to the energy of a molecule in magnetic field within spin-Hamiltonian formalism:

$$\hat{H} = \hat{H}_{ZFS} + \hat{H}_{EZI} + \dots = \hat{S} \cdot \mathbf{D} \cdot \hat{S} + g\mu_B \vec{B} \hat{S} + \dots \quad (8)$$

Since the most SMMs exhibit high magnetic anisotropy, the χ tensor is also anisotropic ($\chi_x \neq \chi_y \neq \chi_z$). The approach we have presented uses a relation between the spin-Hamiltonian parameters and molar magnetic susceptibility tensor anisotropy $\Delta\chi$, which can be accessed by NMR spectroscopy:

$$\chi_a = \frac{N_A kT}{10} \frac{\left(\sum_i e \frac{|\psi_i| \hat{H} |\psi_i|}{kT} \right)}{\partial B_a^2} \quad (9)$$

where $a = x, y, z$.

Limitations and prospects of NMR spectroscopy for SMMs investigation will be discussed during the lecture [3, 4].

Acknowledgements

This study was financially supported by Russian Science Foundation (project №18-73-00113).

References

1. I. Bertini, C. Luchinat, G. Parigi, E. Ravera. NMR of paramagnetic molecules. – “Elsevier”, Amsterdam, 2017.
2. A.A. Pavlov, G.L. Denisov, M.A. Kiskin, Y.V. Nelyubina, V.V. Novikov. – *Inorg. Chem.*, **56**, 14759–14762 (2017).
3. V.V. Novikov, A.A. Pavlov, Y.V. Nelyubina, M.-E. Boulon, O.A. Varzatskii, Y.Z. Voloshin, R.E.P. Winpenny. – *J. Am. Chem. Soc.*, **137**, 9792–9795 (2015).
4. A.A. Pavlov, Y.V. Nelyubina, S.V. Kats, L.V. Penkova, N.N. Efimov, A.O. Dmitrienko, A.V. Vologzhanina, A.S. Belov, Y.Z. Voloshin, V.V. Novikov. – *J. Phys. Chem. Lett.*, **7**, 4111–4116 (2016).

Broadband dielectric and nuclear magnetic resonance spectroscopy study on dynamics of water DMSO mixtures, glycerol, and ethylene glycol in mesoporous silica

Melanie Reuhl, Max Weigler, Nail Karabas and Michael Vogel

Institut für Festkörperphysik, Technische Universität Darmstadt, Hochschulstr. 6, 64289 Darmstadt, Germany

E-mail: melanie@nmr.physik.tu-darmstadt.de

https://www.fkp.tu-darmstadt.de/groups/ag_vogel/

Introduction

Hydrogen bonds are a topic with a long research history but still of scientific interest because of the eminent importance for structure, function and dynamics of countless chemical systems [1]. Hydrogen bonding systems in nature and technology are often restricted or confined, which is why much of the research focuses on the study of confinement influences [2].

To further investigate the influence of confinement on hydrogen bondings, we study water- dimethyl sulfoxid (DMSO) mixtures, glycerol, and ethylene glycol in bulk and in silica confinement. To suppress freezing, a water-DMSO mixture with the eutectic mixing ratio is a suitable choice. Moreover, considerable attention is given to glycerol, a non-freezing liquid with hydrogen bonds and to ethylene glycol (EG) bridges the gap between water and glycerol due to its molecular size.

Using NMR and dielectric spectroscopy, we analyze the dependence of correlation times of the hydrogen bonding systems water-DMSO, glycerol, and EG in confinement on filling degree and pore diameter over a broad temperature range.

Experimental Details

Deuterated DMSO (CD_3)₂SO, partially deuterated glycerol $\text{C}_3\text{D}_5(\text{OH})_3$, EG $\text{C}_2\text{H}_4(\text{OH})_2$, and partially deuterated EG $\text{C}_2\text{D}_4(\text{OH})_2$ were obtained from Sigma-Aldrich. Silica matrices MCM-41 and SBA-15 contain cylindrical pores with defined and adjustable diameters. MCM-41 compounds with various pore diameters were synthesized and characterized by the Buntkowsky group (TU Darmstadt). Details can be found elsewhere [3]. Additionally, SBA-15 with two pore diameters (4 nm and 6 nm) was purchased from Sigma Aldrich. Loading of the over night in a turbo molecular pump dried pores with the solvent was done based on the specific pore volume.

For ^2H NMR experiments home-built spectrometers operating at a ^2H Larmor frequency of $\omega_0 = 2\pi \cdot 46.1$ MHz were used. The ^1H diffusion measurements were carried out at a magnet with a high static field gradient at a ^1H Larmor frequency of $\omega_0 = 2\pi \cdot 92$ MHz.

Due to the arrangement of the superconducting coils in Maxwell configuration, a field gradient of approximately 130 T/m is realized. Further details about the ^2H and ^1H field gradient NMR measurements can be found in previous works [4].

Results and Discussion

For water-DMSO mixtures, BDS and NMR results consistently indicate a slowdown of dynamics due to confinement. However, restrictions of the dynamics do not scale with the pore size, but the effect is greatest for an intermediate pore size.

For Glycerol, we found major influence of the sample preparation on the experimental observations. Glycerol samples initially showed an acceleration of the dynamics due to the restriction in pores. This effect scaled with the pore size: a stronger slowdown for smaller pore diameters. However, this first effect could be removed by a preparation in dry atmosphere.

The dry glycerol samples reveal a slight deceleration of the dynamics for larger pores and no effect for smaller pores.

In line with this, the EG samples also indicated a weak dynamical slowdown due to confinement. At high temperatures, there is an effect of the degree of filling on the dynamics. The deceleration of the dynamics is scaled with the decreasing proportion of EG outside the pores, which leads to a slower movement of the liquid inside. Noteworthy for the nominally fully filled pores is the presence of a second component, corresponding to a frozen phase within the pore.

Acknowledgements

This work is supported by the DFG Research Unit FOR1583.

We thank the Buntkowsky group (TU Darmstadt), specially S. Bothe and M. Brodrecht for providing us with MCM-41 and for access to their glove box. We thank B. Kuttich and F. Pabst from the Stühn group (TU Darmstadt) for access to their DSC and BDS equipment.

References

1. G. Buntkowsky, M. Vogel and R. Winter. Properties of Hydrogen-Bonded Liquids at Interfaces. *The Journal of Chemical Physics* Vol. 232, 2018
2. F. Mallamace, C. Branca, C. Corsaro, N. Leone, J. Spooren, H. E. Stanley and S.-H. Chen. Dynamical Crossover and Breakdown of the Stokes-Einstein Relation in Confined Water and in Methanol-Diluted Bulk Water. *The Journal of Physical Chemistry* Vol. 114, 2010
3. M. Brodrecht, E. Klotz, C. Lederle, H. Breitzke, B. Stühn, M. Vogel and G. Buntkowsky. A Combined Solid-State NMR, Dielectric Spectroscopy and Calorimetric Study of Water in Lowly Hydrated MCM-41 Samples. *Z. Phys. Chem.* 2018
4. M. Rosenstihl and M. Vogel. Static and pulsed field gradient nuclear magnetic resonance studies of water diffusion in protein matrices. *The Journal of Chemical Physics* Vol. 135, 2011

H-MAS

Ago Samoson

Tallinn University of Technology
www.nmri.eu

Many interesting biomolecular systems are not amenable to NMR spectroscopy in aqueous solution for T_2 relaxation getting too fast with a growing molecular mass. The problem ascends with magnetic field. Solid state MAS approach is principally not shunted by this colliding situation, but in case of the most exploited spin species- ^1H , limited by strong homogeneous dipolar interactions. Sample spinning speeds of 100 kHz and more, however, have started to grumble this barrier and many works on viscous biosystems have been published since 2014. We have recently achieved the rates over 170 kHz and based on these data, some generalizations can be made. New MAS technology is also beneficial for catalyses and battery research.

References

1. Agarwal V et al (2014) De novo 3D structure determination from sub- milligram protein samples by solid-state 100 kHz MAS NMR spectroscopy. *Angew Chem Int Ed* 53:12253–12256
2. Sternberg U et al (2018) ^1H line width dependence on MAS speed in solid state NMR—comparison of experiment and simulation. *J Magn Reson* 291:32–39
3. Lin Y-L et al (2018) Preparation of bril nuclei of beta-amyloid peptides in reverse micelles. *Chem Commun* 54:10459–10462
4. Susanne Penzel, Andres Oss, Mai-Liis Org, Ago Samoson, Anja Böckmann, Matthias Ernst, Beat H. Meier, Spinning faster: protein NMR at MAS frequencies up to 126 kHz, *Journal of Biomolecular NMR* <https://doi.org/10.1007/s10858-018-0219-9>

Ion and molecule transport in aqueous salt solutions in bulk and in nanopores – a NMR study

Sarah Schneider, Christoph Säckel, Michael Vogel

Institute of Condensed Matter Physics, TU Darmstadt, 64289 Darmstadt, Germany

E-mail: michael.vogel@physik.tu-darmstadt.de

https://www.fkp.tu-darmstadt.de/groups/ag_vogel

Introduction

We analyze ion and molecule transport in aqueous salt solutions confined to nanopores as part of a project that aims to develop a new generation of nanosensors by combining biological and synthetic nanopores. While being highly selective and sensitive, biological ion channels lack the robustness for technological applications. Contrarily silica pores are well-proven in industrial and clinical environments, but possess inferior capabilities, e.g. no selectivity. A hybrid system would combine the favorable properties of both fields.

Samples and Experiments

To optimize such pores, it is of large interest to understand the influence of the confinement on the T-dependent ion and molecule transport inside. We vary the pore parameters systematically and study their effects on the dynamics by NMR. Using ^1H and ^2H NMR we can selectively investigate water dynamics whereas ^7Li and ^{23}Na NMR analyze the local and long-range dynamics of ionic species. Samples of interest are $\text{LiCl-H}_2\text{O}$ and $\text{LiCl-D}_2\text{O}$ at various concentrations bulk and in MCM-41 with pore diameters of $d=2.8\text{-}3.8\text{nm}$.

Bulk solutions [1]

Analysing the local ion and water dynamics in the bulk solutions reveals a slowdown with increasing salt concentration at ambient temperatures, while this difference vanishes upon cooling due to partial crystallization. Relaxation times and diffusion coefficients of water molecules agree with those of lithium ions in the weakly supercooled regime, indicating that the dynamics are strongly coupled. However, we see a decoupling in the strongly supercooled regime, most notably of the rotational motion of the water molecules, which does not follow the glassy slowdown of the studied salt solutions below $\sim 145\text{ K}$, but it rather resembles that in nanoscopic confinement, molecular solutions, and high-density amorphous ice at low temperatures. This common low-temperature water dynamics is characterized by large-angle reorientation and Arrhenius temperature dependence.

Confinement

At a given concentration there is a slowdown in confinement with more heterogeneous dynamics. This can be explained by a slower layer at the pore walls and bulk-like dynamics in the pore center. Field-gradient NMR is applied to measure self-diffusion. The extent of the effect and the relation between short- and long-range dynamics depend on the confinement properties, including filling degree and pore size, which also strongly affect a possible crystallization.

Acknowledgements

The authors thank the LOEWE project iNAPO funded by the Ministry of Higher Education, Research and the Arts (HMWK) of the Hessen state for financial support.

References

1. S. Schneider, M. Vogel. – *J. Chem. Phys.*, **149**, 104501 (2018).

Study of calcium phosphate by EPR methods

Daria Shurtakova, B. Yavkin^{1,2}, M. Gafurov¹, G. Mamin¹, S. Orlinski¹, L. Kuznetsova³, S. Bakhteev⁴, I. Ignatyev⁵, I. Smirnov⁶, A. Fedotov⁶, V. Komlev⁶

¹Kazan Federal University, Kremlevskaya 18, Kazan 420008, Russia

²Physikalisches Institut, University of Stuttgart, Pfaffenwaldring 57, Stuttgart 70569, Germany

³Kazan State University for Architecture and Civil Engineering, Zelenaya Str. 1, Kazan 420043, Russia

⁴Kazan National Research Technological University, K. Marx Str. 41, Kazan 420015, Russia

⁵Interregional Clinical Diagnostic Centre, Karbyshev Str. 12a, Kazan 420101, Russia

⁶A. A. Baikov Institute of Metallurgy and Materials Science, Russian Academy of Sciences, Leninsky Pr. 49, Moscow 119991, Russia

E-mail: darja-shurtakva@mail.ru

Introduction

Calcium phosphates are found in our lives in both positive and negative aspects. In the body calcium phosphates are involved in formation of atherosclerotic plaques. Synthetic calcium phosphates are usually employed for medical aims: to restore the function of damaged body tissues, for healing bone defects, for treatment of fractures and complete replacement of joints. In both cases, it is necessary to know the exact composition and structure of materials.

The aim of this work is describing EPR spectra of calcium phosphates and suggest which centers are found in the structure of these materials.

Materials and Methods

In this work, we compared EPR spectra of two series of samples: nanosized hydroxyapatite (HA) and octacalcium phosphate (OPC). Samples of hydroxyapatite were synthesized by precipitation from colloidal solutions at the Faculty of New Materials Science, Moscow State University [1]. Samples of octacalcium phosphate were synthesized at the Institute of Metallurgy and Materials Science (A.A. Baikova) [2].

EPR spectra were obtained on an Eleksys-580/680 spectrometer in the X- and W-bands at the room temperature. EPR signals were detected in all samples after the irradiation.

To describe EPR spectra we used «MatlabR2010a» (TheMathWorksInc.) with a special module "Easyspin".

Results and discussions

Describing EPR spectra is shown in figure 1. Our model contains at least three paramagnetic centers.

We associate the first center (R1) with the presence of the nitrogen radical by analogy with hydroxyapatite. It has 3 peaks on the spectrum in X-band due to $I = 1$ for ^{14}N nuclei. The second center (R2) has to relate with carbonate group. In the W-band a broadened signal is visible. Minimal g-factor of this signal correspond to g-factor = 1.9966.

We supposed that nature of the third signal is the ozonide complexes adsorbed on the octacalcium phosphate crystal surface.

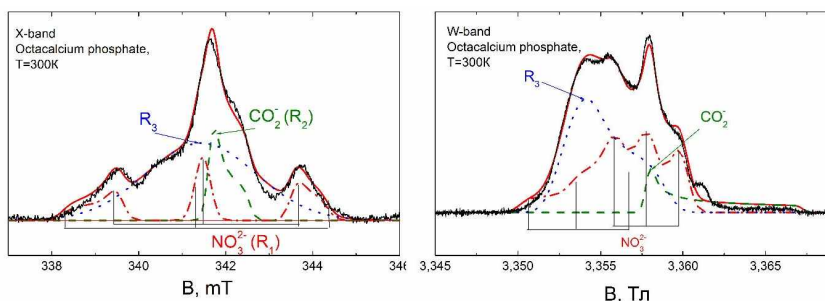


Figure 1. Octocalcium phosphate's EPR spectra with the fitting as a sum of three signals in the X- and W-bands

Parameters of fitting are shown in Table 1 for samples of octocalcium phosphate and hydroxyapatite. If we compare g-factors for these samples, we notice that g_{\parallel} is larger for OCP than for HA and g_{\perp} is less for OCP than for HA. It is due to another environment for nitrogen complex in the structure of OCP compared with the structure of HA.

Table 1. EPR parameters for the stable radical centers used for the simulation of the registered EPR spectrum for samples of octocalcium phosphate and hydroxyapatite

	Octocalcium phosphate			Hydroxyapatite		
Radical	R ₁	R ₂	R ₃	R ₁	R ₂ [3]	R ₃
Complex	NO ₃ ²⁻	CO ₂ ⁻	unknown	NO ₃ ²⁻	CO ₂ ⁻	unknown
g_{\parallel}	2,0055(5)	1,9966(5)	2,0059(5)	2,004(7)	1,996	2,008(7)
g_{\perp}	2,0036(5)	2,0022(4)	2,002(6)	2,008(4)	2,001	2,008(7)
A_{\parallel} (MHz)	85,5(4)			176,0(1)		
A_{\perp} (MHz)	56,1(8)			95,0(2)		

References

- Kovaleva, E.S. Bioresorbable carbonated hydroxyapatite Ca_{10-x}Na_x(PO₄)_{6-x}(CO₃)_x(OH)₂ powders for bioactive materials preparation / E.S. Kovaleva, M.P. Shabanov, V.I. Putlyayev, Y.D. Tretyakov, V.K. Ivanov, N.I. Silkin // Cent. Eur. J. Chem.-2009. –V.7(2). –P. 168
- Komlev V., Barinov S., Bozo I., Deev R.V., Eremin I., Fedotov A., Gurin A., Khromova N., Kopnin P., Kuvshinova E., Mamonov V., Rybko V., Sergeeva N., Teterina A., Zorin V. ACS Appl. Mater. Interfaces 6, 16610 (2014)
- Abdulyanov V. A. et al. Stationary and high-frequency pulsed electron paramagnetic resonance of a calcified atherosclerotic plaque // JETP letters. – 2008. – T. 88. – №. 1. – C. 69-73.

Atomic motion in the bimetallic borohydrides LiLa(BH₄)₃X, X=Cl, Br, I: NMR study

Alexey V. Soloninin¹, Alexander V. Skripov¹, Roman V. Skoryunov¹, Olga A. Babanova¹,
Jacob Grinderslev², Torben R. Jensen²

¹Institute of Metal Physics, Ural Division of the Russian Academy of Sciences, S. Kovalevskoi
18, Ekaterinburg 620108, Russia

²Center for Materials Crystallography, Interdisciplinary Nanoscience Center (iNANO), and
Department of Chemistry, Aarhus University, Langelandsgade 140, DK-8000 Aarhus C,
Denmark.

E-mail: alex.soloninin@imp.uran.ru

Introduction

The bimetallic borohydrides-halides LiLa(BH₄)₃X, X=Cl, Br, I, exhibit both high hydrogen density and high Li ion conductivity. Therefore, they can be considered both as prospective hydrogen storage materials and ionic conductors. The cubic compounds LiLa(BH₄)₃X have spinel-like structures and crystallize in the space group *I-43m* (No. 217), *Z*=8, with La, B, and X atoms fully occupying the 8*c*, 24*g*, and 8*c* Wyckoff sites, respectively, and with Li atoms only in 2/3 of the 12*d* sites¹. The structure contains isolated tetranuclear anionic clusters [La₄X₄(BH₄)₁₂]⁴⁻ with a distorted cubane La₄X₄ core, charge-balanced by Li⁺ cations. The aim of the present work is to study both the reorientational motion of BH₄ groups and Li diffusion in LiLa(BH₄)₃X using ¹H, ¹¹B, and ⁷Li NMR measurements of the spectra and spin-lattice relaxation rates over wide ranges of temperature (5–418 K) and resonance frequency (14–90 MHz). We also discuss a possible relation between the reorientational motion and the translational diffusion in these compounds.

Experimental results

The behavior of the proton spin-lattice relaxation rates measured at three resonance frequencies for LiLa(BH₄)₃Cl is shown in Figure 1.

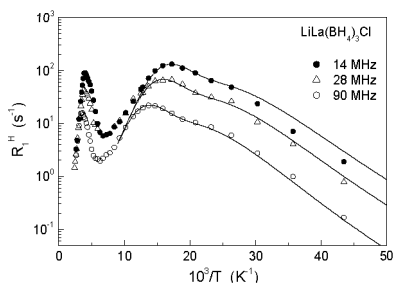


Figure 1. Proton spin-lattice relaxation rates measured at 14, 28, and 90 MHz for LiLa(BH₄)₃Cl as functions of the inverse temperature. The experimental temperature range of the data is 23 – 418 K. The solid lines show the simultaneous fit of the model with a two-peak distribution of the activation energies to the data in the range of the low-temperature $R_1^H(T)$ peak

The temperature dependences of the proton spin-lattice relaxation rates $R_1^H(T)$ measured at two resonance frequencies for the bimetallic borohydrides-halides $\text{LiLa}(\text{BH}_4)_3\text{X}$, $\text{X}=\text{Br}, \text{I}$, have similar behaviour. As can be seen from this figure, the temperature dependences of the ^1H spin-lattice relaxation rate R_1^H exhibit two peaks. Both peaks are frequency-dependent, which is typical of the relaxation mechanism due to the nuclear dipole-dipole interaction modulated by atomic motion. For this mechanism, the $R_1^H(T)$ maximum is expected to occur at the temperature at which the atomic jump rate τ^{-1} becomes nearly equal to the resonance frequency ω . The presence of two well-separated $R_1^H(T)$ peaks indicates a coexistence of at least two types of atomic motion with strongly differing characteristic jump rates.

The expanded view of the $R_1^H(T)$ data in the region of the low-temperature peak is shown in Figure 2 (left). The relaxation data for $\text{LiLa}(\text{BH}_4)_3\text{Cl}$ shown in this Figure exhibit a “shoulder” near 45 K; this suggests a coexistence of at least two low-temperature processes with different average jump rates. It was assumed that the two jump processes contributing to the low-temperature $R_1^H(T)$ peak correspond to the threefold reorientations of BH_4 groups having two or one nearest-neighbor Li ions; the former case should then be ascribed to the slower process, and the latter one to the faster process.² The behaviour of $R_1^H(T)$ for $\text{LiLa}(\text{BH}_4)_3\text{X}$, $\text{X}=\text{Br}, \text{I}$, can be described in terms of a distribution of H jump rates with one type of motion. We can conclude that the H jump rates for $\text{LiLa}(\text{BH}_4)_3\text{X}$, $\text{X}=\text{Cl}, \text{Br}, \text{I}$, increase with increasing size of the halide ion in the structure because the peak of $R_1^H(T)$ is shifted to lower temperatures. The values of the average activation energies at the low-T region for $\text{LiLa}(\text{BH}_4)_3\text{Cl}$ are 41 meV and 50 meV, and for $\text{LiLa}(\text{BH}_4)_3\text{X}$, $\text{X}=\text{Br}, \text{I}$, they are 28 meV and 21 meV, respectively; these values are summarized in table 1.

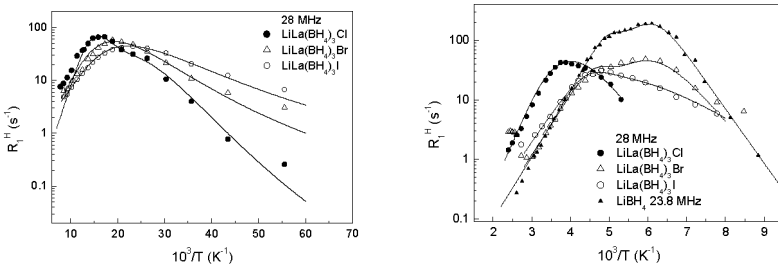


Figure 2. The ^1H spin-lattice relaxation rates at 28 MHz as functions of the inverse temperature for $\text{LiLa}(\text{BH}_4)_3\text{X}$, $\text{X}=\text{Cl}, \text{Br}, \text{I}$, and LiBH_4 at the low-temperature (left) and high-temperature (right) regions. The solid curves show the fits of the model with a distribution of the activation energies to the data

Figure 3 shows the measured temperature dependence of the width of the central ^7Li NMR line for $\text{LiLa}(\text{BH}_4)_3\text{X}$, $\text{X}=\text{Cl}, \text{Br}, \text{I}$. The observed strong narrowing of this line above 200 K is consistent with the onset of Li jump motion at the frequency scale of 10^4 s^{-1} . The value of $\Delta\nu_{\text{Li}}$ in the region of the high-temperature plateau (0.38 kHz) is considerably smaller than the expected line width (1.4 kHz) for the $^7\text{Li}-^7\text{Li}$ dipolar contribution to the rigid lattice second moment. For $\text{LiLa}(\text{BH}_4)_3\text{Cl}$ the position of the high-temperature $R_1^H(T)$ peak ($\sim 250 \text{ K}$ at 28 MHz) (Figure 2 right) shows that this peak may originate from Li diffusion. However, the

amplitude of this peak is too high to result solely from Li diffusion. It was suggested² that the high-temperature $R_f^H(T)$ peak in $\text{LiLa}(\text{BH}_4)_3\text{Cl}$ originates from a combined effect of at least two motional processes occurring at the same frequency scale: Li ion diffusion and another process that involves H jumps. The average activation energy of reorientational motion (264 meV) for this compound is presented in table 1 and is close to the activation energy (300 meV) for Li diffusion. The compounds $\text{LiLa}(\text{BH}_4)_3\text{X}$, X=Br, I contain additional phases, in particular, nanostructured LiBH_4 . The activation energies for these compounds are also presented in table 1, and the values of activation energies for LiBH_4 ³ are shown for comparison. Thus, we observe the decrease of activation energies both for BH_4 reorientations and for cation diffusion with increasing size of halides in these compounds.

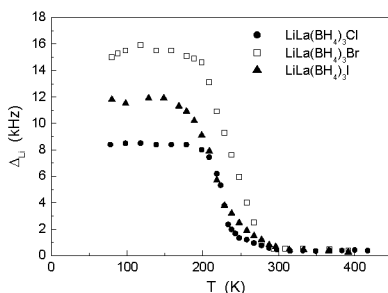


Figure 3. Temperature dependence of the width (full width at half-maximum) of the central ^7Li NMR line measured for $\text{LiLa}(\text{BH}_4)_3\text{X}$, X=Cl, Br, I

Table 1. Average activation energies for BH_4 reorientations, dispersions ΔE_a for Gaussian distributions of E_a for BH_4 reorientations and activation energies for Li diffusion in $\text{LiLa}(\text{BH}_4)_3\text{X}$, X=Cl, Br, I and in $\text{Li}(\text{BH}_4)$

Compound	E_a for BH_4 reorientations (meV)	ΔE_a for BH_4 reorientations (meV)	E_a for Li diffusion (meV)
$\text{LiLa}(\text{BH}_4)_3\text{Cl}$	41 (4), 50 (3), 264 (9)	7 (2), 6 (2), 31 (5)	300 (6)
$\text{LiLa}(\text{BH}_4)_3\text{Br}$	28 (5), 155 (6), 224 (7)	7 (2), 6 (2), 8 (3)	285 (5)
$\text{LiLa}(\text{BH}_4)_3\text{I}$	21 (5), 155 (6), 190 (7)	6 (2), 6 (2), 26 (5)	262 (4)
LiBH_4	180 (5), 250 (6)	-	560 (10)

Acknowledgements

The research was carried out within the state assignment of Minobrnauki of Russia (theme "Function" No. AAAA-A19-119012990095-0).

References

1. S. P. GharibDoust, M. Brighi, Y. Sadikin, D. B. Ravnsbæk, R. Černý, J. Skibsted, T.R. Jensen. – *J. Phys. Chem. C*, **121**, 19010-19021 (2017).
2. A. V. Skripov, A. V. Soloninin, M. B. Ley, T.R. Jensen, Y. Filinchuk. – *J. Phys. Chem. C*, **117**, 14965-14972 (2013).
3. A. V. Skripov, A. V. Soloninin, Y. Filinchuk, D. Chernyshov. – *J. Phys. Chem. C*, **112**, 18701-18705 (2008).

StereoFitter and 3D Computer-Assisted Structure Elucidation

Vadim Zorin¹, Leandro Gil-Silva¹, Maruxa Sordo Touza¹, Esther Vaz¹, Felipe Seoane¹,
Irakusne Lopez¹, Armando Navarro-Vázquez², Roberto R. Gil³, Carlos Cobas¹

¹Mestrelab Research, Santiago de Compostela, Spain

²Departamento de Química Fundamental, CCEN, Universidade Federal de Pernambuco, Brazil

³Department of Chemistry, Carnegie Mellon University, Pittsburgh, PA, USA

E-mail: vadim@mestrelab.com

http://www.mestrelab.com

The ability to elucidate a *de novo* natural product structures in an automated manner has been considered a holy grail in chemistry for many years. [1] Over the last decades, NMR spectroscopy has experienced enormous advances, both in methodology (e.g. new pulse sequences, new alignment media, etc.) and hardware (higher magnetic fields, cryoprobes, improved sensitivity). In parallel, sophisticated software packages have been developed aimed at automating the elucidation of small molecules from NMR data, although most of them have been focused on the determination of the molecular 2D structural constitution (2D structure).

In this work, we present our latest efforts towards a fully integrated Computer Assisted 3D Structure Elucidation (CASE-3D) system for the elucidation of relative configuration and preferred conformations of small molecules (Fig. 1). It has been designed to cover all required tools for the complete 3D elucidation problem.

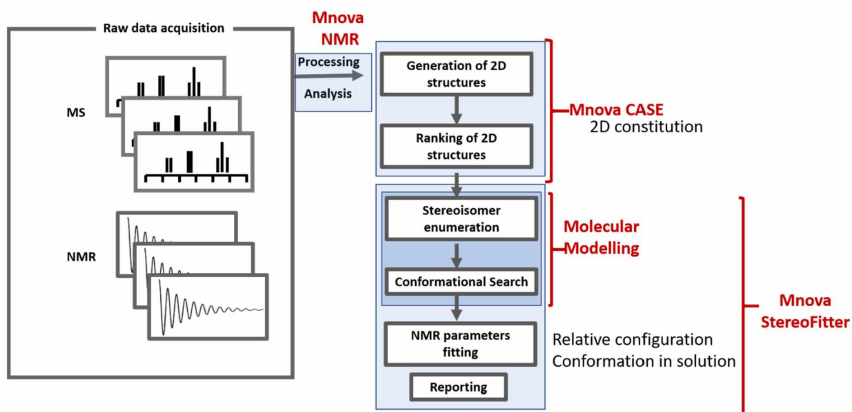


Figure 1. High-level workflow for Computer Assisted 3D Structure Elucidation (CASE-3D)

The main elements of this new software package are:

- A 2D structure elucidation from MS and NMR data.
- Automatic enumeration of diastereoisomers from a 2D structure constitution.
- Generation of minimum energy 3D conformations for each 2D diastereoisomer.
- Manual and automatic assignments of 2D molecules
- Fully automatic NOESY/ROESY analysis and distance restraints calculations
- ¹H and ¹³C chemical shift predictions using DFT
- NMR parameters fitting using:
 - ³J scalar couplings

- NOEs
- Residual Dipolar Couplings (RDCs)
- Isotropic chemical shifts
- Residual Chemical Shifts Anisotropies (RCSAs)
- Statistical analysis of the results for stereoisomers ranking as well as 3D conformational distributions.

The overall architecture of the application, as well as illustrative examples, will be shown in this work.

References

1. Armando Navarro-Vázquez, Roberto R. Gil, and Kirill Blinov, Computer-Assisted 3D Structure Elucidation (CASE-3D) of Natural Products Combining Isotropic and Anisotropic NMR Parameters, *J. Nat. Prod.*, **81** (1), 203–210 (2018)

Poster Session

Progressive saturation technique in ultralow field

Ilgiz Abdullin, Alexandr Voronin, Konstantin Tyutyukin, Andrei Komolkin, Viacheslav Frolov
Faculty of Physics of Saint Petersburg State University, St. Petersburg, Russia
E-mail: abdyllin-ilgiz@mail.ru

The main difficulty of nuclear magnetic resonances experiments in the low field is the bad relation signal/noise. To overcome this difficulty one uses the accumulation of NMR signals that leads to a long time of performance of experiment. In particular, it belongs to measurement of time of spin-lattice relaxation (T_1), especially for samples with long relaxation time. In this situation it is expedient to apply progressive saturation technique [1, 2] instead of standard $180^\circ-90^\circ$ or $90^\circ-90^\circ$ pulse methods which demand performance of a condition repetition time $TR \gg T_1$. The steady state signal after progressive saturation by series of radio-frequency pulses (RFP) is described by expression for transversal magnetization M_x

$$M_x = M_0 \frac{\left(1 - e^{-\frac{TR}{T_1}}\right) \sin\beta}{1 - \cos\beta \cdot e^{-TR/T_1}} \quad (1)$$

where β is rotation angle of longitudinal magnetization by RFP.

On the basis of the equation (1) two methods are offered:

1. At T_1 fixed $TR < T_1$ To receive a dependence M_x on rotation angle of magnetization β by RFP (i. e. on duration of RFP) and to fit the function (1) to experimental curves. The rough estimate can be made under the determination of the maximum position.
2. On the contrary, at fixed β (it is the most convenient to choose $\beta = 90^\circ$) to receive a dependence on TR .

It is necessary to notice that the eq. (1) is correct only on condition of full attenuation of traversal magnetization components before RFP is on. Therefore it is desirable to include in the pulse sequence before each RFP the spoil gradient pulse.

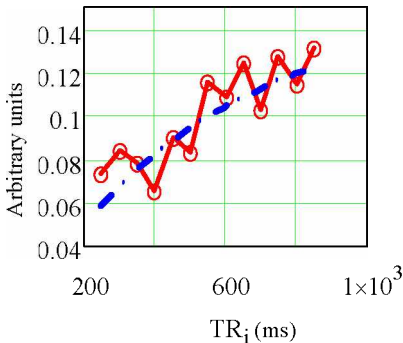


Figure 1. Solid line - experimental;
 dot-dash line - the fitting

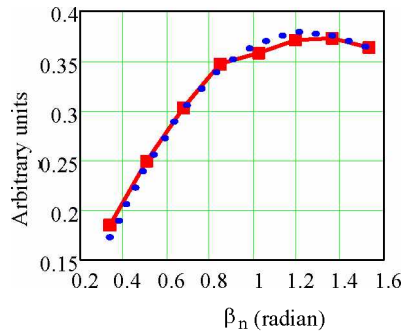


Figure 2. Solid line - experimental;
 dot line - the fitting

The experiment was executed on the homebuilt minitomograph at 7 mT of departments of nuclear physical techniques of research of St.Petersburg State University. In particular, relaxation times were measured in clean Dimetilformamid and solution (0.2%) of Fullerene in it.

In fig. 1 the example of fitting of dependence of the intensity of a steady state signal on the repetition period at $\beta=90^\circ$ is presented. In this case steady state arises since the second pulse. At each value of the period of repetition accumulation of 16 signals was made, the change interval of the period was 50 ms.

Fig. 2 illustrates dependence of similar value for water CuSO_4 solution from β at the constant period of repetition (100 ms). Root mean square deviation of the received dependence from theoretical for T_1 = makes 1.9%.

Generation of the sequences and data reception were provided with programs in LabVIEW. The fragment of the user interface is presented in fig. 3. Final data processing was made by programs in the environment MathCad.

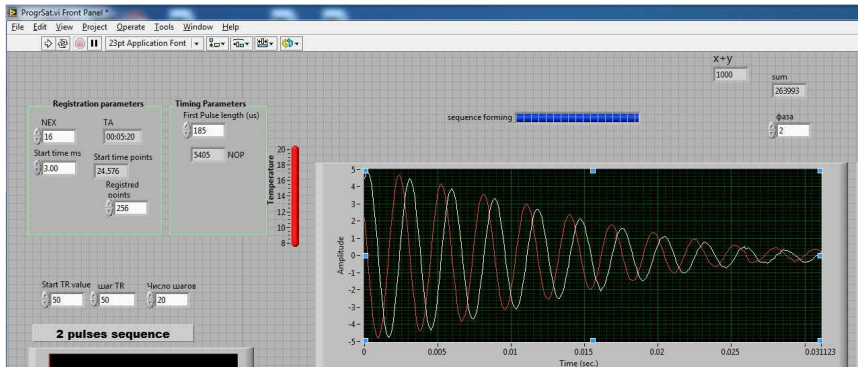


Figure 3

References

1. Chizhik V. I., Chernyshev Yu. S., Donets A. V., Frolov V., Komolkin A., Shelyapina M. G. *Magnetic Resonance and Its Applications*. Springer. Cham, Heidelberg, New York, Dordrecht, London. 2014, XX, 782 p. 234 illus
2. Chizhik V.I. *Yadernaia Magnitnaia Relaksazia*. Saint-Petersburg: Ed. St.Petersburg University. 2014, 385 p. (in Russian)
3. Ernst R.R., Bodenhausen G., Wokaun A. *Principles of Nuclear Magnetic Resonance in One and Two Dimensions*. Clarendon Press. Oxford 1987. 610 p.

Spin state of 2,6-di(pyrazol-3-yl)pyridine complexes of iron(II) and cobalt(II) in solution by paramagnetic NMR method

Dmitry Aleshin^{1,2}, *Yulia V. Nelyubina*^{1,4}, *Igor Nikovskiy*¹, *Alexander V. Polezhaev*^{2,3},
*Nikolay N. Efimov*⁴, *Alexander A. Pavlov*¹

¹*Nesmeyanov Institute of Organoelement Compounds, Russian Academy of Sciences, 119991, Vavilova Str., 28, Moscow, Russia*

²*Mendeleev University of Chemical Technology of Russia, 125047, Miusskaya pl., 9, Moscow, Russia*

³*Bauman Moscow State Technical University, 105005, 2nd Baumanskaya Str., 5, Moscow, Russia*

⁴*Kurnakov Institute of General and Inorganic Chemistry, Russian Academy of Sciences, 119991, Leninsky prosp., 31, Moscow, Russia*

E-mail: dima.aleshin26@gmail.com

Introduction

Spin transition complexes is a class of materials exhibiting electron states bistability, which may be used as molecular switches [1]. Spin transition in spin-crossover compounds is usually studied in the solid state by magnetometry. However, only a few methods exist for studies in solution. Routinely used Evans method measures magnetic susceptibility, but it can lead to significant error of estimate (up to 15 %) due to various method limitations. Here we propose an alternative technique for estimation of spin state populations based on analysis of chemical shifts temperature dependence.

Object of research

Here we show series of cobalt(II) and iron(II) complexes with new 2,6-di(pyrazol-3-yl)pyridine ligands (Fig. 1). The four complexes with composition ML_2 were synthesized by self-assembly of metal(II) perchlorate and corresponding ligand.

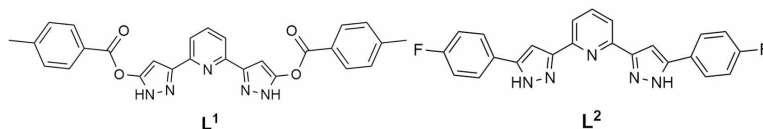


Figure 1. Ligands of the studied compounds

Spin crossover probingfe

The both CoL_2 and CoL_2 show χT values 2.7-3.0 $cm^3 K/mol$ in solid state as well as in solution by the Evans method and magnetometry. This confirms high-spin state of these complexes in temperatures up to 345 K.

Since low-spin state of the Fe(II) ion is diamagnetic, observed chemical shifts takes following form:

$$\delta_{obs} = \eta_{LS}\delta_{dia}^{LS} + \eta_{HS}(\delta_{dia}^{HS} + \delta_{par}^{HS}) \approx \delta_{dia} + \eta_{HS}\delta_{par}^{HS} \quad (1)$$

Where η_{HS} – population of high-spin state, δ_{dia} – chemical shift of diamagnetic analogue, δ_{par}^{HS} – paramagnetic chemical shift of high-spin complex.

For the high-spin state of Fe(II) ion ($S = 2$), the temperature dependence of chemical shifts is well described by a linear function in the frame $\delta - T^{-1}$ [2].

$$\delta_{par}^{HS} = A + BT^{-1} \quad (2)$$

Thus, the population of high-spin state can be calculated through the deviation from the linear function:

$$\eta_{HS} = \frac{\delta_{par}}{A+BT^{-1}} \quad (3)$$

For the studied complexes FeL_1^2 and FeL_2^2 in temperature range of 285–345 K (Fig. 2) the temperature dependence of chemical shifts is linear in the $\delta - T^{-1}$ coordinates indicating a pure high-spin state. At temperatures below 285 K, a deviation from the linear law is observed, which indicates a temperature-induced spin transition; the population of high-spin state at these temperatures were calculated using the equation (3).

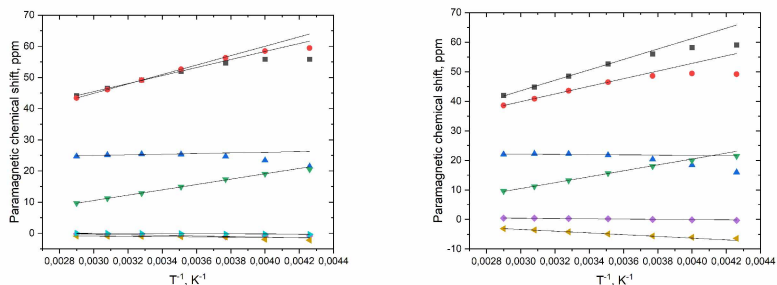


Figure 2. Temperature dependence of paramagnetic shifts for FeL_1^2 and FeL_2^2

The Evans method [3] allows to determine the value of magnetic susceptibility in solution χ , can also be used to estimate populations of spin states. In the case of spin-transition compounds, observed value of χ is weighted average:

$$\chi_{obs} = \eta_{LS}\chi_{LS} + \eta_{HS}\chi_{HS} \quad (4)$$

For Fe(II) ion population of the high-spin state can be estimated as:

$$\eta_{HS} \approx \frac{\chi_{obs}}{\chi_{HS}} \quad (5)$$

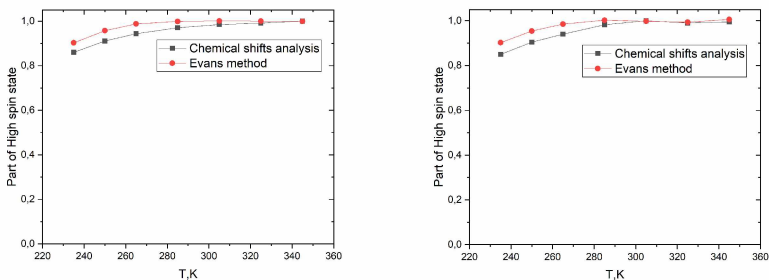


Figure 3. Temperature dependence of high-spin state population for FeL_1^2 and FeL_2^2

For the studied FeL_1^2 and FeL_2^2 complexes, a constant χT value of ~ 3.4 cm³K/mol is observed in the temperature range 285–345 K, which corresponds to a pure high-spin state. At temperatures below 285 K, a decrease of χT value is observed, which indicates a temperature-

induced spin transition. The population values (Fig. 3). of high-spin state at temperatures below 285 K were calculated using the equation (5), and the largest value of χ was chosen as χ_{HS} in temperature range of 235–345 K.

In conclusion, we present new 2,6-di(pyrazol-3-yl)pyridine complexes of iron(II) and cobalt(II). The iron complexes show temperature-induced spin transition at ambient temperatures according to the Evans method as well as original approach based on analysis of temperature dependence of NMR chemical shifts. We showed that for iron(II) complexes deviation from linear function in coordinates $\delta - T^{-1}$ clearly indicates spin transition. The proposed approach has no flaws of the Evans method such as high purity requirement of a studied compound.

Acknowledgements

This study was financially supported by Russian Science Foundation (project №18-73-00113).

References

1. Gütllich, P.; Goodwin, H. A. Spin Crossover in Transition Metal Compounds I–III; Springer-Verlag: Berlin, 2004; Vol. 233.
2. Sidney E. Creutz and Jonas C. Peters Spin-State Tuning at Pseudo-tetrahedral d6 Ions: Spin Crossover in [BP3] Fe^{II}-X Complexes Inorg. Chem. 2007, 46, 6794-6803.
3. D. F. Evans, The determination of the paramagnetic susceptibility of substances in solution by nuclear magnetic resonance, J. Chem. Soc., 1959,0, 2003-2005.
4. Yulia Nelyubina, Alexander Polezhaev, Alexander Pavlov, Dmitrii Aleshin, Svetlana Savkina, Nikolay Efimov, Teimur Aliev and Valentin Novikov, Intramolecular Spin State Locking in Iron(II) 2,6-Di(pyrazol-3-yl)pyridine Complexes by Phenyl Groups: An Experimental Study, Magnetochemistry 2018, 4(4), 46.

Computer simulation of micelle formation in magnesium hexanoate solution

N. A. Antonova, A. M. Ryzhkov, A. V. Komolkin

*St.Petersburg State University, 7-9 Universitetskaya Emb., 190034, St.Petersburg, Russia
E-mail: st054868@student.spbu.ru*

Introduction

Magnesium hexanoate is an amphiphilic molecule. When concentration of the salt in aqua solution exceeds critical micelle concentration (CMC) it forms micelles [1]. Computer simulation of molecular dynamics of concentrated system leads to appearance of incompact aggregates which remotely reminds micelles. For computer simulation, the widespread potentials are OPLS-AA, CHARMM, AMBER [2-4]. In them the magnesium ion charge is +2e, the charge of the acid residue is -1e.

It is possible that the potentials of the atom-atom interactions, especially the electrical charge of the ions, are not acceptable for the simulation of concentrated ionic systems. The purpose of this work is to investigate the structure and dynamics of micelles in such a concentrated solution depending on the model charges of the ions.

Model systems

Magnesium hexanoate molecule was constructed in Jmol [5]. The model of water was chosen SPC/E [6]. The parameters of simulation were taken from the OPLS-AA [2]. The process of micelle formation was carried out by the method of molecular dynamics.

In order to find partial charges of magnesium ion and acid residue, a quantum-chemical simulation of a small system containing the cation, anion, and 10 water molecules was performed. Geometry optimization was made in Gaussian-16 program [7] within 6-31G++(1d)/B3LYP method. The charges were obtained by method 6-31G in GAMESS program [8] in two models. Mulliken model leads to charges of magnesium ion $q=+1.4e$, and Löwdin model leads to $q=+1e$ (Table 1).

Table 1. Charges of ions in the modeled systems

System	Charge of magnesium ion	Charge of acid residue
I	+2	-1
II	+1.4	-0.7
III	+1	-0.5

Three systems in which the magnesium charges were assumed to be +2e, +1.4e and +1e respectively were investigated. The parameters of intra- and intermolecular non-electrostatic interaction were used from OPLS-AA [2] intact.

Systems consisted of 130 ions of magnesium ion, 260 ions of acid residue and 10586 molecules of water. The concentration of the solutions was 0.61 M and the density was 1.04 g/cm³. In the first system (I) the charges of magnesium ion and acid residue was $q=+2e$ and $q=-1e$ respectively, magnesium ion is divalent. In the other solutions the charges of magnesium ion was $q=+1.4e$ (system II) and $q=+1e$ (system III). Charges of acid residues were $-q/2$.

Each system was simulated during 3 ns. The first nanosecond was to equilibrate the system. Behavior of the system were analyzed during 2 ns. All the systems was simulated twice. Final position of the system in a simulation was the initial position of the next simulation.

Results analysis

To analyze the results it was necessary to calculate radial distribution function (RDF), self-diffusion coefficient, also to consider shape and size of the aggregates. RDF shows probability of finding atoms at a certain distance. In the Figure 1 there are RDFs between magnesium ions for three systems.

In the system I the molecules of water and magnesium was very tightly pressed to each other. There was no exchange of water molecules between the hydration shell of magnesium and free water. It prevented the approach of magnesium ions to each other. Undissociated salt molecules existed united throughout the entire simulation (Fig. 2). In the system III the exchange of water molecules took place and there existed Mg-Mg contact pairs (in which the water molecule stands on the side of Mg-Mg line). This result is similar to the result of modeling Na^{1+} by A. Lyubartsev [9]. The charge of magnesium ion $q=+1.4e$ leads to the similar result as in the system I.

The largest aggregate in the system I consisted of 39 acid residues and 26% residues were in monomer state. In the system II there was 70 residues in the largest aggregate and 27% residues were as monomers. In the system III the largest aggregate consisted of 103 residues and there was only 16% residues stayed monomers.

Conclusion

With charge of magnesium ion equal to $+2e$ in the system I, Mg has very stable hydration shell on the scale of the simulation time. Undissociated salt molecules remained united during all the time of simulation. It seems that charges of Mg^{2+} and COO^{1-} too large for this system. In the system III exchange of water in hydration shell and dissociation of salt molecules are faster. As for the structure of micelles, the smaller charge of the acid residue, the larger size of micelles.

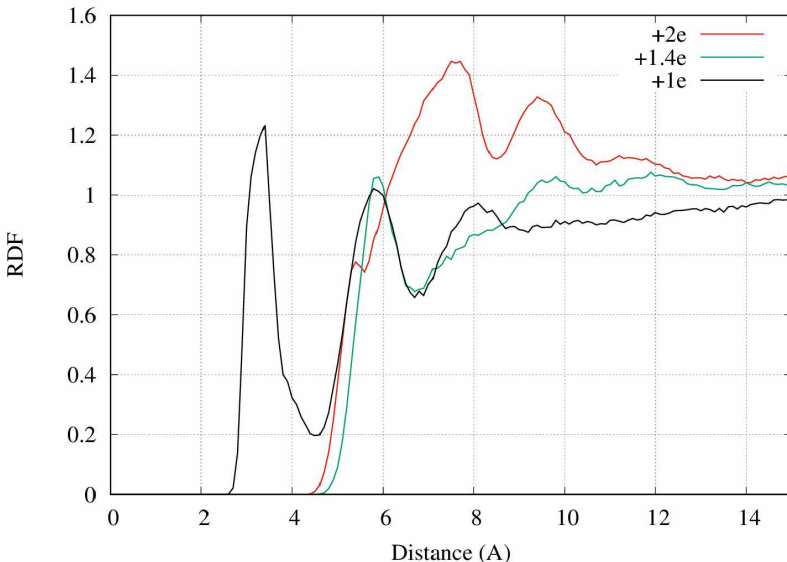


Figure 1. RDFs between magnesium ions

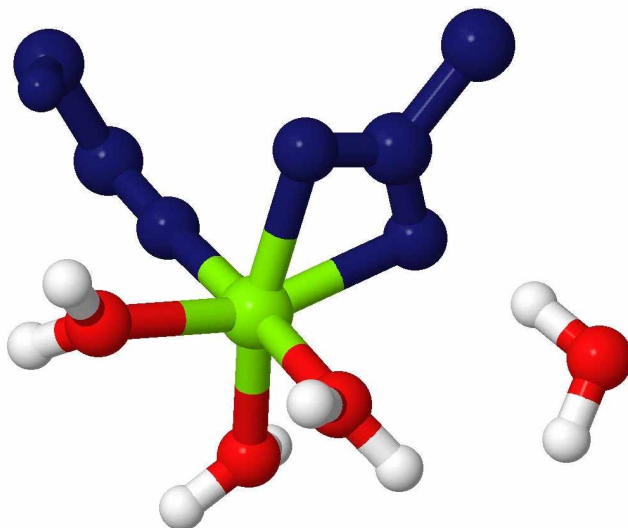


Figure 2. Undissociated molecule of magnesium hexanoate

Acknowledgements

Research was carried out using computational resources provided by Resource Center “Computer Center of SPbU” (<http://cc.spbu.ru>).

References

1. D. Muraviev, R. Khamizov, N. Tikhonov. Peculiarities of the Dynamics of Ion Exchange in Supersaturated Solutions and Colloid Systems. – *Langmuir*, **2003**, v.19, No.26, 10852–10856
2. William L. Jorgensen Research Group — OPLS-AA. URL: <http://zarbi.chem.yale.edu/oplsaam.html> (accessed 01.03.2019)
3. CHARMM (Chemistry at HARvard Macromolecular Mechanics). URL: <https://www.charmm.org> (accessed 01.03.2019)
4. The Amber Home Page | Tools for molecular simulation. URL: <http://ambermd.org/> (accessed 01.03.2019)
5. Jmol: an open-source browser-based HTML5 viewer and stand-alone Java viewer for chemical structures in 3D. URL: <http://jmol.sourceforge.net/> (accessed 01.03.2019)
6. Berendsen H., Grigera J., Stratsmaa T. The missing term in effective pair potentials. – *J. Phys. Chem.* **1987**, v.191, No.24, 6269–6271
7. Gaussian.com | Expanding the limits of computational chemistry. URL: <http://gaussian.com/> (accessed 01.03.2019)
8. The General Atomic and Molecular Electronic Structure System (GAMESS). URL: <http://www.msg.ameslab.gov/gamess/> (accessed 01.03.2018)
9. A. P. Lyubartsev, A. Laaksonen. Concentration Effects in Aqueous NaCl Solutions. A Molecular Dynamics Simulation. – *J. Phys. Chem.*, **1996**, v.100, No.40, 16410–16418

Interaction of fullerene derivative with biomembranes – studied by pulsed field gradient NMR technique

Irina A. Avilova¹, Ekaterina A. Dolgikh², Olga A. Kraevaya¹, Aleksandr V. Zhilenkov¹, George A. Saratov³, Yuliia V. Soldatova¹, Raïsa A. Kotelnikova⁴, Pavel A. Troshin^{4,1}, Vitaliy I. Volkov^{1,5}

¹*Institute of Problems of Chemical Physics RAS, Chernogolovka, Russia*

²*Faculty of Fundamental Physical and Chemical Engineering, Lomonosov Moscow State University, Moscow, Russia*

³*Moscow Institute of Physics and Technology (State University), Dolgoprudnyi, Russia*

⁴*Skolkovo Institute of Science and Technology, Moscow, Russia*

⁵*Science Center in Chernogolovka of RAS, Chernogolovka, Russia*

E-mail: irkaavka@gmail.com

Introduction

According to numerous publications, water-soluble fullerene derivatives (WSFD) are promising in biological and pharmacological practice [1, 2]. From the literature, it is known that these compounds exhibit anti-radical properties, antiviral activity, antitumor effect, etc. Establishing the mechanisms of interaction with biological cells and assessing the effect on the structure of biomembranes of WSFD molecules are important tasks in the study of the biological activity of fullerene derivatives. Direct non-invasive method, which allows measuring the molecular dynamics parameters of the WSFD molecules in biological systems, is the pulsed field gradient NMR technique (PFG NMR).

The aim of the study is to estimate the exchange characteristics of the amphiphilic water-soluble fullerene derivative $C_{60}[S(CH_2)_3SO_3Na]_5H$ in model biological membranes, mouse red blood cells (RBC) and RBC ghosts by pulsed field gradient NMR technique.

Results

In order to obtain information on the mobility of the WSFD molecules in the systems under study (liposomes, RBC, RBC ghost), the 1H NMR spin-echo signal attenuations (diffusion decay) were analyzed shown in Fig. 1. As a comparison system was used the aqueous solution $C_{60}[S(CH_2)_3SO_3Na]_5H$.

The obtained diffusion decays are non-exponential and are described by the equation [3, 4]:

$$A(g) = \sum_{i=1}^m p_i' \exp(-\gamma^2 g^2 \delta^2 t_d D_{si}), \quad (1)$$

where γ is gyromagnetic ratio, $t_d = \Delta - \delta/3$ is the diffusion time, δ is duration of the equivalent rectangular magnetic field gradient pulses, g is the amplitude of the magnetic field gradient pulse, D_{si} is the self-diffusion coefficient of i -th component and

$$p_i' = p_i \exp\left(-\frac{2\tau}{T_{2i}} - \frac{\tau_1}{T_{1i}}\right) / \sum_{i=1}^m p_i \exp\left(-\frac{2\tau}{T_{2i}} - \frac{\tau_1}{T_{1i}}\right)$$

$$\sum_{i=1}^m p_i = 1$$

It was found that the diffusion decays of WSFD molecules in an aqueous solution are two-exponential, while in RBC, RBC ghost and liposomes diffusion decays are described by three exponents. The mobility of WSFD molecules in a solution is characterized by two self-diffusion coefficients and in suspensions by three (Table 1). The value of the smallest self-

diffusion coefficient of WSFD molecules in the suspensions under study is close to the lateral diffusion coefficient of lipid molecules in a biomembrane. The slow movement of WSFD molecules in these systems can be explained by their binding to liposomes, RBC and RBC ghost. Since the slow motion of WSFD molecules was observed for all three systems, it can be concluded that the molecules of this compound penetrate into the lipid bilayer.

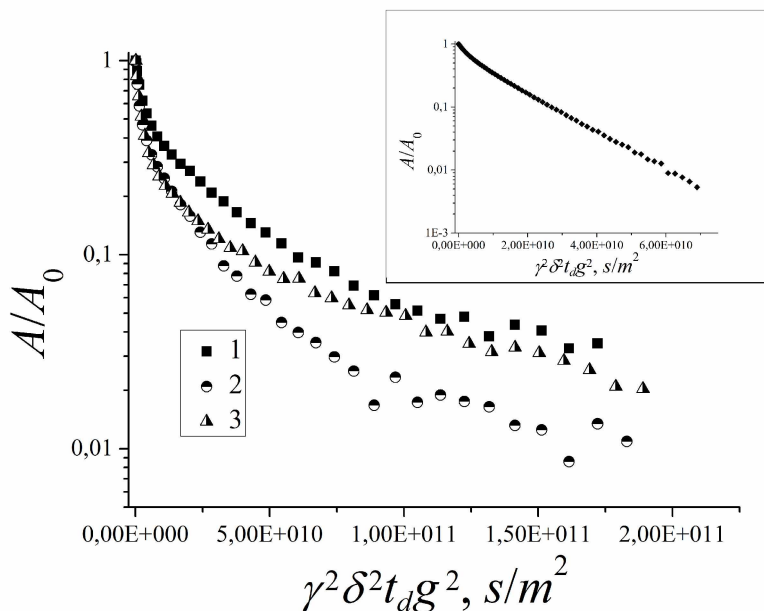


Figure 1. ^1H NMR diffusion decays of the fullerene derivative in RBC (curve 1), RBC ghosts (curve 2) and phosphatidylcholine liposome (curves 3) suspensions and fullerene derivative aqueous solution (insert)

Table 1. Self-diffusion coefficients of the fullerene derivative in the RBC, RBC ghost, liposome suspensions and aqueous solution

	Fullerene derivative partial self-diffusion coefficients			Fullerene derivative partial self-diffusion coefficients in aqueous solution	
	D_{s1}^S , 10^{-12} m ² /s	D_{s2}^S , 10^{-11} m ² /s	D_{s3}^S , 10^{-10} m ² /s	D_{s1}^W , 10^{-11} m ² /s	D_{s2}^W , 10^{-10} m ² /s
RBC	5.5 ± 0.8	3.9 ± 0.6	5.5 ± 0.8	7.4 ± 0.8	4.1 ± 0.4
RBC ghosts	7.9 ± 1.2	5.7 ± 0.9	7.3 ± 1.1		
Liposome	7.7 ± 1.2	5.4 ± 0.8	4.8 ± 0.7		

In accordance with the works [3-6] from the analysis of the dependence of the populations of the WSFD molecules on the diffusion time was estimated the residence time of the fullerene derivative molecules in RBC and the lifetime of the molecular associate. The

values of the fullerene derivative associate lifetime and RBC residence time were found to be 200 ± 30 ms and 440 ± 70 ms, respectively.

Conclusions

The ability of $C_{60}[S(CH_2)_3SO_3Na]_5H$ molecules to penetrate biological membranes was detected by pulsed field gradient NMR technique. Fullerene derivative partial self-diffusion coefficients in liposomes, RBC, and RBC ghost were determined. It has been shown that in a suspension of erythrocytes the WSFD molecules are in the form of isolated and associated molecules in the aqueous phase or are bound to the cell membrane.

Acknowledgements

This work was supported by Russian Foundation for Basic Research (project no. 18-32-00815).

References

1. S. Bosi, T. D. Ros, G. Spalluto, J. Balzarini, M. Prato. – *Med. Chem. Lett.*, 13, 4437-4440, (2003).
2. R. A. Kotelnikova, G. N. Bogdanov, E. C. Frog, A. I. Kotelnikov, V. N. Shtolko, V. S. Romanova, S. M. Andreev, A. A. Kushch, N. E. Fedorova, A. A. Medzhidova, G. G. Miller. – *J. Nanopart. Res.*, 5, 561–566, (2003).
3. A. I. Maklakov, V. D. Skirda, N. F. Fatkullin. Self-Diffusion in Polymer Solutions and Melts (in Russian). –Kazan State University Press, Kazan, 1987.
4. I. A. Avilova, A. V. Smolina, A. I. Kotelnikov, R. A. Kotelnikova, V. V. Loskutov, V. I. Volkov. – *Appl. Magn. Reson.*, 47, 3, 335-347 (2016).
5. Y. S. Hong, K. C. Kim, V. I. Volkov, V. D. Skirda, C.-H. Lee. – *Appl. Magn. Reson.*, 29, 351-361 (2005)
6. I. A. Avilova, A. V. Chernyak, A. V. Zhilenkov, P. A. Troshin, V. I. Volkov. – *Mendeleev Commun.*, 26, 146-148 (2016).

Hydrogen solubility and diffusion in V-Pd substitution alloys studied by DFT

O. Bavrina¹, M. Shelyapina¹, K. Klyukin², A. Livshits³

¹*Saint Petersburg State University, 7/9 Universitetskaya nab., St. Petersburg 199034, Russia*

²*Department of Chemical and Biomolecular Engineering, University of Nebraska-Lincoln, Lincoln, NE 68588, United States*

³*Bonch-Bruевич Saint-Petersburg State University, 22/1 pr. Bolshhevikov, St. Petersburg 193232, Russia*

E-mail: olga.bavrina@gmail.com

Introduction

V-Pd alloys are promising materials for pure hydrogen separation. Palladium moderated hydrogen solubility, which is too high in pure vanadium, whereas vanadium ensures sufficient diffusivity at practical temperatures (about 600K) [1]. It is known from experiment, that alloying Pd to V decreases the hydrogen diffusion coefficient D in several times, although pure Pd itself has good hydrogen throughput. In addition to almost unchanged crystal structure, without considering local distortions, these in some way controversial experimental facts are still not well understood. Here we report on the results of our study of the effect of Pd alloying on the hydrogen solubility and hydrogen diffusion in vanadium carried out within a density functional theory (DFT) approach.

Method of calculation

In order to simulate body-centered cubic (bcc) palladium substituted structure of vanadium with a random Pd atoms distribution over the lattice, a supercell method was used. All calculations were carried out within the framework of the plane-wave pseudo-potential DFT method using the Perdew–Burke–Ernzerhof generalized gradient approximations (PBE GGA) exchange-correlation potential and the ultrasoft Vanderbilt pseudopotentials as implemented in the Quantum Espresso package. The charge and the kinetic energy cut-off were 60 Ry and 360 Ry, respectively. For all the studied supercells, a total number of $3 \times 3 \times 3$ k -points mesh in the irreducible Brillouin zone were used, after testing that a denser mesh does not contribute accuracy to result. Calculations were performed in $2 \times 2 \times 2$ supercells, $V_{16-n}Pd_n$, with $n = 0, 1, 2$, and 3. All self-consistent calculations were made with full structure relaxation.

Hydrogen localization and solubility

In a bcc cell hydrogen atom may occupy two types of interstitial site – tetrahedral (T) and octahedral (O). Within a supercell approach the hydrogen site solubility, the energy that cost to remove a hydrogen atom from a T- or O- site, can be calculated as follows:

$$E_{\text{sol}}[V_{16-n}Pd_nH^{\text{T(O)}}] = E_{\text{tot}}[V_{16-n}Pd_nH^{\text{T(O)}}] - E_{\text{tot}}[V_{16-n}Pd_n] - \frac{1}{2}E_{\text{tot}}[H_2]. \quad (1)$$

Here $E_{\text{tot}}[V_{16-n}Pd_nH^{\text{T(O)}}]$ is the total energy of a considered supercell with a hydrogen atom placed in the corresponding interstitial site; $E_{\text{tot}}[H_2]$ is the total energy of the H_2 molecule. All the energy characteristics are given after full structural relaxation of the corresponding supercells. To calculate $E_{\text{tot}}[H_2]$ the H_2 molecule was put in a box $10 \times 10 \times 10$ Å and the self-consistent field calculations were done using the same method as described but with 1000 k -points in irreducible Brillouin zone. The calculation result to the equilibrium H–H bond length of 0.7419 Å and $E_{\text{tot}}[H_2] = -2.3302$ Ry.

As it was shown previously, in pure bcc vanadium H occupies T-sites. The calculations taking into account full structure relaxation showed that O-sites are not stable. In $V_{16-n}Pd_n$, the lowest E_{sol} value, and hence the strongest metal-H bonding corresponds to hydrogen placed in

a T-site at a Pd-H distance of about 3.5 Å, see Table 1. The stability of the O-sites (for the same distance from the Pd atom) is systematically lower than that one of the T-sites. These features are preserved for other considered $V_{16-n}Pd_nH$ supercells, but for $V_{13}Pd_3H$ the minimum of the E_{sol} value is shifted towards the larger d_{Pd-H} . Summing up the results of the hydrogen solubility study one can conclude that (i) for the hydrogen T-sites that correspond to the Pd alloying first leads to sharp decreasing of the E_{sol} value at about 2 at. % of Pd and then to gradual increasing. However, for T-site furthest from Pd, E'_{sol} , the hydrogen solubility energy monotonously increases with Pd concentration increasing.

Table 1. Hydrogen solubility energy and parameters of hydrogen diffusion calculated for $V_{16-n}Pd_n$ supercells ($n = 0, 1, 2$ and 3)

Parameters	V_{16}	$V_{15}Pd_1$	$V_{14}Pd_2$	$V_{13}Pd_3$
E_{sol} (eV)	-0.42	-0.48	-0.31	-0.25
E'_{sol} (eV)	-0.42	-0.38	-0.21	-0.07
L (Å)	3.009	3.0110	3.0181	3.0314
β	1	0.69	0.47	0.23
E_a (eV)	0.012	0.076	0.066	0.061
$D_0 \times 10^{-8}$ (m ² /s)	1.06	0.731	0.50	0.25
$D^{673K} \times 10^{-8}$ (m ² /s)	8.60	1.97	1.60	0.86

Hydrogen motion mechanism and activation energy

To calculate the activation energy E_a along the minimum energy path (MEP) between two hydrogen positions, the nudged elastic band (NEB) method was applied [2]. The configuration of the system with the maximal energy along the MEP was obtained using the Climbing Image Approach [3]. Then the activation energy E_a was found as the energy difference between the transition and ground states. The lattice parameters of the supercell were optimized all along the hydrogen atom displacement path.

Fig. 1(a) represents the energy profiles for the displacement of a hydrogen atom in $V_{16-n}Pd_n$ supercells (with $n = 0, 1, 2,$ and 3) along MEP from the most stable T-site to the nearest T-site with lower stability.

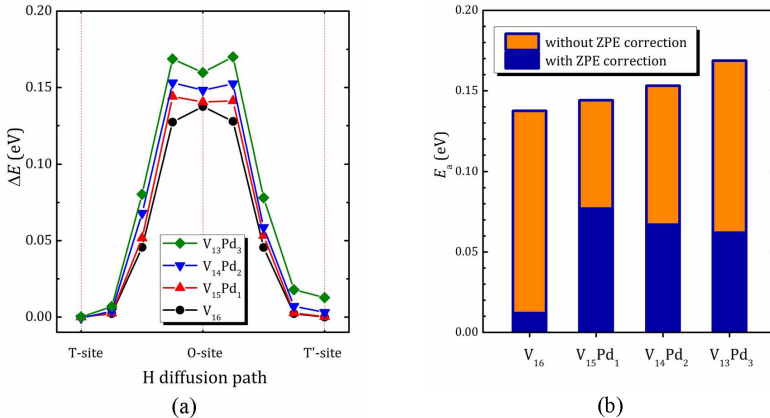


Figure 1. (a) – The energy profiles (without ZPE contribution) for H motion in $V_{16-n}Pd_n$ (with $n = 0, 1, 2$ and 3) along the diffusion path from the most stable T-site to the nearest T-site with lower stability; (b) – the lowest activation energy of hydrogen motion in the considered supercells calculated without and with taken into account ZPE contribution

To gain the time the calculations have been carried out neglecting ZPE contribution. As one can see, for all the considered supercells MEP goes through an O-site, which is unstable for V_{16} , but upon Pd substitution for V a shallow minimum appears in O-site, however, its profoundness is not sufficient enough to consider it as a metastable. The calculated activation energy gradually increases with Pd concentration from 0.14 to 0.15 eV, as it is shown in Fig. 1(b). However, the ZPE correction dramatically affects both the calculated values and the concentration dependence of E_a . For pure vanadium the ZPE corrected activation energy of hydrogen translational motion is only 0.012 eV, that makes V almost transparent for H diffusion.

To evaluate the hydrogen diffusion coefficient the same formalism as reported in Ref. [4] and extended it to supercells in Ref. [5]. In absence of a metastable site on MEP, the diffusion coefficient can be estimated as follows

$$D = \beta \frac{L^2 k_B T}{12 \hbar} \exp \left[-\frac{E_a}{k_B T} \right] = D_0 \exp \left[-\frac{E_a}{k_B T} \right], \quad (2)$$

where L is the jump length projected onto the diffusion direction; E_a is the activation energy of hydrogen motion, which can be determined as the sum of the migration barrier value ΔE and the corresponding zero-point energy correction ΔZPE ; β is a coefficient that takes into account that initial site is occupied by a hydrogen atom and that the target site is empty. All the parameters of hydrogen diffusion, calculated for the studied supercells, are listed in Table 1. The results, obtained for pure V are in agreement with experimental ones, reported in Ref. [6]: $D_0 = 0.35 \times 10^{-7} \text{ m}^2/\text{s}$, $E_a = 0.052 \text{ eV}$.

Conclusions

Summing up the obtained results one can conclude that partial substitution Pd for vanadium results in a cumulative effect: (i) the activation energy increases and (ii) the “effective” diffusion region decreases, since hydrogen tends to avoid the regions near palladium.

Acknowledgements

The calculations were carried out using computational facilities provided by Computing Centre (<http://cc.spbu.ru/en>) and by Computer Center of University of Nebraska-Lincoln.

References

1. V.N. Alimov, A.O. Busnyuk, M.E. Notkin, E.Y. Peredistov, A.I. Livshits, Substitutional V-Pd alloys for the membranes permeable to hydrogen: Hydrogen solubility at 150-400 °C, *Int. J. Hydrogen Energy*. 39 (2014) 19682–19690.
2. H. Jonsson, G. Mills, K.W. Jacobsen, Classical and quantum dynamics in condensed phase simulations, in: B.J. Berne, G. Ciccotti, D.F. Coker (Eds.), *Nudged Elastic Band Method Find. Minim. Energy Paths Transitions*, World Scientific Publishing, Singapore, 1998: pp. 385–404.
3. G. Henkelman, B.P. Uberuaga, H. Jónsson, A climbing image nudged elastic band method for finding saddle points and minimum energy paths, *J. Chem. Phys.* 113 (2000) 9901–9903.
4. K. Klyukin, M.G. Shelyapina, D. Fruchart, DFT calculations of hydrogen diffusion and phase transformations in magnesium, *J. Alloys Compd.* 644 (2015) 371–377.
5. O.O. Bavrina, M.G. Shelyapina, K.A. Klyukin, D. Fruchart, First-principle modelling of hydrogen site solubility and diffusion in disordered Ti-V-Cr alloys, *Int. J. Hydrogen Energy*. 43 (2018) 17338–17345.
6. E. Fromm, E. Gebhardt(Eds.), *Gase und Kohlenstoff in Metallen*, Springer, Berlin. 1976, p. 74.

Simulation and optimization of pulse RF sequences for contrast enhancement of MR images in the presence of magnetic nanoparticles

Yu. V. Bogachev, A. V. Nikitina

*Department of Physics, Saint-Petersburg Electrotechnical University "LETI",
5, prof. Popov st., Saint-Petersburg, 197376, Russia,
E-mail: nastya_nikitina1996@mail.ru*

Introduction

In recent years, there are great prospects for the use of magnetic nanoparticles (MNP) in medicine and biology. MNP can be used for diagnosis, magnetic separation, hyperthermia, drug delivery, etc. [1-3] Such large possibilities of application of these nanoparticles makes the task of optimizing the parameters of MRI studies in the presence of MNPs relevant.

Study of magnetic nanoparticles

For simulation RF sequences for MRI with MNPs, it is necessary to determine their NMR relaxation characteristics. NMR relaxation characteristics of protons in 2% agar-agar for five MNPs concentrations are given in table 3 [4].

Table 1. NMR relaxation characteristics

<i>C, mMol/L</i>	<i>T₁, ms</i>	<i>T₂, ms</i>
0.5	1260	7.13
1	828	3.96
2	488,58	1.64
4	282,21	0.9415
8	151	0.662

For the majority of the investigated MNPs, the dependence of the spin-lattice R_1 and spin-spin R_2 relaxation rates on the concentration of MNPs in water-holding model solutions was linear [4]. Found r_2 relaxation efficiency had a constant value, indicating the aggregation stability of the investigated MNPs.

For some of the studied MNPs, the dependence of the spin-spin R_2 relaxation rate on the MNPs concentration was nonlinear, their dynamic r_{2a} relaxation efficiency decreased when the MNPs concentration increased, indicating a significant aggregation of these MNPs in water-holding model solutions in the presence of the magnetic field. A method for assessing the aggregation stability of MNPs in water solutions has been developed.

There was also a difference in the values of R_1 rates of protons in different magnetic fields, that testified to the presence of frequency dispersion of the spin-lattice relaxation time, typical for heterogeneous media [5].

Optimization of RF sequence parameters on contrast

In the practical use of MNP as negative contrast agents, it is necessary to determine the optimal parameters of pulse RF sequences for different concentrations of MNP. The dependences of the MR signal intensity on the parameters of the three pulse sequences were studied and recommendations were made on the choice of the optimal values of these parameters to achieve the best contrast in the presence of the MNP.

The dependences of the MR signal intensity on the parameters a) TE and b) TR of the "Spin – echo" sequence for different concentrations of MNF (0.5 mmol/l (1), 1 mmol/l (2), 2 mmol/l (3), 4 mmol/l (4), 8 mmol/l (5) are presented on fig. 1.

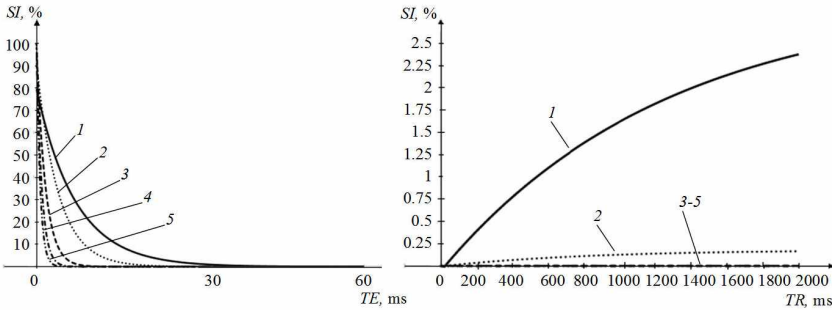


Figure 1. The dependences of the MR signal intensity on the parameters of pulse RF sequences

Recommendations for choosing the optimal values of the parameters of pulse RF sequences for MRI in the presence of an MRI are summarized in table 2.

Table 2. Optimal values of the parameters of pulse RF sequences

RF sequences	Parameter of RF sequences	Optimal values
"Spin-echo"	Echo time (TE)	> 40 ms
	Repeat time (TR)	< 1200 ms
"Inversion-recovery"	Inversion time (TI)	> 800 ms
"Gradient"	Flip angle (FA)	> 60°

Program to optimize parameters of pulse RF sequences

Based on the obtained relaxation characteristics, a program was developed to optimize the parameters of pulse RF sequences for MRI studies both in the absence of MNPs and in the presence of MNPs (the working windows of the program are shown in Fig. 1a and 1b, respectively).

This program implements three sequences: "spin echo", "inversion-recovery", and "gradient sequence". The program provides an opportunity to study graphs of the dependence of the intensity of the MR signal on the parameters of the sequence for white, gray matter and cerebrospinal fluid.

When using magnetic nanoparticles, a graph of the dependence of the MR signal intensity on the sequence parameter for five MNPs concentrations is also displayed. Also in the program window are simulated images showing the intensity of the signal on a scale of gray.

Using this program, the user can evaluate the impact of pulse sequence parameters on the contrast of MR images, choose the optimal sequence parameters and determine the necessary concentration of MNPs to improve the contrast of MR images.

The developed program of control of parameters of pulse RF sequences can be used for training of students and medical personnel too.

Results

Thus, we have analyzed the influence of the parameters of the three most commonly used in MRI pulse radio frequency sequences ("spin-echo", "inversion-recovery", "gradient") on the contrast of magnetic resonance images, as a result of which a program was developed to simulate magnetic resonance tomograms and determine the optimal values of the parameters of RF sequences to achieve the best contrast of MR images. This program has been tested in

magnetic resonance imaging studies using negative contrast agents based on magnetic nanoparticles of iron oxide. The use of this program allows to reduce the time of MRI studies, to evaluate the possibility of using MNP's for contrasting MR images.

The obtained results can be used for medical diagnostics with the use of new contrast agents based on magnetic nanoparticles in vivo and in vitro, and in the development of new methods for magnetic resonance theranostics.

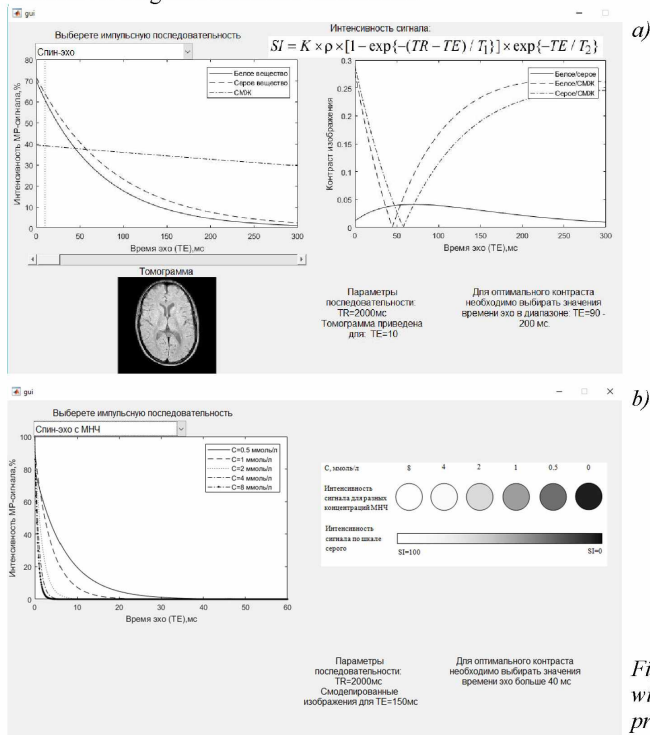


Figure 2. The working windows of the program

References

1. Jinhao Gao, Hongwey Gu, Bing Hu. Multifunctional Magnetic Nanoparticles: Design, Synthesis, and Biomedical Applications // Accounts of chemical research, 2009, vol.42, No.8, pp.1097-1107.
2. Shao H., C Min, Issadore D., Min C., Liong M., Chung J., Weissleder R., Lee H. Magnetic Nanoparticles and microNMR for Diagnostic Applications. // Theranostics. – 2012. - Vol. 2(1). – P. 55-65.
3. R.Thomas, In-Kyu Park, Yong Yeon Jeong. Magnetic Iron Oxide Nanoparticles for Multimodal Imaging and Therapy of Cancer. // Int.J.Mol.Sci. 2013, vol.14, pp.15910-15930.
4. Bogachev Y.V., Nikitina A.V., et al. NMR Relaxation Efficiency of Aqueous Solutions of Composite $Mg_xZn_yFe_{3-x-y}O_4$ Nanoparticles // Applied Magnetic Resonance, 2017. V. 48. I. 7. P.715–722.
5. Chizhik V.I., Chernyshev Yu.S., Donets A.V., et al.: Magnetic Resonance and Its Appli-cations. Switzerland: Springer International Publishing, 2014, 785 p.

EPR study of copper complexes in mordenite channels

*Dmitrii Bogdanov¹, Stanislav Sukharzhevskii¹, Marina Shelyapina¹, Yurii Zhukov¹,
Inocente Rodriguez-Iznaga², Vitalii Petranovskii³*

¹*Saint Petersburg State University, 7/9 Universitetskaya nab., St. Petersburg, Russia 199034*

²*Instituto de Ciencias y Tecnología de Materiales (IMRE) – Universidad de La Habana, Zapata y G, s/n La Habana 10400, Cuba*

³*CNyN, Universidad Nacional Autónoma de México, Ensenada 22860, Baja California, México*

E-mail: d.bogdanov@spbu.ru

Copper-exchanged zeolites are promising heterogeneous catalysts for the decomposition of nitrogen oxides (de-NO_x catalysts), the selective hydroxylation of methane to methanol and other industrial processes [1]. These catalytic properties are governed by both content of copper, which can be localized in various positions in the lattice with different local symmetry, and its valence state. At the current time a large quantity of studies of location and coordination of copper cations in zeolites has been performed. However, often these studies used only low copper content samples, despite the fact that mainly high content zeolites exhibit the best catalytic results.

Among other copper-exchanged zeolites, mordenites demonstrate one of the highest catalytic activity [2], which is strongly affected by various factors, including preparation method. It has been found that microwave assisted ion exchange from sodium form results to an over-exchange [3]

The aim of the current work is to study by applying the electronic paramagnetic resonance (EPR) location of Cu²⁺ cations and their coordination in the high copper containing mordenite samples, prepared by conventional and microwave assisted methods (for more details on the preparation method see Ref. [4]).

Copper-exchanged zeolites were prepared from NH₄⁺- and H⁺-mordenites with nominal Si/Al atomic ratios (AR) equal to 10. The NH₄⁺-mordenite was supplied by Zeolist Int. (Product CBV21A). The proton form was obtained by the calcination of NH₄⁺ mordenite at 300 °C for 2 hours. The calcination temperature has been chosen in accordance with thermogravimetric analysis of the NH₄⁺ mordenite: the temperature at which the deammoniation process has been already finished but the dehydroxylation has not been started yet. The structural and elemental analysis proved that (I) the mordenite framework is kept untouched; (II) the applied ion exchange processes do not lead to an over-exchange, being the level of copper exchange limited to 70%; however, (III) the microwave assisted treatment resulted to a systematically higher copper exchange level.

EPR spectroscopy is a powerful tool for detecting presence of Cu²⁺ ions in the sample and identifying nearest environment and the local symmetry of paramagnetic ions. EPR spectra were acquired with Bruker EleXsys E580 EPR spectrometer (X-band) in the field interval 0-10000 G with microwave power of 1.5 mW, a modulation amplitude of 5.0 G, a modulation frequency of 100 kHz. The spectra were collected at 300 K from the fully hydrated and partially dehydrated samples. To dehydrate the sample, it was heated up to 473 K and 673 K in the same tube under permanent pumping out. The spectra were simulated as a randomly oriented powder using the program EasySpin 5.1.9 as implemented in MATLAB R2016b.

According to our EPR study there are at least two different paramagnetic centers of Cu²⁺ that can be attributed to [Cu(H₂O)_n]²⁺ complexes. Upon the sample dehydration one observe the general decrease of EPR signal intensity that can be explained as follows: Cu²⁺ ions from [Cu(H₂O)_n]²⁺ species loosing water approach to the wall of zeolite channel and form virtual bonds with charge transfer from framework oxygens to Cu²⁺. This charge transfer process is

reversible and rehydration of the sample leads to the recovering of Cu^{2+} ions coordination, similar as found in copper-exchanged mordenites obtained from the sodium form [5].

Acknowledgements

The structural, elemental and EPR analyses were carried out at the Research Park of Saint Petersburg State University: Centre for X-ray Diffraction Studies, Interdisciplinary Resource Centre for Nanotechnology, Centre for Physical Methods of Surface Investigation, and Centre for Magnetic Resonance. This work was supported by RFBR and CITMA according to the research project No 18-53-34004.

References

1. P. Vanelderen, J. Vancauwenbergh, B.F. Sels, R.A. Schoonheydt, Coordination chemistry and reactivity of copper in zeolites, *Coord. Chem. Rev.* 257 (2013) 483–494.
2. E. M. Alayon, M. Nachtegaal, M. Ranocchiari, J. A. van Bokhoven, *Chem. Commun.* 2012, 48, 404
3. Y.M. Zhukov, M.G. Shelyapina, I.A. Zvereva, A.Y. Efimov, V. Petranovskii, Microwave assisted versus convention Cu^{2+} exchange in mordenite, *Microporous Mesoporous Mater.* 259 (2018) 220–228.
4. Y.M. Zhukov, A.Y. Efimov, M.G. Shelyapina, V. Petranovskii, E. V. Zhizhin, A. Burovikhina, I.A. Zvereva, Effect of preparation method on the valence state and encirclement of copper exchange ions in mordenites, *Microporous Mesoporous Mater.* 224 (2016) 415–419.
5. M.G. Shelyapina, I.A. Zvereva, L. V. Yafarova, D.S. Bogdanov, S.M. Sukharzhevskii, Y.M. Zhukov, V. Petranovskii, Thermal analysis and EPR study of copper species in mordenites prepared by conventional and microwave-assisted methods, *J. Therm. Anal. Calorim.* 134 (2018) 71–79.

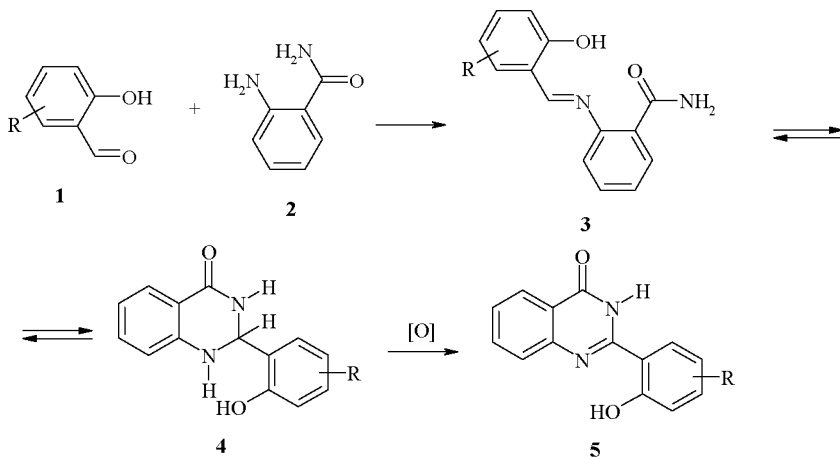
Multinuclear NMR investigation of structure of coupling products of salicylaldehydes and 2-aminobenzamid

*Ima G. Borodkina, Gemadii S. Borodkin, Igor S. Vasilchenko,
Pavel B. Chepurnoy, Natalya V. Stankevich*

*Institute of Physical and Organic Chemistry, Southern Federal University, Stachki pr. 194/2,
344090 Rostov-on-Don, Russian Federation,
E-mail: nmr@ipoc.sfedu.ru*

Introduction

Quinazolinones are important objects of chemistry, medicine and technology. They use as agrochemical and veterinary germicides, as luminescent, pharmacological agents and chemosensors.



Scheme 1

Simplest and most effective method of their obtainment is interaction of carbonyl compounds (for example, salicylaldehydes (1)) and 2-aminobenzamide (2) with subsequent oxydizing of forming dihydroquinazolinone (4) *in situ* (Scheme 1) by different agents. We have investigated peculiarities of these reaction and structure of obtained compounds by IR, multinuclear (^1H , ^{13}C , ^{15}N) 2D NMR (DMSO- d_6 , CDCl_3) spectroscopy and quantum-chemical calculations.

Structure of obtained compounds

IR spectrum of (3: R = 3-OMe) demonstrates absorption bands set of C=N, C=O, NH_2 (two bands), and OH groups that corresponds to the structure 3. At the same time NMR ^1H spectrum in DMSO- d_6 shows two signals of protons of NH_2 group at 7.47 and 7.84 ppm.

It may be explained by unsymmetry of amide group in (3: R = 3-OMe) with formation of two 5- and 6-membered H-cycles that has been confirmed by results of quantum-chemical calculations DFT/B3LYP/6-311++G(d,p) – Fig. 1, 2.

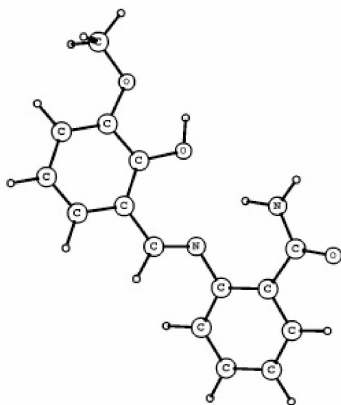


Figure 1. Structure of (**3**: R = 3-OMe) with unsymmetrical amide group ($\Delta E = 1.6$ KCal/Mol)

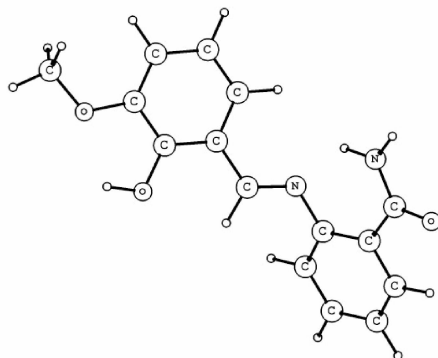


Figure 2. Optimal structure of (**3**: R = 3-OMe) ($E = 0.0$ KCal/Mol)

IR and NMR ^1H spectra of (**3**: R = 5-OMe) resembling to the ones of (**3**: R = 3-OMe), that allows attribute the same structure without formation of five-membered H-cycle.

IR spectrum of (**3**: R = H) demonstrates the same set of bands excluding one at $1600\text{--}1630\text{ cm}^{-1}$. NMR ^1H spectrum of this compound in $\text{DMSO-}d_6$ also differs by the absence of $\text{HC}=\text{N}$ proton signal but shows triplet signal around 6 ppm. NH protons also presented by two peaks. Spectrum NMR ^1H COSY shows three connected signals (Fig. 3) supporting the structure 4 for this aldimine that confirms by results of quantum-chemical calculations.

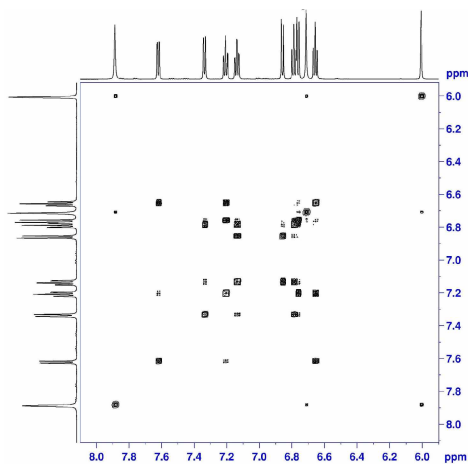


Figure 3. Spectrum NMR ^1H COSY of (**3**: R = H)

Spectrum NMR ^1H of solution of (**3**: R = 5-F) in DMSO- d_6 is more complex showing the mixture of two forms – acyclic and cyclic (2:1). Under heating to 90 °C we registered only one cyclic form. Spectrum NMR ^1H of solution of this compound in CDCl_3 demonstrates another picture – at 30 °C it corresponds to cyclic form but after keeping for one day it shows presence of two forms – cyclic and acyclic ones.

IR and NMR data revealed that product (**3**: R = 5- NO_2) exists in cyclic form **4** both in the solid state and solution.

Using organic acids as solvents in the reactions showing in the Scheme 1 under heating in the presence of air leads to the formation of quinazolones **5**.

2D ^1H - ^{15}N NMR spectra in DMSO- d_6 and CDCl_3 support above inferences on the structure of investigated compounds.

Conclusion

So, we have found that products of salicylaldehydes and 2-aminobenzamide coupling possess aldimine or aldimine/dihydroquinazilone structure for compounds with electron donor substituents in the aldehyde ring and dihydroquinazilone structure for neutral and electron acceptor ones.

Acknowledgements

This work is supported by grant of RF Ministry of education and science (project No 4.5821.2017/8.9).

Computer Simulations of PEDOT:PSS/solid interface

Armando Consiglio¹, Andrei V. Komolkin², Tobias Cramer¹

¹*Department of Physics and Astronomy, Alma Mater Studiorum – Bologna University*

²*Department of Nuclear Physics Research Methods, V. A. Fock Institute of Physics, Saint-Petersburg State University*

E-mail: armconsiglio@gmail.com

Introduction

Among the conducting polymers, poly(3,4-ethylenedioxythiophene):poly(styrene sulfonate) (PEDOT:PSS) is one of the most used materials in the field of bioelectronics [1] due to its biocompatibility, chemical stability and high electronic as well as ionic charge transport mobilities [2].

Despite many experimental findings a microscopic understanding of the materials electronic properties is currently elusive. Main reason is the lack of structural atomistic data of the polymer blend, that is difficult to obtain because of the disordered and nano-crystalline morphology [3].

In this work we develop and use Molecular Dynamics based methods to simulate the structure of PEDOT:PSS in presence of an interface, pointing out the differences between interfacial and bulk behavior.

The results obtained by computer simulations can be used to estimate experimentally accessible parameters and to compare them with already existing experimental data.

Current Results

Our simulations are performed in a box of $\sim 100 \times 100 \times 100 \text{ \AA}^3$ in which we considered 180 PEDOT monomers and 360 PSS monomers, together with 29000 water molecules and 360 Na⁺ counterions.

Each PEDOT oligomers is composed by 6 monomers, while each PSS polymer is composed by 12 monomers.

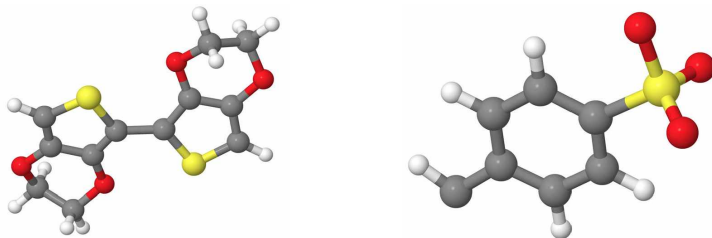


Figure 1. On the left is showed a dimer of PEDOT, while on the right a monomer of PSS, both created with JMOL software. Gray spheres represent carbon atoms, red spheres represent oxygen atoms, yellow spheres represent sulfur atoms and white sphere represent hydrogen atoms

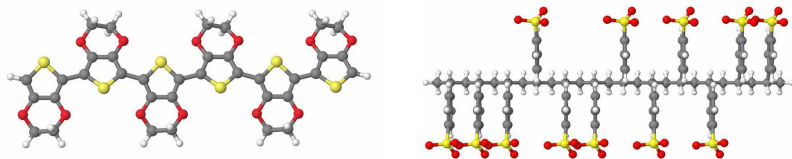


Figure 2. On the left is showed an oligomer of PEDOT, while on the right a polymer of PSS, both created with JMOL software. Note the atacticity of the PSS polymer

Because of the very high amount of water content, the density of the system is $\sim 1 \text{ g/cm}^3$. The first calculations are performed in a NpT ensemble at $T = 298\text{K}$.

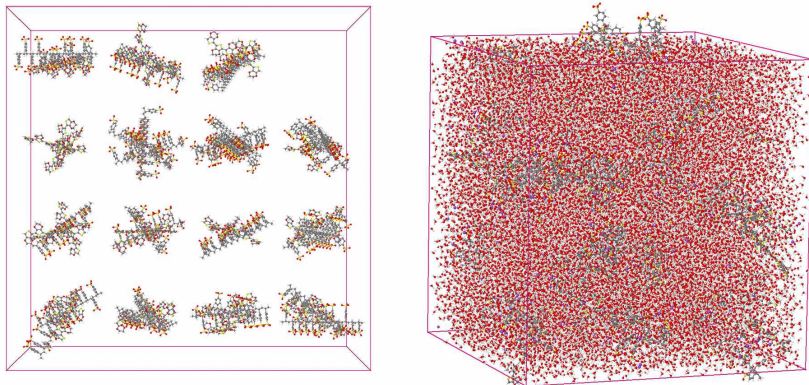


Figure 3. On the left is showed the initial configuration of PEDOT and PSS in the cell box, while on the right the same system after some nanoseconds of calculations, together with water molecules

During our simulation we see that Na^+ counterions are getting closer to SO_3 group of PSS.

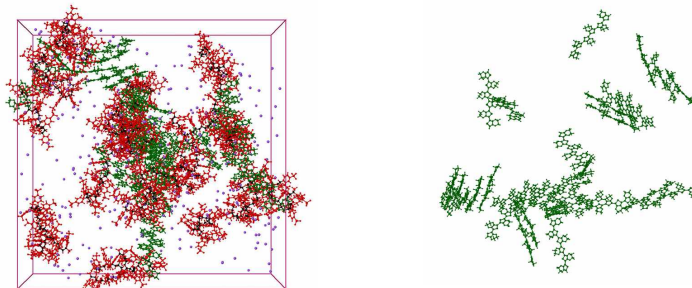


Figure 4. On the left is showed the configuration of PEDOT:PSS after some calculations (PSS in red, backbone of PSS in black and PEDOT in green), without showing water molecules. On the right is showed only the lamellar structure of PEDOT

PEDOT oligomers are getting closer to PSS polymers while PEDOT oligomers are ordering in lamellar structures, with about 3.5 Å spacing between the different pi-orbital planes, as observed in XRD patterns.

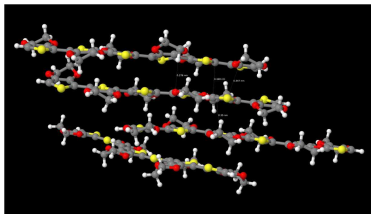


Figure 5. Zoom on the lamellar structure of PEDOT oligomers, after some nanosecond of simulation

Here are reported our data about diffusion coefficient and mean squared displacement. Note how the heaviest molecules are those of PSS, and the lightest one those of water.

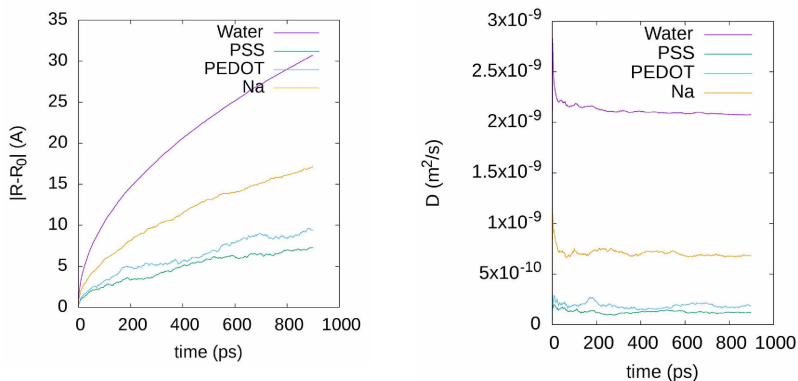


Figure 6. Mean squared displacement on the left and diffusion coefficient on the right

Acknowledgements

Research was carried out using computational resources provided by Resource Center "Computer Center of SPbU" (<http://cc.spbu.ru>).

References

1. J. Rivnay, R. M. Owens, G. G. Malliaras // J. Chem. Mater. 26, 679-685 (2014).
2. D. T. Simon, E. O. Gabrielsson, K. Tybrandt, M. Berggren // Chem. Rev. 116, 13009-13041 (2016).
3. A. V. Volkov et al. // Adv. Funct. Mater. 27, 1-10 (2017).

Behavior of cyclosporine C in solvents of different polarity

S. Darwish, S. V. Efimov, A. A. Balandina, V. V. Klochkov

Institute of Physics, Kazan Federal University, Kazan, 420008 Russia

E-mail: shazadarwish1994@hotmail.com

Introduction

Discovery of cyclosporine in 1971 began a new era in immunopharmacology. It was the first immunosuppressive drug that allowed selective immunoregulation of T cells without excessive toxicity. Cyclosporine was isolated from the fungus *Tolypocladium inflatum* Gams [1] and other fungi imperfecti or via directed biosynthesis or total chemical synthesis.

As early as in 1978, the immunosuppressive action of cyclosporine A was reported to be effective in preventing organ rejections and in the treatment of graft-versus-host diseases. Cyclosporine A is now widely approved for restraining rejection following solid organ transplantations (especially heart, lung and kidney), and preventing and treating graft-versus-host disease after bone marrow transplants. It has also been used in the treatment of numerous autoimmune diseases. However, many additional biological actions of CsA have been reported, including anti-inflammatory, anti-parasitic (anti-malaria), antifungal and antiviral (anti-HIV) action. The drug suppresses T-cell-dependent immune reactions as it inhibits lymphocyte activation by blocking the transcription of cytokine genes for interleukins, in particular IL-4 and IL-2. Developing an efficient oral delivery system for this drug is complicated by its poor biopharmaceutical characteristics (low solubility and permeability) and the need to carefully monitor its levels in the blood [2].

Object

CsA is a hydrophobic peptide with a unique structure consisting of 11 amino acid residues, seven of which are N-methylated (Fig. 1, left panel). The extensive methylation and hydrophobic character of the amino acid residues together with their four intra-molecular hydrogen bonds, which confer a high rigidity to the cyclic structure, mean the drug has a very low aqueous solubility. It has a molecular weight of 1202.6 Da and its molecular formula is $C_{62}H_{111}N_{11}O_{12}$.

There are many natural variants of cyclosporine, for example A, B, C, D, etc. Cyclosporin C is one of them and differs from CsA by the alternation of the second residue. Substitution of threonine for the aminobutyric acid (Abu2) residue yields cyclosporin C (CsC) (Fig. 1, right panel), one of congeners which still has some immunosuppressive activity, though weaker than that of CsA.

Method

Experiments were conducted on a Bruker Avance 500 and Avance HD 700 NMR spectrometers. The samples were prepared at a concentration of ~1 mM in dimethylformamide (DMF). Several one-dimensional experiments were carried out at varying temperatures ranging from 14° to 40°C. Two-dimensional ROESY spectra were also obtained to visualize the pattern of chemical exchange.

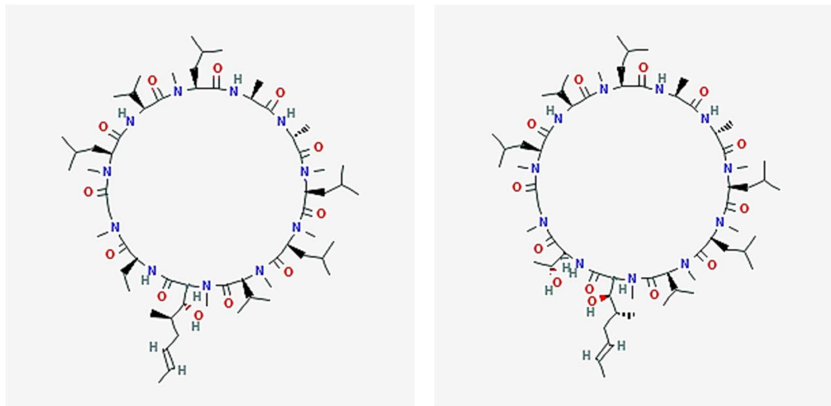


Figure 1. Chemical structures of cyclosporine A (left) and C (right)

Results

So as noticed in the range (4–6 ppm) of ^1H NMR spectra (Fig. 2), there are some weak signals overlapping with the major ones. This spectral region contains signals of the backbone H_α protons, and it is obvious that the number of signals exceeds the number of residues in the cyclosporine chain. Hence, a slow on the NMR time scale chemical exchange occurs when CsC is dissolved in DMF, which is expected in polar media [3].

CsC ^1H , 700 MHz, 25°C

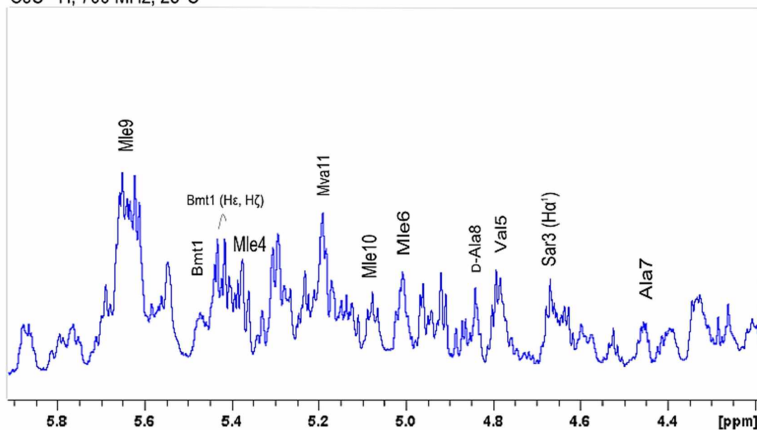


Figure 2. Part of ^1H NMR spectrum of CsC in DMF

To observe the exchange peaks, it was required to do a 2D measurement. The method of exchange spectroscopy gives spectra containing cross-peaks due to slow chemical exchange and nuclear Overhauser effect (Fig. 3). In our case they can be distinguished by the signal phase: NOE peaks are opposite in sign to the diagonal peaks (“negative”), while exchange peaks have the same phase.

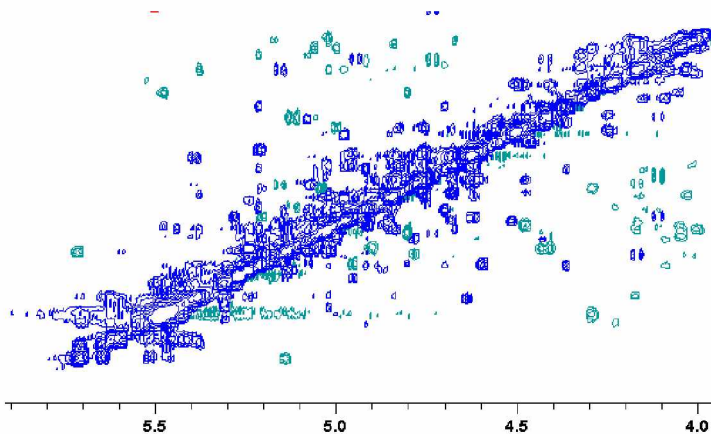


Figure 3. Part of 2D EXSY (ROESY) spectrum of CsC in DMF obtained at 700 MHz, 25°C, with the mixing time of 360 ms

It is evident from Fig. 3, that H α protons in different observed conformers have chemical shifts which differ by up to 1 ppm. Multiple NOE cross-peaks are also observed, which are untypical for this spectral range. They correspond to cases when two H α protons come close to each other in space (by a distance <5 Å), which indicates that the peptide bond between corresponding residues adopts the *cis*-conformation (angle $\omega = 0^\circ$).

Acknowledgements

This work is supported by the Institute of Physics at Kazan Federal University. I would like to express my sincere thanks to PhD S.V. Efimov for his time and efforts.

References

1. The cyclosporine story. – http://www.davidmoore.org.uk/Sec04_01.htm
2. A. Czogalla-cellular & molecular biology letters, volume, 14 (2009) pp 139-152.
3. S. Y. Ko, C. Dalvit. – *Int. J. Peptide Protein Res.*, **662**, 380-382 (1992).

Free colours tetrapyrroles: yellow

Nina Djapic

University of Novi Sad, Technical Faculty "Mihajlo Pupin", Zrenjanin, Serbia

E-mail: nidjapic@gmail.com

Introduction

Tetrapyrrole proton spectra are images where differences between them are to be found. Proton spectra can be merged into one and the differences can be visually noticed. In spot the difference puzzles the solution to the puzzle is printed nearby or at the end of the puzzle book.

Tetrapyrrole proton spectra

Tetrapyrrole proton spectra, in the low field, have vinyl group spin-system (Fig. 1, 2). After vinyl proton signals are assigned, the assignment can continue counterclockwise, since the neighboring groups in the molecule are within the distance less than 5Å. Tetrapyrroles contain chiral carbon atoms and isomers have differences in proton spectra that can be noticed.

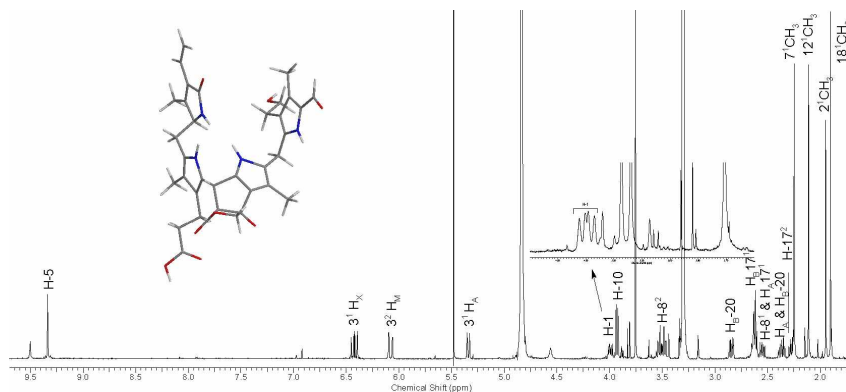


Figure 1. Tetrapyrrole proton spectrum

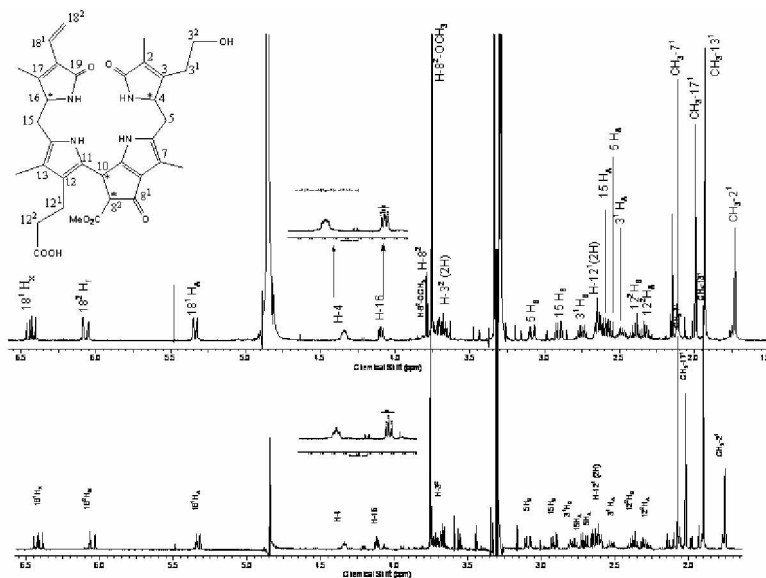


Figure 2. Tetrapyrrole isomers proton spectra

Previous tetrapyrrole molecules are in accordance with the sentence: “The world is chiral and clinal, enjoy the symmetry wherever you find it” [1].

The puzzle game can continue with adopting the bilirubin within chiral molecules.

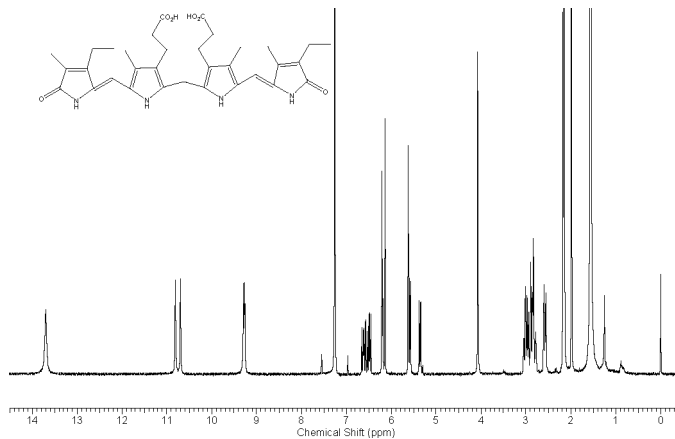


Figure 3. Bilirubin proton spectrum

References

1. E. Heilbronner, J. D. Dunitz. Reflections on symmetry: In Chemistry ... and Elsewhere. – VCH Verlagsgesellschaft mbH, Weinheim, 1993.

Development and study of novel pervaporation membranes based on polyphenylene isophthalamide, modified by Pluronic F127

Mariia E. Dmitrenko, Ramadan R. Atta, Anastasia V. Penkova

*Institute of Chemistry, St. Petersburg State University, 7/9 Universitetskaya nab.,
St. Petersburg, 199034, Russia
E-mail: m.dmitrienko@spbu.ru*

Introduction

Currently, membrane technologies are popular and widely applied in many areas of science and technology due to its characteristics. Among membrane methods, the most promising and evolving process is pervaporation that is environmentally friendly, not energy-intensive and does not require large material costs. The rapid development of pervaporation determines the relevance and the need the creation of highly efficient membranes with improved physicochemical and transport properties. One of the simplest methods to modify polymeric membranes is a bulk modification by combining two or more polymers in different concentration ratios that are fully compatible. This blending of polymers is used to impart desirable properties to the membrane. In this work, one of the most important and widespread aromatic polyamides polyphenylene isophthalamide (PA) was selected as the polymer for the preparation of dense membranes due to its physicochemical properties (high thermal stability, high resistance to organic solvents and rigid structure). Block copolymer of polyethylene glycol and polypropylene glycol (Pluronic F127) was chosen as polymer additive for the bulk modification of PA due to its amphiphilic nature.

The aims was to create and study of new highly efficient pervaporation membranes based on the polyphenylene isophthalamide modified by Pluronic F127 with improved physicochemical and transport properties for highly efficient resource-saving separation of organic mixtures by pervaporation. The structural characteristics and physicochemical properties of the prepared composites were studied by various methods of analysis (IR spectroscopy, scanning electron microscopy (SEM), measurement of the contact angle and sorption experiments). The transport properties of the obtained dense membranes were examined by pervaporation for the separation of industrially significant mixture of methanol-toluene. It was shown that the modification of PA with Pluronic F127 led to the significant changes of structure and physicochemical properties of the polymeric membranes caused the increase of membrane productivity for pervaporation separation.

Acknowledgements

This work was supported by a grant from the Government of St. Petersburg. The experimental work was facilitated by equipment from Resource Centers: Research Centre for Nanotechnology, Research Centre for X-ray Diffraction, Research Centre for Physical Methods Surface Investigation, Magnetic Resonance Research Centre, Thermal Analysis and Calorimetry, Chemical Analysis and Materials Research Centre and GEOMODEL at St. Petersburg State University.

Two-quantum optically detected resonances in NV centers in diamond in zero magnetic field

Alexander K. Dmitriev, Anton K. Vershovskii

*Ioffe Institute, 26 Politekhnikeskaya, St. Petersburg 194021 Russia
E-mail: alexdmk777@gmail.com*

Introduction

The methods for controlling spin states of negatively charged nitrogen-vacancy centers using a combination of microwave (MW) or radiofrequency (RF) excitation field [1,2] for electron spin transitions and RF excitation field for nuclear spin transitions are most effective in strong magnetic fields where level anti-crossing (LAC) occurs [3]. However, LAC in zero field can also be used to control spin states, as well as to excite narrow resonances for metrological application. Here we present magnetically independent resonances arising in the ODMR spectra of NV centers in bulk diamond under two-frequency (MW+RF) resonant excitation in zero magnetic field, and discuss their specificity.

Energy structure of the ground-state of NV center

The level structure of 3A_2 ground state in external magnetic field \vec{B} is defined by the Hamiltonian [4]:

$$H = D(S_z^2 - \frac{1}{3}\vec{S}^2) + E(S_x^2 - S_y^2) + g_s \mu_B \vec{B} \cdot \vec{S} + A_{\parallel} S_z I_z + A_{\perp} (S_x I_x + S_y I_y) + P I_z^2 - g_I \mu_N \vec{B} \cdot \vec{I}, \quad (1)$$

where $\mu_B = h \cdot 13.996 \cdot 10^9$ Hz/T is the Bohr magneton, \vec{I} is the ${}^{14}\text{N}$ nuclear ($I = 1$), \vec{S} is the electron spin of NV center ($S = 1$), $\mu_N = h \cdot 7.622 \cdot 10^6$ Hz/T is the nuclear magneton, $D = 2.87$ GHz and E are axial and transverse zero-field splitting (ZFS) parameters, $g_s = 2.003$ and $g_I = 0.403$ are electron and nuclear g-factors, $A_{\parallel} = -2.16$ MHz and $A_{\perp} = -2.7$ MHz are axial and transverse hyperfine splitting parameters, $P = 4.95$ MHz is the quadrupole splitting parameter. Denote eigenstates of the ground state $|m_s, m_I\rangle$; for the nitrogen isotope ${}^{14}\text{N}$ both electronic and nuclear spin projections take values $m_s, m_I = 0, \pm 1$.

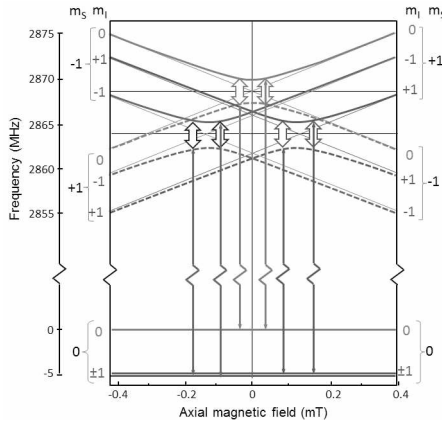


Figure 1. NV center ground-state splitting frequencies' dependence on axial local magnetic field, calculated for a diamond crystal with transverse ZFS parameter $E = 1.8$ MHz. Single arrows represent the MW drive field, double arrows represent the RF drive field

The energy structure of NV center in zero and ultra-weak fields is more complex than in strong ones (Fig.1); it contains both level crossings and anti-crossings, partially masked by the inhomogeneity of the crystal's internal fields. Therefore, pure energy states $|m_s, m_l\rangle$ at $B \approx 0$ mix in superpositions.

Experiment and discussion

The experimental setup was described in [5]: a synthetic diamond of SDB1085 60/70 grade (manufactured by Element Six) with dimensions $0.1 \times 0.3 \times 0.3$ mm was subjected to electron irradiation ($5 \cdot 10^{18}$ cm $^{-2}$) and subsequent annealing in Ar at 800°C over 2 hours. The crystal was used at room temperature; it was attached by optically transparent glue to the end of an optical fiber.

We excited two-frequency ODMR in $B = (0 \div 1)$ mT using MW drive field f_{MW} in combination with additional RF field f_{RF} . This way we have recorded two symmetrical hollows in ODMR spectrum (Fig.2, 3), arising under conditions

$$f_{MW} \pm \frac{1}{2}f_{RF} = D, \quad (2)$$

$$\begin{aligned} \nu_0 - \Delta < 2|f_{MW} - D| < \nu_0 + \Delta, \text{ or} \\ \nu_0 - \Delta < f_{RF} < \nu_0 + \Delta, \end{aligned} \quad (3)$$

where $\nu_0 = (4.34 \pm 0.02)$ MHz is the center of the resonance envelope in RF scale, and $\Delta = (2.14 \pm 0.04)$ MHz is the half-width of the envelope. We have observed similar resonances previously, while applying low-frequency amplitude modulation to the MW field [6]; this time we applied the same modulation to the RF field, which caused at least a two-fold increase in the contrast of the resonances, and changed their shape.

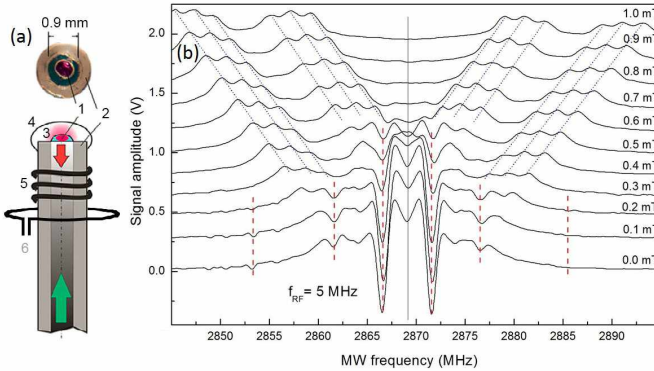


Figure 2. (a) View of the fiber end, and a schematic diagram of magnetometer sensor: 1 - diamond crystal, 2 - optical fiber, 3 - transparent glue, 4 - reflective coating, 5 - MW antenna, 6 - RF antenna. (b) ODMR spectra recorded at external field $B = (0 \div 1)$ mT along $(1,1,1)$ direction with additional RF excitation at $f_{RF} = 5$ MHz

At the optimal (i.e. providing the maximal resonance steepness) values of MW and RF amplitudes, the linewidth (HWHM) of the resonances was found to be about 1.1 MHz. The amplitude of the peaks is maximal at zero magnetic field, and it decreases quickly as the field induction decreases (Fig. 2). Moreover, the frequencies of both resonances proved to be insensitive to B . On the other hand, the fact that according to (2) the combination of resonant MW and RF frequencies depends only on D makes these peaks very attractive for the task of frequency stabilization.

Conditions of resonance observation are typical for a two-quantum resonance, represented by vertical arrows on Fig. 1 (single arrows represent the MW drive field, double arrows represent the RF drive field); a variety of similar multi-frequency resonances arising due to excited state LAC in a strong (51 mT) field have been studied in [3]. However, the resonances discovered in zero field in our work show some peculiarities: they appear as dips in the “normal” one-quantum ODMR signal. Therefore, their nature must be similar to the “dark” resonances due to the coherent population trapping effect (CPT) in Λ -schemes [7].

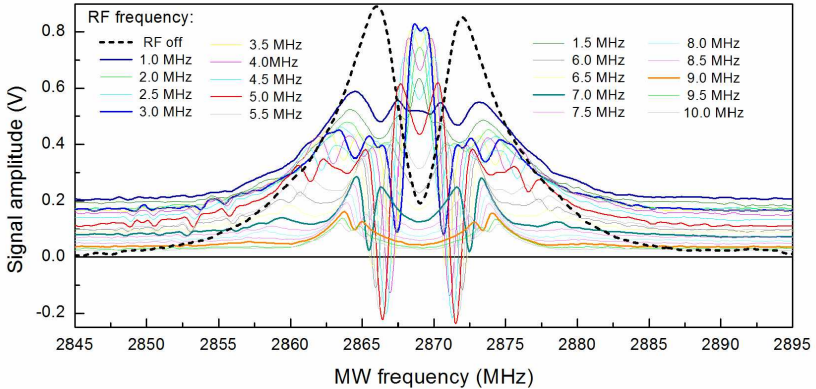


Figure 3. ODMR spectra recorded at zero external field at different radiofrequencies f_{RF} : lowest curve is normal ODMR signal, two symmetrical hollows are two-quantum resonances arising when conditions (2), (3) are fulfilled

Conclusion

We report the detection of high-contrast magnetically independent two-quantum resonances in zero-field ODMR spectra of NV center in diamond, induced by applying an additional modulated RF field. These resonances can only be driven at $|B| < 0.5$ mT (in the case of our diamond sample), and therefore we can assert that they are due to the zero-field level anti-crossing. We attribute them to certain transitions in NV center’s zero-field structure.

References

1. M. V. Gurudev Dutt, L. Childress, L. Jiang, E. Togan, J. Maze, F. Jelezko, A. S. Zibrov, P. R. Hemmer, and M. D. Lukin. – *Science*, **316**, 1312 (2007).
2. N. B. Manson, L. J. Rogers, E. A. Wilson, and C. Wei. – *Journal of Luminescence*, **130**, 1659 (2010).
3. L. Childress and J. McIntyre. – *Phys. Rev. A*, **82**, 033839 (2010).
4. S. Felton, A. M. Edmonds, M. E. Newton, P. M. Martineau, D. Fisher, D. J. Twitchen, and J. M. Baker. – *Phys. Rev. B*, **79**, 075203 (2009).
5. A. K. Dmitriev and A. K. Vershovskii. – *JOSA B*, **33**, B1 (2016).
6. A. K. Dmitriev and A. K. Vershovskii. – *Journal of Physics: Conference Series*, **1135**, 012051 (2018).
7. E. Arimondo and G. Orriols. – *Lett. Nuovo Cimento Soc. Ital. Fis.*, **17**, 33 (1976).

MRI study of magnetic field distortions generated by cellulose microbeads labelled with iron oxide nanoparticles in phantom samples

Aleksandra A. Efimova¹, Anton S. Mazur², Lyudmila Y. Yakovleva³, Peter M. Tolstoy⁴

¹*Faculty of Physics, St. Petersburg State University, Russian Federation*

²*Center for Magnetic Resonance of Saint Petersburg State University Research Park, Russian Federation*

³*State Research Institute of Highly Pure Biopreparations, Russian Federation*

⁴*Institute of Chemistry, St. Petersburg State University, Russian Federation*

E-mail: sashaefimova15@yandex.ru

Introduction

Magnetic resonance imaging (MRI) is non-invasive diagnostic method, which provides image contrast depending on differences in nuclear magnetic relaxation characteristics of tissues. This method has found wide application in medical and clinical fields [1]. For successful MRI diagnosis, among several available classes of contrast agents, superparamagnetic substances are often used, producing significant improvement of signal intensity [2]. Superparamagnetic nanoparticles can offer a high potential for some kinds of biomedical applications, such as tissue repair, cellular therapy, drug delivery, etc. Such nanoparticles provide the shortening of the transverse relaxation time and, thus, are used as negative agents for T2-weighted imaging. Polymer-based magnetic spheres are convenient for therapy, magnetic drug targeting and cell labelling. Therefore, development of such substances is of particular interest.

In this work, we choose cellulose microbeads (CM), which are about 1 mm in diameter, loaded with superparamagnetic iron oxide nanoparticles (SPIONs) as a contrast agent. It is proposed that CM/SPIONs systems may act as a good model for MR study of mesenchymal stem cells [3].

The main goal of this work is to study the influence of such systems on the contrast enhancement of surrounding water molecules in MRI images.

Methods

Cellulose microbeads were created by emulsification condensation of cellulose solution in oil. The SPIONs were prepared by co-precipitation of iron salts $\text{Fe}^{2+}/\text{Fe}^{3+}$ in alkaline media at 80 °C. Magnetic microspheres (CM/SPIONs) were formed by addition of Fe_3O_4 nanoparticles into the pores of cellulose microspheres.

Six phantom samples (1 – with pure cellulose microbeads, 2–6 – with CM/SPIONs systems) in agarose matrix were prepared in 20 mm glass tubes. Each sample contain only one cellulose microsphere. Samples from 2 to 6 are equal to evaluate changes in the MR images caused by the distribution of magnetic dipole moments of CM/SPIONs systems. MR images were collected using Bruker Avance III 400 WB spectrometer with *FLASH* (fast low angle shot) and *MGE-T2star_map* (multiple gradient echo) pulse sequences. Images were taken in frontal plane aligned with the magnetic field.

Results

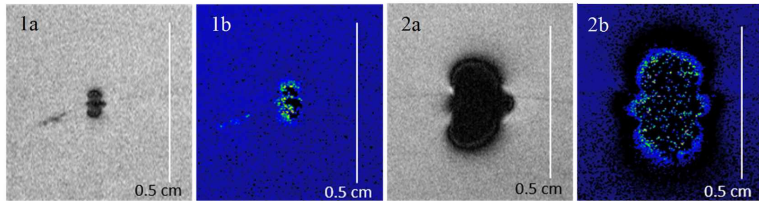


Figure 1. FLASH images (a) and T_2 maps (b) of samples 1 and 2 respectively

Conclusions

- The MR images of the phantom samples establish the contrast efficiency of investigated CM/SPIOs systems and show that these systems behave like a single magnetic dipole ($\vec{B} = 3 \frac{(\vec{m}, \vec{r})\vec{r}}{r^5} - \frac{\vec{m}}{r^3}$).
- Obtained T_2 maps demonstrate the capability of magnetic microbeads to serve as a good negative contrast agent.

Acknowledgments

We are grateful to Nikolaev B.P., Yakovleva L.Y., Marchenko Y. Yu. from the State Research Institute of Highly Pure Biopreparations for preparation of magnetic dispersions and cellulose microspheres, Mazur A.S. for help in conducting the MRI experiments. MRI measurements were performed at Center for Magnetic Resonance of Saint Petersburg State University Research Park. This work was supported by RFBR Grant 19-08-00024.

References

1. Nacher, P.-J., *The Spin: Poincare Seminar 2007*, **2009**, 55, 159–193
2. Gossuin, Y., Gillis, P., Hocq, A., Vuong, Q.L., Roch, A., *Wiley Interdiscip. Rev.: Nanomed. Nanobiotechnol*, **2009**, 1, 299–310
3. Nkansah, M.K., Thakral, D., Shapiro, E.M., *Magn Reson Med*, **2011**, 65, 1776–1785

Fluctuations of local electric fields at Li^+ , Cl^- , and NO_3^- ions in aqueous solution studied by Car-Parrinello molecular dynamics simulations

Maria I. Egorova, Andrei V. Egorov, Vladimir I. Chizhik

Faculty of Physics, Saint-Petersburg State University, Ulianovskaya 1, 198504, Saint-Petersburg, Russia

E-mail: maryaverina@gmail.com

Nuclear quadrupolar relaxation (this relaxation mechanism is dominant for the most of nuclei) is an important tool to explore the structural and dynamic properties of liquid systems. However, the unambiguous interpretation of experimental data is a complicated task. The source of relaxation is the fluctuations of the electric field gradient (EFG) at the site of quadrupolar nucleus. Extracting any microscopic information from relaxation experiments requires a model describing the molecular origin of such fluctuations. In this case, the computer simulations is a promising tool to address the problem [1, 2]. In our work Car-Parrinello molecular dynamics (CPMD) simulations [3] were carried out to investigate the fluctuations of local electric fields at monatomic (Li^+ and Cl^-) and polyatomic (NO_3^-) ions in aqueous solutions. The essence of CPMD approach consists in the fact that the forces which act on atoms are determined from first principles quantum chemistry methods. Thus, there is no need for any model describing the molecular interactions.

In the present study the components of the EFG tensor on quadrupolar nuclei were calculated from simulation data. The tensor was diagonalized and given in terms of three principal components – V_{xx} , V_{yy} , and V_{zz} . The distributions of V_{zz} values for monoatomic lithium ion and nitrogen atom of polyatomic nitrate-anion are shown in Fig. 1. The correlation functions for EFG tensor components were calculated and corresponding characteristic times were estimated.

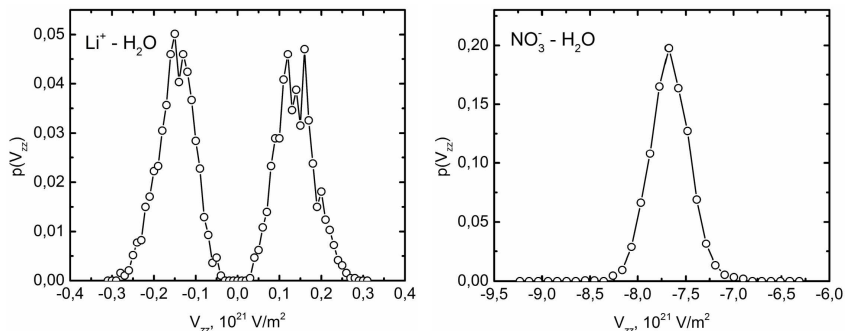


Figure 1. Distributions of V_{zz} values at lithium ion (left panel) and nitrogen atom of nitrate-anion (right panel) in aqueous solution

References

1. S. Badu, L. Truflandier, J. Autschbach, - *J. Chem. Theor. Comput.* **9**, 4074 (2013).
2. A. Carof, M. Salanne, T. Charpentie, B. Rotenberg, - *J. Phys. Chem. B* **118**, 13252 (2014).
3. R. Car, M. Parrinello, - *Phys. Rev. Lett.* **55**, 2471 (1985).

Crystallisation and Dynamics of Water Confined to MCM-41

Verena Fella¹, Yang Yao², George Floudas², Michael Vogel¹

¹*Institut für Festkörperphysik, TU Darmstadt, Darmstadt, Germany*

²*Max Planck Institute for Polymer Research, D-55128 Mainz, Germany*

E-mail: verena.fella@physik.tu-darmstadt.de

https://www.fkp.tu-darmstadt.de/groups/ag_vogel

Introduction

Understanding the properties of water in confinement is an important task due to its many applications in life science and technology. The complex behaviour of water however leaves many questions still unanswered, some owing to the inaccessibility of the ‘no man’s land’ for the bulk liquid. In this region between 150 and 235 K water immediately crystallises, making experiments with bulk water impossible.

Nano-confinement reduces the crystallisation temperature of water to lower values and supercooling to temperatures even below the nucleation temperature is possible. Different experimental methods show a dynamic crossover in the supercooled regime, the origin of which is controversially discussed [1]. Our previous studies using ²H NMR show the existence of a solid water fraction inside the pores and suggest the crossover being caused not by a liquid–liquid phase transition but rather a change from bulk-like to interface-dominated dynamics [2, 3].

Systems and Methods

Using hard confinement in the form of silica nanopores (MCM-41) with different pore diameters between 2 and 5 nm we investigate the effect of confinement on the crystallisation of water and focus on the different liquid and solid water fractions forming inside the pores. By combining nuclear magnetic resonance (NMR) experiments with dielectric spectroscopy (DS) and differential scanning calorimetry (DSC) we are able to probe water dynamics over a broad temperature and dynamic range.

We perform ²H and ¹⁷O NMR spin-lattice relaxation and stimulated-echo experiments to determine rotational correlation times. While ²H NMR is well established to study the rotational motion of confined water ¹⁷O NMR has not been applied to this question yet. Adjei-Acheamfour et al. [4] recently investigated ultraslow dynamics in ice using ¹⁷O NMR by selective excitation of the central line. This approach yields many new possibilities to explore crystalline water phases inside confinements.

Results

Both ²H NMR and DS identify two dynamically distinguishable fractions of water coexisting within the pores at sufficiently low temperatures. These fractions correspond to a liquid interfacial water layer and a less mobile water component in the pore center, and their dynamics can be investigated via correlation times. In the larger pores ice nuclei form as well, possibly in two different forms caused by heterogeneous and homogeneous nucleation. In the smaller pore sizes only the two liquid fractions can be observed over a wide range of temperatures.

To analyse the dynamics of the less mobile water fraction ¹⁷O NMR experiments are applied.

References

1. S. Cerveny, F. Mallamace, J. Swenson, M. Vogel, L. Xu. Confined water as model of supercooled water. – *Chemical reviews*, 116(13), 7608–7625, (2016).

2. M. Sattig, M. Vogel. Dynamic crossovers and stepwise solidification of confined water: a ^2H NMR study. – *J. Phys. Chem. Lett.*, 5(1):174–178, (2013).
3. D. Demuth, M. Sattig, E. Steinrücken, M. Weigler, M. Vogel: ^2H NMR Studies on the Dynamics of Pure and Mixed Hydrogen-Bonded Liquids in Confinement. – *Z. Phys. Chem.*, 232.7-8, 1059-1087, (2018).
4. M. Adjei-Acheamfour, J. F. Tilly, J. Beerwerth, R. Böhmer. Water dynamics on ice and hydrate lattices studied by second-order central-line stimulated-echo oxygen-17 nuclear magnetic resonance. – *J. Chem. Phys.*, 143, 214201 (2015).

Zonal harmonics calculation to compensate the magnetic field heterogeneity in a magnet gap

V. V. Frolov¹, P. A. Kupriyanov¹, A. E. Shilov²

¹St. Petersburg State University

²VNIM of the D.I. Mendeleev, Saint Petersburg

E-mail: vfrolov@bk.ru

Introduction

Now magnetic field in nuclear magnetic resonances spectrometers and nuclear magnetic resonances scanners is, as a rule, created by superconducting solenoids. However for a solution of some tasks (medical MRI of extremities, not medical applications MRI, a measurement of relaxation time, metrology) it is preferably to use normal magnets or electromagnets with flat gaps in view of them considerably smaller cost. At implementation of such equipment there is always a problem of homogeneity of magnetic field. A widespread way of a solution is to use the orthogonal current compensators of the heterogeneity of magnetic field. The long ago known [1] standard method of calculation is a use of spherical harmonics of scalar potential of static magnetic field Φ_{pq} . Each harmonic is created by the line currents flowing along lines of intersection of equipotential surfaces with a surface on which currents flow. Unfortunately, the method well works only for the closed surfaces (the sphere, ellipsoids) that, of course, is unacceptable for constructive reasons. However for zonal harmonics ($q=0$) which by definition have cylindrical symmetry the task can be solved much more simply and at the same time with higher accuracy. It is important for practice that most often the longitudinal gradient ($\Phi_{20}(z, \rho)$, ρ is radius in a cylindrical coordinate system, the main field is directed along z) puts the main contribution to field heterogeneity. Such field distortion arises as a result of a violation of symmetry of a magnet system to a plane of symmetry. It is also reasonable to compensate and possible deviation from linearity, at least in first order. Such compensation is carried out by harmonic Φ_{40} , creating a field with cubic dependence of a field on z .

In the magnet system having a plane of symmetry, a field changes symmetrically at shift from this plane. As a first approximation such change can be compensated by harmonic Φ_{30} .

The calculation of a system of zonal harmonics compensators based on explicit expressions of dependence of magnetic field of ring currents on coordinates is presented in the submitted message.

Calculation method

The calculations of magnetic field components in polar coordinates (z, ρ, φ) were carried out using the well-known formulas for $\rho=0$ and integral formulas based on the Bio–Savart – Laplace law [2, 3]:

$$B_{Gz} = \frac{1}{\pi} \int_0^\pi (R - \rho \cos \varphi) \left[\frac{1}{[R^2 + (z-Z)^2 + \rho^2 + 2\rho \cos \varphi]^{\frac{3}{2}}} - \frac{1}{[R^2 + (z+Z)^2 + \rho^2 + 2\rho \cos \varphi]^{\frac{3}{2}}} \right] d\varphi, \quad (1)$$

$$B_{G\rho} = \frac{z-Z}{\pi} \int_0^\pi \frac{\cos \varphi d\varphi}{[R^2 + (z-Z)^2 + \rho^2 + 2\rho \cos \varphi]^{\frac{3}{2}}} - \frac{z+Z}{\pi} \int_0^\pi \frac{\cos \varphi d\varphi}{[R^2 + (z+Z)^2 + \rho^2 + 2\rho \cos \varphi]^{\frac{3}{2}}}. \quad (2)$$

Here B_{Gz} and $B_{G\rho}$ are the axial and radial components of the magnetic field of the gradient system, respectively. In Eqs. (2) and (3) and below the dimensionless units are used for fields: magnetic fields are expressed in units of $\mu_0 I n / 2R$, where μ_0 is the magnetic constant, I is the electric current in the coils (a filamentary current approximation is supposed); n is the number of turns; Z is the position of the plane with currents and R is the radius of coils.

Calculation was made in several stages.

1. From specifications initial diameters of two or three threadlike current rings were set as a zero approximation. The directions of currents became opposite on different pole pieces for harmonics Φ_{20} and Φ_{40} and identical for Φ_{30} . The system of equations was formed to determine the current ratio for coils:

$$\mathbf{H}\vec{I} = \vec{h}, \tag{3}$$

where \mathbf{H} is the matrix of coefficients of a system is determined as

$$H_{ik} = \int_0^{z_0} b(z)_i b(z)_k dz;$$

here $b(z)_i$ is the field of couple of ring currents located on surfaces of pole pieces; \vec{I} is a vector-column of values of optimum currents (turn out as a result of a solution of (3)); \vec{h} is a vector-column of absolute terms:

2. Within design opportunities the radiuses of ring currents varied, procedure 1 repeated and the optimal variant was selected.

3. Each found threadlike current was replaced with symmetrically located group of ring currents. The relation of numbers of rings in each group corresponded to the relation of currents found at the second stage.

4. Control of the configuration of a field created by the received groups of currents was made.

Results

Examples of the dependences of a field on coordinates received at the second stage are given in fig. 1-5. Fig. 2 and 3 show the good accuracy of reproduction of the set dependences on an axis ($\rho=0$). However at shift from an axis on distance of an order of value of a gap of a magnet strong deviations from set (fig. 1, 4 and 5) begin. As a result of the third stage radiuses of rings of each group are determined. Harmonics Φ_{20} and 40 contain two groups of the 6 and 3 rings on each pole piece. The harmonic Φ_{30} consists of three groups (1, 3 and 6 rings). Control at the 4th stage showed good reproduction of the set dependences, though the worst, than at the first stage (see an example in fig. 6). In Table 1 the relative standard error relative to the set dependences received at the second and fourth stages are compared.

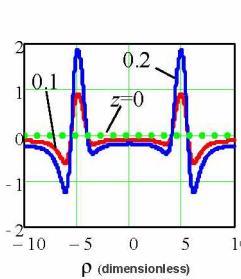


Figure 1. Φ_{20} : Field dependence on ρ (arbitrary units)

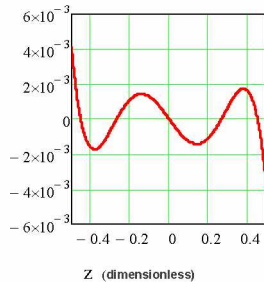


Figure 2. Φ_{20} : Field deviation from set (relative units)

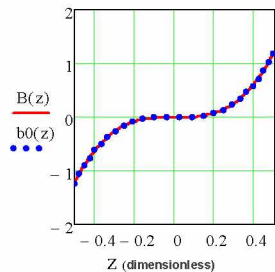


Figure 3. Φ_{40} : $B(z)$ - Field created; $b_0(z)$ - The set field (arbitrary units)

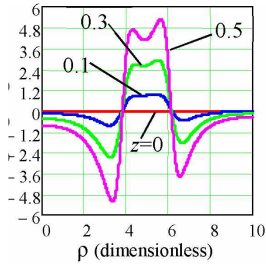


Figure 4. Φ_{40} : Field dependence on ρ (arbitrary units)

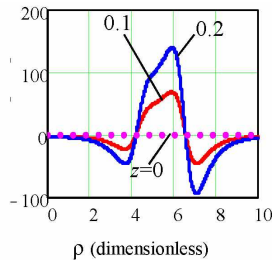


Fig.5. Φ_{30} : Field dependence on ρ (arbitrary units)

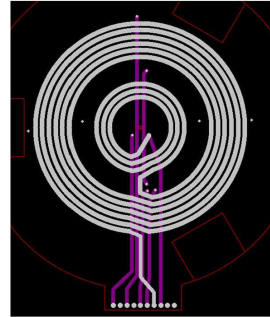


Figure 6. Compensator Φ_{30} in the form of the printed circuit board

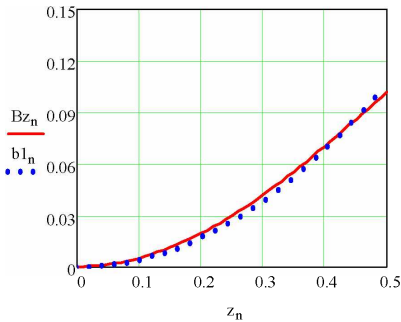


Figure 7. Φ_{30} , three groups of rings. control: B_z -field created; b_1 - the set field (arbitrary units)

Table 1

	Relative Standard Error	
	Thin rings	Groups of rings
Φ_{20}	$2 \cdot 10^{-6}$	$7 \cdot 10^{-3}$
Φ_{30}	$4 \cdot 10^{-4}$	$3.4 \cdot 10^{-3}$
Φ_{40}	10^{-3}	$4 \cdot 10^{-3}$

The numeric computations and graphics were performed using MathCad 15. The example of a printed circuit board for the compensator Φ_{30} is given in fig. 6.

References

1. Golay M. J. E. Field homogenizing coils for nuclear spin resonance instrumentation. The Review of Scientific Instruments. V.28, p.313-315. 1958.
2. B.L. Alievsky, V.I. Orlov. The calculation of the axially symmetric coils magnetic field parameters (in Russian), (Energoatomizdat, Moscow, 1983)
3. W. R. Smyte. Static and Dynamic Electricity, N.Y., McGraw Hill, 3rd Ed. (1968).

NMR studies of various perfluorosulfonated membranes in wide temperature range

Elena Galitskaya^{1,3}, Alexei Privalov², Max Weigler², Michael Vogel², Alexei Kashin³, Ivan Ryzhkin^{1,3}, Vitaly Sinitsyn^{1,3}

¹*Institute of Solid State Physics RAS, 142432, Chernogolovka, Moscow distr., Russia*

²*Institute für Festkörperphysik, Technische Universität, Darmstadt, 64289 Darmstadt, Germany*

³*Inergy LLC, 111524, ul. Elektrodnyaya 12-1, Moscow, Russia*

E-mail: galitskaya@issp.ac.ru

<http://www.issp.ac.ru/main/index.php/ru/education/aspirantura/aspirants/698-galitskayaea.html>

Introduction

The current interest in proton-conductive polymers is related to their practical application in hydrogen-air fuel cells (PEMFC). At present, the most widespread membranes are Nafion® (DuPont™). This polymer consists of long perfluorinated hydrocarbon chains with side branches ending with sulfogroups. In last couple decades were synthesized a number of analogues of Nafion under trademarks Flemion (Asahi Glass Co.), Aciplex (Asahi Chemical Co.), Fumapem (FuMA-Tech) and some others. The most significant breakthrough in new membrane preparations was made by SOLVAY® Co. which synthesized new perfluorinated sulfopolymer Aquivion® with shorter side chains in comparison to Nafion™.

The most important characteristic of proton-exchange membranes is the value of its proton conductivity. It was established [1-4] that both sulfogroups concentration (equivalent weight) and the side chains length strongly effect on protonic conductivity of perfluorinated polymers. Another transport parameter which effected on PEMFC performance at high current density is H₂O self-diffusion coefficient due to flow back water from cathode to anode. The researches of this transport parameter are significantly less than the proton conductivity and were mainly performed on Nafion membrane by field gradient spin echo nuclear magnetic resonance [5]. Moreover, there is a significant spread in the self-diffusion coefficient values at temperatures above room temperature, and in the region of negative temperatures were published contradiction results [6,7]. It should be noted that in a number of the self-diffusion coefficient studies were carried out on samples prepared in different ways and without control of humidity conditions during the measurement process. Thus, it was of interest to measure the self-diffusion coefficient of water in proton-exchange membranes taking into account these disadvantages.

In the work, we investigated the diffusion coefficients of different membranes in a wide temperature range (from -90 to 80C) with humidity control by the spin-echo method in the magnetic field gradient. The investigated membranes possess differed in equivalent weight and different length of the side chains, which allows us to determine the effect of the carrier concentration and the size of the channels on the diffusion coefficient.

Sample preparations

In these researches, we used the following membranes:

1. Nafion 212, with equivalent weight (EW) =1100 gr/eq, long side chain.
2. CTPEM 4, EW =1000 gr / eq, long side chain.
3. Fumapem FS930, EW =930 gr / eq, short side chain.
4. Fumapem F950, EW =950 g / eq, long side chain.

Preliminary all membranes were exposed via the identical procedure of protonation, purification from organic impurities and drying under vacuum at 80C (24h). To obtain a sample

with a certain H₂O composition, they were kept for 2 weeks in a chamber with a fixed partial pressure of water vapor.

The self-diffusion coefficient, DNMR, was studied using NMR echoes in an ultrahigh static field gradient (SFG). The experiments were performed at an NMR frequency of 60 and 162 MHz and at magnetic field gradients of 15 and 141 T/m. Compared to NMR diffusion studies in pulsed field gradients, SFG are much stronger thus allowing for the measurement of smaller diffusion coefficients. The another advantage of SFG is due to the non-necessity of field switching which allows diffusion studies in the case of much shorter spin-spin relaxation times.

Results

The temperature dependencies of self-diffusion coefficient, D , all membranes under investigations in the temperature range from 5C to 80C, at 30 and 80% water humidities are presented on Figure 1.

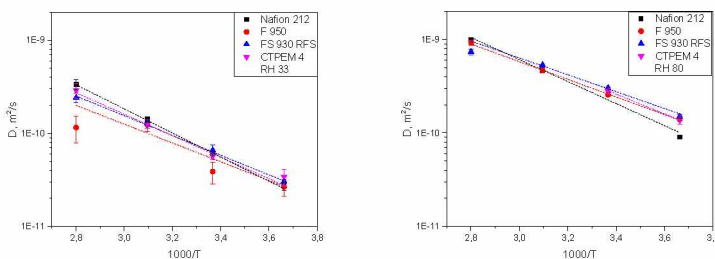


Figure 1. The temperature dependencies of self-diffusion coefficient for investigated membranes at 30 and 80% humidities

It can be seen that the values of D are weakly depend on the type of membrane and are reduced by about 7 times at the same temperature with a decrease in humidity from 80 to 30%. The temperature dependences of the self-diffusion coefficient are well described by the Arrhenius equation $D=D_0\exp(-E/kT)$ and characterized by the activation energy $E=0.2$ eV, which coincides with the activation energy of self-diffusion in water. This indicates the similarity of self-diffusion micromechanisms in proton-exchange membranes and in the water.

Studies at the negative temperatures from -5 to -90C were carried out on the example of Fumapem membranes, differing in the length of the side chain. It was found that at high water concentration the dependences of $D(T)$ for both membranes coincide (within the experimental error), but became high on factor ~ 2 at low humidity for membrane with a short side chain in comparing with a long side chain membrane. The activation energy values were weakly dependent on the humidity and equal to ~ 0.4 eV, which is much higher than in the high temperature region. This fact indicates a change in the micromechanism of self-diffusion with decreasing temperature. A similar behavior was observed for temperature behavior of the Debye relaxation time [8], which indicates on a common mechanism of these two processes in proton-exchange membranes.

Acknowledgements

E. G. thanks DAAD for financial support of her researches in Darmstadt Technical University. The work was partially supported by RFBR №17-02-00512.

References

1. Gebert M, Ghielmi A, Merlo L, Corasaniti M, and Arcella V. *J Solid State Sci Technol.* 26(1):279-83, 2010.
2. Merlo L, Oldani C, Apostolo M, Arcella V. *PFSA Aquivion® membranes: general features and degradation mechanisms.* Solvay Specialty Polymers SPA. 2012.
3. Anita Skulimowska, Marc Dupont, Marta Zaton, Svein Sunde, Luca Merlo, Deborah J.Jones, Jacques Rozière. *International Journal of Hydrogen Energy,* 2014; 39(12): 6307-6316, 2014.
4. Mugtasimova, A.P. Melnikov, E.A. Galitskaya, A.M. Kashin, Yu.A. Dobrovolskiy, G.M. Don, V.S. Likhomanov, A.V. Sivak, V.V. Sinityn *Ionics,* 24, Issue 12, pp 3897–3903, 2018
5. Q. Zhao, P.Majsztrik, J.Benziger, *J. Phys. Chem.,* 115, pp2717-2727, 2011
6. Morihiro Saito, Kikuko Hayamizu, and Tatsuhiro Okada, *J. Phys. Chem. B* 109, 3112-3119, 2005
7. Armel Guillermo, Gerard Gebel, Hakima Mendil-Jakani and Eric Pinton *J. Phys. Chem. B* 113, 6710–6717, 2009
8. Zijie Lu, a,b, Georgios Polizos, Digby D. Macdonald and E. Manias *Journal of The Electrochemical Society,* 155 (2), B163-B171, 2008

Solid-echo signal in a three-spin system with arbitrary dipole-dipole interaction constants

Irina Yu. Golubeva¹, Grigorii E. Karnaukh, Tatiana P. Kulagina²

¹Faculty of fundamental physical and chemical engineering, Moscow state University, Moscow, Russia

²Institute of problems of chemical physics RAS, 142432, Chernogolovka, Russia
E-mail: tan@icp.ac.ru

Introduction

A new method for calculating the solid-echo (SE) signal in three-spin systems with arbitrary values of dipole-dipole interaction constants (DDI) is applied. The basis of the method is the theorem of reduction [1], which allows to simplify calculations by reducing the dimension of the space of spin States.

Theorem about Cast Operation

The space of all spin States R is divided (reduced) into two subspaces of States, even R_e and odd R_o , with respect to the π -pulse ($R = R_e \oplus R_o$).

$$R_e = \hat{P}_e R \text{ and } R_o = \hat{P}_o R,$$

where $\hat{P}_e = \frac{1}{2} \left(\hat{E} + e^{i\pi(\hat{S}^x - \frac{3}{2})} \right)$ and $\hat{P}_o = \frac{1}{2} \left(\hat{E} - e^{i\pi(\hat{S}^x - \frac{3}{2})} \right)$ – the projectors on these subspaces, \hat{E} – unit operator, \hat{S}^x – the operator of the initial polarization.

The method of calculating the signal

Also, the symmetry associated with the spin exchange was used in the calculation of the signal. The space of all spin States R is divided into two subspaces of symmetric R_s and antisymmetric R_a states relative to spin exchange [1, 2].

$$R_s = \hat{P}_s R \text{ u } R_a = \hat{P}_a R,$$

where $\hat{P}_s = \frac{1}{2} (\hat{E} + \hat{E}x)$, $\hat{P}_a = \frac{1}{2} (\hat{E} - \hat{E}x)$ – the projectors.

Then the space of all spin States R can be divided into four subspaces:

$$R = R_{ea} \oplus R_{oa} \oplus R_{es} \oplus R_{os},$$

$$R_{ea} = \hat{P}_e \hat{P}_a R, R_{oa} = \hat{P}_o \hat{P}_a R, R_{es} = \hat{P}_e \hat{P}_s R, R_{os} = \hat{P}_o \hat{P}_s R.$$

This makes it possible to reduce the calculation of the SE signal in the three-spin system from the 8th-order matrix to the calculation of the signal on two 1st-order matrices and two 3rd-order matrices.

Results and discussion

The calculation was carried out for spin systems with arbitrary values of dipole-dipole interaction constants (DDI). The solid-echo signal is observed after the impact of the pulse sequence on the spin system: $\left(\frac{\pi}{2}\right)_y - t - \left(\frac{\pi}{2}\right)_x - \tau$.

Calculation formula of signal:

$$A(t, \tau) = \frac{Tr \hat{S}^x(t) \hat{S}^x}{Tr (\hat{S}^x)^2} = \frac{Tr \hat{S}^x(t) \hat{S}^x}{Tr \sum_i^n (\hat{S}_i^x)^2} = \frac{Tr \hat{S}^x(t) \hat{S}^x}{n 2^{n-2}} = \frac{Tr \hat{S}^x(t) \hat{S}^x}{6}$$

where $\hat{S}^x(t) = \hat{U}^{-1} \hat{S}^x \hat{U}$, $\hat{U} = e^{it\hat{H}_d^z} e^{i\frac{\pi}{2}\hat{S}^x} e^{it\hat{H}_d^z}$.

Then an analytical expression for SE in three-spin systems.

$$\begin{aligned}
 A_2(\tau, t) &= \frac{1}{64}(27\cos^4\beta - 18\cos^2\beta + 7) - \frac{3}{32}(\cos^2\beta + 2\cos\beta + 1)\cos\omega_{12}(\tau - t) \\
 &+ \frac{3}{32}(\cos^2\beta - 2\cos\beta + 1)\cos\omega_{13}(\tau - t) + \frac{27}{128}(\cos^4\beta - 2\cos^2\beta + 1)\cos\omega_{23}(\tau - t) \\
 &- \frac{1}{32}(3\cos^2\beta + 2\cos\beta - 1)\cos\omega_{12}(\tau + t) - \frac{1}{32}(3\cos^2\beta - 2\cos\beta - 1)\cos\omega_{13}(\tau + t) \\
 &+ \frac{3}{128}(9\cos^4\beta - 10\cos^2\beta + 1)\cos\omega_{23}(\tau + t) \\
 &- \frac{3}{32}(\cos^2\beta - 1)(\cos(\omega_{12}\tau - \omega_{13}t) + \cos(\omega_{12}t - \omega_{13}\tau)) \\
 &- \frac{3}{64}(3\cos^3\beta - \cos^2\beta - 3\cos\beta + 1)(\cos(\omega_{12}\tau - \omega_{23}t) + \cos(\omega_{12}t - \omega_{23}\tau)) \\
 &+ \frac{9}{64}(\cos^3\beta - \cos^2\beta - \cos\beta + 1)(\cos(\omega_{13}\tau - \omega_{23}t) + \cos(\omega_{13}t - \omega_{23}\tau)) \\
 &+ \frac{3}{32}(\cos^2\beta - 1)(\cos(\omega_{12}\tau + \omega_{13}t) + \cos(\omega_{12}t + \omega_{13}\tau)) \\
 &+ \frac{3}{64}(3\cos^3\beta + \cos^2\beta - 3\cos\beta - 1)(\cos(\omega_{13}\tau + \omega_{23}t) + \cos(\omega_{13}t + \omega_{23}\tau)) \\
 &- \frac{9}{64}(\cos^3\beta - \cos^2\beta - \cos\beta + 1)(\cos(\omega_{12}\tau + \omega_{23}t) + \cos(\omega_{12}t + \omega_{23}\tau)) \\
 &+ \frac{1}{32}(9\cos^3\beta + 3\cos^2\beta - 5\cos\beta + 1)(\cos\omega_{12}\tau + \cos\omega_{12}t) \\
 &- \frac{1}{32}(9\cos^3\beta - 9\cos^2\beta - \cos\beta + 1)(\cos\omega_{13}\tau + \cos\omega_{13}t) \\
 &- \frac{3}{64}(9\cos^4\beta - 10\cos^2\beta + 1)(\cos\omega_{23}\tau + \cos\omega_{23}t)
 \end{aligned}$$

where $\cos\beta = \frac{\sigma_1}{\sqrt{9\sigma_1^2 - 24\sigma_2}}$, $\sigma_1 = b_{12} + b_{23} + b_{31}$, $\sigma_2 = b_{12}b_{23} + b_{23}b_{31} + b_{31}b_{12}$, b_{ij} - the constant DDI [3].

According to this formula, the graphs of the signals of SE and the line shape for the same and different constants DV were constructed.

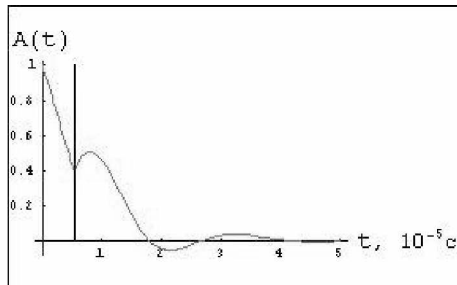


Figure 1. SE with different constants DDI

$$\tau = 10^{-5} c, \sigma_1 = 2 \cdot 10^5 c, \sigma_2 = 5 \cdot 10^9 c^2, \cos\beta \approx 0.41, T_2 = 10^{-5} c$$

Acknowledgment

This work was financially supported by FASO (grant no. 0089-2014-0021).

References

1. I. Yu. Golubeva, G. E. Karnauksh, T. P. Kulagina. Calculation and analysis of the solid-echo in the three-spin system. – col.art. “Structure and dynamics of molecular systems”, publ. XXV, 161-165 (2018)
2. G. E. Karnauksh. The line shape of the NMR of a pair of spins $3/2$. – “Modern methods of NMR and EPR in solid state chemistry”, 118 (1990)
3. T. P. Kulagina, G. E. Karnauksh, S. A. Andrianov. Evolution of polarization of three spin groups and their contribution to line shape NMR in solids. – *Butlerov messages*, T. 35, №7, 1-9 (2013)
4. Yu. N. Moskvich, N. A. Sergeev, G.I. Dotsenko. Two-pulse echo in solids containing isolated three-spin systems. – *Phys. Stat. Solid (a)*, 409-418 (1975)

Spin lattice relaxation of nuclei in magnetic semiconductor compound CuFeS_2

Stanislav O. Garkavyi, Ecaterina V. Schmidt, Vadim L. Matukhin, Rustem R. Khusnutdinov, Georgy V. Mozzhukhin, Nicolay K. Andreev

*Kazan State Power Engineering University, Kazan, 420066, Russia
E-mail: oloioiev77@mail.ru*

Introduction

Chalcopyrite CuFeS_2 is a well-known semiconductor mineral possessing thermoelectric properties [1, 2]. The crystal structure of the tetragonal phase CuFeS_2 (chalcopyrite structure) is represented as alternating metal layers separated by layers of sulphur. In each metal layer, in a successive alternation of copper and iron atoms, the spins of the iron atoms are parallel along the c axis, and antiparallel in the neighboring layers, which leads to an antiferromagnetic ordering of the CuFeS_2 crystal lattice with a Neel temperature of 823 K. The study of the spin-lattice relaxation of nuclei provides information on the magnitude and mechanism of interactions between nuclear magnetic dipole and quadrupole moments and fluctuating local magnetic and electric fields [3]. The aim of this work was to study relaxation of nuclear spins in magnetic semiconductor compound CuFeS_2 by using NMR $^{63,65}\text{Cu}$ in a local field method.

Methods

Samples from two mineral deposits “Talnakh” and “Sibai” were investigated. The nuclear magnetic resonance spectra in the local field and the spin-spin and spin-lattice relaxation times of the $^{63,65}\text{Cu}$ nuclei were measured with a Tecmag-Redstone multipulse NQR/NMR spectrometer. The $^{63,65}\text{Cu}$ spectra were obtained using the standard spin-echo sequence $\pi/2-\tau-\pi$ -echo. Measurements of NMR spectra were carried out with the delay time $\tau = 55 \mu\text{s}$. The spin-spin relaxation time T_2 was measured when the delay time τ between pulses changed in the $\tau = 50-1350 \mu\text{s}$ interval in the spin-echo-pulse sequence. The spin-lattice relaxation time T_1 was measured by the inversion recovery method of nuclear magnetization [4]. The signal was repeatedly accumulated with the repetition time of $5T_1$ to increase the signal-to-noise ratio. The number of accumulations used is 1000.

Results

As is known, in semiconductor compounds, the relaxation of quadrupole nuclei is due to the dipole contribution due to the interaction of the nuclear magnetic dipole moment with charge carriers, and the quadrupole contribution due to the interaction of the nuclear electric quadrupole moment with the gradients of the electric fields at the location of the resonant nuclei. The noticeable difference in the values of gyromagnetic ratios $r_M = (^{65}\gamma_N/^{63}\gamma_N)^2 = 1.167$ and quadrupole moments $r_Q = (^{65}Q/^{63}Q)^2 = 0.872$ nuclei of two common copper isotopes allows to separate the magnetic and electric quadrupole contributions to the nuclear spin-lattice relaxation. The rate of spin-lattice relaxation turns out to be proportional to the spectral density of fluctuations of the internal fields, which cause relaxation transitions in the nuclear spin system. The curves for the recovery of the equilibrium value of nuclear magnetization at a temperature $T = 300 \text{ K}$ for resonance lines ν_i (CL) ($i = 63, 65$), corresponding to central transitions ($I_z = 1/2 \leftrightarrow -1/2$), were of one exponential nature, as an example sample from “Sibai” mineral deposit is presented in Figure. 1. The ratio $T_1(^{63}\text{Cu})/T_1(^{65}\text{Cu}) = 1.06$ was slightly less than the value of r_M . This result allows us to exclude from consideration the quadrupole relaxation mechanism and take into account the magnetic relaxation mechanism due to fluctuations of the dipole local fields.

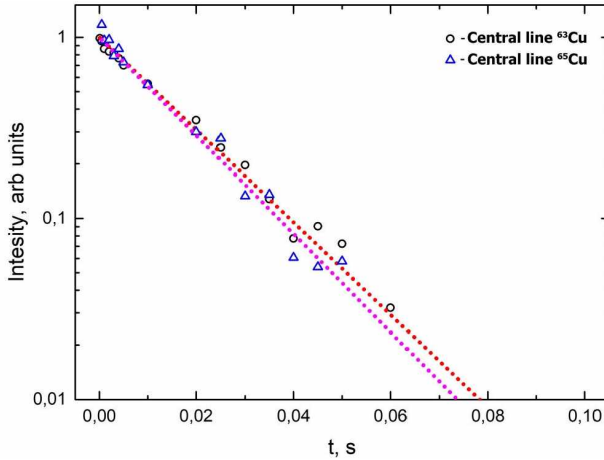


Figure 1. $^{63,65}\text{Cu}$ magnetization recovery of central transitions in a local field at 300K in CuFeS_2 sample from “Sibai” mineral deposit

To further confirm the magnetic nature of nuclear relaxation, we measured spin-lattice relaxation on the satellite ν (SL) line of the ^{63}Cu NMR spectrum corresponding to the $I_Z = 3/2 \leftrightarrow 1/2$ transition. In this case, the recovery curves were also exponential (Fig. 2) and the resulting values of the relaxation rate turned out to be noticeably lower than the corresponding values of the relaxation rate for the central transition.

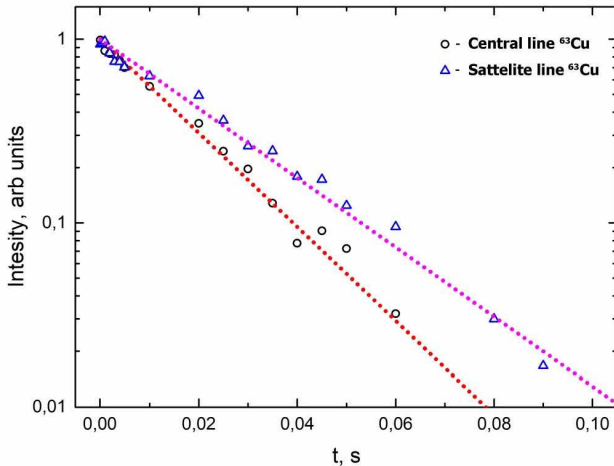


Figure 2. ^{63}Cu magnetization recovery of central and satellite transition in a local field at 300K in CuFeS_2 sample from “Sibai” mineral deposit

The result obtained is an additional confirmation of the magnetic mechanism of spin-lattice relaxation.

References

1. N. Tsujii, T. Mori, Y. Isoda. J. - *Electron. Mater.*, Vol. 43, № 6. P.2371 (2014).
2. Ran Ang, Atta Ullan Khan, NaohitoTsujii, Ken Takai, Ryuhei Nakamura, Takao Mori. - *Angewandte Chemie.*, Vol 54, № 44. P.12909—12913 (2015).
3. V.V. Ogloblichev, I.G. Sevastyanov, A.N. Gavrilenko, V.L. Matukhin, I.J. Arapova, E.J. Medvedev, S.O. Garkavyi, E.V. Schmidt. J. - *Applied Spectroscopy.*, Vol. 83, № 5. P.771-775 (2016).
4. C.P. Slichter. *Principles of Magnetic Resonance (in English)*. – "Clarendon Press" Publ., Oxford, 1961.

Investigation of the nonlinear frequency shift of a ferromagnetic film resonator

Roman V. Haponchik, Alexey B. Ustinov

Department of Physical Electronics and Technology, St.Petersburg Electrotechnical University, St.Petersburg, -197376 Russia

E-mail: ustinov_rus@yahoo.com

Introduction

The spin-wave resonator is a plane rectangular sample of a ferromagnetic film. The dimensions of the resonator, its shape, magnetic parameters of the film and a value of the bias magnetic field determine the resonant frequency spectrum. Practically, resonators based on an yttrium iron garnet (YIG) film are used usually because this material has the lowest parameter of relaxation of magnetization oscillations. It is known that with an increase in the microwave signal power exciting oscillations in a ferromagnetic film resonator, various nonlinear effects could be emerged. The effect of bistability [1] is observed and well enough studied in normally magnetized resonators. In the case of in-plane magnetized resonators, a nonlinear frequency shift and nonlinear damping of magnetization oscillations take place [2,3]. The purpose of this work is experimental investigation of the nonlinear effects emerged in obliquely magnetized ferromagnetic film resonators.

Experimental prototype

The resonator represented an YIG film sample with a thickness of $7 \mu\text{m}$ and lateral dimensions $a = b = 1 \text{ mm}$, which was grown epitaxially on a 0.5 mm thick gallium gadolinium garnet (GGG) substrate. The film had saturation magnetization of 1750 G . The angle was varied from 0 to 50 degrees. Magnetization oscillations were excited in the resonator by a microstrip antenna with a width of $50 \mu\text{m}$ and a length of 2 mm , one end of which was connected to a standard microstrip transmission line with a characteristic impedance of 50Ω , and the other end was grounded. The resonator was positioned immediately on the microstrip antenna as is shown in Fig. 1. The microstrip structure with the resonator was placed between poles of a permanent magnet. The measurement cell was rotated in a magnetic field at an angle from 0 to 360 degrees.

The nonlinear properties of the resonator were studied with measurements of the microwave absorption spectra at various input power levels of the applied microwave signal.

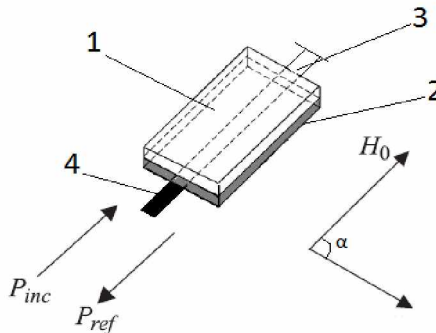


Figure 1. Schematic diagram of the resonator magnetized the film at an angle of α . (1 – GGG substrate, 2 – YIG film resonator, 3 – short circuit, 4 – microstrip antenna)

Experimental results

The resonator reflection spectrum is shown in Fig. 2(a). This characteristic was measured as $S_{11}(f) = 10\lg\left(\frac{P_{ref}(f)}{P_{inc}(f)}\right)$, where f is the microwave frequency and $P_{inc}(f)$ is the incident microwave power, and $P_{ref}(f)$ is the reflected signal power. The magnetic field strength H_0 was 2000, and was directed at an angle of 25 degrees, for which the resonator absorbed at frequencies above 7.3 GHz.

Figure 2(b) shows a fragment of the resonator reflection spectrum corresponding to a main mode of the resonator measured for different input power levels. As is seen from the measured dependences, an increase in the power level leads to a change in resonant frequency due to the effect of a nonlinear frequency shift. Moreover, it leads to an increase in the width of the resonance curve due to the nonlinear damping of spin waves. It was found, that the nonlinear frequency shift is nonmonotonic dependence of input power (see Fig. 3). The resonant frequency demonstrate first the negative shift. Reaching the power level of 13 dBm the resonant frequency shift become positive.

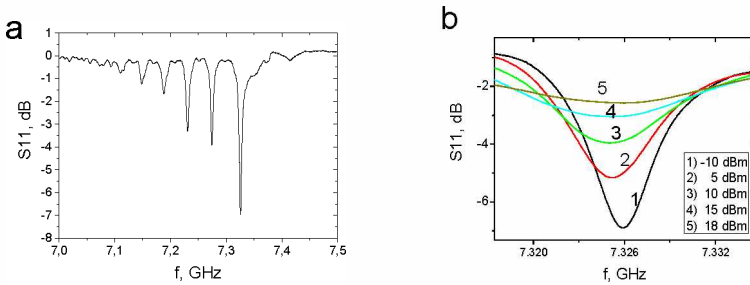


Figure 2. Typical spectra in a linear mode (a) and a family of resonance curves (b) measured for a resonator magnetized at an angle $\alpha = 25$ degrees to the film. (1 – -10 dB, 2 – 5 dB, 3 – 10 dB, 4 – 15 dB, 5 – 18 dB)

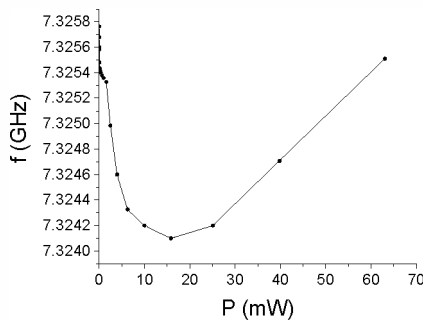


Figure 3. The nonlinear frequency shift as a function of the incident power measured for an angle of 25 degrees

Conclusion

Investigation has shown that obliquely magnetized ferromagnetic film resonator demonstrate a nonlinear shift of the resonant frequency. The nonlinear frequency shift is nonmonotonic dependence of the resonator input power.

Acknowledgements

The work was supported in part by the Ministry of Education and Science of Russian Federation (Project "Goszadanie").

References

1. Y.K. Fetisov, C.E. Patton, V.T. Synogach. IEEE Trans. Mag., **6**, 4511-4521 (1999).
2. H. Yan, Q. Wang and I. Awai. Electron. Lett. **32**, 1787-1789 (1996).
3. A.V. Drozdovskii, A.B.Ustinov. Tech. Phys. Lett. **36**, 834 (2010).

Adjustable tuning range RF-coil for heteronuclear MRI

Viacheslav A. Ivanov, Anna A. Hurshkainen, Georgiy A. Solomakha, Mikhail A. Zubkov

Department of Nanophotonics and Metamaterials, ITMO University, St-Petersburg, Russia, 197101

E-mail: viacheslav.ivanov@metalab.ifmo.ru

In clinical and research MRI, *hydrogen atoms (referred commonly to as protons)* are most often used to generate a detectable radio-frequency signal. However, in addition to hydrogen, several other types of nuclei that can provide a useful magnetic resonance response are present in living organisms [1]. MR measurements using non-proton nuclei, termed X-nuclei, such as deuterium (^2H), phosphorus (^{31}P), sodium (^{23}Na) or fluorine (^{19}F), are also of great value as they offer information which is complementary to that of proton MRI. For example, the information provided by ^{31}P MRI or NMR-spectroscopy can be used to observe changes in energy metabolism and intra-cellular pH [4-6], which can then be used for clinical studies in, for example, oncology [7-9]. The main issue with X-nuclei NMR signal detection is that the relative sensitivity (a function of gyromagnetic ratio) and the concentration of X-nuclei in organic tissue is much less than that of ^1H . That's why in most cases X-nuclei images have significantly lower SNR and/or resolution. The latter impedes obtaining reliable anatomical data from most X-nuclei images and thus they have to be combined with the reference ^1H images.

Whole-body small-animal metamaterial-inspired coil was successfully applied for *in-vivo* ^1H mouse scanning [2], and proof-of-concept MRI tests of preclinical coil for dual-nuclei imaging ($^{19}\text{F}/^1\text{H}$) were also promising [3]. These designs allow to overcome several drawbacks which conventional coils have [2].

We propose double-coil set-up to allow high-SNR broad-range heteronuclear imaging experiments: two independent coils, one of them tuned to ^1H frequency to get anatomical images, and another one, metamaterial-inspired coil tuned to the X-nuclei frequency. In this work our goal was to design a broad-range coil. ^2H and ^{31}P frequencies were chosen as margin frequencies for the second, X-nuclei coil. Such NMR-active nuclei as ^7Li , ^{11}B , ^{13}C , ^{23}Na fall into this range. The higher is the value of constant magnetic field B_0 , the bigger is the absolute frequency gap between the lowest and the highest frequency nuclei. For example, in 11.7 Tesla frequency gap between ^2H and ^{31}P is 127.7 MHz. To have an opportunity of tuning the coil in such a wide range, both structural capacitance and inductance of the coil were made variable.

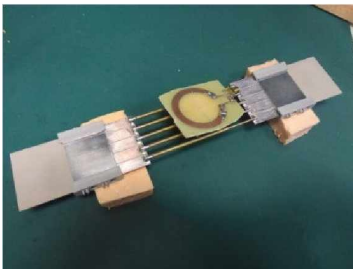


Figure 1. Adjustable tuning range RF-coil

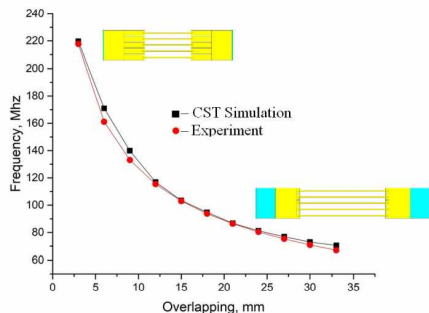


Figure 2. Tuning range of X-nuclei coil

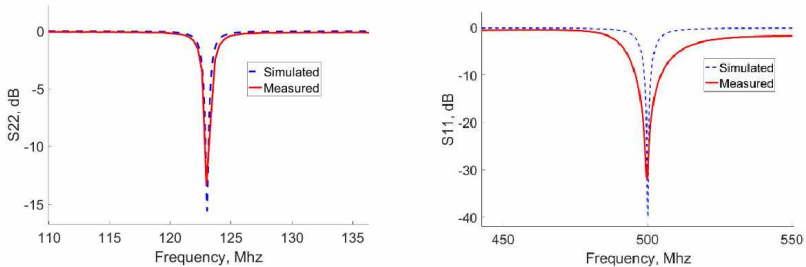


Figure 3. Simulated (CST Microwave Studio) and experimental S-parameters of X-nuclei coil (left picture) and proton coil (right picture). X-nuclei coil here is tuned at 123 Mhz, which approximately corresponds the middle of 76-203 MHz frequency range

We present the results of numerical simulation and initial experimental implementation of whole-body small animal double-coil ^1H -X system with wide frequency tuning range for the X-nuclei for 11.7 T scanner. It was shown that the coils in such system are not coupled and can be effectively tuned to target frequencies: 500 Mhz for proton coil, 76-203 Mhz for X-nuclei coil (Fig. 3). Narrow range tuning in the ^1H coil is achieved via lumped variable capacitance. Broad tuning range in the metamaterial-inspired coil is achieved by simultaneous change of structural capacity (formed by one-side metallized PCBs and metal patches between them which can be shifted along each other) and structural inductance (formed by brass telescopic wires which can vary their length) (Fig. 2).

References

1. M.A.Zubkov, A.E.Andreychenko et al. *Ultrahigh field MRI: new frontiers and possibilities in human imaging. Phys. Usp.* (2018)
2. Zubkov M.A., Hurshkainen A.A, Brui E.A, et al. Small-animal, whole-body imaging with metamaterial-inspired RF coil. *NMR in Biomedicine.*,31, e3952 (2018).
3. A.Hurshkainen, A.Nikulin, E.Georget et al. *A Novel Metamaterial-Inspired RF-coil for Preclinical Dual-Nuclei MRI. Scientific Reports*, 8, Article number: 9190 (2018)
4. Cichocka M., Kozub J. and Urbanik A. PH Measurements of the Brain Using Phosphorus Magnetic Resonance Spectroscopy (31PMRS) in Healthy Men – Comparison of Two Analysis Methods. *Pol J Radiol*, 80, 509–14 (2015)
5. Bachert P., Bellemann M.E. et al. In vivo ^1H , ^31P - $\{^1\text{H}\}$ and ^{13}C - $\{^1\text{H}\}$ magnetic resonance spectroscopy of malignant histiocytoma and skeletal muscle tissue in man. *NMR Biomed.*, 5, 161–70 (1992)
6. Albers M. J., Krieger M. D et al. Proton-decoupled ^31P MRS in untreated pediatric brain tumors. *Magn. Reson. Med.*,53, 22–9 (2005)
7. Lehnhardt F.-G., Röhn G. et al. ^1H - and ^31P -MR spectroscopy of primary and recurrent human brain tumors in vitro: malignancy-characteristic profiles of water soluble and lipophilic spectral components. *NMR Biomed.*, 14, 307–17 (2001)
8. Novak J., Wilson M. et al. Clinical protocols for ^31P MRS of the brain and their use in evaluating optic pathway gliomas in children. *European Journal of Radiology*, 83, e106–12 (2014)
9. Ross B.D., Higgins R.J. et al. ^31P NMR spectroscopy of the in vivo metabolism of an intracerebralglioma in the rat. *Magn. Reson. Med.*, 6, 403–17 (1988)

Textured growth of magnetic nanoparticles in implanted TiO₂ and ZnO single crystals as revealed by FMR

O. Karatas¹, S. Güler¹, C. Okay², S. Kazan¹, R. Khaibullin³, B. Rameev^{1,3}

¹*Gebze Technical University, Department of Physics, 41400, Gebze-Kocaeli, Turkey*

²*Marmara University, Department of Physics, 81040 Göztepe-Istanbul, Turkey*

³*Zavoyiski Physical-Technical Institute, FRC Kazan Scientific Center of RAS, 420029 Kazan, Russian Federation*

E-mail: ozgulkaratass@gmail.com

Abstract

In this work, ferromagnetic resonance studies of magnetic nanomaterials produced by ion-beam implantation of magnetic 3d-ions into TiO₂ and ZnO single crystals are presented. The results of Ferromagnetic Resonance (FMR) studies of ferromagnetic layer formed by high fluence implantation of 3d-ions in the single crystal substrate are presented.

Introduction

An interest to the studies of nanomagnetic materials are driven by their crucial properties for both fundamental science and technology applications. Magnetic resonance technique has been proven as one of the most effective methods to probe various properties of magnetic materials, such as the local site symmetry of dopants, the magnetic anisotropies, exchange interaction energies, damping parameters, crystal electric field, etc. [1-3].

Diluted magnetic semiconductors based on oxide systems, such as titanium dioxide (TiO₂) and zinc oxide (ZnO), doped with transition metal elements have been studied intensively studied due to their potential applications in spintronics. Both TiO₂ and ZnO, which are known as wide-band II-VI semiconductor materials, have drawn much attention due to the theoretical prediction [4] that they may exhibit room-temperature ferromagnetism when doped with magnetic 3d ions [5-8].

In the present study, we investigate the effect of ion-beam implantation on magnetic properties of crystalline TiO₂ and ZnO substances.

Experimental

Single crystals of (100) and (001) TiO₂ substrates as well as (110) and (0001) ZnO substrates have been implanted at room temperature by Co²⁺ and Fe⁺ ions with energy of 40 keV to high dose of 1.5×10^{17} ions/cm² and 8-9 $\mu\text{A}/\text{cm}^2$ beam current density using ILU-3 ion accelerator of Kazan Physical Technical Institute. The magnetic properties of the implanted samples with different crystal orientation have been studied by Ferromagnetic Resonance (FMR) technique at room temperature. FMR spectra have been recorded by using Bruker EMX X-band spectrometer (9.8 GHz) at room temperature. The static magnetic field has been varied in the range of 0-16 kOe. Angular dependences of spectra have been recorded with the static magnetic field rotated in the plane of the plate-like samples (in-plane geometry) and in the perpendicular plane (out-of-plane geometry).

Result and Discussion

Our investigations demonstrate that magnetic resonance is very effective technique to study the local structural and magnetic properties of 3d-ion implanted oxides. Electron paramagnetic resonance (EPR) signals of Mn⁴⁺, Cr³⁺, Fe³⁺, Co²⁺, and other paramagnetic ions have been already observed in the single crystal TiO₂ and ZnO substrates implanted with these ions and subsequently annealed at high temperatures [1,3,9]. It has been shown that post-annealing procedure favours the 3d-ions to enter substitutionally into Ti⁴⁺ (Zn²⁺) site of the host crystal structure.

In the case of the TiO_2 and ZnO single crystal substrates implanted with the magnetic transition metal ions (Co, Fe, Ni) with *no annealing* applied after implantation, the room temperature (RT) ferromagnetic behaviour have been observed. We have shown that the ferromagnetism observed in the as-implanted TiO_2 and ZnO substrates is mainly related to the formation of metal magnetic nanoparticles in the implanted layer.

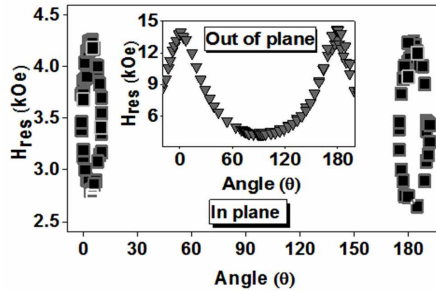


Figure 1. In plane angular dependences and out of plane angular dependences of the FMR resonance fields of Co^+ implanted (100) TiO_2 sample at room temperature

Fig. 1 shows the angular behaviour of ferromagnetic resonance lines in out-of-plane and in-plane geometries for the Co implanted samples. These results reveal strong ferromagnetism even at room temperature with behaviour, which is typical for the continuous epitaxial ferromagnetic films. The out-of-plane FMR measurements (see inset) reflect a high effect of the shape anisotropy on the FMR signal angular dependences because of high effective magnetization value. At the same time, the in-plane FMR results show very large crystal magnetic anisotropy in the samples. The angular behaviour of FMR in the in-plane geometry reveal *uniaxial* crystal magnetic anisotropy for the both substrate orientations.

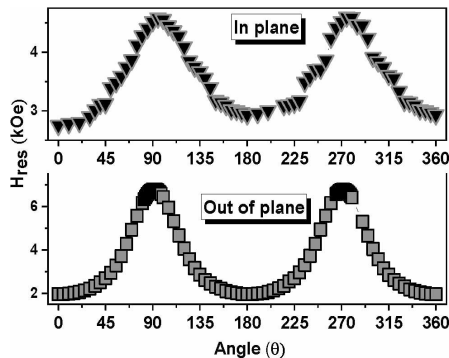


Figure 2. In-plane and out-of-plane angular dependences of the FMR resonance fields of Co^+ implanted (0001)-oriented ZnO sample at room temperature

FMR measurement results of the single crystal TiO_2 substrates implanted with Fe^+ ions (implantation conditions were nearly similar to the samples implanted by Co) have been presented previously in work [5]. As in the case of Co-implanted TiO_2 , the (100) TiO_2 sample reveal the ferromagnetic behaviour conventional for the system with in-plane *uniaxial* magnetic

anisotropy of FMR signal. The in-plane data for the (001) TiO₂ sample shows four fold magnetocrystalline anisotropy. The observed behaviour is attributed to textured growth of ferromagnetic Fe nanoparticles near surface of bulk crystal (see details in the work [5]).

FMR measurements of the single crystal ZnO substrates implanted with Co⁺ ions are presented in Fig.2. Similar to the case of Co-implanted TiO₂, FMR studies reveal a very strong room-temperature ferromagnetism in Co-implanted (0001) oriented ZnO sample (Fig.2). Again, a strong effect of the crystal magnetic anisotropy and the high magnetization value are observed in the in-plane and out-of-plane angular dependences. It should be noted that in some samples we have also observed weak EPR lines due to a small number of Fe³⁺ paramagnetic impurities with the spin-Hamiltonian parameters that are typical for the Fe³⁺ centers at Zn sites in the zinc oxide host.

Conclusions

In summary, magnetic resonance studies of single crystal TiO₂ rutile and ZnO substrates implanted with Co⁺ and Fe⁺ ions have been investigated at room temperature. We have shown the strong room-temperature ferromagnetism and very large crystal magnetic anisotropy of the single-crystalline Co(Fe)-TiO₂ and Co-ZnO samples. The observed behaviour is attributed to textured growth of ferromagnetic nanoparticles near surface of bulk crystal for the both systems (TiO₂ and ZnO).

Acknowledgements

The authors acknowledge support from the Scientific and Technical Research Council of Turkey (TUBİTAK) through the Project No. 115F472.

References

1. Zerentürk, M. Açıkgöz, S. Kazan, F. Yıldız, B. Aktaş, R.I Khaibullin, B RameevJ. - *Magn. Magn. Mater.*, **423**, 145-151 (2017).
2. R.I. Khaibullin, L.R. Tagirov, B.Z. Rameev, Sh.Z. Ibragimov, F. Yıldız, B Aktaş. - *J. Phys.: Condens. Matter*, **16**, L443–L449 (2004).
3. S. Güler, H. Bayrakdar, B. Rameev, R.I. Khaibullin, and B. Aktas. - *Phys. Stat. Sol. (a)*, **203(7)**, 1533–1538 (2006).
4. T. Dietl, H. Ohno, F. Matsukura, J. Cibert, D. Ferrand. – *Science*, **287**, 1019 (2000).
5. C. Okay, I.R. Vakhitov, V.F. Valeev, R.I. Khaibullin, B. Rameev. - *Applied Magnetic Resonance.*, **48(4)**, 347-360 (2017).
6. B. Aktaş, F.Yıldız, B.Rameev, R.Khaibullin, L.Tagirov, M.Özdemir. - *Phys. Stat. Sol. C*, **1(12)**, 3319–3323 (2004).
7. N. Akdoğan, B. Rameev, S. Güler, O. Oztürk, B. Aktaş, H. Zabel, R. Khaibullin and L. Tagirov. - *Appl. Phys. Lett.*, **95**, 102502 (2009).
8. N. Akdogan, B.Z. Rameev, R.I. Khaibullin, A. Westphalen, L.R. Tagirov, B. Aktas, H. Zabel. - *J. Magn. Magn. Mater.*, **300**, e4–e7 (2006).
9. S. Güler, B.Rameev, R.I.Khaibullin, O.N.Lopatin, B.Aktaş. - *J. Magn. Magn. Mater.* **322 (8)**, L13–L17 (2010).

The study of ionic liquids using NMR

K. Kass¹, A. V. Ievlev², E. Sorokina³

¹*Gimnasium № 261, SPb*

²*Department of Nuclear Physics research methods of physical faculty SPbSU,*

³*St. Petersburg Academy of Postgraduate Pedagogical Education, teacher of Gimnasium № 261*

Introduction

NMR is one of the most useful and informative methods in exploration of substances. Benefits of using this technology might be showed with an example of ionic liquid. Method of NMR-diffusometry is a straight way to define self-diffusion coefficient. Therefore the purpose of our study is carry out self-diffusion coefficient by using NMR-diffusometry and its temperature dependence. The object of our study is ionic liquid, on base of cation 1-Butyl-3-methylimidazolium (See on Fig. 1).

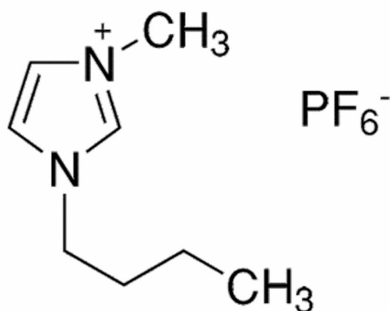


Figure 1. Structural formula of Ionic liquids 1-Butyl-3-methylimidazolium PF₆.

Experimental section

Register pseudo two-dimensional spectra of ionic liquid depending on the magnetic field gradient was measured on spectrometer Bruker Avance 500 Mhz. Further we Get the useful spectra from set of free induction decay by using softwares MestRenova, MagicFlot based on Fourier transform. Now for each temperature we define self-diffusion coefficient of diferent groups of ionic liquid. Create the graph of its temperature dependence. As a result of work spectra of ionic liquid were received, they were processed and analyzed by using softwares MestRenova, MagicFlot. With the help of these programs self-diffusion coefficient and its temperature dependence were defined.

Acknowledgements

The NMR measurements have been carried out in Center for Magnetic Resonance of Research Park of St. Petersburg State University.

Interaction of dendrigraft of second generation with molecules of LVFFAE peptide. Molecular dynamics simulation

Dilorom N. Khamidova, *Emil I. Fatullaev*, Sofia E. Mikhtaniuk, Igor M. Neelov

St. Petersburg National Research University of Information Technologies, Mechanics and Optics (ITMO University), Kronverkskiy pr.49, St.Petersburg, 197101, Russia

E-mail: ximik53@yandex.ru

Introduction

Alzheimer's disease is incurable neurodegenerative diseases. Inhibition of aggregation of amyloid peptides is one of the promising ways of control of this disease [1, 2]. Dendrigrafts are frequently used in biomedical applications for drugs and gene delivery. as antibacterial, antiviral and anti-amyloid agents. The structure of dendrigrafts is similar to structure of short dendritic brushes but they have shape and properties similar to that of lysine dendrimers [3].

Molecular dynamics (MD) method was frequently used for simulation of dendrimers and dendrigrafts [4-27]. In this work the MD simulation of interaction of dendrigraft of 2nd generation with stack of short amyloid peptides (LVFFAE) was performed in water solvent with explicit account of counterions at temperature $T=300\text{K}$ and pressure $P=1\text{atm}$ using the program package Gromacs-4.5.6 with AMBER99SB-ildn force field.

The Results and discussion

Snapshots of systems consisting of dendrigraft, peptides and counterions during simulation are shown on Fig. 1 (water molecules are not shown for clarity). One can see that at the beginning of simulation (Fig. 1, a) stack of peptide molecules is rather far from dendrigraft. After 30ns (Fig. 1, b, e) the stack was already destroyed by interaction with lysine dendrimer but peptide molecules are only partly adsorbed on dendrigraft. At 100 ns (Fig. 1, c, f) all peptide molecules are adsorbed on the surface of dendrigraft.

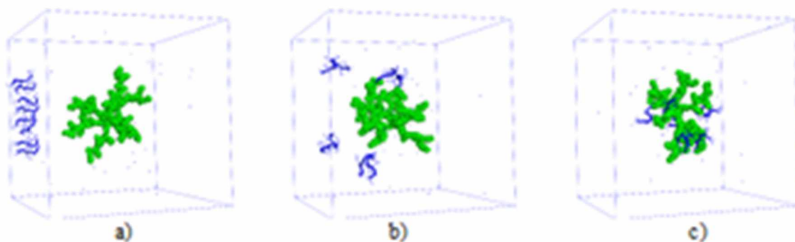


Figure 1. Snapshots of process of destruction of amyloid stack by DG2 dendrigraft and dendrigraft-peptide complex formation (initial, intermediate and final): system consisting of DG2 dendrigraft and 8 peptides at $t = 0$ (a), $t = 30$ ns (b), $t = 100$ ns (c)

The distance between peptide molecules in amyloid stack (Fig. 2a) is important characteristic of its stability. This distance during the first 30-40 ns (during the peptide stack destruction) increases. After 30 ns it become to decrease until 60ns (because peptide begin to adsorb on dendrigraft. And after that the function only fluctuates slightly so all peptide already adsorbed on dendrigraft and form stable complex with it.

We demonstrated that lysine dendrigraft destroy stack of amyloid peptides using molecular dynamics simulation approach. Thus lysine dendrigraft could be used in future as anti-amyloid agent in curing of Alzheimer disease.

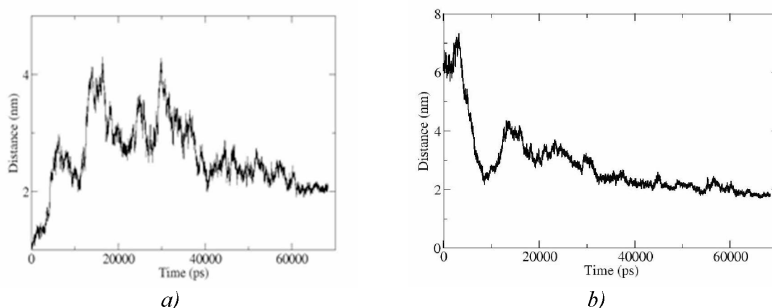


Figure 2. Changes in distances: between neighboring amyloid peptides during destruction of amyloid stack and dendrigraft-peptides complex formation (a) and between dendrigraft and amyloid peptides

Acknowledgements

This work was supported by grant 08-08 of Government of RF and RFBR grants 19-03-00715. The research is carried out using the equipment of the shared research facilities of HPC computing resources at Lomonosov Moscow State University supported by the project RFMEFI62117X0011.

References

- Petkova A.T., Yau W.M., Tycko R. "Experimental Constraints on Quaternary Structure in Alzheimer's β -Amyloid Fibrils". *Biochemistry*, 2006, 45, 498–512.
- Klajnert B., Bryszewska M., Cladera J. "Molecular Interactions of Dendrimers with Amyloid Peptides: pH Dependence". *Biomacromolecules*, 2006, 7, 2186–2191.
- Cottet H., Martin M., Papillaud A., Souaid E., Collet, A. Commeyras H., Determination of dendrigraft poly-L-lysine diffusion coefficients by Taylor dispersion analysis. *Biomacromolecules*, 8, 3235, (2007).
- Falkovich S., Markelov D., Neelov I., Darinskii A., Are structural properties of dendrimers sensitive to the symmetry of branching? Computer simulation of lysine dendrimers. *Journal of Chemical Physics*, 2013, 139, 064903.
- Neelov I.M., Markelov D.A., Falkovich S.G., Ilyash M.Yu., Okrugin B.M., Darinskii A.A. Mathematical simulation of lysine dendrimers: temperature dependences // *Polymer Science, Series C*. 2013, 55(1), 154–161.
- Markelov D.A., Falkovich S.G., Neelov I.M., Ilyash M.Yu., Matveev V.V., Lahderanta E., Ingman P., Darinskii A.A. Molecular dynamics simulation of spin-lattice NMR relaxation in poly-L-lysine dendrimers. Manifestation of the semiflexibility effect // *Physical Chemistry and Chemical Physics*. 2015, 17, 3214–3226.
- Oleg V. Shavykin, Igor M. Neelov, Anatolii A. Darinskii. Is the manifestation of the local dynamics in the spin-lattice NMR relaxation in dendrimers sensitive to excluded volume interactions? // *Phys. Chem. Chem. Phys.*, 2016, 18, 24307-24317.
- Sheveleva N.N., Markelov D.A., Vovk M.A., Mikhailova M.E., Tarasenko I.I., Neelov I.M., Lahderanta E. NMR studies of excluded volume interactions in peptide dendrimers // *Scientific Reports* - 2018, Vol. 8, pp. 8916
- Shavykin O.V., Popova E.V., Darinskii A.A., Neelov I.M., Leermakers F. Computer simulation of local mobility in dendrimers with asymmetric branching by brownian dynamics method // *Scientific and Technical Journal of Information Technologies, Mechanics and Optics*, 2016, 16(5), 893–902.

10. Okrugin B.M., Neelov I.M., Borisov O.V., Leermakers F.A.M. Structure of asymmetric peptide dendrimers: insight given by self-consistent field theory // *Polymer*, 2017, 125, 292.
11. Shavykin O.V., Mikhailov I.V., Darinskii A.A., Neelov I.M., Leermakers F.A. Effect of an asymmetry of branching on structural characteristics of dendrimers revealed by Brownian dynamics simulations // *Polymer*, 2018, 146, 256-266.
12. Shavykin O.V., Leermakers F.A., Neelov I.M., Darinskii A.A. Self-assembly of lysine-based dendritic surfactants modeled by the self-consistent field approach / *Langmuir*, 2018, 34 (4), 1613–1626
13. Okrugin, B., Ilyash, M., Markelov, D., Neelov, I. Lysine dendrigraft nanocontainers. Influence of topology on their size and internal structure // *Pharmaceutics*, 2018, 10(3), 129.
14. Darinskii A., Gotlib Yu., Lyulin A., Neelov I., Vysokomolekularnye Soedineniya. Seriya, 1991, 33, 1211 (translation to English: *Polymer Science*, 33,1116)
15. Darinskii A., Lyulin A., Neelov I., *Makromolekulare Chemie - Theory and Simulations (Macromolecular Theory and Simulations)*, 1993, 2, 523
16. Darinsky A., Gotlib Y., Lukyanov M., Lyulin A., Neelov I., *Progress in Colloid and Polymer Science*, 1993, 91, 13
17. Mazo M.A., Shamaev M.Y., Balabaev N.K., Darinskii A.A., Neelov I.M., *Physical Chemistry Chemical Physics*, 2004, 1285-1289
18. Neelov, I. M.; Janaszewska, A.; Klajnert, B; Bryszewska M., Makova N., Hicks D., Pearson N., Vlasov G.P., Ilyash M.Y., Vasilev D.S., Dubrovskaya N.L., Zhuravin I.A., Turner A.J., Nalivaeva N.N., *Current Medical Chemistry*, 2013, 20, 134
19. Popova E., Khamidova D., Neelov I., Komilov F., Chapter 3. “Lysine Dendrimers and Their Complexes with Therapeutic and Amyloid Peptides: Computer Simulation”, in “Dendrimers Fundamentals and Applications”, (IntechOpen), 2018, 29-45.
20. Neelov I.M., Adolf D.B., 2003, *Macromolecules*, 36, 6914
21. Neelov I.M., Adolf D.B., 2004, *Journal of Physical Chemistry B*, 108, 7627
22. Neelov I.M., Binder K., 1995, *Macromolecular Theory and Simulations* 4, 1063
23. Neelov I.M., Shavykin O.V., Ilyash M.Y., Bezrodnyi V.V., Mikhitarianuk S.E., Marchenko A.A., Fatullaev E.I., Darinskii A.A., Leermakers F.A.M., *Supercomputing Frontiers and Innovations*, 2018, 5, 60
24. Neelov I.M., Shavykin O.V., Ilyash M.Y., Bezrodnyi V.V., Mikhitarianuk S.E., Marchenko A.A., Fatullaev E.I., Darinskii A.A., Leermakers F.A.M., *Supercomputing Frontiers and Innovations*, 2018, 5, 60.
25. Neelov I.M., Okrugin B.M, Markelov D.A. Influence of the charged peptide dendrigrafts topology on the large-scale properties and their internal structure // *Magnetic Resonance and its application*, 2018, 99-100.
26. Bezrodnyi V.V., Neelov I.M., Ilonova E.B. Effect of dendrimer generation on the kinetics of peptide complex formation // *Magnetic Resonance and its application*, 2018, 232.
27. Sheveleva N.N., Markelov D.A., Vovk M.A., Mikhailova M.E., Tarasenko I.I., Neelov I.M., Lahderanta E. Study of local orientational mobility in lysine dendrimers by NMR method // *Magnetic Resonance and its application*, 2018, 242.
28. Shavykin O.V., Mihailov I.V., Neelov I.M., Darinskii A.A. Influence of asymmetry of branching on structural properties of dendrimer. Brownian dynamics simulation// *Magnetic Resonance and its application*, 2018, 239-241
29. Shavykin O.V., Darinskii A.A., Neelov I.M., Leermakers F.A.M. The sensitivity of local dynamics and its manifestations in NMR to excluded volume in dendrimers // *Magnetic Resonance and its application*, 2017, 89.

Temperature dependences of NMR spectra of ionic liquid EAN with addition of inorganic nitrates

M. A. Khasanov, A. V. Ievlev

Department of Nuclear Physics Research Methods, Faculty of Physics, Saint-Petersburg State University

E-mail: makhas18@gmail.com

Ionic liquids (further IL) are molten salts that are in a liquid state with a fairly wide temperature range. They are called ionic due to the fact that this melt contains only ions, or rather consists of bulk organic cations and inorganic or organic anions. High interest in IL is associated with wide application in applied sciences, biotechnology, energy, etc. The advantage is that ILs are used more and more in “green” chemistry.

There is currently a high interest in studying ionic liquids with a melting point lower than water (0 degrees Celsius). One of the widely studied ILs is ethylammonium nitrate (hereinafter EAN), which has the formula $(C_2H_5)_3NH^+NO_3^-$. EAN has many water-like properties, such as micelle formation, hydrocarbon aggregation, negative enthalpy and gas dissolution entropy, etc. Like water, EAN can form three-dimensional hydrogen bonds. In particular, EAN is used as an electrically conductive solvent in electrochemistry and as an agent for protein crystallization.

In this paper, we consider the NMR spectra of both pure EAN and EAN mixtures with the addition of other salts, in our case, aluminum and magnesium nitrates. The temperature dependences of 1H and ^{14}N of the EAN NMR spectra with the addition of $Mg(NO_3)_2 \cdot 6H_2O$ and $Al(NO_3)_3 \cdot 9H_2O$ were obtained. The report will provide a detailed analysis of these dependencies.

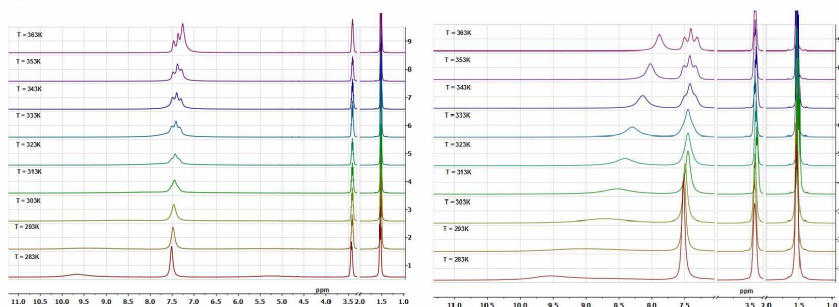


Figure 1. Proton NMR spectra of dried salt solutions in EAN: 1) $Mg(NO_3)_2$; 2) $Al(NO_3)_3$

Also this work is a continuation of the study of systems based on the EAN, conducted by us earlier [1, 2]. We decided to pay attention to systems with nitrates of magnesium and aluminum, or rather shifted the main focus of our work on the study of the temperature dependences of the NMR spectra and the measurement of the NMR relaxation of the residual water line in these samples. The main conclusions of this work will be presented in a report at the conference.

Acknowledgements

The NMR measurements have been carried out in Center for Magnetic Resonance of Research Park of St. Petersburg State University.

References

1. Matveev, V. V., Ievlev, A. V., Vovk, M. A., Cabeza, O., Salgado-Carballo, J., Parajó, J. J., Rodríguez, J. R., Fuente, R. D. L., Lähderanta, E., Varela, L. M. NMR investigation of the structure and single-particle dynamics of inorganic salt solutions in a protic ionic liquid // *J. Mol. Liq.*, Vol. 278, 2019, pp. 239-246.
2. Alexandr V. Ievlev, Vladimir V. Matveev, Mikhail A.Vovk Analysis of NMR spectra of ionic liquid EAN with the addition of inorganic salts// *Magnetic Resonance and its application*, 2018, Issue 15, pp. 71-72.

Nuclear spin-lattice relaxation ^{63}Cu in semiconductor compound CuAlO_2

*Rustem R. Khlusnutdinov¹, Vasilii V. Ogloblichev², Vadim L. Matukhin¹,
Irina Yu. Arapova², Stanislav V. Shmidt¹*

¹Kazan State Power Engineering University, Kazan, 420066, Russia

²M.N. Miheev Institute of Metal Physics of Ural Branch of Russian Academy of Sciences,
Yekaterinburg 620108, Russia
khrr@yandex.ru

Introduction

Recently, the group of transparent conductive oxides with the chemical formula CuMO_2 , where M is a trivalent metal (M-Al, Ga, Sc, Y, Cr), have attracted special attention as the materials for possible application in energy technologies of direct energy conversion [1]. The semiconducting compound CuAlO_2 belongs to this group of transparent conductive oxides with p-type electrical conductivity. The purpose of this work is to study the nuclear relaxation of copper isotopes at low temperatures by the method of nuclear quadrupole resonance (NQR $^{63,65}\text{Cu}$) in the semiconductor compound CuAlO_2 .

Methods

The $^{63,65}\text{Cu}$ NQR measurements were carried out on a pulse spectrometer Avance III 500 ("Bruker" company) in cryostat ("Oxford Instruments" company) in zero external magnetic field. The $^{63,65}\text{Cu}$ spectra were obtained using the standard spin-echo sequence $\tau\text{-}t_{\text{del}}\text{-}2\tau\text{-}t_{\text{del}}\text{-}$ echo. Measurements of NMR spectra were carried out with the delay time $t_{\text{del}}=40\text{-}90\ \mu\text{s}$. The spin-spin relaxation time T_2 was measured when the delay time t_{del} between pulses changed in the $t_{\text{del}}=40\text{-}400\ \mu\text{s}$ interval in the spin-echo-pulse sequence. The spin-lattice relaxation time T_1 was measured by the method of inversion and subsequent recovery of nuclear magnetization. For this measurement, we used pulse sequence $2\tau\text{-}t_{\text{inv}}\text{-}\tau\text{-}t_{\text{del}}\text{-}2\tau\text{-}t_{\text{del}}\text{-}$ echo with a constant delay of $50\text{-}80\ \mu\text{s}$ in the interval $t_{\text{inv}}=10\text{-}900\ \text{ms}$. The spin-spin and spin-lattice relaxation times were handled by exponential dependencies $M(2t_{\text{del}})=M_0\exp(-2t_{\text{del}}/T_2)$ and $M(t_{\text{inv}})=M_0[1-2\exp(-t_{\text{inv}}/T_1)]$, respectively [2]. M_0 is the equilibrium nuclear magnetization of the spin system and $M(t)$ is the nuclear magnetization at time t . The signal was repeatedly accumulated with the repetition time of $4T_1$ to increase the signal-to-noise ratio.

Results

The temperature dependence of the rate of nuclear spin – lattice relaxation rate ($1/T_1$) for the most common copper isotope ^{63}Cu in CuAlO_2 was previously investigated [3]. This dependence has a wide maximum in the range from 100 to 250 K, but no specific features in the behavior of the spectral parameters of the ^{63}Cu NQR (frequency and width of the resonance line) were detected in this temperature range. It should be noted that the value of the spin-spin relaxation time in the investigated temperature range also does not change. It was previously established that the dominant contribution to the rate of nuclear spin-lattice relaxation is due to quadrupole interaction [4] at low temperatures. In this case, an increase in the relaxation rate should be associated with fluctuations of the EFG tensor $V_{\alpha\beta} = \partial^2 V / \partial x_\alpha \partial x_\beta$, where V is the potential of the electric field at the location of the resonant nuclei [3]. As is known, the rate of spin-lattice relaxation ($1/T_1$) is proportional to the spectral density $J(\omega_n)$ of fluctuations of the internal fields causing transitions in the nuclear spin system at the resonance NQR frequency ω . In the case of an exponential correlation function with a correlation time τ_c ($\langle V_{\alpha\beta}(t)V_{\alpha\beta}(0) \rangle = \langle V_{\alpha\beta}^2 \rangle \exp(-t/\tau_c)$), the relaxation rate is determined by the formula [2]:

$$1 / T_1 \sim \Delta^2 \tau_c (T) / [1 + \omega^2 \tau_c (T)^2],$$

where Δ is the magnitude of the transition matrix element of the quadrupolar interaction. This value is proportional to the amplitude of the EFG fluctuations $\langle V_{q\beta} \rangle$ appropriately averaged over different EFG tensor components. Assuming the activation character of the temperature dependence $\tau_c(T) = \tau_c(\infty) \exp(E_A/T)$ from the analysis of $[T_1(T)]^{-1}$, the activation energy of the internal movement $E_A = 45$ (2) meV is obtained.

Fluctuations of the EFG tensor at low temperatures in CuAlO_2 can be associated with hopping charge carriers — holes between different localized states. Earlier it was found that in the low-temperature region ($T < 190$ K), the electrical conductivity obeys the hopping conductivity mechanism with variable hop length. The obtained value of the activation energy corresponds to the values of the activation energy of electrical conductivity in the hopping conductivity mode with a variable jump length obtained for compounds that have a delafossite structure [5].

The results were obtained within the state assignment of Minobrnauki of Russia (theme "Function" No. AAAA-A19-119012990095-0).

References

1. A. N. Banerjee, R. Maity, P. K. Ghosh, K. K. Chhtopadhyay. Thin Solid Films., Vol. 474, № 1-2. P.261-266 (2005).
2. V. I. Chizhik, Y. S. Chernyshev, A. V. Donets, V. Frolov, A. Komolkin, M. G. Shelyapina. Magnetic Resonance and Its Applications (in English). – "Springer" Publ., Berlin, 2014.
3. V. V. Ogloblichev, V. L. Matukhin, I. Ya. Arapova, D. A. Shulgin, R. R. Khusnutdinov. Appl. Magn. Reson., Vol. 49, № 11. pp.1-7 (2018).
4. V. L. Matukhin, D. A. Shulgin, S. V. Shmidt, E. I. Terukov. Semiconductors., Vol. 48, № 6. P.779-782 (2014).
5. W. Lan, M. Zhang, G. Dong, Y. Wang, H. Yan, H. Yan. J. Mater. Res., Vol. 22, № 12. (2007).

Modeling of dynamics and calculation of relaxation parameters for monomer of bovine insulin

Naira R. Khusnutdinova, Aidar R. Yulmetov

Institute of Physics, Kazan Federal University, Kazan, Russia

E-mail: nai.khus@yandex.ru

Introduction

The main effect of insulin is to reduce the concentration of glucose in the blood. If there is insulin disruption of work or secretion disorder one may suffer from diabetes mellitus (DM). It is classified into types: 1, 2, gestational DM, and other cases such as monogenic diabetes syndromes [1]. All patients with type 1 DM and many suffering from the other types have to take insulin injections. So, it is really important to study molecular properties of insulin. In this work computer model of bovine insulin monomer was made and were calculated parameters such as correlation function and cross-relaxation rate, compared with experiment.

Theory

The primary structure of insulin in different species varies, as does its importance in the regulation of carbohydrate metabolism. Closest to human is pig insulin, which differs with only one amino acid residue, next closest variant is bovine insulin – it differs by three amino acid residues: Ala8A–Thr8A, Val10A–Ile10A, Ala30B–Thr30B (former residues belong to the bovine form; latter – human). This difference does not alter the most conservative and important segments of insulin, A1–A3, A12–A17, and B8–B25 [2].

Synthesis of insulin begins with production of a longer peptide, then disulfide bridges are formed and a segment of the chain is removed. Mature insulin molecule consists of two chains called A (shorter) and B (longer). Six insulin molecules are associated in a hexamer (three symmetrical axes are visible). Molecules hold together histidine residues bound by zinc ions. The insulin is injected under the skin in the form of a hexamer, gradually breaking down into biologically active monomers entering the bloodstream [3].

The main quantity from 2D NOE experiments is the cross-relaxation rate σ_{ij} describing how magnetization is transferred between spins i and j via dipolar coupling. Theory, relating relaxation rates from NOE experiments to correlation functions describing molecular motions has been reviewed in publications [4, 5]:

$$\sigma_{ij} = \frac{\pi}{5} \gamma^4 \hbar^2 [6J_{ij}(2\omega) - J_{ij}(0)] \quad (1)$$

where ω – Larmor frequency, γ – gyromagnetic ratio of protons, J_{ij} – spectral densities, which characterize the modulation of dipolar coupling between nuclei with time. While the spectral density is the Fourier transform of the correlation function of the dipole-dipole interaction [6], which may be calculated basing on coordinates of each nuclei.

$$C(t) = \frac{1}{5} \left\langle \frac{P_2(\hat{\mu}_{L,ij}(t)\hat{\mu}_{L,ij}(0))}{r_{ij}^3(t)r_{ij}^3(0)} \right\rangle \quad (2)$$

where $\hat{\mu}_{L,ij}$ – unit vector in the direction of the inter-proton vector, $r_{ij}(0)$ – the distance of the two protons, P_2 – second Legendre polynomial.

Computer modelling

Studied molecule was modeled with GROMACS [7] package (fig. 1). Monomer of bovine insulin was relaxed through an energy minimization, then placed in water. There were made equilibration conducted in two phases – NVT, NPT (constant Number of particles,

Volume (or Pressure) and Temperature). After, trajectories of nuclei of this molecule in water were collected.

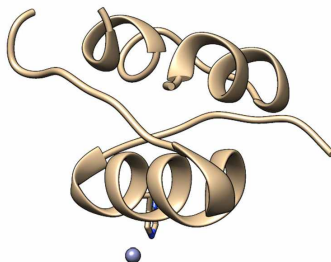


Figure 1. Monomer of bovine insulin

With MatLab package was made code based on GROMACS trajectories data. Example of such correlation function for IleA2 Ha -IleA2 HN is given below (fig. 2):

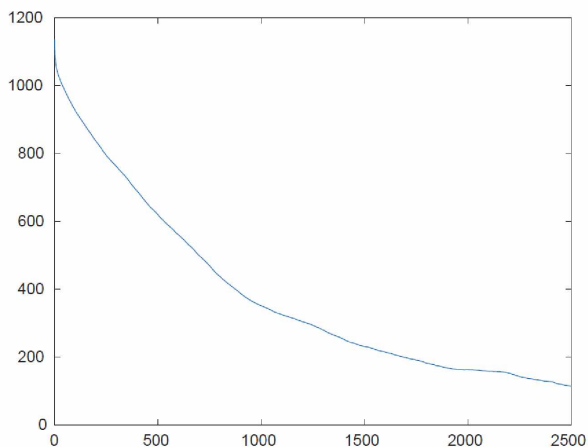


Figure 2. Correlation function

With these correlation functions were calculated cross-relaxation rates, which may be compared with experimental ones.

References

1. S. V. Efimov, Yu. O. Zgadzay, N. B. Tarasova, V. V. Klochkov. Evidence of oligomerization of bovine insulin in solution given by NMR. – *European Biophysics Journal.*, <https://doi.org/10.1007/s00249-018-1310-6> (2018).
2. J Mayer, Z Faming, R DiMarchi. Insulin structure and function. – *Pept Sci.*, 88,687 (2007).
3. X. Chang, AM Jorgensen, P Bardrum, JJ Led. Solution structures of the R6 human insulin hexamer. – *Biochemistry.*, (1997).

4. D. M. LeMaster, L. E. Kay, A.T. Brünger, J.H. Prestegard. Protein dynamics and distance determinations by NOE measurement. – *FEBS Letters.*, 236, 71-76 (1988).
5. C. B. Post. Internal motional averaging and three-dimensional structure determination by nuclear magnetic resonance. – *J. Mol. Biol.*, 224, 1087-1101 (1992).
6. T. R. Schneider, A.T. Brünger, M. Nilges. Influence of Internal Dynamics on Accuracy of Protein NMR Structures: Derivation of Realistic Model Distance Data from a Long Molecular Dynamics Trajectory. – *JMB.*, 285, 727-740 (1999).
7. Berendsen, et al. GROMACS: A message-passing parallel molecular dynamics implementation. – *Comp. Phys. Comm.*, 91, 43-56 (1995).

Magnetic resonance study of the peculiarities of the paramagnetic-ferromagnetic transition in manganites on the example of $\text{La}_{0.78}\text{Ca}_{0.22}\text{MnO}_3$

I. A. Kiselev, V. A. Ryzhov, V. V. Deriglazov

*Petersburg Nuclear Physics Institute named by B. P. Konstantinov of National Research
Centre «Kurchatov Institute»*

E-mail: Kiselev_IA@npni.nrcki.ru

Currently, doped manganites with colossal magnetoresistance (CMR), such as $\text{La}_{1-x}\text{Ca}_x\text{MnO}_3$, are among the most promising materials for applications. They exhibit strong correlations between charge, orbital, magnetic and lattice degrees of freedom leading to a rich phase diagram. In the study of single crystal $\text{La}_{0.78}\text{Ca}_{0.22}\text{MnO}_3$ by the electron magnetic resonance (EMR) spectrometer of wide lines [1] we allocated a signal from small-radius polarons, which are formed above the temperature of a paramagnetic-ferromagnetic (PF) transition ($T_C \approx 186\text{K}$). In addition to the PF transition, an insulator-metal (IM) transition with $T_{IM} \approx 201\text{K}$ also develops in this system. The percolation transition of IM occurs due to an increase in the number of ferromagnetic metal clusters formed in a paramagnetic matrix. In this system, polarons appear at the temperature $T_{pol} \approx 234 - 239\text{K}$ (for different temperature treatments of EMR), which is close to the temperature of a homogeneous nucleation of ferroclusters $T^* \approx 240\text{K}$ [2]. Note that the temperature dependence of the g -factor of the polaron peak correlates with the temperature dependence of the g -factor of the paramagnetic matrix and differs sharply from that of ferroclusters. This indicates a relation between polarons and the paramagnetic matrix in the system under study. Small-radius lattice polarons were earlier detected in $\text{La}_{1-x}\text{Ca}_x\text{MnO}_3$ ($0.21 \leq x \leq 0.45$) by neutron diffraction [3]. In [4], when studying the fine structure of X-ray absorption, it was shown that in $\text{La}_{0.79}\text{Ca}_{0.21}\text{MnO}_3$ polarons are formed at $T \approx 240\text{K}$, which coincides with our EMR data. From the measurement of the resistance $R(T)$, it was found that the dependence $\ln(R/T)$ on $1/T$ in $\text{La}_{0.78}\text{Ca}_{0.22}\text{MnO}_3$ shows a crossover at $T_{cr} \approx 233\text{K}$, which is also close to T_{pol} . These data indicate the influence of polarons on the PF and IM transitions, the formation of the phase-separated magnetic state of the system and the CMR.

References

1. V. A. Ryzhov, E. I. Zavatskii, V. A. Solov'ev, I. A. Kiselev, V. N. Fomichev, V. A. Bikineev, *Zh. Tekh. Fiz.* 65, 133 (1995)
2. V. A. Ryzhov, A. V. Lazuta, O. P. Smirnov, V. P. Khavronin, P. L. Molkanov, Ya. M. Mukovskii and V. I. Chichkov, *Solid State Phenomena*, Vols. 168-169, 485-488 (2011)
3. Pengcheng Dai, J. A. Fernandez-Baca, N. Wakabayashi, E. W. Plummer, Y. Tomioka, Y. Tokura, *Phys. Rev. Lett.*, 85, 2553 (2000).
4. F. Bridges, L. Downward, J. J. Neumeier, and T. A. Tyson, *Phys. Rev. B*, 81, 184401 (2010).

Investigation of the spatial structure of different drugs, proteins & oligopeptides, and their complexes with models of cell membrane in solution by modern NMR spectroscopy

V. V. Klochkov

NMR Laboratory, Institute of Physics, Kazan Federal University, 420008, 18 Kremlevskaya St., Kazan, Russian Federation

Aims of study. Results

The goal of the investigation is to study conformational features and dynamics of different pharmaceutical objects such as cholesterol-lowering drugs (statins), vitamin B₆, cyclosporins. Another aim of this work is investigation of the mechanisms of interaction between these compounds and cell membranes using model membranes by NMR spectroscopy methods.

BioNMR group of NMR laboratory is investigating the role of various peptides and proteins in cellular processes and disease. Our goal is to understand the function of peptides and their mechanism of cellular toxicity in terms of structure. We used high-resolution magnetic resonance (NMR) spectroscopy to determine structures of biological macromolecules such as amyloid β -peptides, antimicrobial peptides protegrins (PG), of the N-terminal fragments of the HIV enhancer prostatic acid phosphatase peptide (PAP), of the N-terminal domain of telomerase, insulins and integrate our structural understanding into further functional studies.

Experimental

All NMR experiments were performed on a Bruker Avance III HD 700 and Bruker Avance II 500 MHz NMR spectrometers equipped with 5 mm probes and using standard Bruker TopSpin software. Assignments of ¹H and ¹³C NMR signals of compounds were achieved from signal multiplicities, integral values and characteristic chemical shifts from the through-bond correlations in 2D COSY spectra, through-space correlations in 2D NOESY spectra as well as from ¹H-¹³C heteronuclear correlations in 2D HSQC and HMBC spectra.

The spatial structure of different drugs and proteins in solution and in a complex with dodecylphosphocholine (DPC) and sodium dodecyl sulfate (SDS) micelles was investigated by ¹H nuclear magnetic resonance spectroscopy and two-dimensional (2D) NMR spectroscopy (total correlation spectroscopy and nuclear Overhauser effect spectroscopy (NOESY)). Analysis of the interproton distances obtained from the 2D NOESY NMR spectra was used to reveal the spatial structure of different drugs and proteins. Complex formation was confirmed by the analysis of ¹H chemical shifts in the NMR spectra of the drugs and the proteins and by the analysis of the signs and values of NOEs in a solution with micelles.

References

1. Structure and function of the N-terminal domain of the telomerase reverse transcriptase /Petrova, O.A., Mantsyzov, A.B., Rodina, E.V., Efimov, S.V., Hackenberg, C., Hakanpää, J., Klochkov, V.V., Lebedev, A., Malyavko, A., Zatsepin, T.S., Zvereva, M.I., Lamzin, V.S., Dontsova, O.A., Polshakov, V.I.// *Nucleic Acids Research.* - 2018. -V. 46, Issue 3. - P. 1525–1540.
2. Sulfur-containing monoterpenoids as potential antithrombotic drugs: research in the molecular mechanism of coagulation activity using pinanyl sulfoxide as an example / L. E. Nikitina, S. V. Kiselev, V. A. Startseva, A. V. Bodrov, Z. R. Azizova, O. T. Shipina, I. V. Fedyunina, S. V. Boichuk, O. A. Lodochnikova, V. V. Klochkov, L. F. Galiullina, A. V. Khaliullina // *Frontiers in Pharmacology.* - 2018. - V.9, Issue 2, Article 116. - P. 1-12.

3. Efimov, S.V. Evidence of Oligomerization of Bovine Insulin in Solution Given by NMR [text] / S.V. Efimov, Yu.O. Zgadzay, N.B. Tarasova, V.V. Klochkov// *European Biophysics Journal*. – 2018.- <https://doi.org/10.1007/s00249-018-1310-6>
4. Spatial Structure and Conformational Mobility of Seven-Membered Cyclic Acetals and Ketals Containing Pyridoxine Moiety in Solution by NMR Methods /I.Z. Rakhmatullin, L.F. Galiullina, A.A. Balandina, F.K. Karataeva, Y.G. Shtyrlin, V.V. Klochkov// *BioNanoScience*.- 2018.- <https://doi.org/10.1007/s12668-018-0562-z>

NMR studies on ion dynamics in solid electrolytes for batteries

Edda Klotz¹, Stefan Spammenberger², Marc Duchardt², Bernhard Roling², and Michael Vogel¹

¹*Institut für Festkörperphysik, TU Darmstadt, Germany*

²*Department of Chemistry, University of Marburg, Germany*

Introduction

In order to improve safety, lifetime, and energy density in batteries, all-solid state ion batteries are of great significance in modern-day research. One of their key components are solid electrolytes with high ionic conductivities. In this area, various materials based on Li⁺-ions as well as Na⁺-ions have been investigated and found to have the potential to outperform the liquid electrolytes currently used in ion batteries, in particular in relation to safety issues.

The improvement of these materials, however, depends directly on understanding the ion dynamics that determine the ion conductivity.

Methods

By combining various NMR techniques such as spin-lattice relaxation, stimulated-echo and line-shape analysis, we are able to investigate local ion dynamics in broad time and, thus, temperature ranges. Additionally, self-diffusion coefficients are determined using static field gradient NMR (SFG).

Results

We apply those methods to investigate the effects of ceramization in glassy Li-ion conductors. In particular, we examine the amorphous system 0.33 LiI + 0.67 (0.75 Li₂S + 0.25 P₂S₅), which shows a significant increase of Li-conductivity upon heat treatment and partial crystallization.

Due to rising energy demands and limited supply of Lithium, it is also crucial to expand research to alternative materials for solid state batteries. Promising candidates for that are selenide- as well as sulfide-based Na⁺ superionic conductors. Via ²³Na central transition excitation we study samples consisting of Na₁₁Sn₂PSe₁₂ and Na₁₁Sn₂PS₁₂ respectively.

We show that local dynamics and macroscopic diffusion can often be consistently described by the same broad distributions of activation energies [1].

References

1. Haaks et al., Phys. Rev. B 96, 104301 (2017)

Studying of Cyclosporin D by High Resolution NMR: Obtaining Information on the Spatial Structure

P. P. Kobchikova, S. V. Efimov, I. A. Khodov, V. V. Klochkov

Institute of Physics, Kazan (Volga region) Federal University, Russia

E-mail: pollymoon@ya.ru

<https://kpfu.ru/physics/struktura/kafedry/kafedra-medicinskoj-fiziki>

Introduction

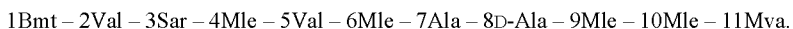
Targeted synthesis of selective biologically active substances, i.e. substances that have no side effects, has been a point of interest for scientists for a long time. Many laboratories both in academics and in industry are aiming to establish a link between the structure of substances and their biological properties. Additional knowledge in the sphere of drug design [1] impacts chemistry, as well as biology and medicine. At first, scientists only paid attention to the chemical composition of substances, but they eventually realized that their molecular configuration is just as important. Although Barton [2] has clearly shown the role molecular conformation plays in chemistry and biology, there have only been weak attempts to study the relationship between conformation and biological activity [3].

There has been a great deal of interest in cyclic peptides as scaffolds in the development of drugs against difficult targets such as protein–protein interactions, based on the premise that large macrocycles are better suited to the inhibition of large binding surfaces. Solving conformations of cyclic peptides can provide insight into structure–activity and structure–property relationships, which can help in the design of compounds with improved bioactivity and/or ADME characteristics.

Object

Considerable progress in transplantation of the last few decades is due to the development and introduction of immunosuppressive drugs to clinical practice, that increase the survival rates of both patients and transplants [4].

Cyclosporin D is a metabolite of cyclosporin A, an immunosuppressive drug that binds to cyclophilin, inhibiting the phosphatase activity of calcineurin in T cells. In the composition of CsD there are 11 amino acids, some of them have several instances:



Different tendencies of cyclosporin molecules A, D etc. to formation of complexes with proteins (especially, cyclophilins) lead to observed differences in their biological activity. The reason for that lies in structural features of specific peptides, which in case of cyclosporin as a representative of cyclic peptides shows special properties [4]: relative stability within organism and the ability to adopt different conformations. Efficiency of CsA as an immunosuppressive drug is considerably higher than that of CsD. However, CsD interests us, because the question of significance of conformation as the main factor, which affects substance's properties, is raised. The only difference between CsD's and CsA's compositions is the second amino acid residue. The structure of CsA is presented below in figure 1; the picture also shows the part of the molecule, which is different in CsA and CsD.

Method

Measurements were carried out on a Bruker Avance III HD 700 spectrometer. Signal assignment was made using a combination of 2D spectra: DQF-COSY, TOCSY, HSQC and HMBC, recorded at 25°C. Strong signal overlap regions hamper identification of some atoms, including Mle4 H α and two protons at the double bond in Bmt1 (~5.35 ppm); atoms Bmt1 H η , H γ and CH $_{2\delta}$ all have close signals in the same region together with some of inequivalent CH $_{2}$

protons of other residues (1.6–1.65 ppm). Heteronuclear spectra were necessary to clarify these overlap regions, assign NCH₃ groups, and determine the place of each residue in the 11-member chain through the signals of carbonyl carbons. Homonuclear 2D spectra were recorded in the spectral window of 10x10 ppm and time domain size of 2048x512 points. HSQC spectra covered the spectral width of 10x140 ppm (centered at 65 ppm) with 2048x512 points; HMBC had the parameters 10x200 ppm (the center at 95 ppm) and 4096x512 data points. HMBC spectra were optimized for the long-range scalar coupling of 6 Hz.

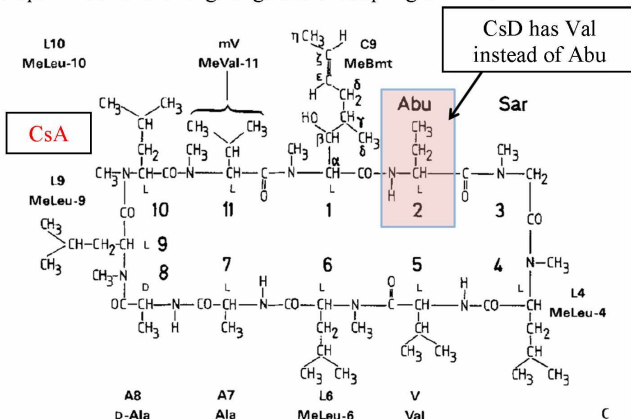


Figure 1. The structure of CsA. The second residue of CsD is replaced with Val

Results

Cyclosporin D has been studied by NMR in CDCl₃. Chemical shift values were obtained from high resolution NMR spectra. Values for CsA were obtained earlier [5]. Results for CsD and CsA are shown in Table 1.

Table 1. Chemical shifts for CsD and CsA

CsD					CsA				
Res. No.	C α	H α	C'	NH	Res. no.	C α	H α	C'	NH
1	59.00	5.555	170.72		1	58.97	5.461	170.6	
2	53.97	4.75	173.90	7.99	2	48.94	5.021	174	7.964
3	50.51	4.72	171.20		3	50.5	4.725	171.4	
		3.183					3.198		
4	55.57	5.32	170.02		4	55.63	5.334	170.2	
5	55.63	4.61	173.80	7.57	5	55.56	4.646	174	7.468
6	55.34	4.97	171.53		6	55.48	4.973	171.8	
7	48.58	4.53	171.05	7.67	7	48.77	4.511	171.4	7.681
8	45.12	4.83	173.39	7.15	8	45.33	4.82	173.7	7.163
9	48.25	5.70	170.30		9	48.35	5.687	170.5	
10	57.64	5.06	170.08		10	57.69	5.069	170.3	
11	57.86	5.2	173.64		11	58.06	5.119	173.7	

Then Table 2 was composed, consisting of the differences between the chemical shifts of the two studied peptides. Thus, the sites where the most noticeable changes of chemical shifts occur due to the replacement of the second residue can be revealed.

Table 2. Differences between chemical shifts for CsD and CsA

Res. No.	ppm(CsD) – ppm(CsA)			
	C α	H α	C'	NH
1	0.03	0.094	0.117	
2	5.033	-0.273	-0.098	0.031
3	0.016	-0.003	-0.198	
		-0.015		
4	-0.057	-0.012	-0.176	
5	0.074	-0.032	-0.192	0.106
6	-0.142	-0.001	-0.274	
7	-0.187	0.021	-0.35175	-0.011
8	-0.208	0.015	-0.3085	-0.01
9	-0.102	0.011	-0.19475	
10	-0.047	-0.009	-0.223	
11	-0.199	0.002	-0.055	

Conclusions

Substitution of the second residue with different amino acids influences mainly the backbone chemical shifts in positions 2, its neighbors 1 and 3, and in more distant positions 5 (valine) and 8 (D-alanine). Residues 5 and 8 were the most sensitive to the amino acid substitution at the position 2. Further detailed information on the spatial structure is needed to clarify how the backbone and side chain orientations are altered, and how this may modify the biological behavior of cyclosporin.

Acknowledgments

The work was supported by the Russian Science Foundation (project 18-73-10088).

References

1. Y. C. Martin, M. Dekker. – *Medicinal Research Series*, **8**, 440 (1978)
2. D. H. R. Barton. – *Angew. Chem.* **82**, 827 (1970)
3. H. Konig. – *Angew. Chem.*, **92**, 802 (1980)
4. D. J. Craik. – *Science*, **311**, 1536-1564 (2006)
5. S. V. Efimov, F. Kh. Karataeva, A. V. Aganov et al. – *J. Mol. Struct.*, **1036**, 298-304 (2013)

Microstructure and dynamics of ions in mixtures of imidazolium-based ionic liquids with water. A molecular dynamics simulation study

V. A. Konovalov, A. V. Egorov, V. I. Chizhik

Department of Nuclear-Physics Research Methods, Faculty of Physics, Saint-Petersburg State University

E-mail: konovalov.phys@gmail.com

Introduction

Water mixtures with imidazolium-based ionic liquids (IL) have been extensively studied in the recent years for both fundamental and technological reasons. However, in spite of considerable efforts, several problems are still unsolved. In the present study atomistic molecular dynamics simulations were employed to investigate the effect of water presence on dynamics of ions in water mixtures with 1-butyl-3-methylimidazolium nitrate and tetrafluoroborate.

Five systems (11, 20, 33, 50, and 100 mol% of IL) were considered. Simulations were carried out using the MDynaMix package [1]. Water was simulated with the rigid five-site TIP5P [2] model. The ions were modeled using the potentials described in the Refs. [3-5]. Each system was simulated in the NPT ensemble at 298 K and atmospheric pressure. The effect of water concentration on the mixture structural and dynamical properties was studied in details. A special attention was given to the water effect on self-diffusion of ions (Fig. 1).

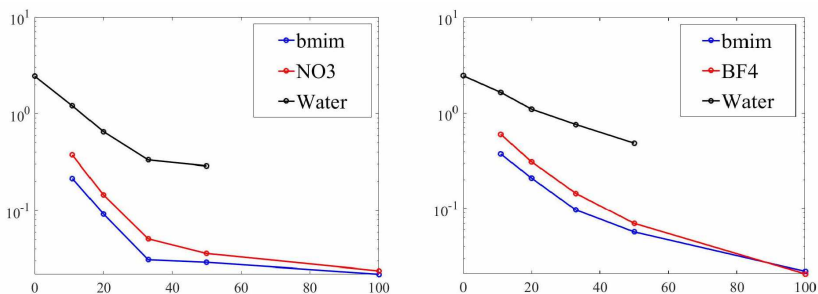


Figure 1. Concentration dependence of self-diffusion coefficients (in $10^{-9} \text{ m}^2/\text{s}$) of mixture components at 298 K and 1 atm. Concentration is given in mol% of IL

Acknowledgements

This work was supported by the Russian Foundation for Basic Research (grant 17-03-00057a).

References

1. A. P. Lyubartsev, A. Laaksonen. – *Comp. Phys. Comm.*, **128**, 565 (2000).
2. W. Mahoney, W. L. Jorgensen – *J. Chem. Phys.*, **112**, 8910 (2000).
3. J. N. C. Lopes, J. Deschamps, A. A. H. Padua – *J. Phys. Chem. B*, **108**, 2038 (2004).
4. J.-C. Soetens, C. Millot, B. Maigret – *Phys. Chem. A*, **102**, 1055 (1998).
5. T. Megyes, S. Balint, E. Peter, T. Grosz, I. Bako, H. Krienke, M.-C. Bellissent-Funel – *J. Phys. Chem. B*, **113**, 4054 (2009).

Influence of fast fluctuation of Earth magnetic field on NMR-spectra

Pavel Kupriyanov, Vladimir I. Chizhik

*St. Petersburg State University, Russia
p.kupriyanov@spbu.ru*

Fluctuations of the Earth magnetic field prevent the accumulation of NMR signals in Earth magnetic field to obtain high-resolution spectra of liquids with small abundance of studied nuclei. There are a few methods for the neutralization of influence of the Earth magnetic field fluctuations [1-3]. Using the reference signal from the second sensor with a special liquid is very promising idea. But techniques, which use directly the reference analog NMR-signal for the synchronous or quadrature detection of a signal from a studied sample, are not suitable for high resolution NMR-spectroscopy. The fact is that in this case the reference signal has significant interferences at the end. For the high-quality detection, it is better to have the reference signal (sine or another mathematical form) with the constant amplitude. Therefore, the method proposed in the work [3] is most suitable, but this way also possesses flaws. It does not take into account the rapid oscillations of the earth's magnetic field during registration NMR-signal. We have investigated methods for registration such rapid fluctuations in the NMR signal (fig. 1) in order to evaluate their effect on the resulting NMR spectrum and further take them into account in our experiments.

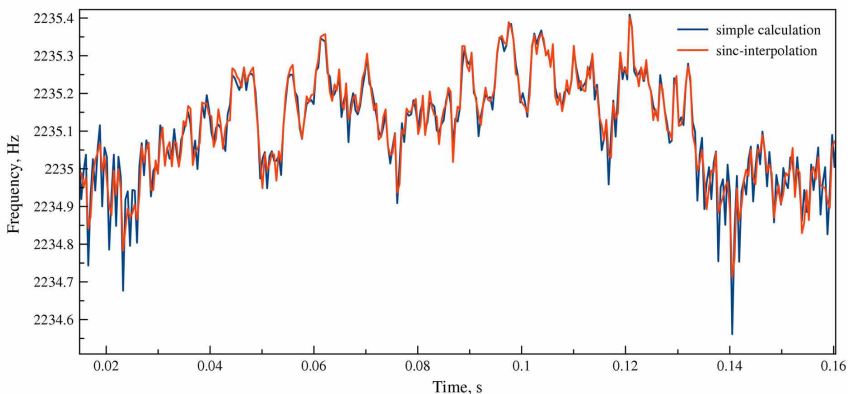


Figure 1. Comparison of two methods to register the fluctuations of the NMR-signal frequency: the simple calculation of a period (blue) and the sinc-interpolation (red)

References

1. Chernyshev Y. S. «A device for conducting nuclear magnetic logging method of spin echo» Certificate of authorship №166419, 1963.
2. Aleš Mohorič, Gorazd Planinšič, Miha Kos, Andrej Duh, Janez Stepišnik, «Magnetic Resonance Imaging System Based on Earth's Magnetic Field» Instrumentation Science and Technology, Vol. 32, No. 6, pp. 655–667, 2004.
3. Chizhik V. I., Kupriyanov P. A. «Device for stabilizing the frequency of nuclear magnetic resonance in the Earth's magnetic field» Utility patent № 175974 Russian Federation, 2017.

Development and investigation of mixed-matrix membranes based on PVA modified by various organic nanoparticles

Anna I. Kuzminova, Anastasia V. Penkova, Maria E. Dmitrenko

St. Petersburg State University, St. Petersburg, 199034 Russia

E-mail: ai.kuzminova@mail.ru

Introduction

Nowadays, the essential improvement of the transport properties of polymer membranes can be achieved by the modification of the polymer matrix by inorganic filler that yields in developing the mixed – matrix membranes (MMMs). The introduction of inorganic filler in the polymer matrix of the membrane allows getting tailoring properties. Hybrid or mixed matrix membranes prepared by dispersing of inorganic filler in a polymeric matrix offer the possibility to overcome the trade-off between the permeability and selectivity of the polymeric membranes. MMMs combine the simplicity of processing polymer membranes with the superior transport properties of inorganic particles. Among the inorganic particles fullerene takes and important place as this nanoparticle saves its unique π -electron structure inside of the polymer matrix.

In the present work the novel membranes based on polyvinyl alcohol were prepared by bulk and surface modification. Bulk modification was carried out by introducing the water-soluble fullerene derivative (fullerenol) and polyelectrolyte (polyallylamine hydrochloride). Surface modification was carried out by layer by layer deposition with application of two polyelectrolytes (polyallylamine hydrochloride and sodium polystyrene sulfonate). The most important investigation of fillers inclusion in polymers is analysis of membranes by spectroscopic methods. Among these methods, nuclear magnetic resonance (NMR) is the best tool for the investigation of polymer nanocomposite materials. NMR allowed to study the interaction between fullerenol and polymer matrix and to confirm the complex structure of MMMs in the present work. The additional characterizations of the polymer samples were studied by scanning electron microscopy and contact angle measurements. Transport properties of the membranes were investigated by pervaporation during separation of water-organic binary mixtures: isopropyl alcohol – water and tetrahydrofuran – water.

Acknowledgements

This work was supported by Russian Science Foundation [grant No. 17-73-20060]. The experimental work was facilitated by equipments from Interdisciplinary Resource Centre for Nanotechnology, Magnetic Resonance Research Centre, Thermogravimetric and Calorimetric Research Centre, Centre for X-ray Diffraction Studies, Chemical Analysis and Materials Research Centre, Nanophotonics Centre and Centre for Geo-Environmental Research and Modelling at St. Petersburg State University.

Investigation of a nonlinear phase shifter based on spin waves

Nikolai A. Kuznetsov, Alexey B. Ustinov

Department of Physical Electronics and Technology, St.Petersburg Electrotechnical University, St.Petersburg, 197376 Russia

E-mail: kuzkolja@gmail.com, ustinov_rus@yahoo.com

Introduction

Stable intensive spin wave (SW) phenomena such as nonlinear damping and phase shift are of great interest due to a possibility of their application for development of new microwave devices with novel functionalities [1-3]. The extensive theory describing stable nonlinear effects, which are taking place when one spin-wave propagate in the magnetic film, was provided in the works [1, 2]. However, the stable effects of simultaneous propagation of two and more spin-waves in the ferrite films are poorly understood. One of the recently investigated phenomenon is intensity-dependent power exchange between the side-coupled magnetic film waveguides [3].

In spite of the aforementioned works, to our knowledge, there have been no investigations of the phase shift of two nonlinearly coupled spin waves propagating in one magnetic waveguide. The purpose of the present work is to study a performance of a nonlinear phase shifter operating on a phenomenon of a carrier spin wave phase shift induced by a high-power pump spin wave of different frequency.

Experimental prototype

The nonlinear phase shifter has a structure shown in Fig. 1. The main part of the structure is a ferrite-film waveguide. An external bias magnetic field H created by electromagnet was perpendicular to the long direction of the YIG strip. The experiments utilized a low loss YIG film strip in a two antennas MSW phase shifter. Thus, a supplied microwave signal excited surface SWs in the YIG film.

This device utilizes two stable nonlinear phenomena. Both of them occur due to the four-wave interaction processes developed with initial power increasing of operating wave (P_1), as well as pumping wave (P_2). The key phenomenon in this case is influence of the pumping wave power on the operating wave nonlinear phase shift.

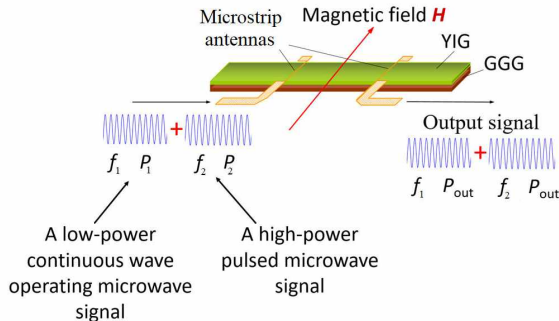


Figure 1. Schematic diagram of the nonlinear spin wave phase shifter

The data presented here were obtained for the device prototype fabricated with two 50- μm -wide and 2-mm-long short circuited microstrip antennas evaporated onto a grounded

alumina substrate of 500 μm thickness. The distance between the antennas d was 5 mm. The antennas were fed by the microstrip transmission lines of 50 Ohm characteristic impedance. A 13.6- μm -thick, 2-mm-wide, and 40-mm-long yttrium iron garnet (YIG) single-crystal film strip was utilized in the nonlinear phase shifter. The film was grown by liquid-phase epitaxy on 500- μm -thick gadolinium gallium garnet (GGG) substrate. The YIG film demonstrated a narrow ferromagnetic resonance linewidth ΔH of 0.5 Oe at the frequency of 5 GHz and a saturation magnetization $4\pi M_0$ of 1750 G. Magnetic field was 1260 Oe that allowed us to carry out investigations in the frequency range of 5320-5800 MHz. The YIG/GGG strip was positioned, with the YIG side down, over the microstrip antennas.

Experimental results

Figure 2 shows the amplitude frequency characteristics (AFCs) of the nonlinear phase shifter. These characteristics were obtained for microwave operating signal having relatively small incident power $P_1 = -10$ dBm. With increasing pump signal power P_2 up to 24.81 dBm excited at a frequency $f_2 = 5575$ MHz, the insertion loss illustrates a slight increase especially after 5500 MHz.

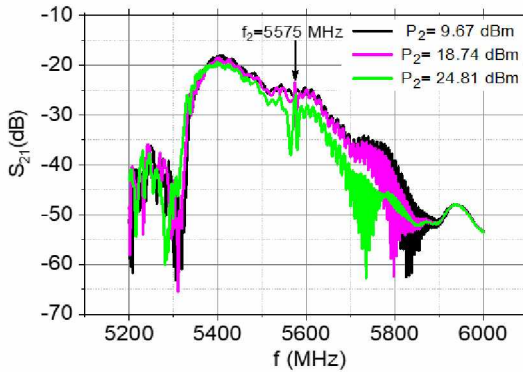


Figure 2. AFC of the nonlinear phase shifter measured for the different input power values P_2 as indicated

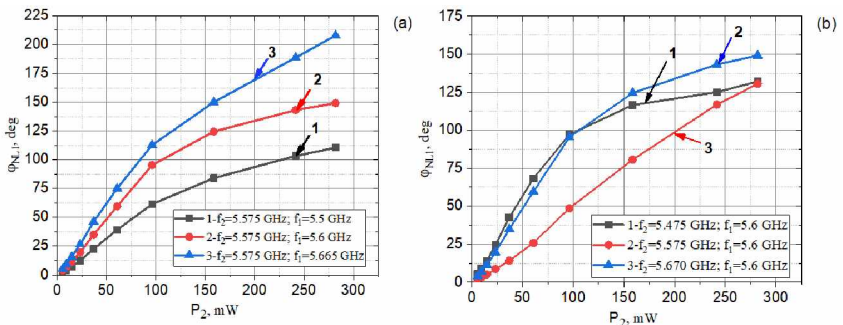


Figure 3. Experimental profiles of the induced nonlinear phase shift of the operating spin wave as a function of input pumping power for various operating f_1 (a) and pumping f_2 (b) frequencies

Fig. 3 shows the experimental dependences of the operating wave nonlinear phase shift φ_{NLI} from pumping wave power P_2 measured for the different frequencies of the operating and pumping signals. The lines connecting the points are a guide for the eyes only. As is evident from Fig. 3(a) increasing of P_2 leads to a growth of the nonlinear phase shift φ_{NLI} at all operating frequencies. Moreover, at $f_1 = 5665$ MHz the induced nonlinear phase shift φ_{NLI} reaches more than 180° that is important for the utilization in microwave applications. Figure 2(b) illustrates similar dependence for different pumping frequencies at a fixed operating signal of 5600 MHz.

Conclusions

The microwave spin wave nonlinear phase shifter based on the YIG film has been investigated. The obtained results will be useful for future work on the nonlinear ferrite-film spin wave devices.

Acknowledgements

The work was supported in part by the Ministry of Education and Science of Russian Federation (Project "Goszadanie").

References

1. A. B. Ustinov, B. A. Kalinikos. Applied Physics Letters, **89**, 172511 (2006)
2. M. M. Scott, C. E. Patton, M. P. Kostylev, B. A. Kalinikos. Journal of Applied Physics, **95**, 6294-6301 (2004).
3. A. V. Sadovnikov, S. A. Odintsov, E. N. Beginin, S. E. Sheshukova, Yu. P. Sharaevskii, S. A. Nikitov. Physical Review B **96**, 144428 (2017)

Single Pulse NQR for Broad Resonance Lines

Thai Ly^{1,2}, Richard Yong¹, John E. Daniels², David Miljak¹

¹CSIRO Mineral Resources, Lucas Heights, New South Wales, 2234, Australia

²School of Materials Science and Engineering, University of New South Wales, Kensington, NSW, 2033, Australia,

E-mail: thai.ly@csiro.au

A singular pulse length that is greater than the transverse relaxation time can be used to effectively detect inhomogeneously broadened lines that span greater than 100 kHz. It is the distribution of resonant frequencies that consequently result in a substantial free induction decay (FID) on resonance after the pulse is applied. The greatest magnetization intensity occurs for lower applied magnetization levels (B_1) than that required for traditional spin-echo sequences. Additionally, resonance offset effects are not required to retrieve signal intensity. The dependence on B_1 and pulse length for ^{63}Cu NQR in covellite (CuS) was investigated experimentally and were theoretically verified via simulation of the phenomenological equations of Bloch.

Introduction

Published works that involve a singular long pulse of quadrupolar specimens have shown that on resonance, there is no signal. To retrieve signal intensity, excitation some frequency $\Delta\omega$ away from the centre of the linewidth was required. However, this was explored for solid state samples such as solid aluminium and copper and cuprite (Cu_2O) which all exhibit a linewidth of ≤ 10 kHz. Inhomogeneously broadened line widths (of ≥ 100 kHz) can be effectively detected with a singular on-resonance radiofrequency (RF) pulse applied for longer than the sample's transverse relaxation time. Naturally-formed copper-sulfur mineral systems such as covellite can exhibit inhomogeneously broadened line widths due to a distribution of electric field gradients (EFG) at the ^{63}Cu site. The application of a pulse with length $t \gg T_2$ has been found to take advantage of the wide linewidth to produce a substantial free induction decay (FID) signal.

While the RF field is active, the transverse component of magnetization decays on the order of T_1 [1]. This excitation method may be grouped as a "spin-locking" pulse sequence along with typical arrangements such as a train of RF pulses or a two phase shifted pulse sequence (a 90 degree pulse followed by a long pulse). However, Redfield's theory of rotary saturation does not satisfactorily explain the phenomena exhibited. Additionally, offset resonance effects do not occur, where typically the null in long pulse spectra corresponds to the peak of the linewidth as seen in literature [2-4]. In this publication, we show that it is possible to completely restore the on-resonance magnetization for wide line quadrupolar chalcogenides and achieve theoretical verification via simulation of the Bloch equations.

Results and Discussion

^{63}Cu zero-field NQR measurements were performed on synthetic covellite (CuS). Covellite has an NQR resonance at 14.28 MHz with a FWHM of 0.144 MHz. The T_1 and T_2 of 6.23ms, 106.73 μs and respectively.

The single pulse method provides a FID with a signal height that is retained after it is subjected to a pulse length that far exceeds T_2 . The length of this signal is longer the dead time of the receiver, however, the true peak of the signal cannot be recorded due to system restraints. The theoretical simulations of the Bloch equations do however, provide the true peak of the signal but staying consistent with the experimental restraints, the signal magnetization is retrieved 40 μs away from the pulse. Since the FID decay time is in the order of T_2^* , the retrieval of the signal tends to be easier than with standard echo techniques where dead time may cutoff the appearance of the echo.

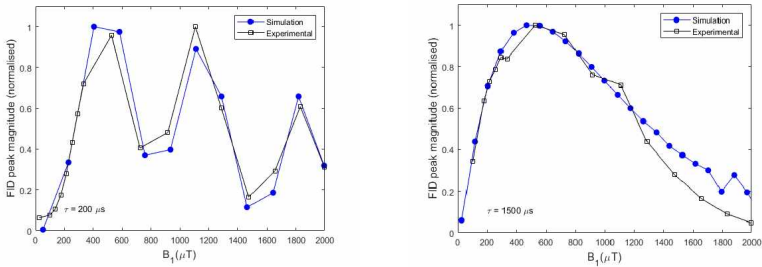
FID Height Dependence on B_1 

Figure 1. Simulations of Bloch equations (blue) compared with experimental results for covellite (black) FID peak magnetization as a result of pulse length $t = 200 \mu\text{s}$ (left) and $t = 1500 \mu\text{s}$ (right)

Figure 1 shows that as B_1 increases, the signal height of the FID reaches a maximum around 500-700 μT and then decreases. This applies for all pulse lengths greater than T_2 of the sample. As evidenced in Figure 1, the simulation of the steady-state Bloch equations verify the experimental results. Both the theoretical and experimental results show the reduction in modulation as pulse length increases, this is indicative of the eventual suppression of transverse components as pulse length increases. These observations are common for quadrupolar specimens, where the greatest signal intensity occurs at magnetization levels much less than what is required in a Hahn spin echo pulse sequence [2, 3].

In cases where RF power is limited and large sensing equipment is used, an increase in power is required to satisfactorily generate the coil current in great sample volumes. These results provide a valuable alternative method for such cases that have limited power supply.

FID Height Dependence on Pulse Length

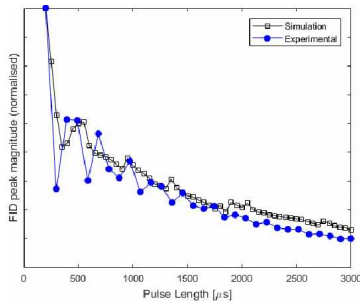


Figure 2. Simulation of Bloch equations (blue) compared with experimental results for covellite (black) for FID magnitude as a result of increasing pulse length with a constant B_1 of 400 μT

The reduction in modulation as the pulse length increases is also evidence of the eventual suppression of the transverse mechanisms (like Figure 1). This suppression is evident in the form of reduction in modulation of the signal magnitude for pulse lengths greater than $15T_2$ (1500 μs). In the high field regime (where the saturation condition is satisfied), it has been noted in literature that Bloch and Redfield's theory are in agreement which extends validity to the simulation [5, 6].

Offset Resonance Effects for Wide Lines

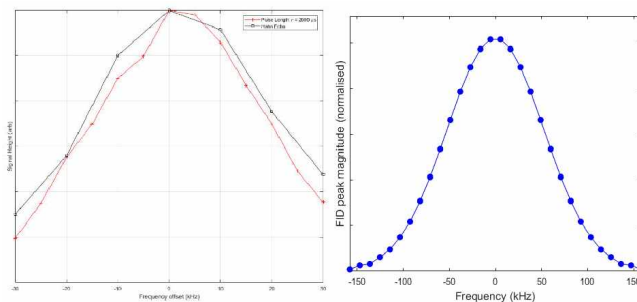


Figure 3. a) The linewidth of synthetic covellite using a single long pulse (red) vs. Hahn spin echo pulse sequence (black) collected experimentally. The simulated offset resonance effect is pictured in b)

It has been published that for linewidths less than 10kHz, the peak of the linewidth correlates to the null point in a long pulse frequency scan and magnetization is retrieved $\Delta\omega$ away from resonance [2-4]. In the current regime, the uppermost point of the frequency scan also appears where the peak of the line is (Figure 3). Linewidth scans using spin echo pulse sequence can lead to convolution issues as the population that is probed is equal to the inverse of the longest pulse (i.e. the π pulse of the Hahn echo pulse sequence). Using a long pulse such as 2000 μs is equal to probing 5 Hz wide, allowing the spacing between frequency scans to be shortened to capture the finer features of the linewidth if needed. However, the signal intensity may not be as great as those generated via spin echo methods and so finer details at the tails of the linewidth may be difficult to retrieve.

Acknowledgements

This work is supported by CSIRO Mineral Resources and also by an Australian Government Research Training Program Scholarship.

About the group

The Magnetic Resonance group is a part of the Mineral Resources division of CSIRO (Commonwealth Scientific and Industrial Research Organisation). The groups focuses on zero field nuclear magnetic resonance techniques for quantitative NMR of copper minerals, detection of explosives and their associated compounds and other practical industrial applications.

References

1. Redfield, A.G., *Nuclear Magnetic Resonance Saturation and Rotary Saturation in Solids*. Physical Review, 1955. **98**(6): p. 1787-1809.
2. B. Bandyopadhyay, G.B.F., S. D. Goren, C. Korn, and A. L. Shames, *One Pulse Spin-locking in NQR*. Z. Naturforsch., 1996. **51**(a): p. 357-362.
3. Furman, G.B., A.M. Panich, and S.D. Goren, *Spin-locking in one pulse NMR experiment*. Solid state nuclear magnetic resonance, 1998. **11**(3-4): p. 225-230.
4. J.C Pratt, P.R., C.A McDowell, *Transient response of a quadrupolar system in zero applied field*. Journal of Magnetic Resonance, Series A, 1969. **20**(2): p. 14.
5. Abragam, P.A. and A. Abragam, *The Principles of Nuclear Magnetism*. 1961: Clarendon Press.
6. Slichter, C.P., *Principles of Magnetic Resonance*. 2013: Springer Berlin Heidelberg.

Micelle formation of azobenzene-containing surfactant: investigation by molecular dynamics method

Veronika V. Mamontova, Andrei V. Komolkin, Irina A. Silanteva

*Department of Physics, Saint Petersburg State University, Russia
E-mail: st048848@student.spbu.ru*

Introduction

Surface-active substances (surfactants) are able to generate the compact complexes with DNA [1]. Such complexes could be used for delivery of genetic material into cells, tissues, or whole organs. According to experiments [2, 3] there is a dependence between concentration of surfactant and precipitation of the solution. Besides the precipitate appears in the some range of concentrations.

Molecular dynamics method is used to research this phenomena. The problem of this work is investigation of surfactant (4-butyl-4'-trimethylammonium-hexoxy-azobenzene, C₄-Azo-OC₆TMA) aggregate formation in aqua solution with different salt concentrations. As experiments on DNA are conducted in saline, two types of solvent were chosen in this work: salt-free and saline.

Investigated model

Each system was examined in cell with periodic boundary conditions. First system (I) consisted of 18 C₄-Azo-OC₆TMA ions, 18 chlorine ions, and about 24000 aqua molecules. Chlorine was added into cell to observe the condition of total cell charge equality to zero. Second system (II) contained 18 C₄-Azo-OC₆TMA ions, 64 sodium and 82 chlorine ions, and up to 23000 aqua molecules. The molality of the solution by sodium was equal to 0.15 mol per liter (saline).

C₄-Azo-OC₆TMA interacts with DNA in trans-conformation only [1]. So during the calculation trans-conformer (fig. 1) was used.

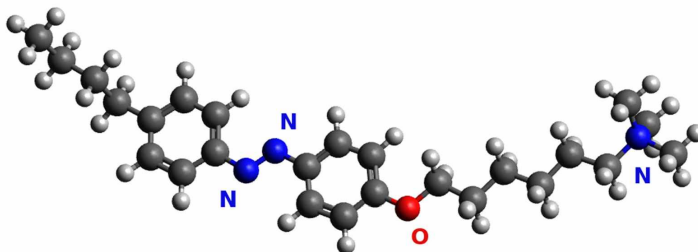


Figure 1. Molecule of C₄-Azo-OC₆TMA, trans-conformer

N(CH₃)₃-group having positive charge called “head”, and the opposite is “tail”.

Results and Discussion

System I was modeled during 24 ns, and time of modeling of system II was 29 ns. Analysis of molecular dynamics trajectories was carried out in the last 10 ns. There was counted average proportion of molecules forming aggregates of the appropriate size (fig. 2). The criterion for location of molecule in aggregate was distance between benzene rings equal to or less than 4.8 Å.

During modeling the molecules aggregated chaotically in both systems. There were originally formed aggregates of “head-tail” and “tail-tail” orientation. And in the latter case, “heads” of C₄-Azo-OC₆TMA repelled from each other.

In saline the aggregate generation was faster, and larger aggregates were formed.

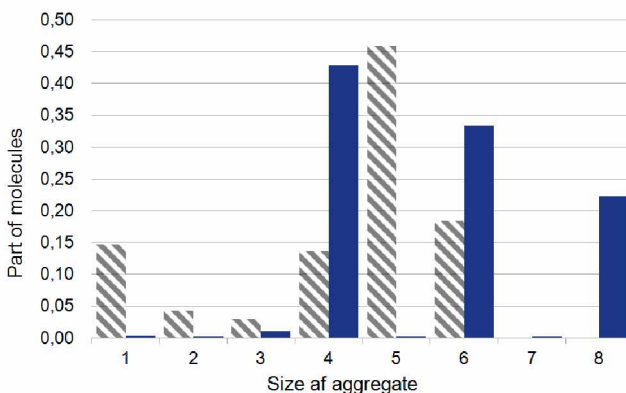


Figure 2. Distribution of molecules by aggregates in salt-free solution (striped columns) and in saline (filled columns)

System I was characterized by a small number of aggregates consisting of 2 or 3 molecules. The largest aggregate contained 6 molecules. Some monomers were in solution throughout the simulation.

In system II, large aggregates prevailed. There were practically no aggregates consisting of an odd number of molecules or containing 2 molecules only. The maximum aggregate had the size of 8.

Conclusions

When modeling was obtained the result that the salt ions promote aggregation of C₄-Azo-OC₆TMA molecules in system, so micelle formation depends on salt containing in solution. Due to this fact it is necessary to add salt ions to simulated cell of DNA and surfactant molecules in aqua solution.

Acknowledgements

Research was carried out using computational resources provided by Resource Center “Computer Center of SPbU” (<http://cc.spbu.ru>).

Reference

1. Yuriy Zakrevskyy, Alexey Kopyshv, Nino Lomadze, Elena Morozova, Ludmila Lysyakova, Nina Kasyanenko, and Svetlana Santer, DNA compaction by azobenzene-containing surfactant, *Physical Review E* 84, 021909 (2011)
2. N. Kasyanenko, L. Lysyakova, R. Ramazanov, A. Nesterenko, I. Yaroshevich, E. Titov, G. Alexeev, A. Lezov, I. Unksov. Conformational and Phase Transitions in DNA — Photosensitive Surfactant Solutions: Experiment and Modeling – *Biopolymers*, 109-122 (2014)
3. Nina Kasyanenko, Ivan Unksov, Vladimir Bakulev and Svetlana Santer. DNA Interaction with Head-to-Tail Associates of Cationic Surfactants Prevents Formation of Compact Particles – *Molecules* 2018, 23, 1576 (2018)

Investigation of complex of lysine dendrimer of 2nd generation with 8 molecules of therapeutic vezugen peptide by computer simulation

*S. E. Miktaniuk, V. V. Bezrodnyi, E. I. Fatullaev, A. A. Marchenko,
E. I. Bychkova, I. M. Neelov*

*St. Petersburg National Research University of Information Technologies, Mechanics and Optics (ITMO University), Kronverkskiy pr.49, St.Petersburg, 197101, Russia
E-mail: i.neelov@mail.ru*

Introduction

Dendrimers are highly branched molecules with regular spherical branching from central core [1]. Dendrimers are used in different biomedical applications including drug and gene delivery [2]. Lysine dendrimers are special type of dendrimers on the base of only one lysine aminoacid residues which have positively charged amine groups [3]. They could be used as antiviral, antibacterial and antiamyloid agents and could make complexes with oppositely charged molecules for example DNA, polysaccharides and peptides.

We have chosen to study vezugen peptide (Lys-Glu-Asp) as a representative of the class of short regulatory drug peptides [4-5] and check does molecule of these peptides make complex with lysine dendrimers. Our simulation was performed using the GROMACS 4.5.6 software and one of the most modern AMBER 99SB-ildn force fields [6, 7]. Molecular dynamics simulation approach used here was described elsewhere [8-20]. We studied the system consisting of one dendrimer and 8 vezugen peptides in water with explicit counterions. We used NPT ensemble (at temperature 300 K and pressure 1 ATM) and PME algorithm for calculation of electrostatic interactions.

Results and discussion

To characterize the size of the subsystems consisting of dendrimer or dendrimer and peptide molecules during the equilibration the mean squared gyration radius $R_g(t)$ was used. This function was calculated using `g_gyrate` function of GROMACS software. The time dependence of gyration radius R_g at the beginning of calculation describes the process of compaction of subsystem consisting of dendrimer and peptide molecules during formation of complex (see Fig. 2).

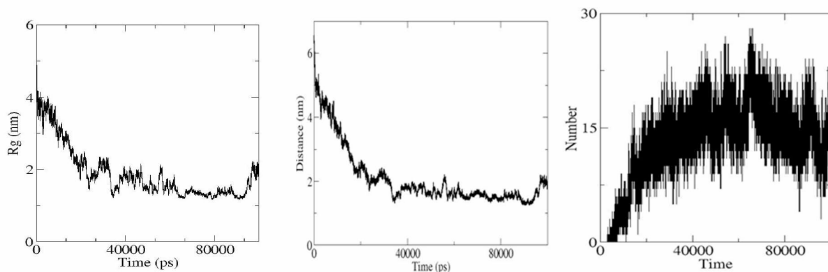


Figure 1. Time dependence of size $R_g(t)$ of subsystems consisting of G2 and 8 molecules of peptide (a), distance d (b) and number of hydrogen bonds (c) between them

From Fig. 1 it can be seen that complex of dendrimer with 8 molecules of vezugen peptide forms within 50 ns. Fig 1a demonstrates time dependence for size of complex R_g . At the beginning (at $t=0$) the peptide are far enough from dendrimer. Then the size decrease for about 50 ns due to attractive interactions between dendrimer and peptide molecules. After this

time the complex size R_g fluctuate slightly, but its average value practically does not change with time. The distance between dendrimer and peptide molecules (Fig. 1b) also decrease during 50 ns and after this time practically does not change. Another quantity that can characterize the rate of complex formation is the total number of hydrogen bonds between dendrimer and 8 peptide molecules (Fig. 1c). This function quickly increase and reaches equilibrium plateau after 50 ns. Therefore, we can assume from all these results the complex forms during first 50ns and become close to equilibrium state after this time.

The value of size R_g of complex and dendrimer in equilibrium state are evaluated by inertia radius averaged through the time t after equilibration of the system (see table 1).

Table 1. Size R_g , main components of inertia tensor R_g^{11} , R_g^{22} and R_g^{33} and axial ratio R_g^{33}/R_g^{11}

System	R_g^{11} , (nm)	R_g^{22} , (nm)	R_g^{33} , (nm)	R_g , (nm)	R_g^{33}/R_g^{11}
G2+8 vezugen	0,85	1,35	1,43	1,52	1,68
G2	0,59	0,89	0,95	1,00	1,06

It was obtained that in equilibrium state the sizes of the complex consisting of G2 dendrimer and 8 molecules of vezugen peptides (see Table 1) is about 1.5 time greater than size of dendrimer itself. The shape of the complex can be characterized by main components (R_{g11} , R_{g22} and R_{g33}) of inertia tensor from Table 1 where R_{g11} is minimal and R_{g33} is maximal eigenvalue of inertia tensor. The rough evaluation of anisotropy of dendrimer and complex could be done using axial ratio R_{g33} / R_{g11} . This ratio is equal 1.68 for dendrimer. The addition of peptide make it more isotropic with ratio $R_{g33} / R_{g11}=1.06$ It means that molecules of peptide are distributed on dendrimer surface by such a way that complex become almost spherical.

In this paper we demonstrated the formation of dendrimer-peptide complex between lysine dendrimer and vezugen peptide. We also obtained its equilibrium size and shape.

Acknowledgements

This work was partly supported by grant 08-08 of Government of RF and RFBR grants 19-03-00715. The research is carried out using the equipment of the shared research facilities of HPC computing resources at Lomonosov Moscow State University supported by the project RFMEFI62117X0011.

References

1. Frechet J.M.J., Tomalia D.A., 2001, Dendrimers and Other Dendritic Polymers, (West Sussex: John Wiley&Sons Ltd.)
2. Mendes L.P., Pan J., Torchilin V.P., 2017, *Molecules*, 22, 1401
3. Denkwalter R.G., Kolc J., Lukasavage W.J., Macromolecular Highly Branched Homogeneous Compound, 1983, US Patent № 4410688.
4. Kozina L.S., 2008, Antioxidant action of geroprotective peptide bioregulators, dissertation for a doctoral (Dr.Sci) degree, St.Petersburg
5. Anisimov V.N., Khavinson V.K., 2009, *Biogerontology*, 11, 139
6. Ennari J., Neelov I., Sundholm F., *Polymer*, 2001, 42, 8043
7. Ennari J., Neelov I., Sundholm F., *Polymer*, 2000, 41, 4057
8. Ennari J., Elomaa M., Neelov I., Sundholm F., 2000, *Polymer*, 41, 985
9. Ennari J., Neelov I., Sundholm F., *Comput Theor Polym Sci*, 2000, 10, 403
10. Ennari J., Neelov I., Sundholm F., *Polymer*, 2000, 41, 2149
11. Ennari J., Neelov I., Sundholm F., *Polymer*, 2004, 45, 4171
12. Darinskii A., Gotlib Yu., Lukyanov M., Lyulin A., Neelov I., *Progress in Colloid & Polymer Science*, 1993, 91, 13

13. Neelov I.M., Adolf D.B., McLeish T.C.B., Paci E., *Biophysical Journal*, 2006, 91, 3579
14. Gowdy, J., Batchelor, M, Neelov, I, Paci, *Journal of Physical Chemistry B*, 2017, 121, 9518
15. Darinskii A., Gotlib Yu., Lyulin A., Neelov I., *Vysokomolekularnye Soedineniya. Seriya*, 1991, 33, 1211 (translation to English: *Polymer Science*, 33,1116)
16. Darinskii A., Lyulin A., Neelov I., *Makromolekulare Chemie - Theory and Simulations (Macromolecular Theory and Simulations)*, 1993, 2, 523
17. Darinsky A., Gotlib Y., Lukyanov M., Lyulin A., Neelov I., *Progress in Colloid and Polymer Science*, 1993, 91, 13
18. Neelov I.M., Adolf D.B., Lyulin A.V., Davies G.R., *Journal of Chemical Physics*, 2002, 117, 4030
19. Mazo M.A., Shamaev M.Y., Balabaev N.K., Darinskii A.A., Neelov I.M., *Physical Chemistry Chemical Physics*, 2004, 1285-1289
20. Neelov, I. M.; Janaszewska, A.; Klajnert, B; Bryszewska M., Makova N., Hicks D., Pearson N., Vlasov G.P., Ilyash M.Y., Vasilev D.S., Dubrovskaya N.L., Zhuravin I.A., Turner A.J., Nalivaeva N.N., *Current Medical Chemistry*, 2013, 20, 134
21. Falkovich S.G., Markelov D., Neelov I., Darinskii A., *Journal of Chemical Physics*, 2013, 139, 064903
22. Neelov, I. M., Markelov D.A., Falkovich S.G., Ilyash M.Y., Okrugin B.M., Darinskii A.A., *Polymer Science*, 2013, 55, 154
23. Neelov, I., Markelov D., Falkovich S.G., Paci E., Darinskii A., Tenhu H., *Molecular Dynamics of Lysine Dendrimers in Computer Simulation and NMR. Dendrimers in Biomedical Applications*, (London: RSC) 2013, 99-114
24. Markelov D.A., Falkovich S.G., Neelov, I. M., Ilyash M.Y., Matveev V.V., Lahderanta E., Ingman, P., Darinskii A.A., *Physical Chemistry and Chemical Physics*, 2015, 17, 3214
25. Sheveleva N.N., Markelov D.A., Vovk M.A., Tarasenko I.I., Neelov I.M., Lahderanta E., *Scientific Reports*, 2018, 8, 8916
26. Okrugin B., Ilyash M., Markelov D., Neelov I., *Pharmaceutics*, 2018, 10, 129 (2018)
27. Neelov, I. M., O.V. Shavykin, Ilyash M.Y., Bezrodnyi V.V., Mikhtaniuk S.E., Marchenko A.A., Fatullaev E.I., Darinskii A.A., Leermakers F.A.M., *Supercomputing Frontiers and Innovations*, 2018, 5, 60
28. Popova E., Khamidova D., Neelov I., Komilov F., Chapter 3. "Lysine Dendrimers and Their Complexes with Therapeutic and Amyloid Peptides: Computer Simulation", in "Dendrimers Fundamentals and Applications", (IntechOpen), 2018, 29-45.
29. Neelov I.M., Adolf D.B., 2003, *Macromolecules*, 36, 6914
30. Neelov I.M., Adolf D.B., 2004, *Journal of Physical Chemistry B*, 108, 7627
31. Neelov I.M., Binder K., 1995, *Macromolecular Theory and Simulations* 4, 1063
32. Neelov I.M., Shavykin O.V., Ilyash M.Y., Bezrodnyi V.V., Mikhtaniuk S.E., Marchenko A.A., Fatullaev E.I., Darinskii A.A., Leermakers F.A.M., *Supercomputing Frontiers and Innovations*, 2018, 5, 60
33. Shavykin O.V., Neelov, I. M., Darinskii A.A., *Physical Chemistry Chemical Physics*, 2016, 18, 24307
34. Shavykin O.V., Mikhailov I.V., Darinskii A.A., Neelov I.M., Leermakers F.A.M., *Polymer*, 2018, 146, 256.
35. Okrugin B.M., Neelov I.M., Leermakers F.A.M., Borisov O.V., *Polymer*, 2017, 125, 292
36. Shavykin O.V., Leermakers F.A.M., Neelov I.M., Darinskii A.A., *Langmuir*, 2018, 34, 1613
37. B.M. Okrugin, R.P. Richter, F.A.M. Leermakers, I.M. Neelov, O.V. Borisov, E.B. Zhulina, *Soft Matter*, 2018, 14, 6230
38. Zhulina E.B., Neelov I.M., Sheiko S.S., Borisov O.V., *Polymer Science, Series C*, 2018, 60, 76.

Partitioning of solutes between micelles and water studied by diffusion NMR and micellar liquid chromatography

Anastasia V. Nam, Alina S. Koneva, Peter M. Tolstoy

*St. Petersburg State University, Institute of Chemistry, 198504, Saint Petersburg, Russia
E-mail: nv.a@inbox.ru*

Introduction

Surfactants are substances which contain hydrophilic and hydrophobic parts. With increasing surfactant concentration in aqueous solution, micelles are formed as soon as the surfactant-specific threshold concentration value is reached, called the critical micelle concentration (cmc). Micelles are self-assembled supramolecular aggregates containing hydrophilic shell and hydrophobic core, see Fig. 1a, which can solubilize poorly water-soluble organic substances. This property is used, for example, in extraction [1]. The criterion for choosing a suitable surfactant is the solubilization capacity of its micelle. In this work we attempt to determine the maximum number of molecules of model organic substances which can be solubilized by one micelle of nonionic surfactant Brij-35.

Nonionic surfactant Brij-35

Polyoxyethylene lauryl ether (Brij-35) (Fig. 1b) is one of the nonionic surfactants widely used both in biochemical and chemical processes because of its high stability, high solubility in water and ability to easily mix with other surfactants for its usage in mixed micelles [2]. It has been reported that one Brij-35 micelle contains approximately 40–50 surfactant molecules [3]. The characteristic property of Brij-35 micelles is large hydrophilic shell, which also participates in the process of solubilization [3].

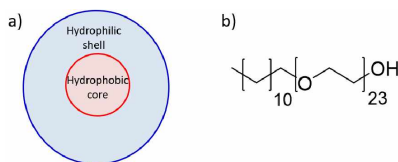


Figure 1. a – scheme of spherical micelle, b – structure of Brij-35

Partitioning of solutes between micelles and water

In analogy with binary two-phase systems, the distribution of solutes between the aqueous phase and the micelles can be described by partition coefficient [4], which is defined as

$$P^{MW} = \frac{x_{mic}}{x_{free}}$$

where x_{mic} is the fraction of organic molecules in micellar phase, x_{free} is the fraction of organic molecules in aqueous phase. The micelle/water partition coefficient is a measure for the solubilisation capacity of micellar solution [5]. The partition coefficient is usually measured by micellar liquid chromatography (MLC) in the limit of infinite dilution of organic substance [6]. Using this method, we have measured P^{MW} for a series of substances shown in Fig. 2.

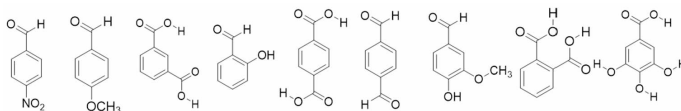


Figure 2. Structures of organic substances studied in this work

Apart of partition coefficient the solubilizing properties of micelles can be described by the maximum number of organic molecules which can fit into a micelle. This number depends on the size of solutes and the number and location of their functional groups. In this work, we have tried to estimate the capacity of Brij-35 micelles using diffusion NMR.

Diffusion NMR in micellar solution

The chemical shifts of protons of free molecules and micelles of Brij-35 are very similar and corresponding signals do not resolve in ^1H NMR spectra. However, the diffusion coefficients of free molecules and micelles differ by an order of magnitude: ca. 10^{-10} m^2/s for free molecules, ca. 10^{-11} m^2/s for micelles. Thus, the diffusion coefficient of ca. 10^{-11} m^2/s would be characteristic also for solutes incorporated into a micelle. Luckily, the signals of solutes in micelles and water are sometimes resolved as shown in Fig. 3 for an aldehyde proton of vanillin. Comparing the diffusion coefficients measured for these signals with those previously established for Brij-35 micelles, one could assign the signals to free vanillin molecules and vanillin molecules encapsulated into the micelle. Using the relative integrated intensities of these signals the partitioning of vanillin molecules can be estimated, and thus the capacity of the micelles. For example, Fig. 3b shows that upon an increase of vanillin concentrations from 0.02 mM to 0.16 mM the relative integrated intensities of signals – and thus the fraction of vanillin in micelles – change. However, the absolute amount of vanillin molecules in micelles stays almost constant (it grows from 0.017 mM to 0.026 mM), reflecting the fact that the maximum capacity of micelles has been practically reached. We estimate that no more than one vanillin molecule can fit into one Brij-35 micelle.

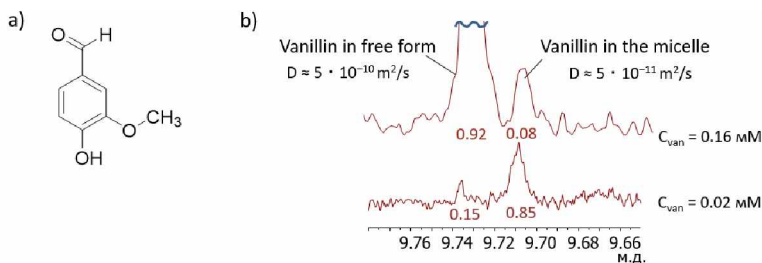


Figure 3. a – molecule of vanillin, b – ^1H NMR spectra of aldehyde groups area of vanillin in micellar system Brij-35 in deuterated water (pH 2)

Acknowledgements

MLC experiments were carried out in the Center for Chemical Analysis and Materials Research, NMR studies were performed in the Center for Magnetic Resonance, St. Petersburg State University Research Park.

References

1. A. Chakraborty, S. Kamalika. – *J. Mol. Liq.*, 241, 182-187 (2017).
2. J. Mao, et al. – *J. the Taiwan Institute Chem. Eng.*, 95, 424-431 (2019).
3. A. S. Koneva, et al. – *Colloids Surf.*, 538, 45-55 (2018).
4. T. Mehling. Partition coefficients in mixed surfactant systems. Diss. Technische Universität Hamburg, 2013.
5. M. H. Fatemi, F. Karimian. – *J. Colloids Interf. Sci.*, 314, 665-672 (2007).
6. D.W. Armstrong, F. Nome. – *Anal. Chem.*, 53, 1662-1666 (1981).

Phosphine oxides as probes in study of halogen bonds: quantum chemistry approach

A. S. Ostras, P. M. Tolstoy

*St. Petersburg State University, Institute of Chemistry, St. Petersburg, Russia
E-mail: st052055@student.spbu.ru*

Introduction

Halogen bond (XB) is one of the most abundant non-covalent interactions, which can be formed by electron donors and halogen-containing (Cl, Br, I, in some cases F and At) molecules and ions, in which halogen atom is bonded to an electron-withdrawing group. Therefore, halogen atom has an electron poor region, so-called σ -hole, due to which it acts as an electron density acceptor (i.e. halogen donor). Various molecules, ions and individual atoms (e.g. Hal, O, S, Se, N etc.) can act as electron-donating halogen bond acceptors.

Detection of halogen bonding

Halogen bonds can be observed in solids, in solution and in gas phase. They play an important role in catalysis, drug design, crystal engineering and design of new materials with various useful properties (e.g. luminescent emitters). Halogen bonds are usually detected by their geometric (valence angles and bond lengths) or energetic characteristics. While geometric parameters can be rather straightforwardly determined for single crystals by X-Ray analysis, complexation energy is notoriously hard to determine, especially in other media (liquids and solutions, where the information on interatomic distances is absent) and especially for intramolecular halogen bonds (where the complexation energy needs an additional definition). Besides, it is desirable to design tools for prediction of the complex's characteristics based on the electronic properties of halogen donor molecules.

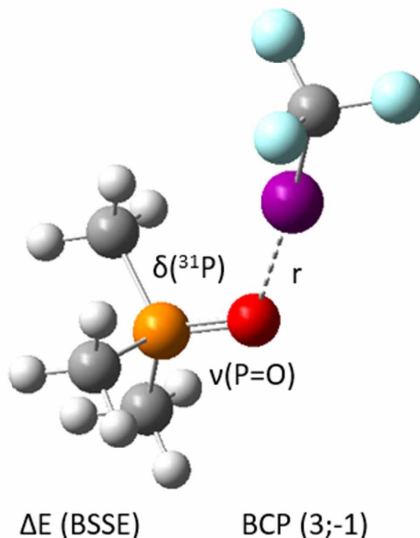


Figure 1. Equilibrium structure of halogen-bonded complex of trimethylphosphine oxide $(CH_3)_3PO$ and trifluoroiodomethane CF_3I

Novel method of determining of parameters of halogen bond

Our first goal is to evaluate the possibility to use ^{31}P NMR chemical shift, $\delta(^{31}\text{P})$, and P=O stretching vibrational frequency, $\nu(\text{P}=\text{O})$, as descriptors of halogen bond energy and geometry. Our second goal is to analyze the QTAIM (Quantum Theory of Atoms In Molecules) parameters at the halogen bond critical point (3; -1) in order to construct correlations that would allow one to use topological analysis of the electron density in order to predict the energy and geometry of O...XR halogen bonds.

Acknowledgements

This work was supported by RSF grant 18-13-00050.

Projection reconstruction in ultralow field MRI

Vladislav Panov, Oleg Dmitriev, Konstantin Tyutyukin, Viacheslav Frolov

Faculty of Physics of Saint Petersburg State University, St. Petersburg, Russia

E-mail: st069302@student.spbu.ru

Introduction

The main difficulty of nuclear magnetic resonance in the low field is a small signal strength that results in the long accumulation for obtaining the image. One of obstacles to accelerate the reception of NMR signals is the long time demanded for restitution of magnetization after action of a 90° -pulse. One of paths to overcome this difficulty is receiving a series of signals in a single interval between two 90° -pulses. In particular, it is possible to realize the projection reconstruction method with receiving several projections in one series of signals of a spin echo.

Results of an experiment on reconstruction of the image on the projections received by means of a spin echo in ultralow magnetic field are given in this message.

Method

For reconstruction the standard method [1] allowing to receive 2D distribution of nuclear magnetization $f(x, y)$ was used:

$$f(x, y) = \int_0^{2\pi} d\varphi \int_0^\infty v R_\varphi(v, \varphi) e^{i2\pi v(x\cos\varphi + y\sin\varphi)} dv$$

where $R_\varphi(v, \varphi)$ is Fourier transform of the Radon function. At data To interpret the experimental data the discrete option of Radon transformation $R(s, \varphi)$ which in turn turns out as a result of Fourier transform of a NMR signal in a magnetic field with a gradient along direction s is used.

Experiment

The experiment is executed on the self-made minitomograph in field 7 mT. In fig. 1 examples of signals of an echo from two containers with water with addition of a paramagnetic received at the gradients directed along the base magnetic field (a) and under 40° (b) to it are given.

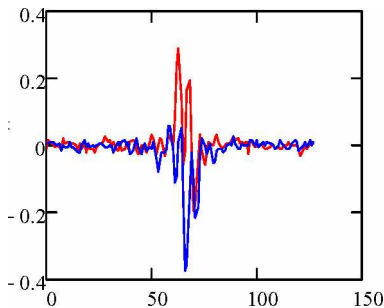


Figure 1a

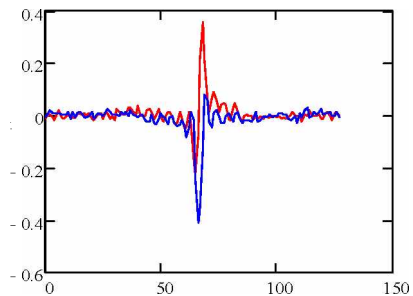


Figure 1b

In fig. 2 the corresponding projections (a, b) after Fourier transform of these signals are shown, and on fig. 3 the turned-out images are submitted.

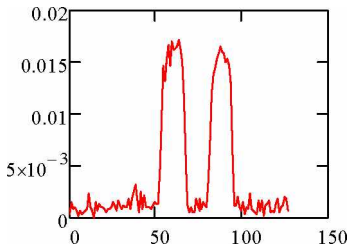


Figure 2a

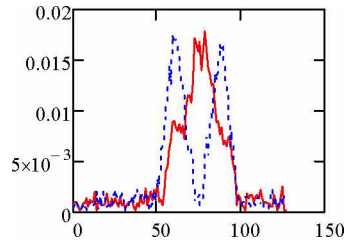


Figure 2b

The processed images of section of two test tubes received with use of 6 projections with a step of 30° are provided on fig. 4.

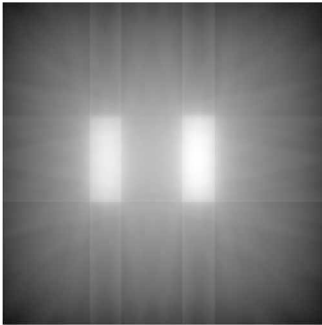


Figure 3

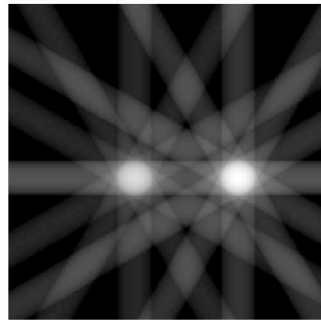


Figure 4

References

1. I. N. Troizkiy. Statisticheskaya teoriya tomourafii. M.: "Radio i sviaz" 1989 (In Russian).

Isotopic shift of Xe nuclei precession frequencies caused by spatial inhomogeneity of optically oriented alkali atoms

Vladimir I. Petrov¹, Anatoly S. Pazgalev² and Anton K. Vershovskii²

¹Concern CSRI Electropribor

²Ioffe Institute, 26 Politekhnicheskaya, St. Petersburg 194021 Russia

E-mail: antver@mail.ioffe.ru

Introduction

The effect of the isotopic shift, or precession-frequency mismatch arising between ^{129}Xe and ^{131}Xe xenon-isotope nuclei in the presence of optically oriented alkali atoms (Cs or Rb) has been discovered recently [1], and it was shown that it drastically affects the characteristics of gyroscopic devices based on balanced schemes with spin-exchange pumping of xenon isotopes [2]. The first attempt to explain this effect was made in [3]; here we present our recent experimental results approving our theory.

Experimental

The experiment was carried out on a setup based on the standard scheme [1, 3] with a longitudinal (i.e., oriented parallel to the dc magnetic field) circularly polarized optical pumping beam and transverse linearly polarized detection beam. Besides, we have added a system of magnetic coils in anti-Helmholtz configuration for forming a magnetic field gradient along the optical pumping axis (z axis). The gas cell contained Cs vapor, nitrogen, and natural xenon (containing 26.4% ^{129}Xe , 21.2% ^{131}Xe). The measurements were carried out in a multilayer magnetic shield. The magnetic field was stabilized by the optically pumped quantum ^{85}Rb magnetometer. Comparing to [3], the gradient coils setup were modified, and two compensating coils were added in order to minimize the influence of the scattered cell gradient field on the ^{85}Rb magnetometer. The isotopic shift effect was measured at 45 – 95 °C temperatures and the magnetic field gradient range of ± 400 nT/cm.

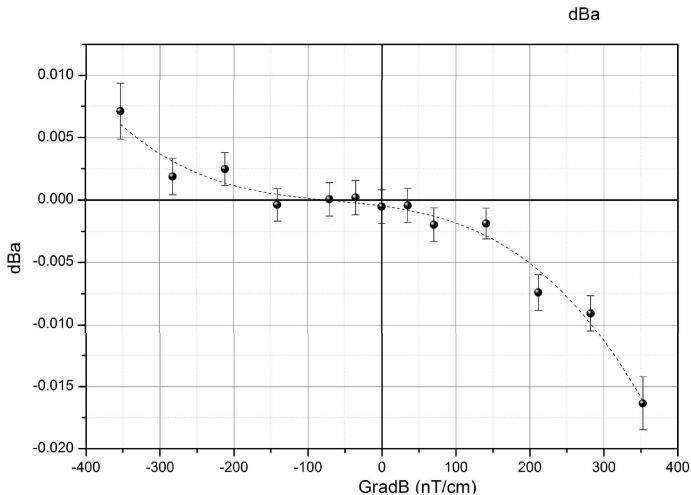


Figure 1. The dependence of isotopic shift on the external magnetic field gradient at $T=85$ °C

Conclusion

We conclude that main part of isotopic shift (or the effect of precession frequency mismatch between ^{129}Xe and ^{131}Xe) is originated from peculiarities of Xe isotopes spin-exchange pumping and diffusion in the presence of non-uniform distribution of the optical pumped alkali atoms. Thus, we confirmed the isotopic shift dependence on the magnetic field gradient, and on the difference of the nuclear spins relaxation times. It is shown that the isotopic shift could be minimized by introducing the gradient of the external magnetic field, which compensates the gradient of the cell internal field. Isotopic shift could be as well eliminated by maintaining the cell at the temperature, providing the equal relaxation times of xenon isotopes.

References

1. M. Bulatowicz, R. Griffith, M. Larsen, J. Mirjaniyan, C. B. Fu, E. Smith, W. M. Snow, H. Yan, and T. G. Walker, *Phys. Rev. Lett.* 111, 102001 (2013).
2. T. G. Walker and M. S. Larsen, *Adv. At. Mol. Opt. Phys.* 65, 373 (2016).
3. A.K. Vershovskii, A.S. Pazgalev, V.I. Petrov, *Technical Physics Letters*, 2018, Vol. 44, No. 4, pp. 313–315.

On the realization of an extremely small TFC value at a magnetic resonance frequency 6.834 GHz in rubidium atomic clocks on ^{87}Rb absorption cell with two anti-relaxation components (coating + buffer gas)

Evgeny Pestov¹, Dmitry Pestov¹, Alla Besedina², Sergei Ermak³ and Roman Lozov³

¹*The Federal State Scientific / Prod. Enterprise "Geologorazvedka", Saint-Petersburg, 192019, Russia*

²*Joint- Stock Company "Russian Institute of Radio Navigation and Time" ("RIRT"), Saint-Petersburg, 192012, Russia*

³*Peter the Great St. Petersburg Polytechnic University, Higher school of applied physics and space technologies, St. Petersburg, 195251, Russia*

E-mail: infra-ball@peterlink.ru

Introduction

It is known that the basic devices of modern global navigation satellite systems (GPS, GLONASS, Galileo, etc.) are atomic clocks (quantum frequency standards), in which magnetic resonance (MR) is realized at the hyperfine 0-0 transition, in particular, in ^{87}Rb atoms at $\nu_{0-0} = 6.834$ GHz frequency under optical pumping conditions, lamp (or laser), in absorption cells with buffer (inert) gases.

Achieving the relative instability $\sigma_y(\tau)$ of the output frequency of the rubidium atomic frequency standard (RAFS) at the level $(1 \div 3) \cdot 10^{-13} \cdot \tau^{-1/2}$, where $\tau = (10^3 \div 10^4)$ s, requires solving complex physical problems to ensure high stability of the quantum frequency discriminator parameters (Milstar and AEHF programs) [1].

The central element of the discriminator is absorption cell with operating atomic gas ^{87}Rb . The cell contains anti-relaxation (AR) component: buffer gas or wall coating ($\sim 10\mu$ thick) from refractory paraffin (for example, tetracontane, $\text{C}_{40}\text{H}_{82}$).

Cells, that are made by using the AR-coating technology of cell walls in a vacuum, have an obvious advantage over cells with buffer gases. They have higher values of effective relaxation times τ_1 and τ_2 , signal-to-noise ratio (S/N) and also have narrower MP line width in discriminator. For the first time ever, ^{133}Cs cells with an AR-coating were used in the USSR (IZMIR AN, Moscow) in cosmic quantum ^{133}Cs magnetometers installed on the "Kosmos-321" and "Kosmos-356" satellites (1969; 1971) whose quantum sensors operated in rough conditions of open space [2].

Nevertheless, the use of cells with AR-coating in rubidium frequency standards (RAFS) was restrained by the opinion of possible instability of the coating for a long time. However, due to the high efficiency of laser pumping of ^{87}Rb atoms [3, 4], interest in the study of AR coatings and the use of such ^{87}Rb cells in RAFS has sharply increased.

So, in [5], it was found that the AR-coating is very weakly "aging". Four types of cells manufactured during 40 years by different manufacturers showed the frequency drift of MR quantum transition in time of less than 10 Hz over 30 years, which confirmed the long-term stability of AR coating properties. In such a ^{87}Rb -cell ($\varnothing 40$ mm), the line width $\Delta\nu \sim 47$ Hz was achieved [5], which is 14 times less than in commercial ^{87}Rb -standards on cells with buffer gases. The frequency shift $\delta\nu$ of the magnetic resonance from collisions of ^{87}Rb atoms with the coating material relative to the reference value ν_{0-0} was -68 Hz versus $+4000$ Hz in cells with mixtures of buffer gases.

The problem, especially of space RAFS, is the necessity to realize TFC at the level of $\sim 10^{-13}$ Hz/ $^{\circ}\text{C}$ and to expand the temperature zone of frequency shifts compensation, ~ 1 $^{\circ}\text{C}$, in conditions of high operating temperature $\sim (65\div 75)$ $^{\circ}\text{C}$ of ^{87}Rb -cells with a buffer gases

mixture. Solving this problem will allow us to obtain the required instability of RAFS frequency $\sigma_y(\tau) \sim 10^{-14}$ in the daily averaging time interval.

Based on the results of studies [6-9], the authors suggested solving the problem of reducing TFC to the level of 10^{-13} Hz/°C at a lower temperature of the RAFS discriminator in the operating temperature range of $(-35 \div +45)$ °C, which is set inside the satellite [1].

The proposal was to use a new type of cell with the combination of two different-type AR components in this cell (coating + buffer gas) for efficiency of temperature frequency shifts $\delta\nu(T)$ compensation from these AR-components: positive from the coating, $+\delta\nu_{coat}(T)$, and negative, $-\delta\nu_{buff}(T)$, from the buffer (inert) gas in a certain temperature range. Ar⁴⁰ was chosen as the inert gas.

This paper presents the following

1. In order to obtain the minimum value of TFC, the technological stage of increasing the ripening time of the coating material (tetracontane, C₄₀ H₈₂) in the rubidium absorption cell was additionally performed.
2. The optimal inert gas (Ar⁴⁰) pressure has been determined to expand the temperature zone of frequency shift compensation, $+\delta\nu_{coat}(T)$ and $-\delta\nu_{buff}(T)$.
3. Experimental dependences (see Fig. 1) of the frequency change ($\nu = 6.834$ GHz) of rubidium atoms magnetic resonance on the absorption cells temperature in the range of $(35 \div 63)$ °C (with AR-coating, pos.1, and with a combination of AR- components, coating + buffer gas, Ar⁴⁰, pos.2) were obtained. Cylindrical cells: $\varnothing 22 \times 22$ mm.
4. A TFC value of $3 \cdot 10^{-13}$ Hz/°C was obtained in the temperature 'A - B' range of $(35 \div 44)$ °C (Fig. 1, pos.2), which gives grounds for increasing the average time stability of the RAFS frequency to $\sigma_y(\tau) \sim 10^{-14}$.
5. The frequency measurement error for dependences 1 and 2 (Fig. 1) was less than 0.02 Hz. (The reference frequency of the hydrogen generator was used in the measurements). The stability of the temperature value at each reference points did not exceed 0.05 °C.

Conclusion

The experiment showed that the temperature frequency coefficient, TFC, can be realized at the level $\sim 10^{-13}$ Hz/°C in a wide range of a temperature change, ~ 8 °C, in the RAFS quantum discriminator when using an ⁸⁷Rb absorption cell with two dissimilar AR -components (coating + buffer gas) due to the effective compensation of frequency shifts with a different sign of these components, $+\delta\nu_{coat}(T)$ and $-\delta\nu_{buff}(T)$.

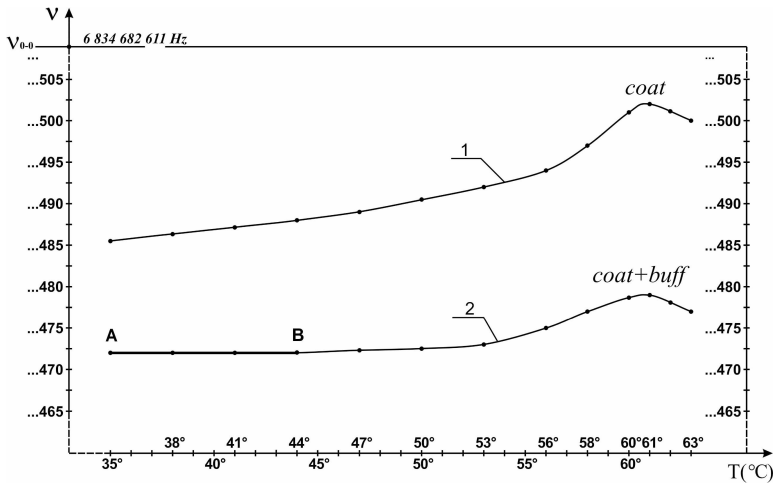


Figure 1. Dependences of the ^{87}Rb atoms magnetic resonance frequency $\nu(T) = 6.834\text{ GHz}$ of the atomic clocks (RAFS) quantum discriminator on the change in the temperature of the absorption cells.

1 – dependence $\nu(T)$ for the absorption cell with AR-coating;

2 – dependence $\nu(T)$ for a cell with a combination of AR-components, coating + buffer gas (Ar^{40})

References

1. McClelland T., White Y., Wilson D. “Space-Glass Rubidium Atomic Frequency Standard with Improved Performance for GNSS Systems” – Proc. 43rd Annual Precise Time (PTTI) Systems and Applications Meeting, pp. 325-340 (2011).
2. Dolginov Sh. and Kozlov A., “Magnetometers for Space Measurements”, Rev. de Phys. Appl., vol. 5, № 1, pp. 178-182 (1970).
3. Pellaton M., Affolderbach C., Mileti G., et al. “Wall-coated cells for Rb atomic clocks” – Proc. Joint Conf. of the IFCS-EFTF, Gottenberg, Sweden, pp. 87-90 (2012).
4. Besedina A., Berezovskaya O., Zholnerov V., “Study of a ^{87}Rb Vapour Discriminator with Laser Pumping for a High Stability Onboard Frequency Standard” – Proc. of the 21th EFTF, Geneva, Switzerland, pp. 607-612 (2007).
5. Gusman J.S., Wojciechowski A., Stalnaker J.E., et al. “Nonlinear magneto-optical rotation and Zeeman and Hyperfine relaxation of potassium atoms in a paraffin-coated cell” – Phys. Rev. A, vol. 74, p. 053415 (2006).
6. Knappe S. and Robinson H.G. “Double-resonance lineshapes in a cell with wall coating and buffer gas” – New Journal of Physics, vol. 12, pp. 1-12 (2010).
7. Balabas M.V., Karaulanov T., Ledbetter M.P., et al. “Polarized alkali vapor with minute-long transverse spin-relaxation time” – Phys. Rev. Lett., 105(8), R 070801 (2010).
8. Pestov E.N., Azarov V.P. and Besedina A.N., Zholnerov V.S. “Creation of ^{87}Rb -absorption cells with anti-relaxation wall coating for highly stable atomic clocks” – Proc. IAA RAS., St.-Petersburg, Russia, № 27, pp. 507-511 (2013).
9. Pestov E.N., Pestov D.E. and Azarov V.P. “Rubidium absorption cell” – Patent Russia, № 151192 (2014).

Electronic spin resonance in the study of the processes of association of gallstones

Alina A. Pichugina, Larisa V. Tsyro

Institute of Natural and Technical Sciences, Surgut State University, Lenina avenue 1, Surgut, Russian Federation

E-mail: alina.com9@mail.ru

http://www.surgu.ru

Introduction

Gallstones are divided into three types (cholesterol, pigment and mixed), with the most common type being cholesterol [1]. Currently, there is no consensus on the mechanism of gallstone formation. So according to many authors [2–5] the formation of gallstones occurs as a result of changes in the composition of bile and the formation of free radicals in it. So in a normal state, the main components of bile are primary lipids - bile acids, phospholipids and cholesterol. In addition to primary lipids, components such as water, lipids, electrolytes (Na^+ and K^+), fatty acids, polysaccharides, carbonates and proteins are present in bile [6, 7]. As a result of various pathogenic disorders (age, nutrition, ecology), bile undergoes changes and its cholesterol is oversaturated. Bile supersaturated with cholesterol is characterized by an excess of cholesterol crystals, on which other insoluble components are precipitated, which subsequently form a gallstone. Since the process of formation of gallstones is not completely clear, it is relevant to study the processes of association of gallstones.

Results

According to X-ray phase analysis (XRD), the gallstones examined are a mixture of cholesterol phases ($\text{C}_{27}\text{H}_{46}\text{O}$, PDF No. 00-007-0742), desmosterol ($\text{C}_{27}\text{H}_{44}\text{O}$, PDF No. 00-010-0627) and calcium carbonate in the form of two polymorphic modifications – calcite (CaCO_3 , PDF No. 01-072-4582) and vaterite (CaCO_3 , PDF No. 00-025-0127). Data of elemental analysis showed that such stones as Ca, Cu, Mn, Fe, Zn, K, P, S, Cl are present in these stones.

According to electron spin resonance (ESR) data, gallstones contain centers characteristic of bilirubin radicals, as well as centers related to high-spin iron(III), manganese(II) and copper(II), and bio-organic complexes of copper(II). Despite the fact that the spin centers in all studied gallstones are almost the same, they differ in their different contents and their environment (Table 1). This fact indicates that radical processes take place in the process of gallstone formation in the human body.

The study of the association of gallstones was carried out by dissolving them in benzene (at ratios from 1–10 to 1–100), followed by precipitation with hexane. The particle size in the resulting systems was measured by the method of photon correlation spectroscopy.

When dissolving gallstones in benzene, a colloidal system is formed, based on exchange interactions. In such a system, there is a decrease in particle size with an increase in the amount of solvent. Thus, when the ratio of gallstone to benzene is 1–10, the particle size in the colloidal system is about 2000 nm, and when the ratio of gallstone to benzene is 1–100, the particle size decreases to 250 nm. This fact can be explained by the fact that in the colloidal system "gallstone – benzene" with a low solvent content particles are close to each other, as a result of which they can collide with each other, i.e. their agglomeration occurs, with the formation of a larger associate. With the introduction of more solvent agglomeration of particles is very slow, or does not occur, because the energy of interaction between the particles decreases, due to the fact that they are at large distances from each other.

Table 1. ESR data on gallstones

Sample	C_{general} , spin/g	Peak I		Peak II		Peak II		Peak IV	
		g	C_{I} , spin/g	g	C_{II} , spin/g	g	C_{III} , spin/g	g	C_{IV} , spin/g
No. 1	$4,66 \cdot 10^{18}$							2,001	$4,00 \cdot 10^{18}$
No. 2	$1,17 \cdot 10^{19}$					2,049	$2,18 \cdot 10^{18}$	1,998	$1,74 \cdot 10^{16}$
No. 3	$1,85 \cdot 10^{20}$	5,615	$6,90 \cdot 10^{17}$					2,004	$3,62 \cdot 10^{16}$
No. 4	$1,91 \cdot 10^{19}$	4,189	$2,50 \cdot 10^{17}$	2,366	$3,12 \cdot 10^{16}$	2,140	$8,45 \cdot 10^{16}$	2,004	$4,48 \cdot 10^{15}$
No. 5	$9,60 \cdot 10^{18}$	4,238	$2,39 \cdot 10^{15}$					2,004	$2,10 \cdot 10^{15}$
No. 6	$5,51 \cdot 10^{18}$						$1,15 \cdot 10^{18}$	2,003	$1,57 \cdot 10^{18}$
No. 7	$2,63 \cdot 10^{19}$							2,004	$9,97 \cdot 10^{15}$
No. 8	$9,37 \cdot 10^{19}$							2,001	$2,33 \cdot 10^{14}$

When introduced into such a colloidal system of hexane, the particles present in the dispersed system are combined. Thus, with the introduction of 0,1 ml of hexane in the colloidal system, a process of gradual enlargement of the particles begins. As a result, large associates are formed, which, reaching their maximum size, precipitate in the form of an agglomerate. This process is repeated many times, because it is dynamic (table. 2). This process is repeated until the concentration of radical particles becomes minimal. As a result, the colloidal system will be observed formation of a large associate – agglomerate, which will precipitate.

Table 2. The average radius of the particles in the system "gallstone–benzene" with the addition of *n*-hexane

Sample	The ratio "Gallstone – benzene"	$V(C_6H_{14})$, ml									
		0,1	0,2	0,3	0,4	0,5	0,6	0,7	0,8	0,9	1,0
No. 8	1 : 50	2140 ± 100	3780 ± 100	690 \pm 40	31 \pm 5	1045 ± 90	630 \pm 40	7 \pm 1	20 \pm 5	18 \pm 5	—
	1 : 100	530 \pm 40	516 \pm 40	645 \pm 40	1390 ± 90	23 \pm 5	38 \pm 5	1041 ± 90	—	—	—

To confirm that the process of Association of gallstones is radical, i.e. with the participation of particles with unpaired electrons, ESR spectra of solutions of gallstones and residues from dissolution – precipitation were removed (table. 3).

Table 3. ESR data on gallstone solutions

Sample	$C_{\text{general, spin/g}}$	$C_{\text{general, spin/g}}$ narrow peak ($g=2,0$)
Sample No. 8 in C_6H_6 (1-50) solution	$8,58 \cdot 10^{17}$	$5,49 \cdot 10^{12}$
Sample No. 8 in $C_6H_6+0,2C_6H_{14}$ (1-50) solution	$1,33 \cdot 10^{18}$	$1,06 \cdot 10^{13}$
Sample No. 8 in $C_6H_6+0,4C_6H_{14}$ (1-50) solution	$1,19 \cdot 10^{18}$	$5,66 \cdot 10^{12}$

Thus, it can be concluded that during the dissolution of the gallstone in benzene, a colloidal system is formed, in which an increase in the particle size is observed. Part of the particles with unpaired electrons acts as associative combinations that are evenly distributed throughout the volume of the colloidal system and are characterized by a certain size, which is determined by photon correlation spectroscopy.

References

1. J. R. Ramya, K. T. Arul, M. Epple, U. Giebel, J. Guendel-Graber, V. Tayanthi, M. Sharma, M. Rela, S. N. Kalkura. – *Material Science and Engineering C*, 78, 878-885 (2017).
2. A. Parviainen, C. Marchesi, J. M. Suarez-Grau, C. J. Garrido, R. Perez-Lopez, J. M. Nicto, G. Cobo-Cardenas. – *Science of the Total Environment*, 624, 1031-1040 (2018).
3. H. W. Admirand, D.M. Small. – *J. Clin. Invest.*, 47, 1043-1052 (1968).
4. H. Wittenburd. – *Best Pract. Res. Clin. Gastroenterol.*, 24, 747-756 (2010).
5. F. G. Unger, L. V. Tsyro, A. A. Pichugina, D. A. Afanasiev, S. A. Kiselev. – *Herald of the Bauman Moscow State Tech. Univ., Nat. Sci.*, 4, 107-122 (2016).
6. T. R. Rautray, V. Vijayan, S. Panigrahi. – *Nucl. Instr. Meth. Phys. Res. B*, 225, 409-415 (2007).
7. F. Cetta. – *Ann. Surg.*, 213, 315-326 (1991).

Application of solid-state NMR to the study of water sorption with hydrolysis lignin

Yu. A. Popova, S. L. Shestakov, A. Yu. Kozhevnikov, D. S. Kosyakov, A. V. Faleva

Northern (Arctic) federal university named after M.V. Lomonosov

Severnaya Dvina Emb. 17, Arkhangel'sk, Russia; 163002

E-mail: yuliya.popova01@mail.ru

Introduction

Lignin, the second most abundant biopolymer in nature (after cellulose), can be considered as the most important renewable source of valuable aromatic compounds. The hydrolysis lignin (HL) is the main component of pulp and paper industry waste. However, the structure and properties of HL are difficult to study because it is insoluble in organic solvents and alkalis [1].

The ability of HL to absorb and retain some water is an important aspect for the study of its properties and for development of its modification methods, because the water in polymer can affect its mechanical and chemical properties. The study of the water sorption processes in lignin and, in particular, the identification of priority sorption centers in macromolecules is the urgent task which can be solved with solid-state NMR spectroscopy.

Experimental part

As a research object, softwood hydrolysis lignin was used, obtained at the Kirov Biochemical Plant and containing 65.2% lignin (according to Klason), 14.3% of extractive substances and 12.5% of residual polysaccharides, the ash content was 7.6% [2].

During the samples preparation dry lignin samples were saturated with water in desiccators with various fixed relative air humidity (RH) at the room temperature until the reach of constant weight. The ^1H and ^{13}C NMR spectra were registered with NMR spectrometer Bruker AVANCE III 600 MHz. We used standard one-pulse sequence for ^1H -NMR spectra and CP/MAS for ^{13}C -NMR spectra. MAS rate was equal to 7 kHz in all experiments, spectra were registered at the room temperature. NMR spectra were processed in standard software "TopSpin".

Results and discussion

^1H NMR spectra of lignin

The most intense signal in the ^1H -NMR spectra of the studied lignin samples is observed in the region of 5-10 ppm (Fig. 1). The set of signals is observed between 2 and 4 ppm, their chemical shift slightly varies depending on the moisture content of the sample.

The position of the ^1H -NMR signal is determined by the sorption capacity of the polymer relative to the water sorbed from the air at a determined relative humidity. The values of the sorption capacity (Fig. 1) are 7,4% (2), 10,6% (3), 14,8% (4), 31,6% (5) and 39,7% (6).

The NMR signal width $\Delta\nu_{1/2}$ is determined by the transverse relaxation time T_2 , and decrease of the signal width indicates the increase in the mobility of a corresponding group of atoms, and vice versa [3].

The dependences of the width of the most intense ^1H -NMR signal on moisture content are presented in Fig. 2.

According to data of ^1H -NMR spectra, we can conclude that the entire sample volume is hydrated during moisture saturation, the water penetrates into deeper structures of the natural polymer during swelling, and the majority of protons are involved in fast exchange processes. One powerful signal is observed in the ^1H -NMR spectra of hydrolysis lignin, which is the weighted average sum of the signals of most protons. Because of this, the mechanism of

hydration and, particularly, the distribution of water sorption sites in the lignin seem to be interesting.

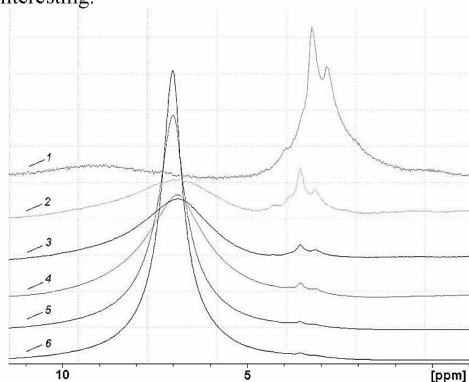


Figure 1. ^1H -NMR spectra of the hydrolysis lignin samples prepared at RH: 1 – 0%; 2 – 32%; 3 – 58%; 4 – 75%; 5 – 95%; 6 – 100%

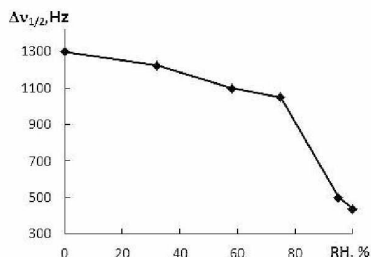


Figure 2. The dependencies of the most intensive band width in ^1H -NMR spectrum on water content

^{13}C -NMR spectra of lignin

After registration of the ^{13}C NMR spectra of the samples, it was observed that the residual polysaccharides in the samples play a significant role in the processes of water sorption [4]. Fig. 3 shows the structure of a cellulose unit as a polysaccharide, predominantly present in the technical lignin. With further assignment of spectrum bands, the presence of polysaccharides was taken into account.

When the relative humidity changes, the chemical shifts of the ^{13}C -NMR signals remain almost constant, but the resolution of the spectra improves as the moisture content increases, which means that the width of the signals changes. Thus, the mobility of groups of atoms corresponding to the selected signals also changes.

Fig. 4 shows the dependence of the linewidth of some ^{13}C -NMR signals on the moisture content of the samples.

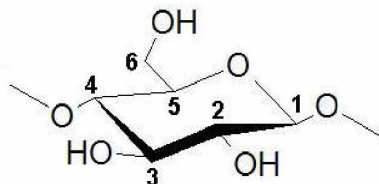


Figure 3. Structure of the cellulose monomer

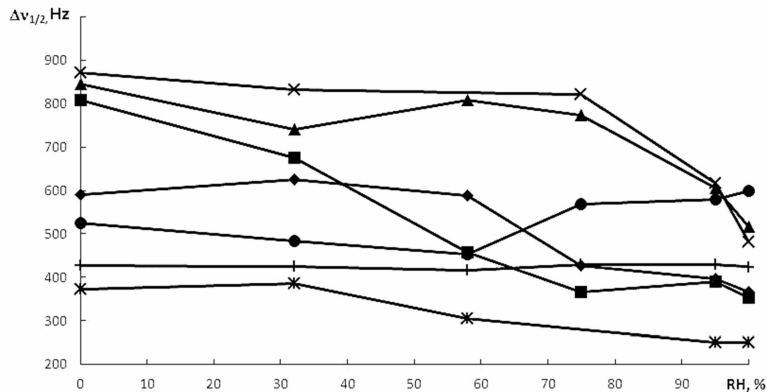


Figure 4. The dependencies of band widths in the ^{13}C -NMR spectra on relative humidity with chemical shifts 106.7 ppm (♦), 76.7 ppm (▲), 73.9 ppm (×), 66.6 ppm (*), 63.5 ppm (■), 58.3 ppm (+), 31.8 ppm (●)

We assigned the observed signals to the atomic groups according to the tables of chemical shifts [5] and assignment of spectrum bands [4]. Table 1 shows the relative changes in the peak width of the selected signals when the moisture content varies from 0% to 100%.

Based on the relative changes in the peak width of the selected signals, we can conclude that the sample fragments are hydrated differently, and some groups absorb water more actively than others. Assuming that all absorbed water accumulates around these functional groups, it is possible to calculate the relative shares of the total amount of water per type of group. The results of the calculations are presented in table 1.

Table 1. $\Delta\nu_{1/2}$ (Hz) band widths in the ^{13}C -NMR spectra of hydrolyzed lignin with different moisture content (RH) and mass fractions of water absorbed by various functional groups

δ , ppm	Groups*	Band widths, Hz		Width change multiplicity	Amount of weight parts	Water mass fraction, %
		RH = 0%	RH = 100%			
31.8	CH ₃ COO- (hemicell.)	525.4	599.1	0.877	-	-
58.3	-OCH ₃ (aliph.)	427.7	423.8	1.009	-	-
63.5	-OCH ₃ (aryl.)	807.2	353.5	2.283	1.51	25.89
66.6	C-6	372.0	250.7	1.484	1.00	16.82
73.9	C-2, C-3, C-5, C-OH (aliph.)	872.0	482.2	1.808	1.22	20.50
76.7	C-2, C-3, C-5, C-OH (aliph.)	845.3	516.7	1.636	1.10	18.55
106.7	-CH-(aryl.), C-1	589.8	366.5	1.609	1.08	18.24

*carbon atoms are numbered according to positions in cellulose monomer (Fig. 3).

According to calculations, the largest amount of water is accumulated around the methoxyl and hydroxyl groups of lignin and polysaccharides. Since the mobility of atoms that are not associated with these groups also increases with increasing moisture content, it is assumed that hydrophobic fragments of macromolecules are hydrated to a certain extent.

Conclusion

We proposed the approach to the study of water binding by hydrolysis lignin, based on the use of solid-state NMR spectroscopy. It has been established that technical hydrolysis lignin is able to sorb up to 40% of water by mass from the gas phase. Hydration of a high-molecular compound proceeds through both the hydrophilic and hydrophobic regions of the macromolecules, with the bulk of the adsorbed water (~64%) associated with the hydroxyl and methoxyl groups of lignin and polysaccharide residues.

Acknowledgments

The work was carried out using the equipment of the Center for Collective Use of Scientific Equipment "Arctic" of the Northern (Arctic) Federal University with financial support from the Ministry of Education and Science of the Russian Federation (state assignment No. 4.2518.2017 / 4.6).

References

1. Heitner C., Dimmel D.R., Schmidt J.A. Lignin and lignans: advances in chemistry / ed. by C.Heitner. Boca Raton: CRC Press, 2010.
2. Kosyakov D. S., Ipatova E. V., Krutov S. M., Ul'yanovskii N.V., Pikovskoi I.I. – Journal of Analytical Chemistry, Vol. 72, № 14, 1396–1403 (2017).
3. Blümich B. Essential NMR. For scientists and engineers (In Russian). – M.: Technosphaera, 2011.
4. Lequin S., Chassagne D., Karbowski T., Gougeon R., Brachais L., Bellat J.-P. – Journal of Agricultural and Food Chemistry, Vol. 58, 3438–3445 (2010).
5. E. Pretsch, P. Bühlmann, C. Affolter. Structure determination of organic compounds. – Berlin: Springer-Verlag, 2000.

EPR of calixarenes doped by Lu³⁺, La³⁺, Tb³⁺, Gd³⁺, Yb³⁺, Er³⁺, Dy³⁺ ions

*E. A. Razina¹, A. S. Ovsyannikov^{1,2}, S. E. Solovieva^{1,2}, I. S. Antipin^{1,2}, A. I. Kononov¹,
G. V. Mamin¹, M. R. Gafurov¹, M. S. Tagirov¹, S. B. Orlinskii¹*

¹Kazan Federal University, 420008, Kazan, Russian Federation

²A.E. Arbuzov Institut of Organic and Physical Chemistry of Kazan Scientific Center of Russian Academy of Science, 420088, Kazan, Russian Federation

E-mail: helenrazi@yandex.ru

Introduction

The development of current computation technologies is closely related to creation of new type materials based on the application of quantum states such as metal-organic grids. Calixarenes doped by rare-earth metal ions are a promising molecular platform for the realization of metal-organic grids, and, accordingly, have great potential for use as functional materials.

The studied samples and experimental methods

The studied substances were BuS₄CH₂COOH calixarenes doped by rare-earth metal ions Lu³⁺, La³⁺, Gd³⁺, Yb³⁺, Er³⁺ and S₈CH₂COOH doped by Tb³⁺, Dy³⁺ ions. Samples were synthesized in Laboratory of Organic Chemistry at the Institute of Chemistry of KFU [1]. For the EPR studies calixarenes doped by Lu³⁺, La³⁺, Tb³⁺, Gd³⁺, Yb³⁺, Er³⁺ and Dy³⁺ ions were grown in the form of crystals by evaporating from saturated solution. Important to note, calixarenes were doped by rare-earth metal ions during the synthesis of the molecules in order to allow metal ions to take place in the inner cavity of the calixarene's molecule.

The EPR spectra were measured by W-band Elexsys-680 (Bruker) spectrometer, at a temperature of 15-300K in the CW mode.

It is important to point out the calixarene crystals are stored in a special solution. Before the EPR studies, the samples were placed on the absorbent solution surface and dried thoroughly. There are then two cases:

1. The ampoule's volume is filled with disordered microcrystals (>200). This is done for better EPR sensitivity.
2. The largest crystal from the set is chosen and oriented in the ampoule in a way that the basic plane is perpendicular to the magnetic field. In this case, the magnetic field orientation dependencies of the microcrystal could be registered, but the sensitivity of the EPR spectrometer was not enough to measure all of the presented samples within a reasonable timeframe.

The optic microscopy of the samples

In order to ascertain that the studied substances were microcrystals, and also in order to measure the size of the biggest microcrystals, optic microscopy was done. The photo of the thiacalix[4]arenes doped by Lu³⁺ ions microcrystals taken with a Carl Zeiss Jena optical microscope at the zoom x25 is shown in figure 1. One may see from the photo, the studied substance consists of microcrystalline plates in a fluid. The size of the biggest microcrystals was about 100x100x4 μm (fig. 1). Generally, the size of the microcrystals ranged from 20x20x2 up to 300x300x100 μm.

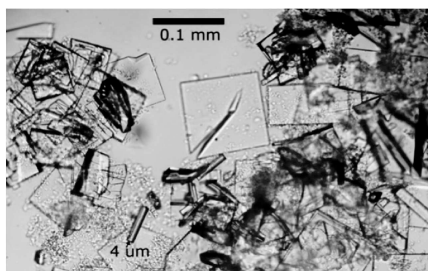


Figure 1. $Bu_4S_4CH_2COOH$ calixarene crystals doped by rare-earth metal ions Lu^{3+}

EPR studies of rare-earth metal ions in calixarenes

The EPR spectra of rare-earth metal ions in the thiocalix[4]arenes powders

The lines of the EPR spectra of $Bu_4S_4CH_2COOH$ calixarenes doped by Lu^{3+} , La^{3+} ions, and S_8CH_2COOH doped by Tb^{3+} weren't observed in the measured spectra due to Lu^{3+} , La^{3+} and Tb^{3+} being nonparamagnetic ions. Thus unwanted paramagnetic dopants weren't detected in the samples.

The EPR spectra of $Bu_4S_4CH_2COOH$ doped by Gd^{3+} , Yb^{3+} , Er^{3+} ions and spectra of S_8CH_2COOH doped by Dy^{3+} ions are shown in figure 2. The shape of the lines was complicated to calculate spectroscopic parameters directly so, to deal with it, the approximation was held. The approximation results are shown in figure 2 by dotted lines, and its parameters are presented in table 1.

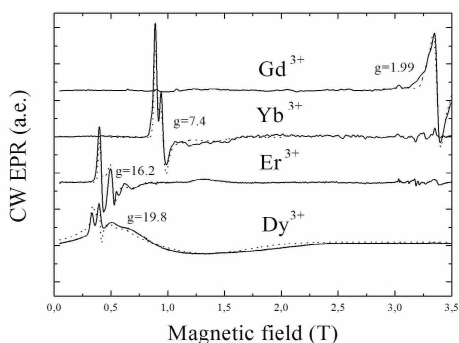


Figure 2. Continuous wave EPR spectra of $Bu_4S_4CH_2COOH$ doped by Gd^{3+} , Yb^{3+} , Er^{3+} ions and spectra of S_8CH_2COOH doped by Dy^{3+} ions

The calculated g-factors of rare-earth metal ions in the calixarenes were compared with the g-factors of free Gd^{3+} , Yb^{3+} , Er^{3+} , Dy^{3+} ions and the g-factors of Gd^{3+} , Yb^{3+} , Er^{3+} , Dy^{3+} ions in $CaWO_4$ [2]. The comparison showed the proximity of the calculated g-factor values to the values obtained for the ions in $CaWO_4$ and the strong discrepancy with the g-factor of free ions values.

The EPR spectra of rare-earth metal ions in a single thiocalix[4]arene microcrystal

A standard test of a dopant localization inside the microcrystal is the registration of magnetic field orientation dependencies of the microcrystal.

Table 1. Comparison of g-factors

	S	g_{zz}	g_{yy}	g_{xx}	D (MHz)	g-factors of free ions	g-factors in CaWO_4 [2]
S8-Tb	3/2	-	-	-	-	1.5	17.7-17.8
S4-Gd	7/2	2.01(1)	1.98(1)	1.98(1)	880(9)	2	1.9915-1.9916
S4-Yb	1/2	4.70(5)	6.95(5)	7.50(5)	--	1.1	1.05-3.90
S4-Er	1/2	9.5(1)	13.0(1)	16.8(1)	--	1.2	1.25-8.38
S8-Dy	1/2	19.8(5)	16.5(5)	12.0(5)	--	1.3	5.5-7.5
		13.0(5)	5.7(5)	5.7(5)	--		

At first, the orientation dependence of the thiacalix[4]arene microcrystal doped by Gd^{3+} ions was measured. However, changes in the EPR spectra were poorly expressed because of the wide width of the lines. To reduce the spin interaction, and by extension the line width, the calixarenes must contain both paramagnetic and nonparamagnetic rare-earth metal ions in 1:99 ratio or less. Unfortunately, the sensitivity of the spectrometer did not allow to register the EPR spectrum of thiacalix[4]arenes doped by $\text{Gd}^{3+}/\text{Lu}^{3+}$ ions in a 1:99 ratio.

However, the sensitivity of the spectrometer was sufficient to record the EPR spectra of one thiacalix[4]arene microcrystal doped by $\text{Er}^{3+}/\text{Lu}^{3+}$ ions in a 1:99 ratio (fig. 3). The spectrums shown in the figure 3 demonstrate the magnetic field orientation dependencies of the microcrystal and point out the localization of dopants inside the microcrystal.

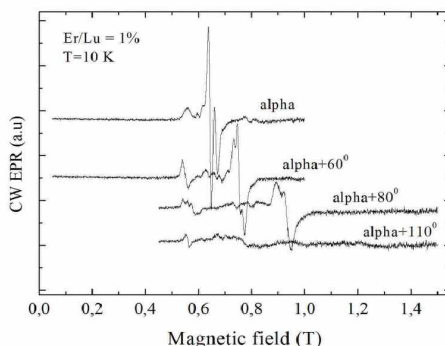


Figure 3. Magnetic field orientation dependencies of one particle (microcrystal) $\text{BuS}_4\text{CH}_2\text{COOH}$ calixarene with Er^{3+} (1%)

References

1. I. S. Antipin, V. Burilov, A. Valiyakhmetova, D. Mironova. Thiacalix[4]arene derivatives bearing polymerizable 1,3-butadiyne fragments: Synthesis and incorporation into polydiacetylene vesicles. *-RSC Advances.*, 6-50., 44873-4877 (2016).
2. I. N. Kurkin. EPR of trivalent ions of a group of rare earths in a homologous series of crystals having the structure of CaWO_4 . *-Collected Paramagnetic Resonance.*, 5, 31-73 (1969).

Analyzing the parameters of atom-atom interactions for Molecular dynamics simulations of micelle formation

A. M. Ryzhkov, N. A. Antonova, A. V. Komolkin

Faculty of physics, Saint Petersburg State University, 7-9 Universitetskaya embankment, Saint Petersburg 199034, Russia

E-mail: st054892@student.spbu.ru

Introduction

Various parameters of atom-atom interactions are used in studies of ionic surfactants by molecular dynamics method. Widely used parameters are AMBER, CHARMM, OPLS-AA [1-3]. Charges of ions in all the parameters are multiple of electron charge, for example, Na^+ , Ca^{2+} , Cl^- , $[\text{C5H11COO}]^-$. In the case of organic anions the total charge is distributed among atoms of acid residue. Such charges may lead to improper aggregation of amphiphiles [4]. In the beginning of this work, during the simulation of concentrated aqueous solution of sodium salt of carboxylic acids an inverse bilayer was formed. The concentration of the salt was equal to 4 CMC (critical micelle concentration) (fig. 1). Amphiphilic molecules glued together by hydrophilic parts through sodium ion, and hydrophobic parts were dissolved in water. The same aggregates were found in the following simulations with smaller concentration (fig. 2). Also there was sodium-sodium couples at a distance of several ångströms, not separated by a water molecule.

Due to non-physical simulation results, the following goal was set: to vary the parameters of interactions of ions in order to reproduce spherical form of micelles in a concentrated media. In this paper, the model charges of ions were studied.

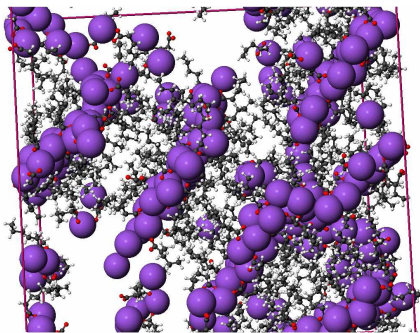


Figure 1. Inverse bilayer in water solution with salt concentration equal to 4 CMC

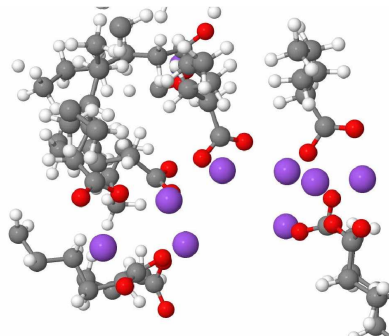


Figure 2. Inverse bilayer in water solution with salt concentration equal to 1.5 CMC

Computer model

For the experiment, the sodium salt of hexanoic acid was chosen as a substance that can form micelles. The solvent used was plain water. Parameters of atom-atom interactions for the acid residue were taken from the OPLS-AA [3] directory, for sodium ion from the article by Dang [5], water model was SPC/E [6]. The charges of ions were subjects to vary.

Three systems were created and modeled. For the first system charge was taken from the OPLS-AA. For the second and third systems, the charges were considered using quantum chemistry methods. The Hartree-Fock and DFT methods (6-31G**+/B3LYP) were used to find the optimal geometry of the system, consisted of one molecule of substance and several

water molecules. Then the ion charges were found using the Mulliken and Löwdin methods with 6-31G basis. The calculations were carried out for a dissociated molecule (the distances between the C atom of the COO group and Na varied from 3 Å to 5.5 Å with a step of 0.25 Å) surrounded by water molecules. There was a tendency to increase the ion charge at a distance. The resulting charges were averaged over distances and presented in the table 1.

Molecular dynamics method used for simulating systems with 3 different charge distribution of ions. It were simulated sequentially in the following order: recommended OPLS-AA charges, charges by Mulliken and charges by Löwdin. Equilibration of each following system took 1 ns. Data was recorded for 2 ns, each nanosecond being analyzed separately to ensure that the system went to equilibrium. To verify that the simulation result does not depend on the initial arrangement of atoms, the simulation sequence was repeated.

Table 1: charge distribution of the sodium salt of hexanoic acid

	Na ⁺	COO group		First methylene group from acid residue		Other methylene groups		Methyl group	
		C	O	C	H	C	H	C	H
OPLS-AA	1	0.7	-0.8	-0.12	0.06	-0.12	0.06	-0.18	0.06
Mulliken	0.7	0.76	-0.78	-0.12	0.11	-0.12	0.06	-0.18	0.06
Löwdin	0.5	0.4	-0.5	-0.12	0.11	-0.12	0.06	-0.18	0.06

Results and discussion

As a result, the following characteristics were obtained: diffusion coefficients of ions and water; radial distribution functions (RDF) of pairs: Na-Na (fig.3), COO-COO, H₂O-COO, H₂O-Na; the resident times of the water molecule in the sodium hydration shell; the distribution of the resulting aggregates in size and their shape.

In the figure 3, the first peak on RDF for Na¹⁺ agrees with the results of early simulations [7]. It corresponds to two ions of Na¹⁺ separated by 3 Å and without any water molecule between them. In the real solution this state would be unstable and the atoms will repel by the Coulomb's forces. Contrary, the RDF for Na^{0.5+} has no maxima after achieving unit value. It means uniform distribution of ions throughout the volume.

During the simulation the aggregates of acid residues were formed in each simulated system (fig. 4). The distance between aliphatic part of the anion in an aggregate is less than 4.8 Å. The number of molecules in one aggregate reached 52 molecules for the Löwdin charge distribution. The smallest aggregate size was observed in the system with standard charge distribution.

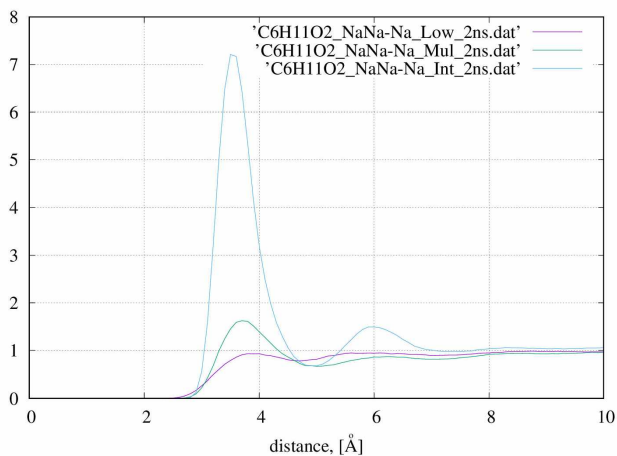


Figure 3. Radial distribution functions for sodium-sodium pairs with different charges

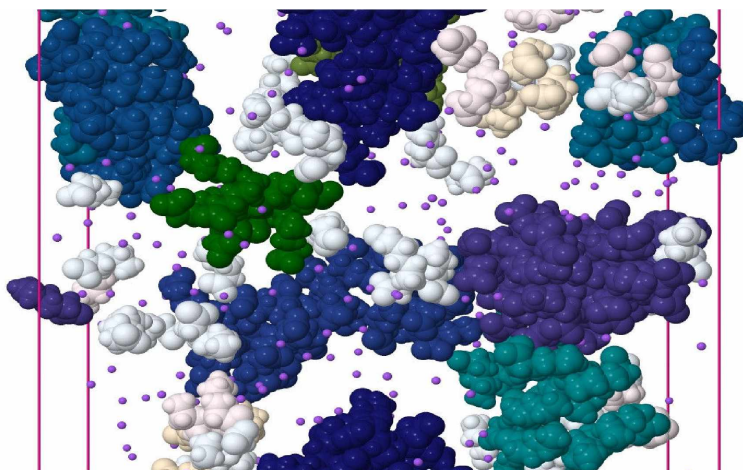


Figure 4. Snapshot of the simulated system with aggregates showed in different colors.
The monomers and dimers are colored in light

Conclusion

Potentially, the modeling of high concentrated solutions which consist of amphiphilic molecules needs to use the charge distribution not equal to ± 1 electron charge for ions in order to get more reasonable results.

Acknowledgements

Research was carried out using computational resources provided by Resource Center "Computer Center of SPbU" (<http://cc.spbu.ru>).

References

1. Yuan-Ping Pang. Use of multiple picosecond high-mass molecular dynamics simulations to predict crystallographic B-factors of folded globular proteins. – *Heliyon*, 2, (2016) e00161
2. S. Sen, Y. Han, P. Rehak, L. Vuković, P. Král. Computational studies of micellar and nanoparticle nanomedicines. – *Chem Soc Rev*, 47, 3845-3860 (2018)
3. S. Aparicio-Martínez, P. B. Balbuena. On the properties of aqueous amide solutions through classical molecular dynamics simulations. – *Molecular Simulation*, 11, 925-938 (2007)
4. B. Jönsson, O. Edholm, O. Teleman. Molecular dynamics simulations of a sodium octanoate micelle in aqueous solution. – *The Journal of Chemical Physics*, 85, 2259-2271 (1986)
5. L. X. Dang. Mechanism and thermodynamics of ion selectivity in aqueous solutions of 18-crown-6 ether: a molecular dynamics study. – *J. Am. Chem. Soc.*, 117, 6954-6960 (1995)
6. H. J. C. Berendsen, J. R. Grigera, T. P. Straatsma. The missing term in effective pair potentials. – *J. Phys. Chem.*, 1987, 91 (24), pp 6269–6271
7. A. P. Lyubartsev, A. Laaksonen. Concentration Effects in Aqueous NaCl Solutions. A Molecular Dynamics Simulation. – *J. Phy. Chem.*, 100 (40), 16410-16418 (1996)

Protein unfolding (denaturation) as monitored by PFG NMR measurements of translational diffusion

V. A. Salikov¹, I. S. Podkorytov¹, B. B. Kharkov¹ and N. R. Skrynnikov^{1,2}

¹Laboratory of Biomolecular NMR, SPbSU, St. Petersburg, 199034, Russia

²Department of Chemistry, Purdue University, West Lafayette, IN 47906, USA

E-mail: vladislav.salikov@inbox.ru

Titration of a protein with denaturant (such as urea) leads to progressive loss of protein structure and, ultimately, transformation of a protein molecule into a random-coil polypeptide chain. This progression can be monitored by a number of different experimental technique, e.g. circular dichroism, tryptophan fluorescence, 1D NMR spectroscopy, etc. In this report, we introduce an alternative method based on pulsed-field gradient NMR measurements of translational diffusion. Of note, this method is complementary to other techniques since it probes different properties of a protein. Specifically, protein diffusion is sensitive to the degree of expansion of the polypeptide chain, undergoing order-to-disorder transition.

For this study, we have chosen a well-known globular protein, ubiquitin. It has been expressed in *E. coli* (Rosetta strain) and purified as described previously [1]. The sample conditions (room temperature, D₂O-based solvent, pH 5.0, 50 mM sodium acetate buffer) have been chosen based on the previous circular dichroism study [2]. The samples have been prepared with low protein concentration, 230 μ M, in order to avoid the influence of (weak) ubiquitin dimerization [3]. Special precautions have been taken to account for the increased viscosity of the urea-containing solvent. To factor out this effect, we have used 1,4-dioxane as internal standard [4]. For PFG-NMR measurements, we have used the standard stimulated echo experiment, employing bipolar gradients [5]. The series of experiments has been conducted for urea concentration in the range from 0 to 10 M. The data were processed using the scripts written in-house, including special script for baseline correction. The obtained values of translational diffusion coefficient of ubiquitin plotted as a function of urea concentration follow the sigmoidal profile. This result demonstrates that measurements of translational diffusion are indeed suitable to monitor the process of protein unfolding (denaturation).

As a second part of this study, we intend to obtain a similar characteristic for the intrinsically disordered protein, α -synuclein. The results should shed new light on the presence of residual secondary/tertiary structure in α -synuclein in relation to the random-coil polypeptide chain. In addition, we will also investigate the sample of peptide H4, imitating the sequence of the corresponding histone tail, which is believed to be almost completely unstructured. Furthermore, we will also use a tripeptide GSF in order to elucidate the effect of urea “coat” around the peptide molecule.

Acknowledgements

This work is supported by the RSF grant 15-14-20038. All NMR measurements were performed at the Center for Magnetic Resonance in the Research Park of SPbSU.

References

1. Lazar G.A., Desjarlais J.R., Handel T.M. *Protein Science*. 1997. 6, 1167–1178.
2. Loladze V.V. et al. *Biochemistry*. 1999. 38, 16419–16423.
3. Liu Z. et al. *Angewandte Chemie International Edition*. 2012. 51, 469–472.
4. Wilkins D.K. et al. *Biochemistry*. 1999. 38, 16424–16431.
5. Wu D. H. et al. *Journal of Magnetic Resonance*. 1995. 115, 260-264.

Temperature dependence of NMR-relaxation rate in IL BmimAc

A. A. Selivanov, A. V. Ievlev

*Faculty of Physics, Saint Petersburg State University, Russia
E-mail: aleks74.seliv2000@gmail.com*

Introduction

In recent years, ionic liquids (IL) have been increasingly used as components of polymer electrolytes for new current sources. They have several advantages, such as low flammability, low vapor pressure, a wide space of thermal, chemical and electrochemical stability [1], which make it possible to produce more environmentally friendly current sources on the basis of IL. One of the most informative methods of studying ionic liquids is nuclear magnetic resonance, and in particular, the NMR relaxation method. For several decades, this method has been an effective tool for studying the structure of IL and the processes occurring in them.

The aim of this work was to study an ionic liquid based on the 1-Butyl-3-methyl-imidazolium cation, which could be used in new current sources in the future. The interest in this object in the literature [2] [3] has recently increased, but the properties of this cation have not been fully understood yet. The properties of the resulting ionic liquid also strongly depend on the anion, which can be either monatomic, for example Cl^- , Br^- , I^- , [4], or polyatomic, for example BF_4^- , PF_6^- , CH_3COO^- , TFSI^- , SCN^- [5]. In our opinion, the least studied anion is the acetate ion CH_3COO^- . Therefore, in our work we paid attention to this counterion. In this study we had to determine the relaxation rate and the correlation time of each nonequivalent proton group in the IL molecule.

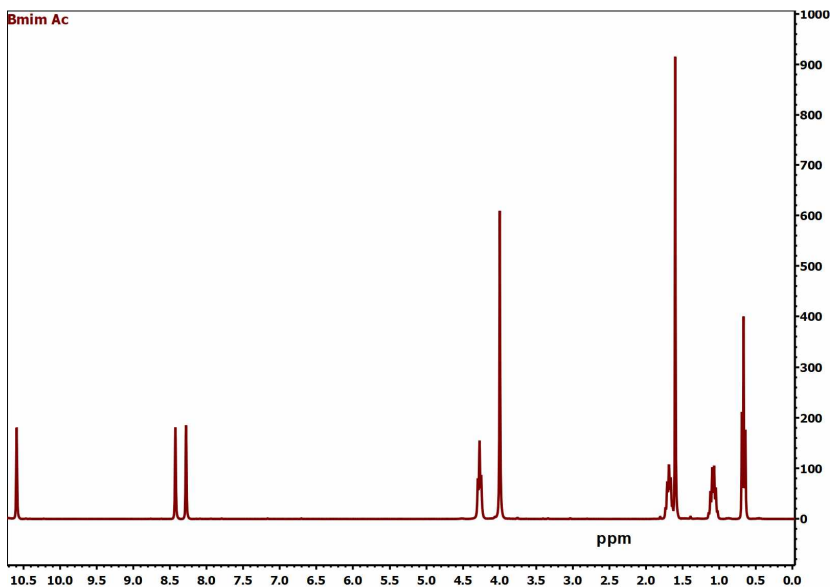


Figure 1. NMR-Spectre of BmimAc

Experimental section

The main goal of this experiment was to determine the temperature dependence of the relaxation rate of each nonequivalent group of atoms, as well as to find their correlation times. The measurements were carried out in the temperature range from 298K to 363K at a proton resonance frequency of 300 MHz using the equipment of the SPSU science park. The error in obtaining experimental data didn't exceed 3%. The sample for the study is placed in a radio frequency circuit located inside a constant magnetic field created by a superconducting solenoid. In our study we have used inversion-recovery method: $\pi - \tau - \frac{\pi}{2}$. Time of delay τ changed from 10 μ s up to 12 s. After the processing of the relaxation curves, we have defined the dependence of the relaxation rate on the reversed temperature:

Table 1: Relaxation rate of individual spectral lines

T, K	1000/T, K ⁻¹	R, S ⁻¹							
		4H	5H	CH2-N	CH3-N	CH2	CH3-COO	CH2	CH3
298	3,36	1,19	1,08	1,84	1,22	2,10	1,32	1,92	1,48
303	3,30	1,19	1,08	2,06	1,30	2,32	1,38	1,98	1,47
308	3,25	1,18	1,10	2,17	1,39	2,46	1,38	1,98	1,46
313	3,19	1,25	1,11	2,40	1,50	2,50	1,38	1,93	1,39
318	3,14	1,26	1,13	2,53	1,60	2,45	1,37	1,87	1,35
323	3,10	1,27	1,15	2,65	1,72	2,41	1,37	1,79	1,29
328	3,05	1,27	1,14	2,72	1,80	2,34	1,32	1,68	1,22
333	3,00	1,27	1,14	2,75	1,86	2,24	1,27	1,60	1,16
338	2,96	1,23	1,12	2,74	1,90	2,14	1,20	1,47	1,07
343	2,92	1,19	1,09	2,70	1,90	2,03	1,14	1,38	1,01
348	2,87	1,12	1,02	2,61	1,87	1,88	1,05	1,27	0,92
353	2,83	1,05	0,96	2,48	1,81	1,72	0,97	1,16	0,85
358	2,79	0,99	0,90	2,37	1,74	1,64	0,91	1,08	0,79
363	2,75	0,92	0,84	2,22	1,65	1,50	0,83	0,99	0,72

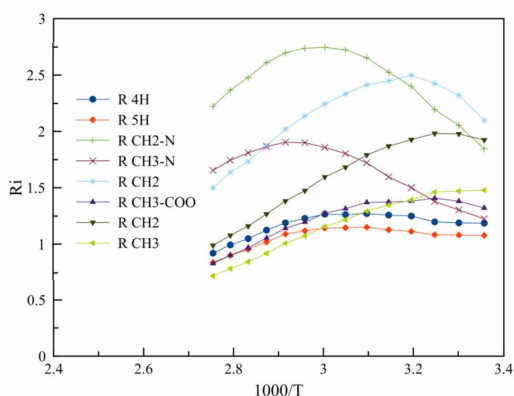


Figure 2. Dependence of relaxation rate on inverse temperature

In this figure we can see that the maximum relaxation rate for each line is reached at different temperatures. This can be explained by the fact that each group has a different mobility.

As we wanted to find out how the proton mobility behaves in imidazolium ring, we have found τ_c for 2H, 4H и 5H, using relaxation B.P.P. model. Figure 3 represents the dependence of the correlation time of these groups on the inverse temperature:

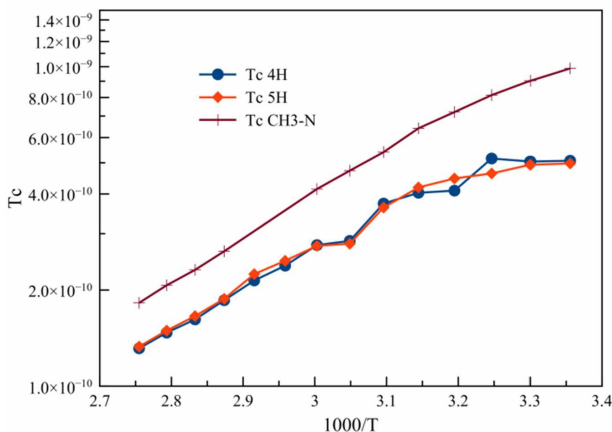


Figure 3. The dependence of the correlation time on the inverse temperature for different groups of protons

Acknowledgment

The authors thank the science park of St. Petersburg State University for providing the equipment for the experiment.

References

1. Влияние добавки ионных жидкостей EMIBF₄ и BMIBF₄ на свойства сетчатых полимерных электролитов для литиевых источников тока. *А.В. Юдина, А.А. Игнатова, Н.И. Шувалова, В.М. Мартыненко, О.В. Ярмоленко* *Электрохимическая энергетика*. 2014 Т.14, №3 с.158-163
2. Collective rotational dynamics in ionic liquids: A computational and experimental study of 1-butyl-3-methyl-imidazolium tetrafluoroborate *C. Schröder C. Wakai H. Weingärtner and O. Steinhauser* *The Journal Of Chemical Physics* 126, 084511 (2007)
3. Electrical conductivity and translational diffusion in the 1-butyl-3-methylimidazolium tetrafluoroborate ionic liquid. *J. Sangoro, C. Iacob, A. Serghei, S. Naumov, P. Galvosas, J. Kärger, C. Wespe, F. Bordusa, A. Stoppa, J. Hunger, R. Buchner, and K. Kremer* *The Journal Of Chemical Physics* 128, 214509 (2008)
4. Revised and Extended Values for Self-Diffusion Coefficients of 1-Alkyl-3-methylimidazolium Tetrafluoroborates and Hexafluorophosphates: Relations between the Transport Properties *Kemeth R. Harris, and Mitsuhiro Kanakubo* *J. Phys. Chem. B* 2016, 120, 12937–12949
5. Recent NMR Studies of Ionic Liquids *Krishnan Damodaran* *Annual Reports on NMR Spectroscopy, Volume 88, 216*

Computer simulation of orientational dynamics in alpha- and epsilon-lysine peptides

Oleg V. Shavykin, Valeriy V. Bezrodny¹, Sofia E. Miktaniuk¹, Igor M. Neelov², Denis A. Markelov²

¹St. Petersburg National Research University of Information Technologies, Mechanics and Optics (ITMO University), Kronverkskiy pr. 49, St.Petersburg, 197101, Russia

²St.Petersburg State University (SPbSU), 7/9 Universitetskaya nab., St.Petersburg, 199034, Russia

E-mail: kupala-89@mail.ru

Introduction

The poly-L-lysine homopeptides consisting of only lysine amino acid residues with α - and ϵ -amino group have many biomedical applications. There are two types of such linear peptides: poly(α -L-lysine) chains and poly(ϵ -L-lysine) chains in accordance with type of amino groups which form peptide bonds. We study here the difference in orientational mobility of two of such short chains consisting of 8 lysine residues. The fragments of these poly(α -L-lysine) and poly(ϵ -L-lysine) chains as well as their combinations exist also in the poly-L-lysine dendrimers, poly-L-lysine dendrigrafts and poly-L-lysine brushes. It was shown earlier by Markelov et al. that terminal and side (ϵ -L-lysine) groups of lysine dendrimers are more mobile than the same groups but in main chain (inner CH₂ groups) of dendrimer. In present work we compare orientational dynamics of H-H vectors of the same CH₂ groups of lysine residues in side chains of α -L-lysine linear peptide and in main chain of ϵ -L-lysine linear peptide. We performed the molecular dynamics simulation of orientational mobility [1-6] in these two different poly-L-lysine chains consisting of the same number of lysine monomers in water solvent with explicit account of counterions at temperature T=300K and pressure P=1atm using the program package Gromacs-4.5.6 with AMBER99SB-ildn force field.

The difference in the orientational dynamics

We estimated mobility of the chosen vector d between two hydrogens in the last hydrocarbon CH₂ of ϵ -amino group using the first order autocorrelation function (ACF) $P_1(t)$

$$P_1(t) = \frac{\langle \mathbf{d}(t), \mathbf{d}(0) \rangle}{|\mathbf{d}(t)| |\mathbf{d}(0)|}$$

and the second order autocorrelation function (ACF) $P_2(t)$

$$P_2(t) = \frac{3}{2} \frac{\langle (\mathbf{d}(t), \mathbf{d}(0))^2 \rangle}{|\mathbf{d}(t)|^2 |\mathbf{d}(0)|^2} - \frac{1}{2}$$

Monomers of poly(α -L-lysine) peptides has 3 chemical bonds in main chain as in all normal α -peptides. At the same time each monomer of poly(ϵ -L-lysine) chain contains 7 chemical bonds in its main chain. Due to this reason the poly(α -L-lysine) has more than 2 times shorter contour length and correspondingly smaller global end-to-end orientational relaxation time. We found that the local orientational mobility of H-H vector in CH₂ group neighboring to NH₂ group in side chains of poly(α -L-lysine) (see Fig.1, the right panel) is also smaller than mobility of H-H vector in CH₂ group nearest to NH group in main chain of poly(ϵ -L-lysine). The results of this work are in agreement with the theoretical predictions about anisotropy of local orientational motion in linear polymers (i.e. about different mobility of vectors oriented along and perpendicular to main chain of polymer) obtained by Gotlib et al [7-9] and results for lysine dendrimers obtained by Markelov et al. [3] and our previous results on local mobility in lysine dendrimers [11-18].

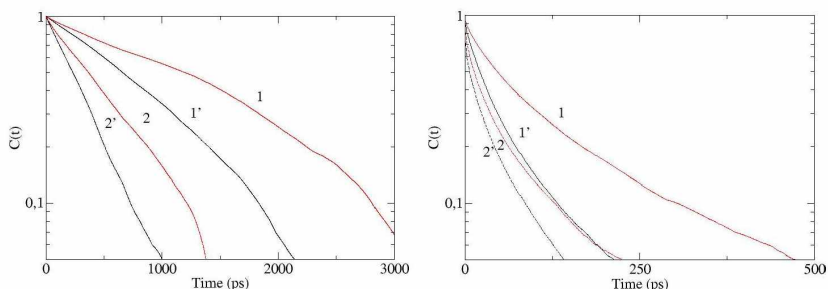


Figure 1. The autocorrelation function (ACF). The left panel: ACFs of 1st and 2nd order for end-to-end vector of ϵ -L-lysine (1,2) and α -L-lysine (1',2'). The right panel: ACFs of 1st and 2nd order for vector H-H in inner $C_{\alpha}H_2$ groups (1 and 2) and in terminal $C_{\alpha}H_2$ groups (1' and 2'). The first order $P_1(t)$ and the second order $P_2(t)$ ACFs depicted on graphs as number 1 (1') and 2 (2') correspondingly

Acknowledgements

This work was partly supported by grant 08-08 of Government of RF and RFBR grants 19-03-00715. The research is carried out using the equipment of the shared research facilities of HPC computing resources at Lomonosov Moscow State University supported by the project RFMEFI62117X0011.

References

1. D. A. Markelov, M. Dolgushev, Y. Y. Gotlib and A. Blumen. NMR relaxation of the orientation of single segments in semiflexible dendrimers // *J. Chem. Phys.*, 2014, 140, 244904.
2. Neelov I.M., Markelov D.A., Falkovich S.G., Ilyash M.Yu., Okrugin B.M., Darinskii A.A. Mathematical simulation of lysine dendrimers: temperature dependences // *Polymer Science, Series C*. 2013, 55(1), 154–161.
3. Markelov D.A., Falkovich S.G., Neelov I.M., Ilyash M.Yu., Matveev V.V., Lahderanta E., Ingman P., Darinskii A.A. Molecular dynamics simulation of spin-lattice NMR relaxation in poly-L-lysine dendrimers. Manifestation of the semiflexibility effect // *Physical Chemistry and Chemical Physics*. 2015, 17, 3214–3226.
4. Oleg V. Shavykin, Igor M. Neelov, Anatolii A. Darinskii. Is the manifestation of the local dynamics in the spin-lattice NMR relaxation in dendrimers sensitive to excluded volume interactions? // *Phys. Chem. Chem. Phys.*, 2016, 18, 24307-24317.
5. Shavykin O.V., Popova E.V., Darinskii A.A., Neelov I.M., Leermakers F. Computer simulation of local mobility in dendrimers with asymmetric branching by brownian dynamics method. *Scientific and Technical Journal of Information Technologies, Mechanics and Optics*, 2016, 16 (5), 893–902
6. Mikhailov I.V., Darinskii A.A. Does symmetry of branching affect the properties of dendrimers? *Polymer Science. Series A*, 2014, 56(4), 534–544.
7. Gotlib Yu. Ya., Darinskii A.A., Neelov I.M. The anisotropy of relaxation properties of flexible polymer molecules, *Vysokomol. soyed.*, 1976, A18(7), 1528-1533.
8. Darinsky A., Lyulin A., Neelov I. Computer simulation of molecular motion in liquid crystals by the method of Brownian dynamics // *Macromolecular Theory and Simulations*. 1993, 2(4), 523-530.

9. Darinskii A., Gotlib Y., Lukyanov M., Lyulin A., Neelov I. Computer simulation of the molecular motion in LC and oriented polymers // *Progress in Colloid & Polymer Science* 1993, 91, 13-15.
10. Darinskii, A.A., Gotlib, Yu.Ya., Lyulin, A.V., Neelov, I.M. Computer simulation of local dynamics of a polymer chain in the orienting field of the LC type // *Vysokomolekularnye Soedineniya. Seriya, A* (6), c. 1211-1220 (English translation: *Polymer Science*, 1991, 33,1116)
11. Okrugin B.M., Neelov I.M., Borisov O.V., Leermakers F.A.M. Structure of asymmetric peptide v dendrimers: insight given by self-consistent field theory // *Polymer*, 2017, 125, 292-302.
12. Shavykin O.V., Mikhailov I.V., Darinskii A.A., Neelov I.M., Leermakers F.A. Effect of an asymmetry of branching on structural characteristics of dendrimers revealed by Brownian dynamics simulations // *Polymer*, 2018, 146, 256-266.
13. Shavykin O.V., Leermakers F.A., Neelov I.M., Darinskii A.A. Self-assembly of lysine-based dendritic surfactants modeled by the self-consistent field approach // *Langmuir*, 2018, 34 (4), 1613–1626
14. Okrugin, B., Ilyash, M., Markelov, D., Neelov, I. Lysine dendrigraft nanocontainers. Influence of topology on their size and internal structure // *Pharmaceutics*, 2018, 10(3), 129.
15. Neelov I.M., Okrugin B.M, Markelov D.A. Influence of the charged peptide dendrigrafts topology on the large-scale properties and their internal structure // *Magnetic Resonance and its application*, 2018, 99-100.
16. Bezrodnyi V.V., Neelov I.M., Пloпова E.B. Effect of dendrimer generation on the kinetics of peptide complex formation // *Magnetic Resonance and its application*, 2018, 232.
17. Sheveleva N.N., Markelov D.A., Vovk M.A., Mikhailova M.E., Tarasenko I.I., Neelov I.M., Lahderanta E. Study of local orientational mobility in lysine dendrimers by NMR method // *Magnetic Resonance and its application*, 2018, 242.
18. Sheveleva N.N., Markelov D.A., Vovk M.A., Mikhailova M.E., Tarasenko I.I., Neelov I.M., Lahderanta E. NMR studies of excluded volume interactions in peptide dendrimers // *Scientific Reports* - 2018, Vol. 8, pp. 8916
19. Shavykin O.V., Mihailov I.V., Neelov I.M., Darinskii A.A. Influence of asymmetry of branching on structural properties of dendrimer. Brownian dynamics simulation// *Magnetic Resonance and its application*, 2018, 239-241
20. Shavykin O.V., Darinskii A.A., Neelov I.M., Leermakers F.A.M. The sensitivity of local dynamics and its manifestations in NMR to excluded volume in dendrimers // *Magnetic Resonance and its application*, 2017, 89.

Molecular dynamics simulation of global and local dynamics in dendrigraft of second generation

Oleg V. Shavykin, Maxim Yu. Ilyash¹, Emil I. Fatullaev¹, Igor M. Neelov¹, Denis A. Markelov²

¹*St. Petersburg National Research University of Information Technologies, Mechanics and Optics (ITMO University), Kronverkskiy pr. 49, St.Petersburg, 197101, Russia*

²*St.Petersburg State University (SPbSU), 7/9 Universitetskaya nab., St.Petersburg, 199034, Russia*

E-mail: kupala-89@mail.ru

Introduction

The dendrigrafts are interesting object for many biomedical applications including drug and gene delivery. The topological structure of these molecules is similar to structure of short dendritic brushes. Long dendritic brushes have cylindrical shape and large relaxation times. However the dendrigrafts and in particular lysine dendrigrafts have a shape close to spherical and size close to size of lysine dendrimers [1-6] consisting of the same number of aminoacid residues. Due to this reason it can be assumed that rotation of these molecules as a whole could contribute significantly to local orientational mobility, as it occurs in the case of dendrimers. In this work the molecular dynamics simulation of orientational mobility of dendrigraft of 2nd generation was performed in water solvent with explicit account of counterions at temperature T=300 K and pressure P=1 atm using the program package Gromacs-4.5.6 with AMBER99SB-ildn force field.

The comparison of orientational mobility of inner and terminal groups

We estimated mobility of the chosen vector \mathbf{d} between two hydrogens in the last hydrocarbon CH₂ of ϵ -amino group using the first order autocorrelation function (ACF) $P_1(t)$

$$P_1(t) = \frac{\langle \mathbf{d}(t), \mathbf{d}(0) \rangle}{|\mathbf{d}(t)| |\mathbf{d}(0)|}$$

and the second order autocorrelation function (ACF) $P_2(t)$

$$P_2(t) = \frac{3}{2} \frac{\langle (\mathbf{d}(t), \mathbf{d}(0))^2 \rangle}{|\mathbf{d}(t)|^2 |\mathbf{d}(0)|^2} - \frac{1}{2}$$

The global orientational mobility (Figure 1, left panel) was characterized by autocorrelation functions (ACFs) of 1st and 2nd order for end-to-end vector (see Figure 1, left panel). The local mobility was characterized by ACFs of 1st and 2nd order for H-H vectors in inner and in terminal C₂H₂ groups, correspondingly (Figure 1, right panel).

It was shown that global orientational time is essentially greater (more than one order of magnitude) than local orientational times. And local orientational times for inner H-H vectors is in turn is essentially greater (more than one order of magnitude) than orientational times for terminal H-H vectors.

The results of this work are in accordance with theoretical prediction of anisotropy of local orientational mobility in linear polymers (i.e. about different mobility of vectors oriented along and perpendicular to main chain of polymer) obtained by Gotlib et al [7-10] and results for lysine dendrimers obtained by Markelov et al. [3] and our previous results on local mobility in lysine dendrimers [11-18].

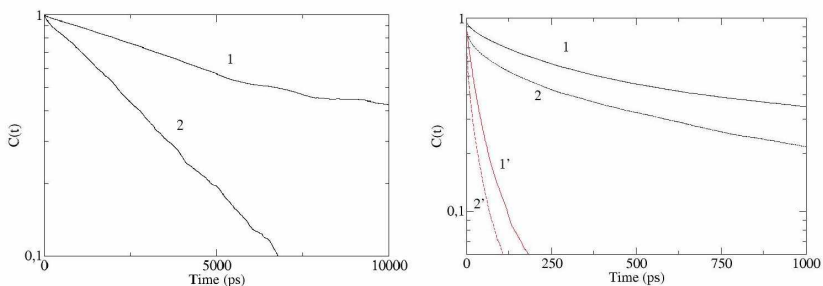


Figure 1. The autocorrelation function (ACF).

The left panel: ACFs of 1st (1) and 2nd order for end-to-end vector.

The right panel: ACFs of 1st and 2nd order for vector H-H in inner C₂H₂ groups (1 and 2) and in terminal C₂H₂ groups (1' and 2'). The first order P₁(t) and the second order P₂(t) ACFs depicted on graphs as number 1 (1') and 2 (2'), correspondingly

Acknowledgements

This work was partly supported by grant 08-08 of Government of RF and RFBR grants 19-03-00715. The research is carried out using the equipment of the shared research facilities of HPC computing resources at Lomonosov Moscow State University supported by the project RFMEFI62117X0011.

References

1. D. A. Markelov, M. Dolgushev, Y. Y. Gotlib and A. Blumen. NMR relaxation of the orientation of single segments in semiflexible dendrimers // *J. Chem. Phys.*, 2014, 140, 244904.
2. Neelov I.M., Markelov D.A., Falkovich S.G., Ilyash M.Yu., Okrugin B.M., Darinskii A.A. Mathematical simulation of lysine dendrimers: temperature dependences // *Polymer Science, Series C*. 2013, 55(1), 154–161.
3. Markelov D.A., Falkovich S.G., Neelov I.M., Ilyash M.Yu., Matveev V.V., Lahderanta E., Ingman P., Darinskii A.A. Molecular dynamics simulation of spin-lattice NMR relaxation in poly-L-lysine dendrimers. Manifestation of the semiflexibility effect // *Physical Chemistry and Chemical Physics*. 2015, 17, 3214–3226.
4. Oleg V. Shavykin, Igor M. Neelov, Anatolii A. Darinskii. Is the manifestation of the local dynamics in the spin–lattice NMR relaxation in dendrimers sensitive to excluded volume interactions? // *Phys. Chem. Chem. Phys.*, 2016, 18, 24307–24317.
5. Shavykin O.V., Popova E.V., Darinskii A.A., Neelov I.M., Leermakers F. Computer simulation of local mobility in dendrimers with asymmetric branching by brownian dynamics method // *Scientific and Technical Journal of Information Technologies, Mechanics and Optics*, 2016, 16(5), 893–902
6. Mikhailov I.V., Darinskii A.A. Does symmetry of branching affect the properties of dendrimers? // *Polymer Science. Series A*, 2014, 56, (4), 534–544.
7. Gotlib Yu. Ya., Darinskii A.A., Neelov I.M. The anisotropy of relaxation properties of flexible polymer molecules // *Vysokomol. soyed.*, 1976, A18(7), 1528–1533.
8. Darinsky A., Lyulin A., Neelov I. Computer simulation of molecular motion in liquid crystals by the method of Brownian dynamics // *Macromolecular Theory and Simulations*. 1993, 2(4), 523–530.

9. Darinskii A., Gotlib Y., Lukyanov M., Lyulin A., Neelov I. Computer simulation of the molecular motion in LC and oriented polymers // *Progress in Colloid & Polymer Science* 1993. C. 13-15.
10. Darinskii, A.A., Gotlib, Yu. Ya., Lyulin, A.V., Neelov, I.M. Computer simulation of local dynamics of a polymer chain in the orienting field of the LC type // *Vysokomolekularnye Soedineniya. Seriya, A* (6), c. 1211-1220 (English translation: *Polymer Science*, 1991, 33,1116)
11. Okrugin B.M., Neelov I.M., Borisov O.V., Leermakers F.A.M. Structure of asymmetric peptide dendrimers: insight given by self-consistent field theory // *Polymer*, 2017, 125, 292-302.
12. Shavykin O.V., Mikhailov I.V., Darinskii A.A., Neelov I.M., Leermakers F.A. Effect of an asymmetry of branching on structural characteristics of dendrimers revealed by Brownian dynamics simulations // *Polymer*, 2018, 146, 256-266.
13. Shavykin O.V., Leermakers F.A., Neelov I.M., Darinskii A.A. Self-assembly of lysine-based dendritic surfactants modeled by the self-consistent field approach // *Langmuir*, 2018, 34 (4), 1613-1626
14. Okrugin, B., Ilyash, M., Markelov, D., Neelov, I. Lysine dendrigraft nanocontainers. Influence of topology on their size and internal structure // *Pharmaceutics*, 2018, 10(3), 129.
15. Neelov I.M., Okrugin B.M, Markelov D.A. Influence of the charged peptide dendrigrafts topology on the large-scale properties and thir internal structure // *Magnetic Resonance and its application*, 2018, 99-100.
16. Bezrodnyi V.V., Neelov I.M., Понова E.B. Effect of dendrimer generation on the kinetics of peptide complex formation // *Magnetic Resonance and its application*, 2018, 232.
17. Sheveleva N.N., Markelov D.A., Vovk M.A., Mikhailova M.E., Tarasenko I.I., Neelov I.M., Lahderanta E. Study of local orientational mobility in lysine dendrimers by NMR method // *Magnetic Resonance and its application*, 2018, 242.
18. Sheveleva N.N., Markelov D.A., Vovk M.A., Mikhailova M.E., Tarasenko I.I., Neelov I.M., Lahderanta E. NMR studies of excluded volume interactions in peptide dendrimers // *Scientific Reports - 2018*, Vol. 8, pp. 8916
19. Shavykin O.V., Mihailov I.V., Neelov I.M., Darinskii A.A. Influence of asymmetry of branching on structural properties of dendrimer. Brownian dynamics simulation// *Magnetic Resonance and its application*, 2018, 239-241
20. Shavykin O.V., Darinskii A.A., Neelov I.M., Leermakers F.A.M. The sensivity of local dynamics and its manifestations in NMR to excluded volume in dendrimers // *Magnetic Resonance and its application*, 2017, 89.

Multinuclear NMR for structural study of lamellar mordenite and ZSM-5 zeolites

M. G. Shelyapina¹, E. A. Krylova¹, Yu. Zhelezniak¹, V. Petranovskii²,
R. Yocupicio-Gaxiola², J. Antunez-Garcia², S. Fuentes²

¹Saint Petersburg State University, 7/9 Universitetskaya nab., St. Petersburg, Russia 199034

²CNyn, Universidad Nacional Autónoma de México, Ensenada 22860, Baja California, México

E-mail: krylovaea2803@mail.ru

Organic-inorganic layered hybrid nanomaterials have drawn great attention due to their widespread use in various areas. Layered zeolite precursor is an attractive intermediate to design hierarchical mesoporous/nanoporous catalysts. To control the growth of 2D zeolite nanosheets in hydrothermal synthesis, some complex surfactants are employed. For the successful development of these composite organic-inorganic nanomaterials, knowledge on the structure and dynamics of both structural parts is essential. Nowadays Nuclear Magnetic Resonance (NMR) spectroscopy and relaxation have become very powerful techniques for characterizing hybrid organic/inorganic nanomaterials since they can provide information on structural and dynamic issues associated with both organic intercalated molecules and the inorganic part as well.

Here we report the results of our multinuclear ¹H, ¹³C, ¹⁵N, ²³Na, ²⁷Al, ²⁹Si NMR at 9.4 T studies of two class of materials: mesostructured zeolite materials, with the MOR and ZSM-5 structures, grown as lamellar phases using cetyltrimethylammonium bromide and polyethylene glycol (CTAB-PEG) as a mesopore creating agent in a one-pot synthesis. ¹³C and ¹⁵N MAS spectra were obtained in cross polarization regime.

Theoretical calculations of XRD patterns were performed, and compared with the experimentally obtained data to confirm the lamellar array of the both zeolite structures and determine their crystallographic orientation. This allows the cell parameters and the spatial arrangement of the above-mentioned systems to be estimated. The lamellar structure of the obtained materials is confirmed by TEM data.

The NMR studies prove the regularity of the zeolite framework. To support the theoretical results concerning the binding and staking mode of the organic molecules two-dimensional ¹H-²⁹Si and ¹H-¹³C HETCOR NMR experiments were performed.

Acknowledgements

The synthesis and structural characterization of the materials were done at the Nanoscience and Nanotechnology Centre of UNAM. The thermal analysis and NMR studies were carried out at the Research Park of SPSU: Centre of Thermal Analysis and Calorimetry and Centre for Magnetic Resonance. The work was partly supported by SENER-CONACYT (project 117373), RFBR and CITMA in accordance with research Project No. 18-53-34004.

Precise definition of γ ^{133}Cs with resolved structure in magnetic fields higher than 0.8 mT

V. Ya. Shifrin¹, D. I. Belyakov¹, D. D. Kosenkov^{1,2}, and A. E. Shilov¹

¹NIL-2205, VNIIM of the D. I. Mendeleev, Saint-Petersburg

²Faculty of Control Systems and Robototechnics, ITMO University, Saint-Petersburg

E-mail: V.Ya.Shifrin@vniim.ru

For implementation of a problem of transfer of the T unit size from GET12-2011 to the area of “medium” fields, in the range of 1 – 25 mT, in VNIIM the prototype of quantum AMR MZ type magnetometer [1]) working at the resolved structure of atoms of caesium was developed and made (KTsM). KTsM based on a method of a double radio optical atomic magnetic resonance which is Basic Element of the comparator of unit of MI of “medium” fields. The method is widely applied with the geomagnetic measurement range of MI (20 000 – 100 000 nT), however in the considered area of stronger magnetic fields, in practice of magnetic measurements are implemented for the first time.

Advantage of the developed caesium magnetometer before traditional nuclear magnetic resonances and AMR magnetometers in this application, is the possibility to significantly reduce sensor volume (the sphere of \varnothing of 10 mm), while saving rather high signal-to-noise ratio in AMR frequency range, optimum for creation of an electronic part of the equipment (3.5 – 90 MHz).

By experimental assessment the accidental component of an error of measurements of frequency of AMR the caesium magnetometer TsMK does not exceed $1 \cdot 10^{-7}$ in all the frequency range of a magnetic resonance from 3.5 – 90 MHz.

For measurements of MI on the basis of AMR in Cs_{133} , application of quantum transitions between magnetic subtotals of $m_F=4 \rightarrow m_F=3$ and $m_F=-3 \rightarrow m_F=-4$ is provided, at angular momentum $F=4$, providing the maximum signal AMR amplitude in a series of resonances.

Theoretical researches of the magnetometer showed that the dependence of the measured induction of B on the measured frequency of f represents a polynom of the fifth order:

$$B = K_1 \cdot f + K_2 \cdot f^2 + K_3 \cdot f^3 + K_4 \cdot f^4 + K_5 \cdot f^5$$

For assessment of coefficients of a polynom (K_1, K_2, K_3, K_4, K_5) two series of checkings were carried out: checking with EGM from structure of GET12-2011 in the range 0.8 – 2 mT and checking with specially developed nuclear magnetic resonance teslameter for range 8 – 25 mT.

When checking in the range 0.8 – 2 mT in a work space of ETMK full automatic compensation of an external magnetic field, including magnetic noises of an alternating magnetic field of the industrial frequency of 50 Hz is carried out. After that in the center of a measure of ETMK two reference quartz C4-2 and ESTV solenoids are being installed, their magnetic axes are guided vertically and the centers of work spaces are combined. As researches showed, uniformity of MI created by MI package of measures it is sufficient for ensuring required accuracy of checkings of two magnetometers with significantly different sizes of detectors – a cylindrical form diameter and 40 mm long (Ne4) and sphere with a diameter of 10 mm (Cs_{133}). Generation of current in solenoids is made by means of the current regulator ST-2 from structure of GET12-2011 of LCard34-4 DAC which is in addition stabilized in the system of feedback coupling on the basis of the Agilent 3458A voltmeter and managed. Additional stabilization of ST-1 allows to support current with relative instability at the level of $1 \cdot 10^{-7}$.

Checking of magnetometers in the range 8 – 25 mT is made in the comparator which is specially developed quantum atomic and resonant. Basic elements of the created comparator are: caesium AMR magnetometer TsMK, 4th section measure comparator of MKMI with the generator of a stable direct current, devices of measurements of current, correction of uniformity of MI and compensation of man-made interference.

The scheme of the comparator placed in figure 1 is structural, includes also nuclear and resonant teslameter for checkings with TsMK in MKMI measure comparator, the personal computer with the special software for process control of measurements of frequencies of a magnetic resonance, temperature and stabilization of current of a measure of MKMI and also a set of measuring instruments of current intensity on the basis of a precision multimeter of Agilent 3458A and a measure of electrical resistance with the face value of 1 Ohms.

As experimental data showed, the dependence of indications of the magnetometer on change of position of the center of a detector of the caesium sensor on the center of a measure does not exceed $1 \cdot 10^{-7} / 2$ mm.

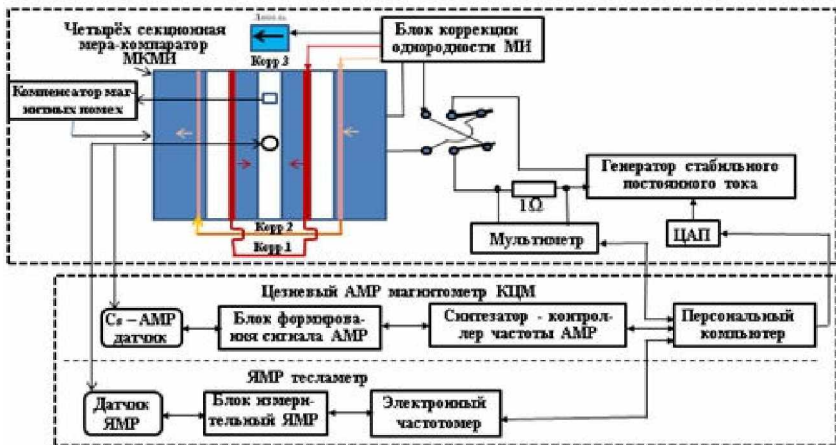


Figure 1. The block diagram of the quantum comparator of unit of magnetic induction of constant field 1 – 25 mT

The special settlement program was developed for assessment of coefficients of polynomial regression. Calculation in the program consists of two stages.

At the first stage, processing data of checking with EGM, the program by means of a method of the smallest squares estimates coefficients of K1 and K2 at the senior orders of regression. Coefficients are fixed in memory of the program and later are used at the second stage of calculation as set.

The logic of the program of the second stage differs from logic of the first program.

Unlike checkings with EGM where unit of magnetic induction of the constant field is actually transferred from GET12-2011, when checking in “average” fields KTSM it is compared with YaMR-teslametrom, having checked in practice and linearity of coefficient of transformation, sufficient for the carried-out experiment, in the considered range.

Assessment of coefficients of the highest orders was constructed as follows. The size MI measured YaMR-teslametrom is considered with experimentally certain multiplier, for the rest assessment of coefficients is made similar to the first program.

The user has an ability to set an interval of values of a multiplier and a step of iteration of search. The program in the automatic mode calculates coefficients and SKO of a row for all coefficients from the specified interval and finds the values corresponding to the minimum SKO. The regression coefficients corresponding to the minimum SKO are recognized as real coefficients of regression.

As a result of implementation of the similar procedure, by transfer of the size of unit of MI to the range of “average” fields, total SKO of measurements it was reduced to size of $2 \cdot 10^{-6}$.

References

1. DI Belyakov, VN Khorev, AE Shilov, V.Ya. Shifrin, *Measuring Technology*, 2017, No. 12, pp. 28-31.

Experimental results of an impact of the spin echo pulse sequence on a J-coupled two-spin system

S. A. Shubin, V. V. Frolov, K. V. Tyutyukin

St. Petersburg State University, 1, Ulyanovskaya str., St. Petersburg, 198504, Russian Federation

E-mail: shubinsal@gmail.com

Introduction

This work presents the experimental results of the display of phosphorus-containing components by the methods of double magnetic resonance, performed in a weak magnetic field (7 mT). The working substance is the compound Trimethyl phosphate – (CH₃O)₃PO. Obtaining MR images of the distribution of phosphorus in a sample is based on the spin echo double resonance (DRSE) technique. When the 90-τ-180-τ-echo pulse sequence acting on protons, while at the time of the action of 180° pulse at the hydrogen frequency, 180° pulse are sent at the phosphorus frequency. RF pulse sequence applied to the ¹H – ³¹P two-spin system is shown in Fig. 1.

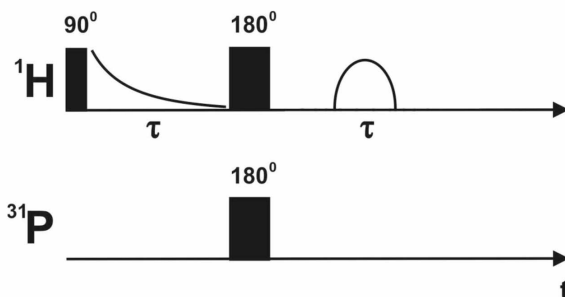


Figure 1. RF pulse sequence applied to the ¹H – ³¹P two-spin system

The applying of this method allows to obtaining an MR image of the distribution of phosphorus with a sensitivity of 16 times greater than the direct method. This is due to the fact that the image is obtained indirectly, due to the subtraction from the MR image obtained from all protons in the sample MR image of protons that are not connected by indirect spin-spin interaction with phosphorus nuclei. As a result, we obtain an MR image of ¹H nuclei associated with ³¹P nuclei, which is identical to the distribution of ³¹P nuclei.

To implement the experiment, a transmit-receive channel for phosphorus was developed, consisting of:

- A two-channel high-frequency generator (channel ¹H – hydrogen and ³¹P – phosphorus) at 300 and 125 kHz, respectively.
- Power amplifier at the NMR frequency of phosphorus.
- Dual frequency sensor.
- Electronic control software.

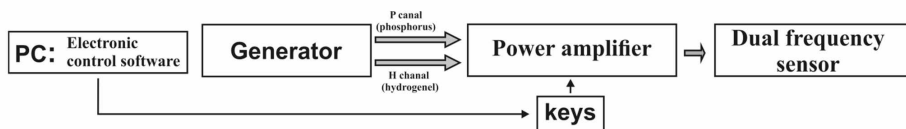


Figure 2. Block diagram transmit-receive channel for phosphorus

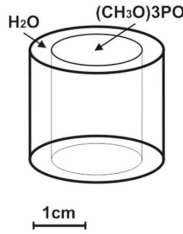


Figure 3. Sample water-Trimethyl phosphate

Using the theory of the average Hamiltonian, one can obtain the formula for the intensity of the observed signal from phosphorus:

$$S(t) = Tr\{(I_x(\cos(2\pi J\tau) + 2I_y S_z \sin(2\pi J\tau)) + S_z)(I_x + iI_y)\}.$$

Since in the experiment only the first term is directly detected, for minimization of the observed signal from the coupled $^1\text{H} - ^{31}\text{P}$ pairs, the following condition must be fulfilled: $2\pi J\tau = \frac{\pi}{2}$, which leads to $\tau = \frac{1}{4J}$.

Experimental results

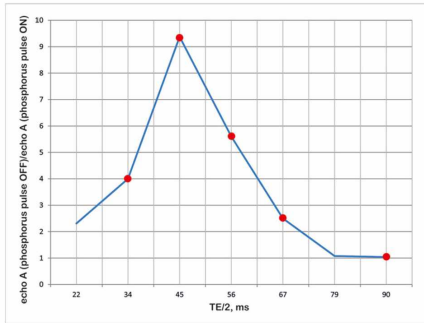


Figure 4. The ratio of the amplitudes of the echo when off and on the pulse to phosphorus from τ ($\tau = TE/2$)

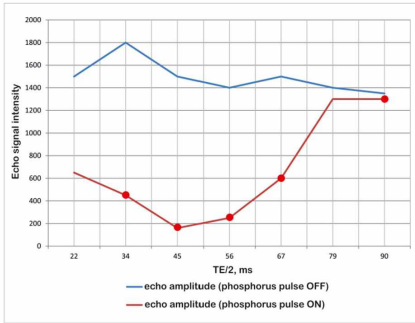


Figure 5. The dependence of the echo amplitude from τ ($\tau = TE/2$)

In Fig. 4 and Fig. 5, red dots indicate the signal intensity and τ values at which MR images were taken (see Fig. 6).

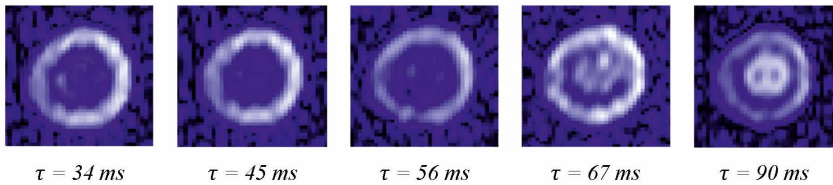


Figure 6. MR images with suppressed phosphorus signal at different values of the τ

Summary

The graphs presented in Fig. 4, Fig. 5 and MR images with signal suppression from ^{31}P in Fig. 6 shows that the theoretical calculation is fully consistent with the obtained experimental data. The maximum effect, suppression of the signal from ^{31}P , is observed at $\tau = \frac{1}{4J}$.

References

1. A. G. Webb, S.C.R. Williams, and L. D. Hall. Generation of Coupled Spin-Only Images Using Multiple-Echo Acquisition. *Journal of Magnetic Resonance* 84 p.159-165 (1989).
2. Ernst R. R., Bodenhausen G., Wokaun A., *Principles of Nuclear Magnetic Resonance in One and Two Dimensions*. Clarendon Press, Oxford 1987. 610 Seiten: 1988.
3. Laurance D. Hall, Timothy J. Norwood, and Steve C.R. Williams. Coupled-Spin-Filtered Imaging in an Inhomogeneous Magnetic Field. *Journal of Magnetic Resonance* 79 p.363-368 (1988).
4. Malcolm H. Levitt, *Spin Dynamics Basic of Nuclear Magnetic Resonance* 2nd ed.

Multiparameter MRI protocol for evaluating the results of surgical treatment of brain gliomas

P. I. Simeshchenko, V. M. Cheremisin, I. G. Kamyshanskaya, M. Yu. Podgornyyak, V. V. Prits

St. Petersburg State University, Faculty of Medicine

Radiation Diagnostics and Radiotherapy Course, Department of Oncology

199106, St. Petersburg, 21 line V.O., d. 8.

SPb GBUZ "City Mariinsky Hospital"

194104, St. Petersburg, Liteiny pr., 56

E-mail: simeshchenko@gmail.com

Relevance

Gliomas account for up to 70% of all primary brain tumors. Each year, the incidence of malignant gliomas is 3-5 cases per 100,000 population with a slight predominance of males. Treatment tactics and prognosis depend on the degree of glioma malignancy. So the median survival in astrocytoma is about 5 years, with anaplastic astrocytoma - 2.5 years and with glioblastoma - 1 year. Five-year survival for glioblastoma does not exceed 5% [1, 2].

The standard of treatment for high-grade gliomas of the brain is safe and most radical surgical resection followed by adjuvant radiation or chemoradiotherapy [3].

The postoperative assessment of the volume of the residual tumor, the severity of cerebral edema and early postoperative changes is important for determining the further tactics of treating patients with gliomas [4].

The use of standardized MRI protocols in the early postoperative period does not always give a complete picture of the extent of the surgery performed. Differential diagnosis of residual tumors on the background of the presence of hemostatic materials, impaired blood-brain barrier, and hemorrhagic impregnation of the tumor bed is an extremely difficult task.

Purpose of the study

Assess the capabilities of modern magnetic resonance imaging techniques, such as spectroscopy, tractography and perfusion, in assessing the radical nature of surgical treatment in the early (up to 2 days) and remote (1 month) periods after surgery.

Material and methods

The study was conducted on a Philips Ingenia high-field tomograph with 3T magnetic field induction at St. Petersburg State University in St. Petersburg City Hospital Mariinsky Hospital. MR-spectroscopy, MR-perfusion, MR-tractography with subsequent postprocessing were carried out for multiparametric evaluation of pre- and postoperative changes in a patient with glioblastoma.

Results

The use of MRI spectroscopy patient S. with a neoplasm of the left hemisphere of the brain during the preoperative period allowed differential diagnosis of the identified tumor between the various volume lesions of the central nervous system, which determined the indications and radicalism of the subsequent surgical procedure (Fig. 1).

The use of MR perfusion in the preoperative period allowed us to estimate the degree of blood supply to the formation, to reliably determine the volume of the residual tumor in the early postoperative period, and to determine the continued growth of glioblastoma in the background of pronounced postoperative changes in the remote period based on the dynamics of perfusion parameters (Fig. 2).

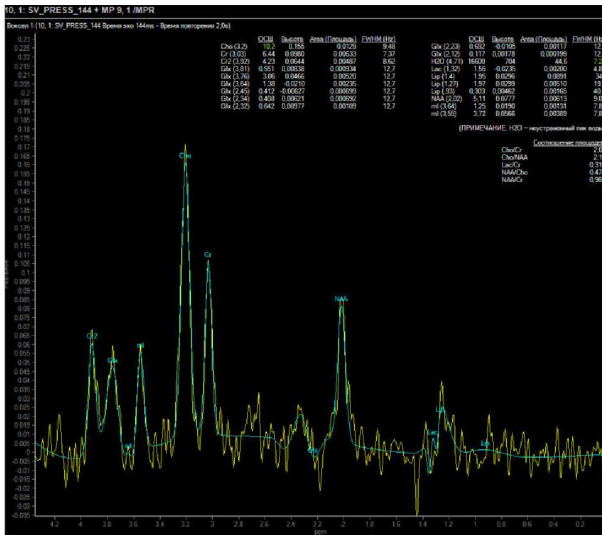


Figure 1. Mr spectroscopy Patient S., glioblastoma. High peaks of choline (Cho), a decrease in the peak of N-acetylaspartate (NAA), an increase in the content of lipids (Lip) and lactate (Lac) are characteristic of tumors of the glial series. The ratios of metabolites indicate a high degree of malignancy of the tumor

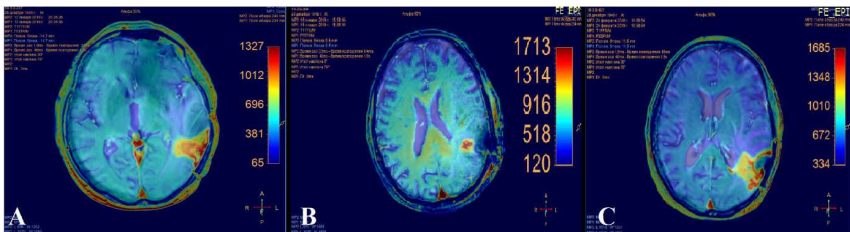


Figure 2. MR perfusion with overlay of perfusion cards on native images. Patient S., glioblastoma. MR perfusion demonstrates tumor volume before surgery (A). On the 2nd day after surgical treatment, the residual tumor tissue is revealed (B). At 1 month after surgery, the continued growth of glioblastoma (C) is determined

With the standard protocol of the MR study, it is not possible to differentiate the continued tumor growth with other postoperative changes (Fig. 3).

The use of MR-tractography with subsequent 3D reconstruction allowed us to visualize the conductive paths of white matter, to evaluate their topography and integrity in the field of localization of the volumetric process. These data allowed us to speak indirectly about the histology of the tumor and the degree of its malignancy, as well as to plan the surgical treatment and its volume without the risk of impairment of vital cerebral functions. In the post-operation period, the visualization of the tracts made it possible to assess their condition after the resection of the tumor (Fig. 4).

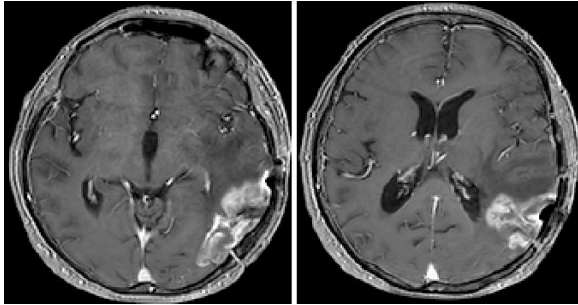


Figure 3. T1-VI with contrast enhancement. Patient S., glioblastoma, 1 month after surgical treatment

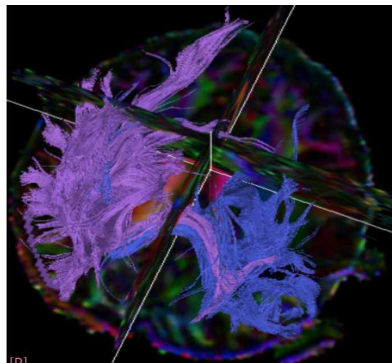


Figure 4. MR tractography. Patient S., glioblastoma. Depletion and destruction of paths in the area of localization of a malignant neoplasm are determined

Findings

The use of the multiparametric protocol MRI in patients with brain gliomas in the postoperative period is promising for solving complex differential diagnostic problems in evaluating the radical nature of the surgical treatment.

References

1. Porsaev A.I. Comprehensive assessment of the degree of radicalization of the removal of glial supratentorial brain tumors in the early postoperative period: dissertation ... Candidate of Medical Sciences. Russian Research Neurosurgical Institute named after Professor A.Polenov, St. Petersburg, 2014.- 164 p.
2. Shashkov K.V. Postoperative assessment of the radicalism of surgical removal of astrocytic gliomas of the brain (CT and MRI diagnostics): dissertation ... Candidate of Medical Sciences. Research Institute of Neurosurgery named after Acad. H.H. Burdenko RAMS, Moscow, 2010.
3. E.K. Dusembekov, D.I. Dubchev Modern methods of diagnosis and treatment of gliomas of the brain // KazNMU Bulletin. 2015. №1.
4. Kobayakov G. L., Smolin A. V., Bekyashev A. Kh., Absalyamova O. V., Kobayakova E. A., Poddubsky A. A., Inozemtseva M. V. Treatment of glioblastoma recurrence: is there any success? // Tumors of the head and neck. 2014. №3.

Influence of morphology on the magnetic behavior in nano-EuFeO₃: NMR study

A. Sklyarova¹, V. I. Popkov², I. V. Pleshakov², V. V. Matveev³, and H. Štěpánková¹

¹Department of Low Temperature Physics, Faculty of Mathematics and Physics, Charles University, Prague, Czech Republic

²Ioffe Institute, 26 Polytekhnicheskaya Str., St. Petersburg, Russian Federation

³St. Petersburg State University, 7/9 Universitetskaya nab., St. Petersburg, Russian Federation

E-mail: asklyaro@gmail.com

In this topic the magnetic properties study of EuFeO₃ materials using NMR will be presented. Being perspective for spintronics application, nano-MFeO₃ (M = Bi, Y, Tb, Eu...) materials show the relation between their functional properties and used synthesis route, which is responsible for the morphology of produced material. Here we will show the local properties study and the comparison of micro- and nano-EuFeO₃ carried out with a purpose to clarify the emerging patterns between the obtained particle size, surface condition and crystal structure of these nanomaterials and their magnetic properties.

NMR characterization of structure of cyclosporin B

A. V. Slivka, S. V. Efimov, O. V. Aganova, V. V. Klochkov

Institute of Physics, Kazan Federal University, Kazan, 420008 Russia

E-mail: aslivka95@mail.ru

Introduction

Cyclosporins belong to a series of peptides produced by fungi, parasites of insects; among these peptides immunosuppressive compounds were found which are used in treatment of autoimmune diseases and after organ transplantations [1]. Cyclosporins are produced by various fungi genera, including *Trichoderma*, *Tolypocladium*, *Fusarium*, etc. Typically these peptides possess antifungal activity [2, 3]. Cyclosporin A is widely used in medicine as immunosuppressive agent and has been widely studied [4].

Object

Little is known about cyclosporine variants other than CsA. Cyclosporin B (CsB) was chosen as the object of investigation. It differs from CsA by a single amino acid replacement: Abu2→Ala2, which somehow leads to inactivation of immunosuppressive activity. The aim of our work is to reveal changes which can be responsible for this fact with the aid of NMR spectroscopy. Chemical formula of CsB is presented in Figure 1.

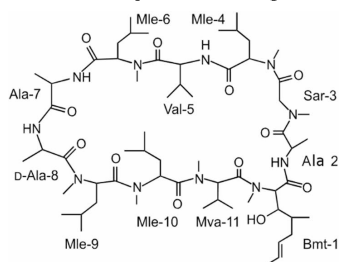


Figure 1. Structural formula of CsB

Method

The studied peptide was dissolved in deuterated chloroform (0.7 mg, concentration $c = 0.98$ mM). NMR spectra were acquired on a Bruker Avance III HD spectrometer (operating at 700.13 MHz in the ^1H channel) at 298 K. Spectra were processed and analyzed using NMRPipe and Sparky software [5, 6]. Two-dimensional homonuclear experiments (DQF-COSY, TOCSY) were used to assign the NMR signals (COSY allows finding the nearest neighbor of a given proton in the chemical structure). ROESY experiments are useful for determining the sequence of amino acid residues, and also allow observing slow chemical exchange. Ambiguous assignments were clarified with the aid of heteronuclear experiments HSQC and HMBC.

Results

Total ^1H signal assignment of cyclosporin B was made by interpreting cross-peaks in the mentioned 2D spectra (see example in Fig. 2). Integral intensities of the signals in ROESY spectra, obtained with different mixing times, were measured. A list of nuclei with their chemical shifts and corresponding ROESY signal intensities was prepared, which were transformed then into the internuclear distances (Table 1).

Obtained data are necessary for further investigation of the spatial structure of the peptide (internuclear distance will be input data for molecular modelling).

Acknowledgements

This work is supported by the Russian Science Foundation (grant no. 18-73-10088).

References

1. R. Laeijendecker, T. Van Joost, B. Tank et al. – *Journal of Pediatric Dermatology*, **22**, 299-304 (2005).
2. A. Survase, D. Kagliwal, S. Annapure, S. Singhal. – *Biotechnology Advances*, **29**, 418-435 (2011).
3. Z. De-xiu, M. Beran, J. Kozová, Z. Řeháček. – *Folia Microbiologica*, **36 (6)**, 549-556 (1991).
4. V. Mikol, C. Papageorgiou, X. Borer. – *Journal of Medicinal Chemistry*, **38**, 3361-3367, 1995.
5. T. D. Goddard, D.G. Kneller. Sparky. – <http://www.cgl.ucsf.edu/home/sparky/>
6. NMRPipe. – <https://www.ibbr.umd.edu/nmrpipe/>
7. S. Macura, B. T. Farmer, L. R. Brown. – *Journal of Magnetic Resonance*, **70**, 493-499 (1986).

Measurements of molecular velocity auto-correlation of water in mixtures with glycerol by NMR MGSE method

Janez Stepišnik^{1,2}, Carlos Mattea³, Siegfried Stapf³ and Aleš Mohorič^{1,2}

¹University of Ljubljana, Faculty of mathematics and physics, Jadranska 19, 1000 Ljubljana, Slovenia, EU

²Institute Jozef Stefan, Jamova 39, 1000 Ljubljana, Slovenia, EU

³Ilmenau University of Technology, Ehrenbergstrasse 29, Ilmenau, Germany, EU

E-mail: janez.stepisnik@fmf.uni-lj.si

<http://www.fmf.uni-lj.si/~stepisnik/index.html>

Abstract

The NMR of modulated gradient spin echo is only method allowing direct measurements of the low frequency part of velocity auto correlation (VAS) of molecules in liquids and the monitoring of its evolution during the diffusion through non-homogeneities in a medium. Method was used to study the molecular dynamics of water in mixtures with the glycerol in the frequency range between few 50 Hz to 10 kHz. Taking into account the Stokes-Einstein relation, we believe that obtained spectra of mixtures of above 10 vol% fraction of glycerol show their viscosity thickening property. It might explain the mechanisms that lies behind their role in the process of spontaneous folding of disordered poly-peptides into biologically active protein molecules.

Introduction

Although the earliest models of liquids as totally disordered structures have been replaced by the models of a long range-disordered and short range-ordered system in which the associations of molecular clusters can be created due to intermolecular interaction, there is still lack of understanding about the molecular dynamics in liquids, which play an important role in biological systems. It concerns particularly the liquids with the hydrogen bonding as water, alcohols, glycerol and their mixtures, in which unknown molecular mechanisms spontaneously folds a disordered poly-peptides into a unique structure of biologically active protein molecules and prevents organelle disruption by freezing. Velocity autocorrelation function (VAF) has a deep meaning in the statistical physics of fluid by containing information about the underlying processes of molecular interaction, which is related to many physical properties of the system such as thermal and mass diffusion, sound propagation, e.t.c., having either a single-particle or a collective nature. VAF is quite generally considered as quantity that cannot be measured directly. Some information can be obtained by scattering experiments, like with neutron and light scattering, but a short time scale of these methods limits the extraction of its asymptotic long time behavior in liquids and their mixtures. It leads to the conclusion that the computer simulation of molecular dynamics seems to be the most suitable tool for the study of the translational dynamics in molecular systems. The current understanding of liquid is mostly derived from the experimental results in combination with the results of computer simulations, but they are entirely dependent upon on the models of resulting interatomic and intermolecular force fields and the conclusions derived from these models concerning molecular structure and dynamics remain inconclusive.

Measurement of velocity autocorrelation by NMR MGSE method

The NMR of modulated gradient spin echo is (MGSE) only method allowing direct measurements of the low frequency part of velocity auto correlation (VAS) of molecules. MGSE is basically a Carr-Purcell-Meiboom-Gill sequence (CPMG) consisting of initial $\pi/2$ -RF-pulse and the train of N π -RF pulses separated by time intervals T , applied in the background of fixed the magnetic field gradient, G , (MFG). Although the CPMG sequence was initially

introduced to reduce the effect of diffusion on measurement of spin relaxation by shortening the pulse spacing, but the presence of MFG imprints also information on the spectrum of velocity autocorrelation (VAS) [1, 2]. The application of this method for the measurements in liquids, requires that consideration be given to other spin interactions besides that with MFG. Although, the rapid molecular motion on the time scale of pico- or nanoseconds nullifies the spin dipole-dipole and first order quadrupole interactions completely, spin interactions with electrons in the molecular orbitals remain in liquids, resulting in the chemical shifts of NMR spectrum, and the electron mediated spin-spin interactions, considered as a J -couplings. We have shown [5] that with a fixed and strong enough MFG, these interactions can be neglected and the attenuation of the spin echo decay can be described by

$$E(\tau, \omega) = \sum_i E_{0i} e^{-\frac{\tau}{T_{2i}} - \frac{8\gamma^2 G^2}{\pi^2 \omega^2} D_{zz}(\tau, \omega) \tau}$$

where the $D_{zz}(\tau, \omega)$ is the value of the tensor in the direction of applied MFG at the modulation frequency $\omega = \pi T$ and where T_{2i} describes the spin relaxation of i -th sub-ensemble. The method gives the VAS in a frequency range that is limited above with the RF transmitter power and the size of the MFG and down with spin relaxation. The advantage of the new MGSE technique was demonstrated by measurements of the VAS of restricted diffusion, the VAS of the granular dynamics in fluidized granular systems and by the discovery of a new low frequency mode in the VAS of melted polymers [3]. The method may also use the internal MFG in porous systems, generated by the susceptibility differences on interfaces, to obtain information on the pore morphology and the distribution of internal MFG [4].

Results and discussion

Figures 1 show the changes of ADC spectra after the addition of glycerol to water.

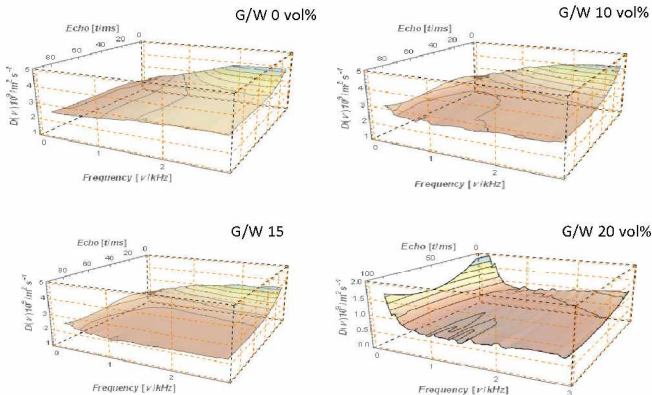


Figure 1. 3D frequency/temporal plot of velocity auto-correlation spectra of the glycerol/water mixtures

The characteristic bulge in the 3D temporal frequency plot of VAS for water [6] is disappearing in mixtures with the increase of glycerol concentration. But there appear also a new spectrum with a peak rising toward zero frequency, which is leveled in the high frequency range above 500 Hz.

We assume that a new spectrum belongs to the formation of clusters of water molecules accumulated around the glycerol molecule. The form of the spectra shows that the mixtures have a viscosity thickening property, given the validity of the Stokes-Einstein ratio.

Conclusion

In conclusion we can state that MGSE measurements unveil the low frequency VAS of water and its mixture with glycerol. The spectrum of water can be explained as a combination of molecular self-diffusion and eddy diffusion processes in the vortexes of hydrodynamic fluctuation, while the expected long time tail is supposed to be hidden by intermolecular interactions [5]. In the mixture with glycerol the molecular dynamics is strongly affected by a strong interaction between water and glycerol molecules. They form clusters, which effect the hydrodynamic of mixture that results into the viscosity thickening property of these mixture. It might explains the molecular mechanism behind of their role in the process of spontaneous folding of disordered poly-peptides into biologically active protein molecules

Acknowledgements

We acknowledge the financial support in the program P1-0060 given by the Slovenian research agency, ARRS.

References

1. J. Stepišnik, Analysis of nmr self-diffusion measurements by density matrix calculation, *Physica B* 104 (1981) 350.
2. P. Callaghan, J. Stepišnik, *Advances in Magnetic and Optical Resonance*, ed. Warren S. Warren, Vol. 19, Academic Press, Inc, San Diego, 1996, Ch. Generalized Analysis of Motion Using Magnetic Field Gradients, pp. 326.
3. J. Stepišnik, A. Mohorič, C. Matea, S. Stapf, I. Serša, Velocity autocorrelation spectra in molten polymer measured by NMR modulated gradient spin-echo, *EuroPhysics Letters* 106 (2014) 27007.
4. J. Stepišnik, I. Ardelean, Usage of internal magnetic fields to study the early hydration process of cement paste by MGSE method, *Journal of Magnetic Resonance* 272 (2016) 100–107.
5. J. Stepišnik, C. Mattea, S. Stapf, A. Mohorič, Molecular velocity auto-correlation of simple liquids observed by NMR MGSE method, *European Physics Journal B*, 91 (2018) 293.

Investigation of Re-Pt vinylidene complex $\text{Cp}(\text{CO})_2\text{RePt}(\mu\text{-C}=\text{CHPh})(\text{PPh}_3)_2$ by solid-state NMR

K. T. Smolyarov¹, A. N. Matsulev^{1,2}, A. A. Kondrasenko^{1,2}

¹*Kirensky Institute of Physics, Federal Research Center KSC SB RAS,*

²*Institute of Chemistry and Chemical Technology, Federal Research Center KSC SB RAS Krasnoyarsk, Russia*

E-mail: smokost@iph.krasn.ru

Introduction

In this paper, the heterobinuclear vinylidene complex $\text{Cp}(\text{CO})_2\text{RePt}(\mu\text{-C}=\text{CHPh})(\text{PPh}_3)_2$ [1] was studied using solid-state ^{31}P and ^{195}Pt nuclear magnetic resonance (NMR) spectroscopy. Heterometallic vinylidene complexes of rhenium and platinum can be used in the synthesis of organometallic compounds and organic substances and also have a prospect in the synthesis of functional polymetallic materials [2].

NMR spectroscopy in the liquid and solid states is traditionally used to study molecular structure, nature of chemical bonds and intermolecular interactions of substances. The molecular structure of the complex was established by X-ray diffraction analysis [3]. This complex was not studied by solid-state NMR spectroscopy methods earlier.

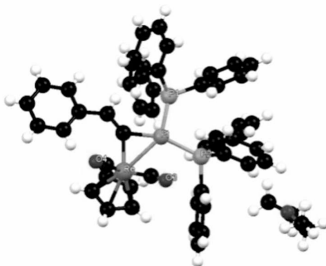


Figure 1. Molecular structure of complex according to X-ray data

Analysis of NMR spectra

^{31}P NMR spectra

The ^{31}P and ^{195}Pt NMR cross-polarization (CP) spectra of powdered complex in static and magic-angle spinning (MAS) conditions were acquired using the Bruker AV300 spectrometer operating at 121.5 MHz (^{31}P) and 64.2 MHz (^{195}Pt) frequencies.

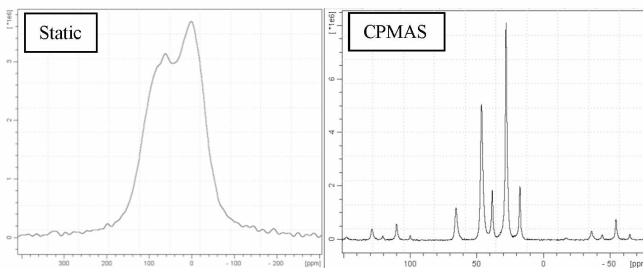


Figure 2. ^{31}P static and CP/MAS NMR spectra

Each of the two nonequivalent phosphorus nuclei in complex are bonded to the platinum nucleus. The static spectrum represents a line broadened by dipole-dipole interaction and high chemical shift anisotropy. The peaks assigned to both phosphorus nuclei are clearly distinguishable. The same is observed on the well resolved ^{31}P CP/MAS NMR spectrum. The CP/MAS spectrum consisted to two pseudo-triplets due to indirect spin-spin interaction with the ^{195}Pt nucleus. The magnitudes of J-coupling for nonequivalent phosphorus nuclei ($J_1 = 4600$ Hz and $J_2 = 2600$ Hz) are clearly exhibit ligand *trans*-effect. Prior to determination of ^{31}P chemical shift tensor parameters, the isotropic chemical shift was determined based on the CP/MAS spectrum. In the next step the model spectrum was fitted to the static spectrum (fig.3). Fitted parameters of the chemical shift tensor of ^{31}P are summarized in the table 1, where nucleus P_1 (46.5 ppm) is in a *trans*-position relative to rhenium, and nucleus P_2 (28 ppm) is in a *trans*-position relative to the vinylidene fragment.

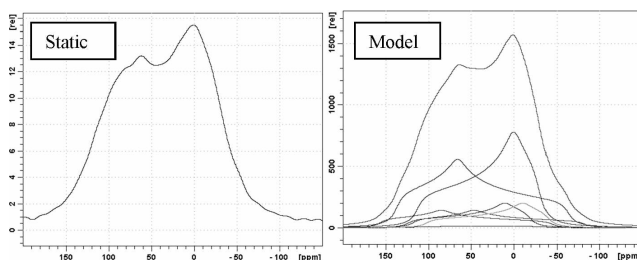


Figure 3. Approximation of the ^{31}P static NMR spectrum

^{195}Pt NMR spectra

Due to 33.8% natural abundance of NMR-active platinum isotope the NMR spectra has a low signal-to-noise ratio. The spectrum is broadened by chemical shift anisotropy. Because of this difficulties arise in the study of samples for this nucleus.

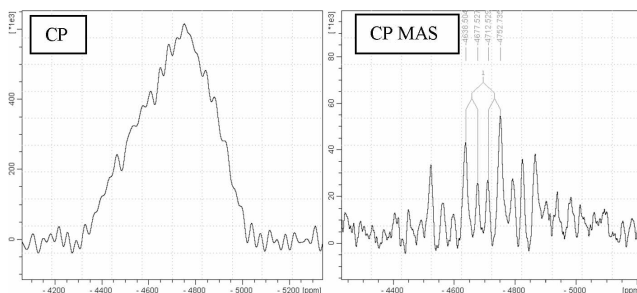


Figure 4. ^{195}Pt CP-static and CP/MAS NMR spectra

The width of static spectrum on the half height is about 25 kHz and largely determined by chemical shift anisotropy. Application of MAS at low frequencies a large number of rotational satellites appear on the spectrum complicating the analysis of the spectrum. However, while spinning the sample at high frequencies was not applicable since information about the chemical shift anisotropy is lost. Therefore, information evident from ^{31}P spectra was used to set the MAS frequency to 7200 Hz ($J_1 + J_2$) so that the rotation satellites from first and fourth split resonance lines overlap. This allowed to gain greater signal-to-noise ratio and to acquire spectrum which was sufficient for determination of the chemical shift tensor.

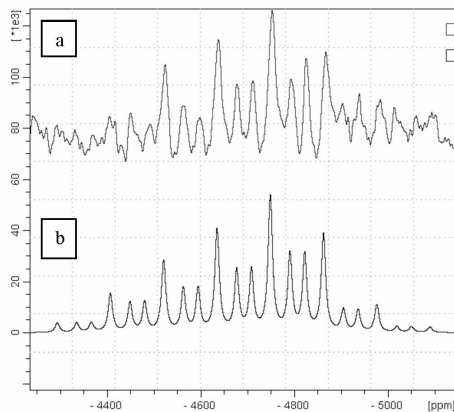


Figure 5. Comparison of model and experimental spectra, a) ^{195}Pt NMR CP/MAS spectrum, b) model spectrum

Characteristic features of rotational satellites overlapping in the model spectrum are in good agreement with the experimental spectrum. The parameters of the ^{195}Pt chemical shift tensor are summarized in the following table:

Table 1 – The parameters of the chemical shift tensor of ^{31}P and ^{195}Pt

Nucleus	δ_{iso} , ppm	Δ , ppm	η	δ_{11} , ppm	δ_{22} , ppm	δ_{33} , ppm
$^{31}\text{P}_1$	46.5	-110	0.65	136.35	64.85	-64.4
$^{31}\text{P}_2$	28	85	0.35	112.6	0	-31.78
^{195}Pt	-4670	350	0.6	-4314	-4734	-4944

Denotation: Δ – anisotropy, η – asymmetry, δ_{ii} – principal axis of tensor

High chemical shift anisotropy of nuclei is due to the electron configuration of molecular orbitals, when unpaired electrons on the unfilled shells induce paramagnetic currents at the location of sensitive nuclei and shift the resonant line to a strong or weak field depending on the direction of the constant magnetic field. For further analysis of the electron density along interatomic bonds, quantum-mechanical calculations are planned in order to estimate the paramagnetic contribution of electrons to the chemical shift of nuclei.

References

1. Chudin O. S. et al. Chemistry of Vinylidene Complexes. XVII. The First μ -vinylidene Complex with the Re-Pt Bond: Synthesis, Spectroscopic Study and Structure of $(\eta^5\text{-C}_5\text{H}_5)(\text{CO})\text{RePt}(\mu\text{-C}=\text{CHPh})(\text{PPh}_3)_2$ //Journal of Siberian Federal University. Chemistry. – 2008. – T. 1. – №. 1. – C. 60-70.
2. Antonova A. B., Ioganson A. A. Transition metal complexes of unsaturated carbenes: synthesis, structure, and reactivity //Russian Chemical Reviews. – 1989. – T. 58. – №. 7. – C. 693-710.
3. Vasiliev A. D., Chudin O. S., Antonova A. B. μ -Carbonyl-1: 2 κ 2C-carbonyl-1 κ C-(η^5 -cyclopentadienyl)(μ -phenylvinylidene) bis (triphenylphosphine-2 κ P) rheniumplatinum (Re–Pt) diethyl ether hemisolvate //Acta Crystallographica Section E: Structure Reports Online. – 2007. – T. 63. – №. 9. – C. m2272-m2272.
4. Xiao J., Puddephatt R. J. Pt-Re clusters and bimetallic catalysts // Coordination chemistry reviews. – 1995. – T. 143. – C. 457-500.

Analysis of the kerns of the Yuzhno-Cheremshansky field by the method of electron spin resonance

Larisa V. Tsyro, Alina A. Pichugina

*Institute of Natural and Technical Sciences, Surgut State University, Lenina avenue 1, Surgut,
Russian Federation*

E-mail: tsyro@xf.tsu.ru

http://www.surgu.ru

Introduction

The kern research is an important task to answer such questions as:

1. The influence of metals contained in rocks on the process of oil formation.
2. Relationship of composition with the transformation of organic matter rocks.

By chemical composition, rocks mainly consist of silica, alumina, ferrous oxide, magnesium oxide, calcium, sodium, potassium, and water. The main types of sedimentary rocks are clays, shales (80%), sands and carbonate rocks (limestones). The main minerals are feldspar, kaolin, etc.

Methods for the study of kerns include chemical, physico-chemical, optical spectral, X-ray spectral, mass spectrometry and other types of analysis. The direction of using "combined" methods of analysis has been developing lately. They provide an increase in the sensitivity of physical methods and eliminate the influence on the result of the analysis of the material composition of the sample.

The study of kerns is mainly descriptive, so it is important to use physical and chemical methods of analysis to study the composition and properties. Laboratory studies have shown that core samples have high paramagnetism. Information on the presence and number of spin centers in the sample can be obtained from the spectrum of electron spin resonance (ESR).

The purpose of this work was to analyze the kerns of the Yuzhno-Cheremshansky field using the ESD method.

Research Methods

The electron spin resonance (ESR) method was used to analyze the cores. Preliminary preparation consisted of grinding a core sample in ball mills. The powder thus obtained was placed in an ampoule made of quartz glass, the ampoule was placed in the resonator of an ESR spectrometer. A spectrometer of the SE/X brand operating in the X-band was used. The device was tuned (the corresponding microwave modulation was selected), the spectrum was recorded. Conditions of spectrum shooting: a) field width 700 mT; b) sweep time 16 min; c) ν 9 GHz; d) the sensitivity was selected depending on the sample. Microwave modulation was selected in such a way that saturation would not occur for the sample.

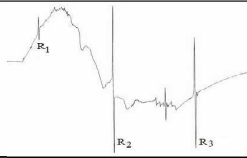
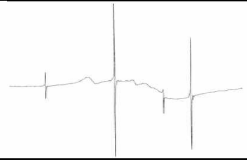
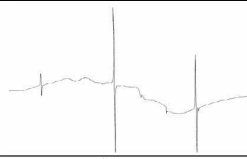
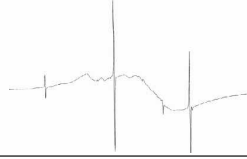
The methodical approach used in the work is that an analysis is made of the shape of the first derivative of the absorption line of an ESR, followed by integration in the EPRAMR computer program and the calculation of the area under the curve. Area is measured in abstract units. It is proportional to the number of spin centers in the sample. The transition from abstract to absolute units is carried out by using the standard. The calibration is carried out using a ruby rod calibrated according to vanadyl acetylacetonate. (VAA). In the spectrum, the signals from the reference correspond to the lines R1, R2 and R3 (see the example of the spectrum in Table 1).

Results

Table 1 shows examples of the kern spectra of the Yuzhno-Cheremshansky field of various rocks. For the ESR spectra, similar lines are observed, since the rocks studied have a

similar chemical composition, but differ in the size of cemented particles. For kern samples of this field, the C_{SC} concentration is about $10^{21} \div 10^{23}$ spin / g.

Table 1. Examples of spectra of different rocks of the Yuzhno-Cheremshansky field

h, m	№ wells	rock	$C_{SC} \cdot 10^{-21}$, spin/g	Spectrum view
2247,8- 2254,5	1	layered	25,49	
1779,1- 1784,1	2	sandstone	14,37	
2307,0- 2314,3	1	siltstone	101,77	
2313,1- 2318,1	2	argillite	3,70	
1886,7- 1892,1	1	clay	8,89	

The ESR spectra of all types of rocks have a high intensity, a wide line and a rather complex and unresolved form. Analysis of the spectra indicates the presence in the samples of multi-spin atoms with zero nuclear spin — unresolved fine interaction (for example, atoms of the iron group and some rare earths, actinides). Elements of a more or less resolved hyperfine structure, manifested in peak systems of 6 lines, indicate the presence of low-spin atoms in the rock with nuclear spin $5/2$ (for example, manganese, aluminum, isotopes of magnesium, oxygen, titanium, zinc, zirconium, ruthenium, palladium, tin, some rare earths). Narrow peak in the region $g = 2$ – singlet of the spectrum of free radicals of organic matter.

The change in the concentration of spin centers on the depth of the rock has a peak dependence (Fig. 1).

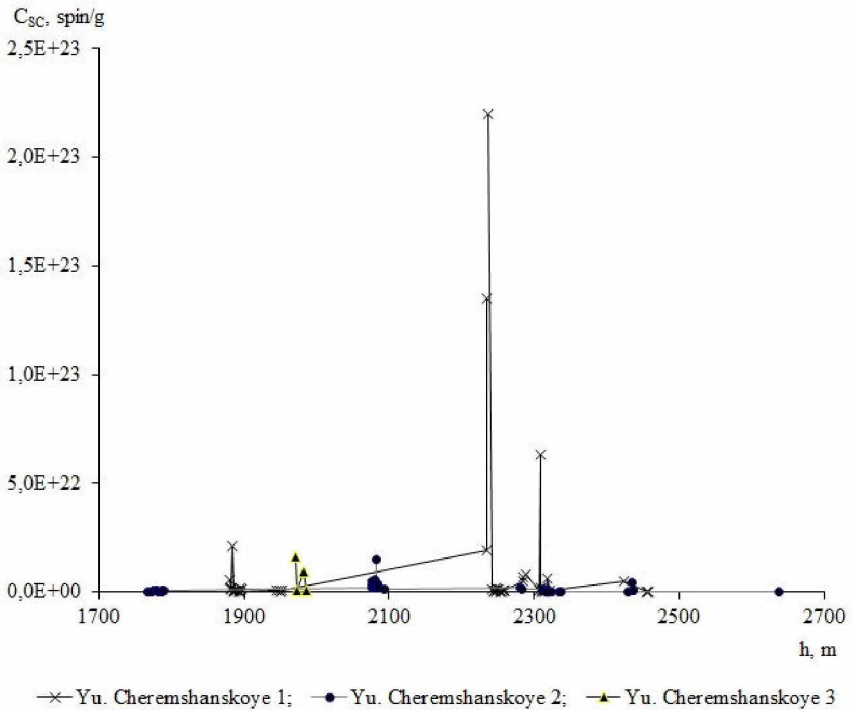


Figure 1. The change in C_{sc} for fields with a set of kerns in a wide range of depths

The largest surge is observed for 1 well in the area of 2250-2300 m. Along with Mn (II) and free radicals of organic nature [1], the total concentration of spin centers can be used as criteria for predicting the oil and gas content of rocks.

The effectiveness of solving applied and fundamental problems in the field of exploration, production and refining depends on information about the physicochemical properties of oil and the enclosing sedimentary rocks. Therefore, it is promising to use the spin properties of rocks when searching for deposits of oil and gas in geological sections.

Any possibility of introducing into the well-known complex of parameters determining the oil and gas potential of the section, new signs, allowing to divide the rocks into productive and unproductive, increases the accuracy of the forecast. These features include sedimentary rocks with spin properties that are associated with productive horizons.

References

1. L. A. Tyo, M. K. Jexsenov, B.K. Kuspanova, I.M. Batirbaev, R. Nasirov. – *Reports of NAS RK*, 6, 93-98 (2002) (in Kazakhstan)

Conformational dynamics of the two-domain Pax5 protein in aqueous solution. A molecular dynamics simulation study

Milosh Ubovich¹, Sergei A. Izmailov², Andrei V. Egorov¹

¹Faculty of Physics, Saint-Petersburg State University, Russia

²Laboratory of bio-NMR, Saint-Petersburg State University, Russia

E-mail: ubovich.milosh@yandex.ru

Introduction

Multi-domain proteins play an important role in the nature. Such proteins are capable of executing many targeted activities in catalysis, signaling, regulation of gene expression, and other cellular processes [1]. The relative positioning and dynamics of protein domains is essential for their functions. However, in solution multi-domain proteins adopt multiple conformations and it is challenging to characterize such conformational diversity by traditional experimental techniques. In this case, the atomistic molecular dynamics (MD) simulations is a promising tool to address the problem.

In the present study, a two-domain Pax5 protein (PDB code 1MDM) was modeled. The protein consists of two domains (75 and 57 residues correspondingly) flexibly connected by a 17-residue linker. It has been implicated in certain types of cancer [2].

Simulations details

MD simulations were performed using the Amber14 package [3] with ff14SB force field. Two simulation protocols were considered. First, a single Pax5 protein molecule was centered in the periodic cell which has the form of a truncated octahedron and the rest of the cell were filled with 32523 TIP3P [4] water molecules. The simulations were carried out in a *NPT* ensemble at 298 K and atmospheric pressure. In the second case, the Pax5 molecule was centered in the orthorhombic periodic cell with dimensions 85×109×101 Å which were filled with 26029 water molecules. The simulations were carried out in a *NVT* ensemble at 298 K. Each system was equilibrated during the 1 ns simulation. The following production run was 1 μs long generating a pool of 1000 structures. In carrying out the simulations using two protocols, we tried to estimate the possible effects of computational methodology on modeling the structure and dynamics of two-domain proteins with significant domain mobility.

Results

In the present study MD simulations were employed to rationalize the complicated conformational dynamics of Pax5 protein. To characterize the overall evolution of the protein structure, the root-mean-square deviation (RMSD) of backbone alpha carbons (see, for instance, Fig. 1), pair distance distribution function, as well as radius of gyration were calculated. At the same time, the simulation data were used to describe the dynamics of individual domains and inter-domain orientations. A special attention was given to the calculation of small-angle X-ray scattering profiles from MD data.

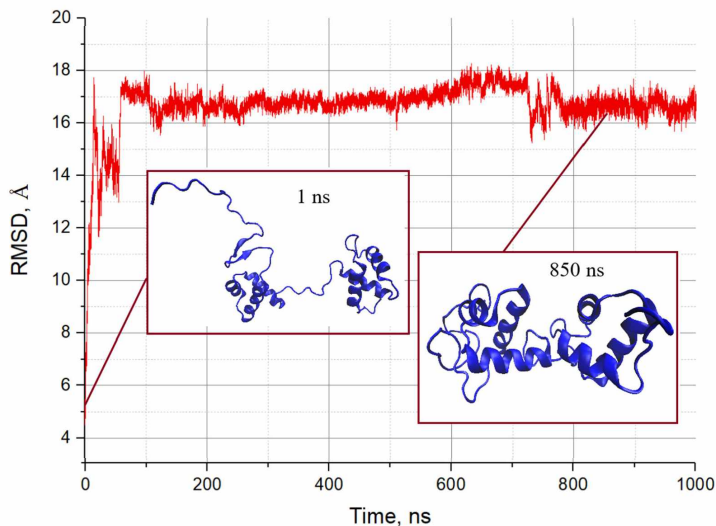


Figure 1. C_{α} atoms RMSD between the MD structures and initial conformation for Pax5 protein. Data taken from MD simulations performed in the NPT ensemble

Acknowledgements

The project was conducted using the computer facilities of the Laboratory of bio-NMR at Saint-Petersburg State University. We thank N. R. Skrymikov for drawing our attention to this problem.

References

1. K.T. Debiec, M.J. Whitley, L.M.I. Koharudin, L.T. Chong, A.M. Gronenborn, – *Biophysical Journal*, **114**, 839–855, (2018).
2. C. Perez-Borrajero, M. Okon, L.P. McIntosh, – *Journal of Molecular Biology*, **428**, 2372-2391, (2016).
3. D.A. Case, V. Babin, J.T. Berryman, R.M. Betz, Q. Cai, D.S. Cerutti, T.E. Cheatham, III, T.A. Darden, R.E. Duke, H. Gohlke, A.W. Goetz, S. Gusarov, N. Homeyer, P. Janowski, J. Kaus, I. Kolossváry, A. Kovalenko, T.S. Lee, S. LeGrand, T. Luchko, R. Luo, B. Madej, K.M. Merz, F. Paesani, D.R. Roe, A. Roitberg, C. Sagui, R. Salomon-Ferrer, G. Seabra, C.L. Simmerling, W. Smith, J. Swails, R.C. Walker, J. Wang, R.M. Wolf, X. Wu, P.A. Kollman. AMBER 14, University of California, San Francisco, 2014.
4. W.L Jorgensen, J. Chandrasekhar, J.D. Madura, R.W. Impey, M.L. Klein, – *Journal of Chemical Physics*, **79**, 926-935, (1983).

NMR method for assessing the inhibitory properties of drilling fluids

E. I. Uskova¹, I. H. Fatkhutdinov², M. M. Dorogynitskii¹, V. D. Skirda¹

¹*Kazan (Volga Region) Federal University, Kazan, Russia*

²*Mirrico Group of Companies, Kazan, Russia*

E-mail: elen.uskova@mail.ru

www.kpfu.ru/physics

Introduction

One of the informative methods for the study of molecular structures and molecular mobility is the method of NMR-relaxometry. Recently, in NMR studies, a new method for obtaining 2D-maps of joint distributions of nuclear magnetic relaxation times has been widely used [1, 2]. It should be noted that the one-dimensional distributions of the spin-lattice relaxation times T_1 and spin-spin relaxation T_2 as well as the joint two-dimensional distribution of nuclear magnetic relaxation times $P(T_1, T_2)$ depend on the main characteristic of the NMR devices - the resonance frequency. Comparing the results of calculating such distributions over data from various NMR instruments, additional information is needed on the dispersion dependence of the times T_1 and T_2 .

New approach to 2D-map T_1 - T_2

Based on the method of obtaining 2D-maps of joint distributions of nuclear magnetic relaxation times, in this paper a new NMR method is proposed for estimating such molecular characteristics of the interaction as:

- A spectrum of correlation times of molecular motion, leading to fluctuations of the interaction potential of water molecules and hydrophilic mineral components of the rock;
- A spectrum of the second moments, which is determined by the magnetic environment of water molecules;
- 2D-maps of joint distributions of correlation times τ_c and second moments $\Delta\omega^2$, which allow typing both the composition and the mobility of individual dynamic phases of the mud – mudstone system.

The technique is based on an a priori assumption about the mechanism of nuclear magnetic relaxation. The calculated two-dimensional distribution of $P(\tau_c, \Delta\omega^2)$ does not depend on the characteristics of NMR-relaxometers, which opens up the possibility of a simple comparison of the NMR data obtained in different laboratories. For the analysis of two-dimensional data, specially developed software was used to calculate the $P(T_1, T_2)$ and $P(\tau_c, \Delta\omega^2)$. 2D-maps of these distributions are shown in Figure 1. For analysis mechanisms can be used such as the Wangness-Bloch model [3] for spin in a random field, the Kubo-Tomita theory [4] for the homonuclear dipole-dipole interaction, the Solomon-Blombergen-Morgan theory [5] for the heteronuclear dipole-dipole and scalar interactions, the relaxation mechanism due to the anisotropy of McConnell-Holm electron screening [6], and also the theory of spin-rotational relaxation [7].

The correlation time τ_c is determined by the dynamic state of the molecules, which depends on the temperature and the potential of the molecular interaction. For the liquid state, this value has values of the order of 10^{-12} s, and for a solid, more than 10^{-9} s. The value of the second moment $\Delta\omega^2$ is determined by the magnetic environment, for example, of the ^1H hydrogen atom in molecules of different molecular structures and can be estimated using the well-known Van-Vleck formula [8]. Thus, the $P(\tau_c, \Delta\omega^2)$ distribution contains information on the structural and dynamic molecular characteristics and allows typing both the composition

and the mobility of individual dynamic phases. Figure 1 shows the original data and the results of calculating the 2D-maps of the joint distributions $P(T_1, T_2)$, $P(T_1/T_2, T_2)$ and $P(\tau_c, \Delta\omega^2)$.

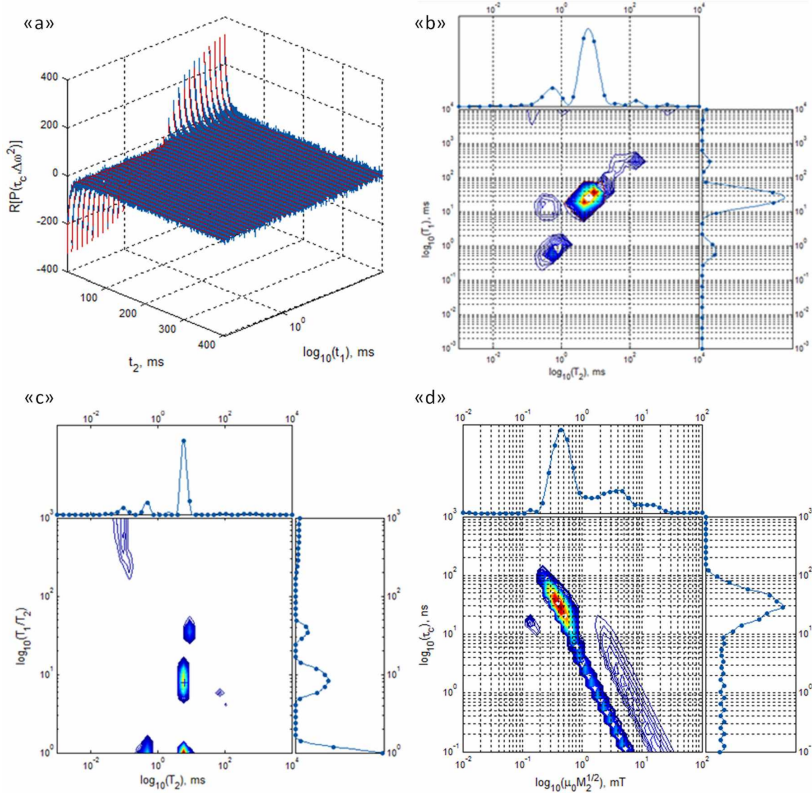


Figure 1. “a” – The original data in the 2D T_1 - T_2 experiment; “b” – the 2D-map of the joint distribution $P(T_1, T_2)$; “c” – the 2D-map of the joint distribution $P(T_1/T_2, T_2)$; “d” – the 2D-map of the joint distribution $P(\tau_c, \Delta\omega^2)$

Application of the new analysis method

The proposed method was applied to the study of water sorption on the hydrophilic mineral components of the rock - argillite. To study nuclear magnetic relaxation, the NMR-relaxometer Chromatec Proton-20M was used. For measurements used pulse sequence «IR(t_1)CPMG(t_2)» [2]. Figure 2 shows the results of calculations of 2D maps $P(\tau_c, \Delta\omega^2)$ for water-mudstone samples with various degrees of saturation. On the 2D-maps of $P(T_1, T_2)$, two peaks are distinguished due to the interaction of water with different hydrophilic components of the mudstone. One of the peaks is characterized by the ratio $T_1=T_2$ and the corresponding wide “tail” of poorly resolved correlation times, the other peak is characterized by the ratio $T_1 \geq 10T_2$ and a separate peak on the map $P(\tau_c, \Delta\omega^2)$. Depending on the increase in the degree of saturation, the distribution of the correlation times remained almost unchanged, while the distribution of the second moments shifted to a region with smaller second moments. This

behavior can be explained by an increase in the distance between the paramagnetic centers on the surface of the clay mineral component due to the wedging action of water molecules.

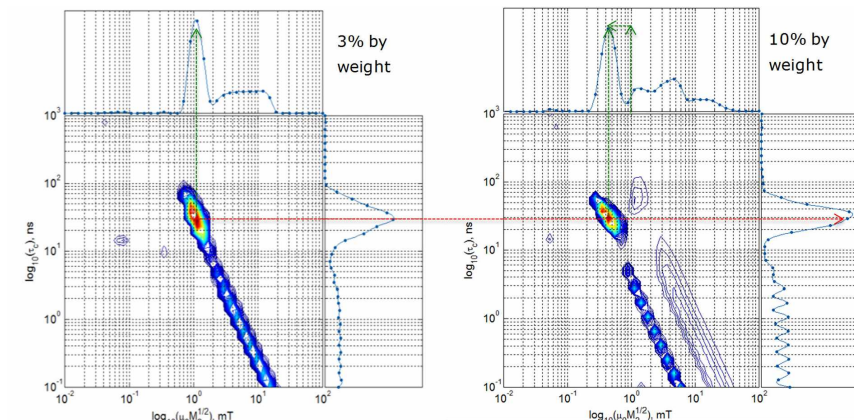


Figure 2. Change of the 2D-map $P(\tau_c, \Delta\omega^2)$ with increasing saturation of the argillite with water

In conclusion

The method of constructing a 2D map of the joint distributions $P(\tau_c, \Delta\omega^2)$ of the second moments and correlation times for autocorrelation function of the interaction Hamiltonian allows to obtain unique information about the structure of the environment molecules and to compare the mobility of molecules.

References

1. Y.-Q. Song, L. Venkataramanan, M.D Hürlimann, M. Flaum, P. Frulla, and C. Straley T1–T2 Correlation Spectra Obtained Using a Fast Two-Dimensional Laplace Inversion – *Journal of Magnetic Resonance*, 154, 261–268 (2002).
2. B. Gizatullin, A. Savinkov, T. Schipunov, D. Melnikova, M. M. Doroginitskii, V.D. Skirda Investigation of molecular mobility and exchange of n-hexane and water in silicalite-1 by 2D 1H NMR relaxometry – *Magnetic Resonance in Solids*, 20 i.1, 1-9, (2018).
3. R.K. Wangsness and F. Bloch. The Dynamic Theory of Nuclear Induction – *Physical Review*, 89 n.15, 728-739 (1953).
4. R. Kubo and K. Tomita. A General Theory of Magnetic Resonance Absorption – *Journal Chemical Society of Japan*, n.9, pp. 888-919 (1954).
5. I. Solomon. Relaxation Processes in a System of Two Spins - *Physical Review*, 99 n.2, 559-565 (1955).
6. H.M. McConnell, C.H. Holm. Proton Resonance Shifts in Nickelocene – *Journal Chemical Physics*, 27, 314-31(1957).
7. P.S. Hubbard. Theory of Nuclear Magnetic Relaxation by Spin-Rotational Interactions in Liquids – *Physical Review E*, 131 n.31, 1155-1165 (1963).
8. J. H. Van Vleck. The Dipolar Broadening of Magnetic Resonance Lines in Crystals – *Physical Review*, 74 i.9, 1168-1183 (1948).

NMR studies of nanocomposite based on the organic ferroelectric DIPAB

N. I. Uskova¹, D. Yu. Podorozhkin¹, E. V. Charnaya¹, D. Yu. Nefedov¹, S. V. Baryshnikov²

¹*St. Petersburg State University, St. Petersburg, 198504 Russia*

²*Blagoveschensk State Pedagogical University, Blagoveschensk, 675002 Russia*

E-mail: natalyauskova.spbu@gmail.com

Introduction

New organic ferroelectrics such as diisopropylammonium bromide (Curie temperature of 426 K and spontaneous polarization $23 \mu\text{C}/\text{cm}^2$) are an interesting object to study [1-4]. They exhibit all the basic physical properties observed in type BaTiO_3 inorganic ferroelectrics. In addition, organic ferroelectrics are generally simple and environmentally friendly in processing, have lightweight and can be mechanically flexible. NMR methods allow for research at the microscopic level and in contrast to other methods, identifying new peculiar properties.

In this work, the main attention was paid to the influence of the size effect on the temperature of phase transitions in the diisopropylammonium bromide (DIPAB)

Samples and experiment

The sample under investigation was DIPAB embedded in opal matrices. The results were compared to the results obtained for crystal powder of DIPAB.

The measurements were performed using a pulse Bruker Avance 400 NMR spectrometer in the temperature range from room temperature to 440 K. The pulse sequence used for acquiring the spectrum was a standard cross-polarization (from proton to ^{13}C) MAS pulse sequence.

Results

The ^{13}C CP-MAS NMR spectrum of DIPAB ($\text{C}_6\text{H}_{16}\text{NBr}$) at room temperature demonstrates six lines, corresponding to 6 crystallographically non-equivalent carbon positions. However, on the spectrum of the DIPAB in opal, there are additional lines. This is due to the presence of particles that are in a different crystalline phase. Above the temperature of the ferroelectric phase transition for both samples, only two lines are observed, corresponding to two crystalline nonequivalent carbon groups.

The results confirm the presence of two structural transitions in bulk DIPAB (one of which can be attributed to the ferroelectric phase transition). It is shown that in the DIPAB nanocomposite, two phases coexist in a wide temperature range ($\text{P}2_12_12_1$ and $\text{P}2_1$) during the first heating, and the temperature of the ferroelectric phase transition (from $\text{P}2_1$ to $\text{P}2_1/m$) rises about 7 K compared to the bulk sample.

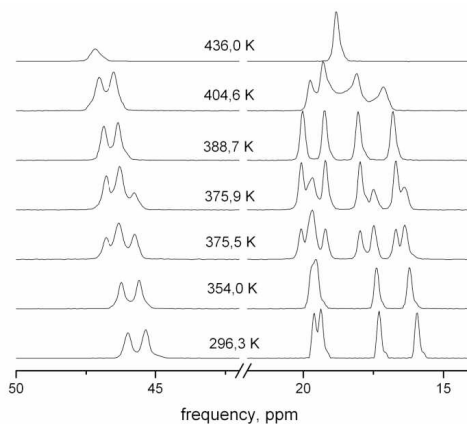


Figure 1. ^{13}C NMR CP-MAS spectra of DIPAB at different temperatures

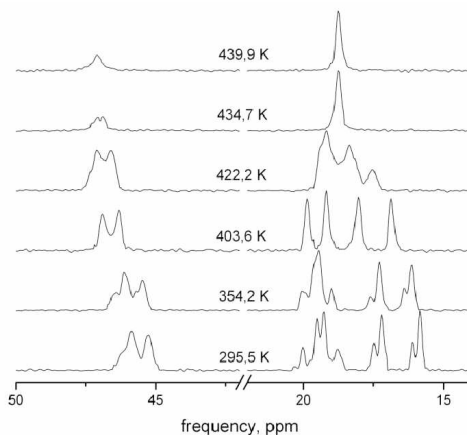


Figure 2. ^{13}C NMR CP-MAS spectra of DIPAB in opal at different temperatures

In conclusion, NMR methods allowed structural changes have been identified indicating a more complex nature than previously thought.

References

1. Owczarek M, Hujzak KA, Ferris DP, et al. Flexible ferroelectric organic crystals. *Nat Commun*, 7, 1–10 (2016).
2. Horiuchi S, Tokura Y. Organic ferroelectrics. *Nat Mater*, 7, 357–366 (2008).
3. Piecha A, Gagor A, Jakubasa R. Room-temperature ferroelectricity in diisopropylammonium bromide. *CrystEngComm*, 15, 940–944 (2013).
4. Fu D-W, Cai H-L, Liu Y, et al. Diisopropylammonium Bromide Is a High-Temperature Molecular Ferroelectric Crystal. *Science*, 339, 425–428 (2013).

Magnetic resonance studies of atomic hydrogen in porous Ne at ultra-low temperatures

S. Vasiliev¹, J. Ahokas¹, J. Järvinen¹, S. Sheludiakov¹, V. V. Klmelenko² and D. M. Lee²

¹*Department of Physics and Astronomy University of Turku, 20500 Turku, Finland,*

²*Department of Physics and Astronomy, Texas A&M University, College Station, TX, 77843, USA*

E-mail: servas@utu.fi

http://hturku.utu.fi

The freezing temperature of solid hydrogen may be significantly lowered below bulk value by encapsulating it in a restricted geometry. This can be realized by slow deposition of mixtures of rare gases (Ne, Kr) and molecular hydrogen at sufficiently low temperatures [1]. The films deposited at such conditions exhibit a high degree of porosity with nano-clusters of H₂ inside the pores. Small amounts (<0.1%) of H₂ can be dissolved in the Ne crystalline lattice. From our previous work with mixtures of H isotopes including tritium, we got a tiny amount of T diffused into the metal of the sample cell walls. 5.7 keV electrons resulting from β -decay of tritium escape from the walls and flying through the thickness of the Ne-H₂ films lead to a dissociation of molecular hydrogen into atoms. We utilize ESR at 130 GHz for characterization of the properties of these atoms stabilized inside the Ne-H₂ films in strong magnetic fields of 4.6 T and temperatures below 1 K. We found that H atoms may be trapped in two different substitutional positions in the Ne lattice as well as inside clusters of pure molecular H₂ in the pores of the Ne film. The latter type of atoms was very unstable against recombination at temperatures 0.3-0.6 K. Based on the observed nearly instant decays after rapid small increases of temperature, we evaluate the lower limit of the recombination rate constant $k_r \geq 5 \cdot 10^{-20} \text{ cm}^3 \text{ s}^{-1}$ at 0.6 K, five orders of magnitude larger than that previously found in the thin films of pure H₂ at the same temperature. Such behavior assumes a very high mobility of atoms and may indicate a solid-to-liquid transition for H₂ clusters of certain sizes, similar to that observed in experiments with H₂ clusters inside helium droplets [2]. We found that the efficiency of dissociation of H₂ in neon films is enhanced by 2 orders of magnitude compared to that in pure H₂ as a result of strong action of secondary electrons.

References:

1. S. Sheludiakov *et. al.*, Phys. Rev. B 97, 104108 (2018).
2. Kirill Kuyanov-Prozument and Andrey F. Vilesov, Phys. Rev. Lett 101, 205301 (2008).

Synthesis and NMR study of adducts of ninhydrin-derived azomethine ylide with cyclopropenes

Siqi Wang, Alexander S. Filatov, Alexander V. Stepanov, Stanislav I. Selivanov

Institute of Chemistry, State University of Saint-Petersburg, University prospect 26, 198504, Saint-Petersburg, Russia

E-mails: wangsiqi@inbox.ru; nmr.group.spbu@gmail.com

Introduction

1,3-Dipolar cycloaddition of azomethine ylides with alkenes is a universal synthetic tool for creating five-membered nitrogen-containing heterocyclic fragments, which are part of many natural alkaloids, as well as pharmacologically and biologically important compounds. Cyclopropenes occupy a special place among alkenes. Their unique reactivity due to high ring strain and low distortion energy makes them valuable synthetic intermediates [1-3]. We synthesized a series of adducts of ninhydrin-derived azomethine ylide with cyclopropenes. The products **4** are obtained by reacting ninhydrin **1**, triphenylcyclopropene **3** and amino acids **2** in a mixed solution of methanol, water and acetic acid (Figure 1). Structural analysis of the products **4a-c** obtained was carried out using some physical methods (IR, MS, X-ray and NMR-spectroscopy).

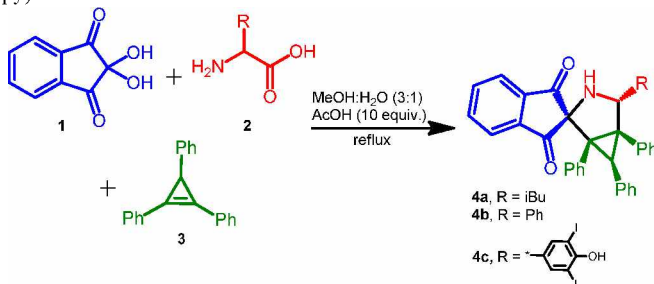


Figure 1. Scheme of synthesis

Among them NMR-spectroscopy is one of the most informative and sensitive method for determination of adduct spatial structure and for estimation of their conformational mobility in the solution. Application of NMR spectroscopy in structural and conformational analysis is mostly based on measurements of spin-spin coupling constants and through-space interactions between magnetic nuclei in the molecules under investigation. Relationship between vicinal scalar constant 3J on dihedral angle θ [4] and very strong dependence of nuclear Overhauser effect (nOe) on internuclear distance r : $\eta_{(nOe)} \sim r^{-6}$ [5] are well-known and widely used in practice. In this work the results of NMR study of adducts **4a-c** are presented.

Experiments and results

The main problem of signal identification in ^1H NMR spectra of compounds **4a-c** is the absence of scalar interactions between protons of different aromatic rings. Therefore for this purpose, the NOESY experiment data on through space interactions were used most intensively. COSY method turned out to be useful for finding in the spectrum of *ortho*-proton signals H^{28} , H^{29} of ring "b" at 6.42 ppm and H^{16} , H^{17} of ring "d" at 7.46 ppm for adduct **4c** due to the long-range scalar interactions with protons H^{13} (3.36 ppm) and H^{14} (2.64, 2.78 ppm), respectively. In case of compound **4c** the signals of the four protons H^1 - H^2 - H^3 - H^4 are located in region 7.55 – 7.8 ppm and represent a strongly coupled system of the ABCX-type, in which signal at 7.77 ppm is an X-proton and, obviously, it belongs to either the proton H^1 or H^4 .

The choice between them was made in favor of the proton H^4 on the basis of detecting in the NOESY spectrum a very small cross-peak between the singlet signal of H^{13} at 3.36 ppm and the doublet signal under study at 7.77 ppm since, in accordance with the calculation by the molecular mechanics method MM2, the distance $r_{13-4} = 5.66 \text{ \AA}$ is much less than the distance $r_{13-1} = 7.05 \text{ \AA}$. As an example of complete signal assignments 1H NMR spectrum of compound **4c** are shown in Figure 2.

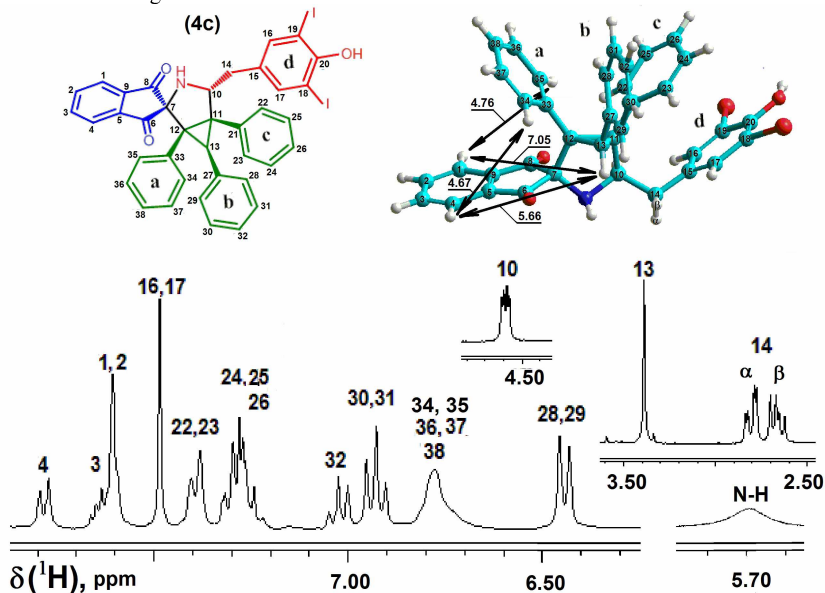


Figure 2. Signal assignments in 1H NMR spectrum of compound **4c** in $CDCl_3$ and spatial structure of its most preferred conformation. Numbering of atoms is shown by figures and aromatic rings marked with letters “a”, “b”, “c” and “d”. Some interproton distances are shown by double arrows and their calculated (MM2) values are given in angstroms (\AA)

Comparison at a qualitative level of the cross-peak intensities in the NOESY spectrum confirms the structure of compound **4c** in which three phenyl groups “a”, “b” and “c” at carbons (respectively) C^{12} , C^{13} and C^{11} of the cyclopropane ring are facing us and the tolyl group “d” at carbon C^{10} is back to us. In this case proton H^{10} is far from both the N-H proton (2.8 \AA) and the H^{13} proton (3.8 \AA), while the distance r_{NH-H13} is only 2.3 \AA (Figure 3).

Quantitative comparison of the intensity ratio of cross peaks 13/14 β and 13/14 α which is equal only to 3.8 with its calculated value 12.7 for the most preferred conformation (A) of compound **4c**, in where the proton $H^{14\beta}$ is situated in the *trans*-orientation relative to the proton H^{10} (see Newman's projection for conformer (A) in Figure 3), as well as the underestimated value of the vicinal constant $^3J_{10-14\beta} = 8.9 \text{ Hz}$ compared to its calculated value of 11.88 Hz prove the existence of product **4c** in the form of fast (in NMR time scale) conformational equilibrium (A) \rightleftharpoons (B), which is associated with a hindered rotation of the tolyl group around C^{10} - C^{14} bond. The experimental determination of the fraction of the minor conformer (B) was obtained on the basis of the value $^3J_{10-14\beta} = 8.9 \text{ Hz}$ and two calculated its vicinal constant values 11.88 and 2.69 Hz for conformers (A) and (B), respectively. The fraction of the conformer (B) equals to $(32 \pm 3)\%$.

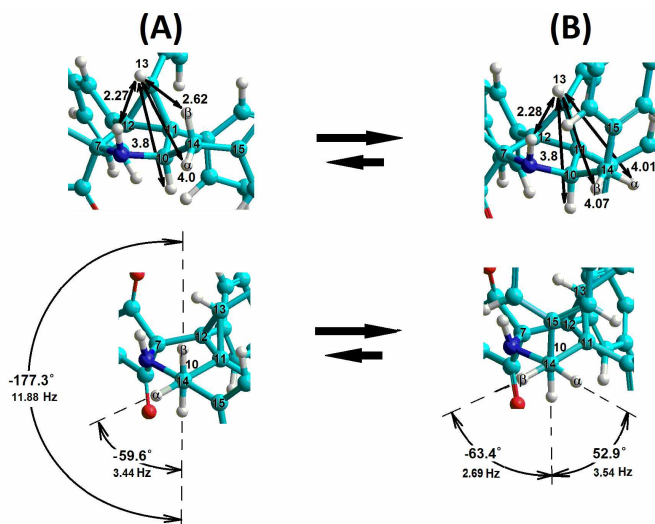


Figure 3. Fragments of rigid part of adduct **4c** for most preferred conformers (A) and (B) on which by using double arrows some important interproton distances r_{H-H} and dihedral angles θ_{H-H} are shown and their calculated (MM2) values are given by figures in angstroms (Å) or in angle degrees ($^{\circ}$), respectively. The vicinal constant values (in Hz) between protons of fragment $C^{10}H-C^{14}H_2$, calculated on base Karplus-type relationship ${}^3J_{H-H}^{calc.} = f(\theta_{H-H})$ [6], are shown on Newman's projection relatively $C^{10}-C^{14}$ bond

Conclusion

Using NMR spectroscopy, we established the structure of the products in reaction of ninhydrin-derived azomethine ylide with cyclopropenes and proved the existence of fast (on the NMR time scale) two-position conformational equilibrium in the solution associated with hindered rotation of the tolyl group around $C^{10}-C^{14}$ bond. The ratio of conformers in a $CDCl_3$ at the temperature 20 $^{\circ}C$ has been determined.

Acknowledgments

Spectral investigations were performed in the Resource Centers "Magnetic Resonance Research Centre", "Chemical Analysis and Materials Research Centre", "X-ray Diffraction Centre" and "Educational Resource Center of Chemistry" of the Saint-Petersburg State University. The study was carried out under the financial support of the Russian Foundation for Basic Research (grant no. 18-33-00464).

References

1. A.S. Filatov, A.V. Stepakov, et al. *J. Org. Chem.*, 2017, 82(2), 959-975.
2. A.S. Filatov, A.V. Stepakov, et al. *Org. Chem. Frontiers*, 2018, 5(4): 595-605.
3. A.S. Filatov, A.V. Stepakov, et al. *Synthesis*, 2019, 51, 713-729.
4. L.B. Krivdin, R.N. Contreras, *Ann. Reports on NMR Spect-py*, 2007. vol. 61. p. 133–245.
5. D. Neuhaus, M.P. Williamson, "The Nuclear Overhauser Effect in Structural and Conformational Analysis" (2nd ed.), Wiley-VCH, New York, 2000. 619 P.
6. C.A.G. Haasnoot, F.A.A.M. Leeuw, C. Altona, *Tetrahedron* 1980. vol. 36(19), 2783–2792.

NMR and EPR in mechanochemically synthesized chalcopyrite nanocrystals

Radik R. Zaynullin¹, Stanislav O. Garkavyi¹, Ekaterina V. Shmidt¹, Stanislav V. Shmidt¹, Vadim L. Matukhin¹, Nikolay K. Andreev¹, Erika Dutkova²

¹Kazan State Power Engineering University, Kazan, 420066, Russia

²Institute of Geotechnics, Slovak Academy of Sciences, Košice, Slovakia

E-mail: oloioiev77@mail.ru

Introduction

Recently, semiconductor nanocrystals of chalcopyrite CuFeS_2 have attracted special attention as materials for possible application in technologies of direct energy conversion. The possibility of the tuning the value of the band gap in wide range caused an interest in nanocrystal chalcopyrite for its use in solar cells. Some investigations [1, 2] show that CuFeS_2 nanoparticles have a larger band gap (1.06 eV in [1] and 0.9 eV in [2]) than bulk chalcopyrite (0.6 eV). And this feature depends on the size and shape of the particles. Thereby, some scientific groups devoted a special attention to the development of new methods for the preparation of chalcopyrite nanocrystals [3-5]. These facts stimulated authors of the paper to perform measurements of the magnetic features of the a nanocrystal powder sample of chalcopyrite CuFeS_2 prepared by mechanochemical synthesis [3, 4, 6, 7] by the $^{63,65}\text{Cu}$ nuclear magnetic resonance (NMR) in a local field and electron paramagnetic resonance (EPR) methods.

A brief review of available results of the investigation of the physical properties of chalcopyrite CuFeS_2 samples

The studied nanocrystal samples of CuFeS_2 were prepared by using mechanochemical synthesis by high-energy milling for 60 min in a planetary mill from copper, iron and sulphur elements [1]. The measured temperature dependence of magnetization $M(T)$ represents itself the curve with smooth increasing to the direction of low temperatures. It exhibits a small shoulder at 125 K and sharp increasing at temperatures lower than 50 K. The low-temperature and high-pressure thermoelastic and structural properties of chalcopyrite, CuFeS_2 were studied by K. S. Knight et al [8]. The temperature dependences of the unit-cell dimensions a and c showed the minima at ~ 86 K and ~ 131 K, respectively. The unit cell volume has a minimum at about 100 K. The Mössbauer spectra of these samples indicated to the $\text{Cu}^+\text{Fe}^{3+}\text{S}_2^{2-}$ valance state of chalcopyrite. In the reported results of the magnetic susceptibility measurements in applied magnetic fields of 0.1, 0.5 and 2.0 T, in each case a cusp-like anomaly is observed, which suggests the onset of additional antiferromagnetic ordering. The local maxima of these cusps are found to be at the temperatures 55.0 K, 52.6 K and 52.3 K, respectively. The anomaly near 55 K in each set of data is indicative of a small antiferromagnetic transition identified by Woolley et al. (1996) [9] as the ordering of the copper magnetic moments.

A pyrite/chalcopyrite mineral sample from Mangampet barite mine, Kadapa, Andhra Pradesh, India is used in the present study. An EPR study on the powdered pyrite sample confirms the presence of iron whereas in chalcopyrite both iron and Mn(II) are present. The EPR spectrum of pyrite represents the wide line at $g = 2.3$. The optical absorption spectrum of chalcopyrite is due to copper, which is in a distorted octahedral environment [10, 11]

NMR spectrum of $^{63,65}\text{Cu}$ in a local field

The $^{63,65}\text{Cu}$ NMR spectra in a local field for the nanopowder sample of CuFeS_2 (Fig. 1a) represent itself two wide lines with maxima at the frequencies corresponding to central NMR transitions ($1/2 \leftrightarrow -1/2$) of two nuclear spins of isotopes ^{63}Cu and ^{65}Cu . Satellite lines, for the transitions ($-3/2 \leftrightarrow -1/2$) and ($1/2 \leftrightarrow 3/2$) registered for the natural CuFeS_2 in Figure 1b, were not observed in the case of mechanochemically synthesized nanocrystals.

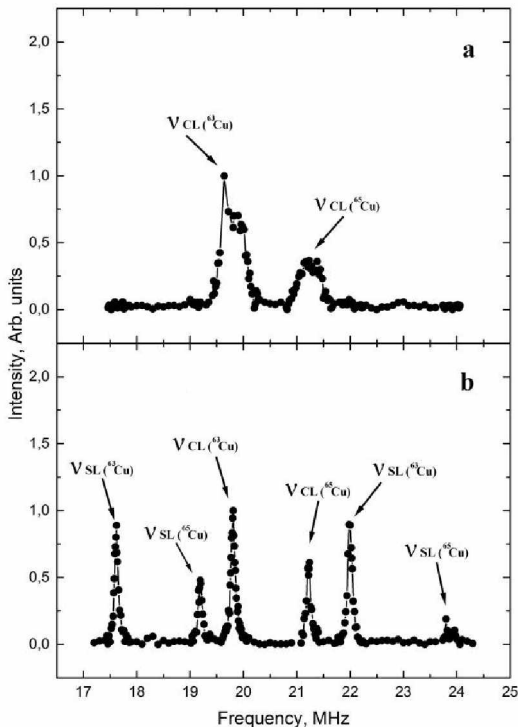


Figure 1. NMR spectrum of $^{63,65}\text{Cu}$ in a local field at 77 K in CuFeS_2 samples, *a* – mechanochemically synthesized nanopowder sample, *b* – natural mineral sample

The observed difference of the spectral line form of the nanocrystal sample of chalcopyrite of that of $^{63,65}\text{Cu}$ NMR of a semiconductor sample of natural chalcopyrite allows us to suggest that the magnetic structure of the nanocrystal sample is more complex and associated with its defective structure. According to the results of the study it was concluded that the nanocrystal sample of mechanically synthesized CuFeS_2 has the heterogeneous state: simultaneously in a powder paramagnetic and ferromagnetic states coexist in an antiferromagnetic matrix. The experimentally observed NMR spectra of $^{63,65}\text{Cu}$ are probably due to antiferromagnetic ordered areas of chalcopyrite nanocrystals. The satellite lines of the spectra cannot be observed due to defectiveness of a nanopowder under study that leads to high spread of local electric and magnetic fields, large width of resonance lines with low amplitudes [12, 13].

EPR measurements

EPR spectra for chalcopyrite powdered samples were recorded using a Varian E12 X-band spectrometer both at room (RT) and liquid nitrogen temperature (LNT) operating at X band frequency ($\nu = 9.40620$ GHz for chalcopyrite) having a 100 kHz field modulation to obtain first derivative EPR spectrum. DPPH with a g value of 2.0023 is used for g factor calculation.

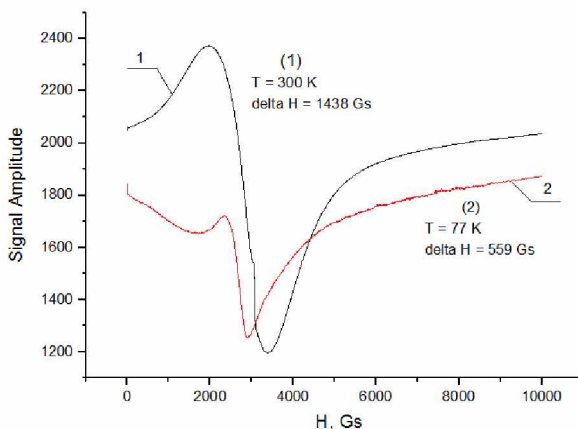


Figure 2. EPR spectra of the nanopowder sample of CuFeS_2 : 1 (black) – at 300 K, linewidth $\Delta H = 1438$ Gs; 2 (red) – 77 K, $\Delta H = 559$ Gs; the resonance field $H_0 = 5000$ Gs (0.5 T), wavelength $\lambda = 3.2$ cm; sweep range 10000 Gs; sweep time 4 min

The Fig. 2 illustrates that there is no hyperfine structure in all ESR spectra of the investigated powder samples. Two types of lines can be distinguished: 1) the wide lines near $g = 2.3$; 2) the narrow line of the very small intensity at $g = 2.0023$. As can be seen from the Fig. 2, the spectrum at 300 K with $g = 2.3$ represents the intensive wide line with $\Delta H = 1438$ Gs (0.1438 T) whereas the spectrum at 77 K is of less intensity and narrower (559 Gs or 0.0559 T). Two interpretations can be suggested to explain the observed EPR spectra.

The first one consists of that the high temperature spectrum (at 300 K) is due to Fe^{3+} state of iron with $S=5/2$ in a crystal tetrahedral position. Because the nanocrystal particles are in a stressed and defective state the EPR line is wide. Such wide spectra with $g = 2.1 - 2.4$ due to Fe^{3+} state of iron were recorded in natural minerals such as montmorillonite [14], pyrite [10] kaolinites [5] and also in polymers [6]. As experience shows, the g -factor value for such samples is dependent on the origin and technology of a sample preparation. The hyperfine structure of the spectrum cannot be recorded due to high values of the linewidth. The spectrum at 77 K can be attributed to the phenomenon of exchange line narrowing. The regular and pair wise organization of iron spins can favor to such line narrowing. Thus, in connection with the minima of the temperature dependences of the unit-cell dimensions a and c showed the minima at ~ 86 K and ~ 131 K, respectively, that of the unit cell volume at about 100 K, the change of the sign of the thermal linear and volumetric expansion, higher value of magnetization (0.0082 emu/g at 300 K and 0.0094 emu/g at 77 K) EPR line narrowing at 77 K can be ascribed to higher than at 300 K exchange interactions between adjacent spins of Fe^{3+} ions.

The second explanation is that the narrow and less intensive line at 77 K is due to the phenomenon of spin crossover. Spin Crossover (SCO) is a phenomenon that occurs in some metal complexes wherein the spin state of the complex changes due to external stimuli such as a variation of temperature, pressure, light irradiation or an influence of a magnetic field. The proof of this assumption is that the integral intensity of the EPR line ($\int f(H)dH$) decreases with decreasing temperature. According to the Boltzmann law, the integral intensity of the line should increase as the temperature decreases [15-17].

At the same time, it can be noted that these two versions of the explanation do not contradict each other. Both effects can occur simultaneously.

References

1. N. P. Yushkin. Ultrafine Mineral State (in Russian). – “Geoprint” Publ., Syktyvkar, 2000.
2. A. V. Vakhrushev, V. P. Lutoev, V. I. Silaev. - Vestnik., № 10. P.14-18 (2012).
3. E. Dutkova, Zdenka Bujnakova, I. Skorvanek, M. J. Sayagues, A. Zorkovska, J. Kovac, P. Balaz. Proceedings-of the 16th Czech and Slovak Conference on Magnetism., Vol. 131, № 4. P.1156-1158 (2017).
4. E. Dutkova, Z. Bujnakova, J. Kovac, I. Skorvanek, M. Sayagues, A. Zorkovska, J. Kovac Jr., P. Balaz. Adv. Powder Technology., Vol 29. P.1820-1826 (2018).
5. E. Balan, T. Allard, B. Boizot, G. Morin, J.-P.Muller. Clays and Clay Minerals., Vol. 47, № 5. P.605-616 (1999).
6. I. S. Lyubutin, S. S. Starchikov, Yu-Jhan Siao. Acta Materialia., Vol 61, № 11. P.3956-3962 (2013).
7. P. Balaz, M. Balaz, M. Achimovicova, Z. Bujnakova, and E. Dutkova. J. Mater. Sci., Vol 52. P.11851-11890 (2017).
8. K. S. Knight, W. G. Marshall, S. W. Zochovski. The Canadian Mineralogist., Vol. 49. P.1015-1034 (2011).
9. A. Woolley, S. Bergman, A. Edgar, M. Le Bas, R. Mitchel, N. Rock, B. Scott Smith. The Canadian Mineralogist., Vol. 34. P.175-186 (1996).
10. N. C. Gangi Reddy, R. Ramasubba Reddy, G. Siva Reddy, S. Lakshmi Reddy, B. Jagannatha Reddy. Cryst. Reser. Tech., Vol. 41. P.400-404 (2006).
11. Ebin Bastola, Khagendra P. Bhandari, Indra Subedi, Nikolas J. Podraza, Randy J. Ellingson. MRS Communications., Vol. 8, № 3, P.970-978 (2018).
12. S. O. Garkavyi, E.V. Schmidt, S.V.Schmidt, V.L.Matukhin, N.K.Andreev, E. Dutkova. Magnetic resonance and its applications. Spinus-2018. Abstracts book., P.181-182 (2018).
13. A. N. Gavrilenko, A. I. Pogoreltsev, V. L. Matukhin, B. V. Korzun, E. V. Schmidt, I. G. Sevastianov. J. Low Temp. Phys., Vol. 185, № 5-6. P.618-626 (2016).
14. C. Cracuin, A. Meghea. Clay Minerals., Vol. 20, № 3. P.281-290 (1985).
15. V. E. Vorobeva, N. E. Domracheva, A. V. Pyataev, M. S. Gruzdev, U. V. Chervonova. J. Low Temp. Phys., Vol. 41, № 1. P.22-27 (2015).
16. M. S. Gruzdev, N. E. Domracheva, U. V. Chervonova, A. M. Kolker, A. S. Golubeva. Journal of Coordination Chemistry., Vol. 65, № 10. P.1812-1820 (2012).
17. V. E. Vorobeva, N. E. Domracheva, M. S. Gruzdev. Electronic Journal., Vol. 18, № 2, P.1-4 (2016).

Some capabilities of the NMR relaxometer for evaluation of the age-related changes in muscle tissue

Aleksey N. Zolotov^{1,2}, Yuriy I. Neronov^{1,2}, Denis D. Kosenkov^{1,2}

¹*Mendeleyev Institute for metrology, St. Petersburg, Moskovskiy pr. 19, Russia*

²*Saint Petersburg National Research University of Information Technologies, Mechanics and Optics, St. Petersburg, Kronverkskiy pr. 49, Russia*

E-mail: alexzolotov2014@gmail.com, wdenkosw@gmail.com, yineronov@mail.ru

Introduction

The increase in life expectancy in developed countries has drawn the attention of scientists to the problems of age-related loss of muscle tissue. As a rule, the age-related decrease in muscle fibers is accompanied by the growth of adipose tissue. It was also noted that in some cases, fat cells can increase in size and at the same time trigger an over-expression of the protein: N-methyltransferase nicotinamide (NNMT). This protein manifests itself as a metabolic inhibitor, because of which it is increasingly difficult for cells to burn fat. As a result, a process is launched in which weight increases, leading to significant deterioration of the quality of life of not only the old but also the younger people. A drug solution to this problem is associated with the development of drugs that can actively block the action of NNMT in fat cells and speed up the metabolic process. In the new work [1] it is reported about the development of such a drug and its first successful tests on mice.

However, so far there are no treatments that could delay, stop or reverse age-related muscle degeneration. For people with good genetic inheritance, this process can be partially slowed down with exercise. However, this raises the question of the duration and intensity of physical exertion. In this regard, it is of interest to develop such widely available devices that can allow you to control the process of adipose destruction of muscle tissue. It is known, that the dynamics of the proton magnetization of living tissues, determined by the times of spin-lattice and spin-spin relaxation, is very sensitive to changes in the concentrations of active metabolites, which can be used to estimate age-related changes.

1. Description of the experimental setup

Earlier in works [2], the development of a mini-NMR tomograph using a permanent desktop magnet with a field $B = 0.128$ T was reported. The use of this type of a device turns out to be more effective in the registration mode of the relaxation time [8]. Moreover, if linear recording of the signal amplitudes (at the level of $dA/A < 1\%$) in such NMR relaxometers is ensured, then the parameters T1 and T2 can record the dynamics of metabolic processes.

In the present version of our NMR tomograph, spin echo signals were recorded using resonant inductance of the surface type. It is made in the form of an annular winding containing 20 conductors (ring diameter ≈ 27 mm) and having a bend for optimal semi-coverage of a cylindrical ampoule or a portion of the muscle tissue of the palm of an experiment participant (Fig. 1).

The resonance inductance was shielded from the sample under investigation by an electrostatic screen. The screen is a curved plane containing a set of thin conductors grounded at one end. Such a screen does not reduce the Q-factor of the resonant circuit and allows one to maintain stable conditions with the optimal settings of the radio frequency resonance when examining objects of various shapes. The device consumes no more than 30 watts of power, has a compact design and can be controlled from a laptop. The decrease in signal amplitudes for ampoules with water solutions is well described by a single exponent $A(t) = A_0 \times \exp(-t/T_2)$. However, in living tissues, the decrease in the NMR amplitude of echo signals from time has a more complex dependence.

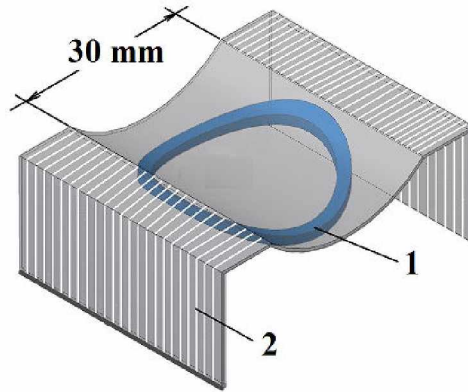


Figure 1. The shape of the coil NMR signals sensor:

1 - the location of the turns of the resonant inductance; 2 - electrostatic screen

If only one exponent with T_{20} is used to describe the decrease in the amplitudes of 40 of echo NMR signals from living tissues, then the standard deviations for the forty experimental amplitudes A_i from the calculated amplitudes $A(t_j)$ are usually at the level of three to four percent: $dA/A \approx (3 \div 4) \%$, where:

$$dA/A = 100 \times (1/A_1) \times \sqrt{\{\sum [A(t_j) - A_i]^2\} / (N - 1.5)} \quad (1)$$

In the relaxometer software, the second version of mathematical data processing was provided (as in [2-5]) using two exponentials and two weight parameters:

$$A(t) = A_0 [w_a \times e^{\frac{-t}{T_{2a}}} + w_b \times e^{\frac{-t}{T_{2b}}}] \quad (2)$$

Using (2), the standard deviations in the study of living tissue, as a rule, decreased to: $dA/A \approx (0.5 \div 0.8) \%$, depending on the noise level. At the same time, the deviations $dA/A \approx 0.7\%$ were provided by calculating the three parameters T_{2a} , T_{2b} and w_a using the method of minimizing the sum of square deviations отклонений $\sum [A(t_j) - A_i]^2$ and taking into account the normalization ($A_0 = 100 \%$; $w_a + w_b = 1$).

2. The estimation of the age related changes

In the current work, muscle tissue was studied, in which the authors used the following tissues: muscular abductor pollicis brevis, muscular abductor minimi brevis; muscular brachioradialis; muscular *humero* triceps (latine).

These four muscle groups are the most convenient for comfortable placement of the hands of a participant in the experiment in the registration area of the desktop magnet. For the time interval between successive 90-degree pulses, $TR = 2$ sec was used. During this time interval between the excitation pulses, the restoration of the equilibrium magnetization associated with the spin orientation of the water protons of living tissues was observed.

Table 1.

Age	22 +/- 3 years			75 +/- 4 years			Wa1 Wa2
	T2a, ms	T2b, ms	Wa1, %	T2a, ms	T2b, ms	Wa2, %	
Musculus genus							
Abductor pollicis brevis	31.3(2)	140(3)	89(1)	31.8(6)	106(3)	76(1)	1.17
Abductor minimi brevis	30.5(3)	127(3)	72(2)	31.6(3)	113(2)	63(2)	1.14
Brachioradialis	30.2(1)	126(3)	70(1)	30.9(4)	119(2)	57(1)	1.23
Triceps brachii	30.3(2)	125(2)	62(1)	29.8(2)	123(2)	52(1)	1.19

The Table 1 presents a comparison of the study results, which were obtained from the participation of a group consisting of students and teachers. Moreover, the participants had a typical lifestyle. We assume that a shorter relaxation time ($T2a \approx 31$ ms) should be attributed to the tissues that provide motor function. A longer time ($T2b \approx 120$ ms) should be attributed to a looser connective tissue, which is obviously less saturated with active metabolites. It follows from the presented data that the percentage of muscle tissue in the group of teachers was reduced. This decrease ranged from 14 to 23%, depending on the area of study. Authors believe that if we improve a number of technical parameters of such an instrument, then such relaxometers can be widely used to control the age-related loss of muscle tissue.

References

1. Harshini Neelakantan and other authors, «Small molecule nicotinamide N-methyltransferase inhibitor activates senescent muscle stem cells and improves regenerative capacity of aged skeletal muscle», *Biochemical Pharmacology*, Available online 10 February 2019; <https://newatlas.com/muscle-medication/58503/>.
2. Y. I. Neronov, A. N. Seregin. «Mini-MRI scanner and some possibilities for its use for studying living tissues»; *Measurement techniques*, Vol. 54, № 1, p. 103-107 (2011).
3. Y. I. Neronov, N. N. Seregin. «Precision determination of the difference in shielding by protons in water and hydrogen and an estimate of the absolute shielding by protons in water». *Metrologia*. 2014. Vol. 51. p. 54-60.
4. Zolotov A.N., Neronov Yu.I., Kosenkov D.D.; «An estimate of the change in the spin-spin relaxation time of protons of living tissue upon its cooling». In book: «*Magnetic resonance and its applications*». *Spinus - 2018*. Saint Petersburg State University, Department of Nuclear Physics Research Methods. 2018. p. 130-132.
5. Kosenkov D.D., Neronov Yu.I., Zolotov A.N., Seregin N.N. «NMR relaxometer for the estimation of the spin-spin proton relaxation time of the living tissue». In book: «*Magnetic resonance and its applications*». *Spinus - 2018*. Saint Petersburg State University, Department of Nuclear Physics Research Methods. 2018. p. 77-79.

Poems about School

* * *

Чижик-Spinus, где ты был?
– «Я сигнал за хвост ловил!
Сделал я ему “Фурье” –
Закружилось в голове!»

Цели «Spinus»’а просты:
Дать научные мосты!
Пусть у вас здесь будет шанс
Пообщаться «в резонанс»!

В Школе здесь научат всех
Сочетать с наукой смех,
Дисотеки с Э-Пе-эР,
Я-Ка-эР и Я-эм-эР!

В Школе много новых лиц,
Будем превращать их в птиц:
Вдруг хотя б одной из ста
Дастся «Нобель-высота»!

2010

* * *

Spinus, Spinus, where you were?
Did you dive in the Resonance world?
– “Yes! I dived with my great joy –
Resonance is a pleasant toy!”

“Spinus” school invited you
To look for a knowledge clue.
We will show the signal birth
In the field of our Earth!

If you wish to have success,
At the School achieve progress!
We will teach you all to fly
In the scientific sky!

We desire you to get
Many victories-побед!
It will be a good surprise
If you catch the Nobel prize!

2010

Author Index

- Abdullin, Ilgiz*, 125
Aganov, A. V., 101
Aganova, O. V., 262
Ahokas, Janne, 80, 281
Aitkulova, Aisuluu, 57
Aleshin, Dmitry, 127
Andreev, Nikolay K., 173, 285
Antipin, I. S., 234
Antonova, N. A., 130, 237
Antunez-Garcia, J., 251
Arapova, Irina Yu., 190
Atta, Ramadan R., 64, 155
Avila, Dahiana, 65
Avilova, Irina A., 133
Babanova, Olga A., 117
Bakhteev, S., 115
Balandina, A. A., 150
Bali, Rantej, 57
Baranauskaite, Valeriia, 67
Barton, Craig, 57
Baryshnikov, S. V., 38, 279
Bavrina, O., 136
Becher, Manuel, 68
Belyakov, D. I., 252
Bertmer, Marko, 46
Besedina, Alla, 224
Bezrodnii, Valeriy V., 213, 245
Bogachev, Yu. V., 139
Bogdanov, Dmitrii, 65, 142
Borodkin, Gennadii S., 144
Borodkina, Inna G., 144
Böttger, Roman, 57
Brauer, Delia, 65
Bunkov, Yury, 40
Bychkova, E. I., 213
Bystrov, Sergei, 70
Cabal Mirabal, Carlos Alberto, 41, 98, 100
Charnaya, E. V., 38, 279
Chepurnoy, Pavel B., 144
Cheremisin, V. M., 258
Chizhik, Vladimir I., 45, 70, 161, 202, 203
Cobas, Carlos, 120
Consiglio, Armando, 147
Cramer, Tobias, 147
Cunningham, T. F., 56
Dai, Jing, 72
Daniels, John E., 208
Darwish, S., 73, 150
Denisov, G. S., 60
Deriglazov, V. V., 195
Djapic, Nina, 153
Dmitrenko, Mariia E., 64, 155, 204
Dmitriev, Alexander K., 156
Dmitriev, Oleg, 220
Dolgikh, Ekaterina A., 133
Dorogynitskii, M. M., 276
Duchardt, Marc, 198
Dutkova, Erika, 285
Dvinskikh, Sergey V., 72
Efimov, Nikolay N., 127
Efimov, S. V., 73, 150, 199, 262
Efimova, Aleksandra A., 159
Egorov, Andrei V., 161, 202, 274
Egorova, Maria I., 161
Eichhoff, Uwe, 43
Ermak, Sergei, 224
Faleva, A. V., 230
Fassbender, Jürgen, 57
Fatkhutdinov, I. H., 276
Fatullaev, Emil I., 185, 213, 248
Fedotov, A., 115
Fella, Verena, 162
Filatov, Alexander S., 282
Floudas, George, 162
Fraissard, Jacques, 44
Frolov, Viacheslav V., 76, 125, 164, 220, 255
Fuentes, S., 251
Fujii, Yutaka, 80
Gafurov, M. R., 115, 234
Galitskaya, Elena, 167
Garcia Naranjo, Juan Carlos, 98, 100
Garkavyi, Stanislav O., 173, 285
Giba, I. S., 60
Gil, Roberto R., 120
Gil-Silva, Leandro, 120

- Golubeva, Irina Yu., 93, 170
 Grinderslev, Jacob, 117
 Grunin, Leonid Yu., 77, 78
 Guerrero Piña, Edalis, 100
 Güler, S., 181
 Gulina, L. B., 53
 Haase, Jürgen, 46
 Haponchik, Roman V., 176
 Hasanbasri, Z., 56
 Höfler, Mark, 91
 Hurshkainen, Anna A., 179
 Ievlev, Alexandr V., 47, 184, 188, 242
 Ignatyev, I., 115
 Il'yasov, Kamil A., 85
 Ilyash, Maxim Yu., 248
 Indeykina, M. A., 56
 Ivanov, Viacheslav A., 179
 Ivanova, Maria S., 78
 Izmailov, Sergei A., 56, 274
 Järvinen, Jarno, 80, 281
 Jensen, Torben R., 117
 Kamyshanskaya, I. G., 258
 Karabas, Nail, 111
 Karatas, O., 181
 Karnaukh, Grigorii E., 93, 170
 Kashin, Alexei, 167
 Kass, K., 184
 Kazan, S., 181
 Khaibullin, R., 181
 Khamidova, Dilorom N., 185
 Kharkov, Boris B., 72, 241
 Khasanov, M. A., 188
 Khmelenko, V. V., 281
 Khodov, I. A., 199
 Khrapichev, Alexandr A., 81
 Khusnutdinov, Rustem R., 173, 190
 Khusnutdinova, Naira R., 192
 Kiselev, I. A., 195
 Klochkov, V. V., 101, 150, 196, 199, 262
 Klotz, Edda, 198
 Klyukin, K., 136
 Kobchikova, P. P., 73, 199
 Komlev, V., 115
 Komolkin, Andrei V., 82, 125, 130, 147, 211, 237
 Kondrasenko, A. A., 268
 Koneva, Alina S., 216
 Konopleva, Lidia V., 85
 Konovalov, A. I., 234
 Konovalov, V. A., 202
 Kosenkov, Denis D., 88, 252, 289
 Kosyakov, D. S., 230
 Kotelnikova, Raisa A., 133
 Kozhevnikov, A. Yu., 230
 Kraevaya, Olga A., 133
 Kresse, Benjamin, 91
 Krylova, E. A., 251
 Kulagina, Tatiana P., 93, 170
 Kupriyanov, Pavel A., 45, 164, 203
 Kupriyanova, Galina S., 50, 96
 Kurnosenko, Sergei, 99
 Kuzminova, Anna I., 204
 Kuznetsov, Nikolai A., 205
 Kuznetsova, L., 115
 Latfullin, I. A., 101
 Laurent, Sophie, 98
 Lee, D. M., 281
 Lenz, Kilian, 57
 Lindner, Jürgen, 57
 Livshits, A., 136
 Lopez, Irakusne, 120
 Lores Guevara, Manuel Arsenio, 98, 100
 Lozov, Roman, 224
 Lushpinskaya, Irina, 99
 Luzik, D. A., 56
 Ly, Thai, 208
 Mamadazizov, Sultonazar Sh., 50, 96
 Mamin, G. V., 115, 234
 Mamontova, Veronika V., 211
 Maraşlı, A., 103
 Marchenko, A. A., 213
 Marichal Felue, Maria A., 100
 Markelov, Denis A., 245, 248
 Matsulev, A. N., 268
 Mattea, Carlos, 265
 Matukhin, Vadim L., 173, 190, 285
 Matveev, Vladimir V., 47, 261
 Mazur, Anton S., 159
 Meersmann, T., 48
 Mengana Torres, Yulianela, 98, 100

- Michel, Dieter*, 46
Mikhtaniuk, Sofia E., 185, 213, 245
Miljak, David, 208
Mohorič, Aleš, 265
Mozzhukhin, Georgy V., 50, 96, 103, 173
Muller, Robert, 98
Mulloyarova, V. V., 60
Murin, I. V., 53
Musabirova, G. S., 101
Nam, Anastasia V., 216
Navarro-Vázquez, Armando, 120
Nedopekin, Oleg V., 85
Neelov, Igor M., 185, 213, 245, 248
Nefedov, D. Yu., 279
Nelyubina, Yulia V., 127
Neronov, Yuriy I., 88, 289
Nikitina, A. V., 139
Nikovskiy, Igor, 127
Novikov, Valentin V., 109
Ogloblichev, Vasilii V., 190
Okay, C., 103, 181
Orlinskii, S. B., 115, 234
Ostras, A. S., 218
Ovsyannikov, A. S., 234
Pankratova, Yanina A., 106
Panov, Vladislav, 220
Pavlov, Alexander A., 106, 109, 127
Pazgalev, Anatoly S., 222
Penkova, Anastasia V., 64, 155, 204
Pestov, Dmitry, 224
Pestov, Evgeny, 224
Pestova, Olga, 67
Petranovskii, Vitalii, 142, 251
Petrov, Vladimir I., 222
Philippé, Jan, 100
Pichugina, Alina A., 227, 271
Pleshakov, I. V., 261
Podgornyak, M. Yu., 258
Podkorytov, I. S., 56, 241
Podorozhkin, D. Yu., 279
Polezhaev, Alexander V., 127
Popkov, V. I., 261
Popova, Yu. A., 230
Potzger, Kay, 57
Prits, V. V., 258
Privalov, Alexei F., 53, 91, 167
Rabdano, S. O., 56
Rameev, B. Z., 50, 103, 181
Razina, E. A., 234
Reisert, Marco, 85
Reuhl, Melanie, 111
Ricardo Ferro, Beatriz T., 100
Rodríguez Reyes, Inocente C., 100
Rodríguez-Iznaga, Inocente, 142
Rogacheva, O. N., 56
Roling, Bernhard, 198
Ryzhkin, Ivan, 167
Ryzhkov, A. M., 130, 237
Ryzhov, V. A., 195
Säckel, Christoph, 114
Salikov, V. A., 241
Samoson, Ago, 113
Saratov, George A., 133
Saxena, S., 56
Schmidt, Ecaterina V., 173
Schneider, Sarah, 114
Selivanov, A. A., 242
Selivanov, Stanislav I., 282
Semisalova, Anna, 57
Seoane, Felipe, 120
Shavykin, Oleg V., 245, 248
Sheludiakov, S., 281
Shelyapina, Marina G., 99, 136, 142, 251
Shestakov, S. L., 230
Shifrin, V. Ya., 252
Shilov, A. E., 164, 252
Shmidt, Ekaterina V., 285
Shmidt, Stanislav V., 190, 285
Shubin, S. A., 255
Shurtakova, Daria, 115
Silanteva, Irina A., 82, 211
Silyukov, Oleg, 99
Simeshchenko, P. I., 258
Simón Brada, Teresa, 100
Sinitsyn, Vitaly, 167
Skirda, V. D., 276
Sklyarova, A., 261
Skoryunov, Roman V., 117
Skripov, Alexander V., 117
Skrynnikov, N. R., 56, 241

- Slipchenko, L. V.*, 56
Slivka, A. V., 73, 262
Smirnov, I., 115
Smolyarov, K. T., 268
Soldatova, Yuliia V., 133
Solomakha, Georgiy A., 179
Soloninin, Alexey V., 117
Solovieva, S. E., 234
Sordo Touza, Marixa, 120
Sorokina, E., 184
Spannenberger, Stefan, 198
Stankevich, Natalya V., 144
Stapf, Siegfried, 265
Steinrücken, Elisa, 68
Stepakov, Alexander V., 282
Štěpánková, H., 261
Stepišnik, Janez, 265
Suárez Beyrio, Lidia C., 100
Sukharzhevskii, Stanislav, 142
Tagirov, M. S., 234
Thomson, Thomas, 57
Tolstoy, Peter M., 60, 159, 216, 218
Troshin, Pavel A., 133
Tsyro, Larisa V., 227, 271
Tupikina, E. Yu., 60
Tyutyukin, Konstantin V., 47, 76, 125,
 220, 255
Ubovich, Milosh, 274
Uskova, E. I., 276
Uskova, N. I., 279
Ustinov, Alexey B., 176, 205
Varela, Luis M., 47
Vasilchenko, Igor S., 144
Vasiliev, Sergey, 80, 281
Vaz, Esther, 120
Vershovskii, Anton K., 156, 222
Vlasenko, Leonid, 80
Vogel, Michael, 53, 68, 91, 111, 114,
 162, 167, 198
Volkov, Vitaliy I., 133
Voronin, Alexandr, 125
Wang, Siqi, 282
Weigler, Max, 53, 111, 167
Yakovleva, Lyudmila Y., 159
Yao, Yang, 162
Yavkin, B., 115
Yocupicio-Gaxiola, R., 251
Yong, Richard, 208
Yulmetov, Aidar R., 192
Zaynullin, Radik R., 285
Zgadzay, Yu. O., 73
Zhelezniak, Yu., 251
Zhilentov, Aleksandr V., 133
Zhukov, Yuri, 142
Zolotarev, Andrey A., 64
Zolotov, Aleksey N., 88, 289
Zorin, Vadim, 120
Zubkov, Mikhail A., 179
Zvereva, Irina, 99
Zvezdov, Denis, 80

Magnetic Resonance and its Applications

Proceedings

Saint Petersburg State University
March 31 — April 5, 2019

Подписано в печать 20.03.2019. Формат $60 \times 84\frac{1}{16}$.
Бумага офсетная. Гарнитура Times. Печать цифровая.
Усл. печ.л. 17 67. Тираж 150 экз. Заказ № 814

Отпечатано в Издательстве ВВМ.
198095, Санкт-Петербург, ул. Швецова, 41.

Schedule of Spinus-2019

	31.03.19 Sunday	01.04.19 Monday	02.04.19 Tuesday	03.04.19 Wednesday	04.04.19 Thursday	05.04.19 Friday	06.04.19 Saturday
08:45 – 10:00		BREAKFAST				9:10-10:30	BREAKFAST
10:00 – 11:30		Registration 30 Opening 10 Chlzhik 30 GROUP PHOTO 20	Tolstoy 40 Zorin 20 Järvinen 15 Baranauskaitė 15	Excursion Day	Cabal 40 Lores I 20 Lores II 15 Musablrova 15	Matveev 30 Bystrov 15 Khrapichev 15	Departure
11:30 – 12:00		COFFEE BREAK			COFFEE BREAK		
12:00 – 14:00		Privalov 40 Schneider 15 Kresse 15 Reuhl 15 Lushpinskaya 15 SoloninIn 20	Fralssard 40 Meersmann 40 Samoson 20 Dvinskikh 20		Elchhoff 40 Efimov 15 Skrynnikov 40 Komolkin 25	Michel 40 Semisalova 40 Shurtakova 15 Avlla 15 Neronov 15	
14:00 – 15:30		LUNCH			LUNCH		
15:30 – 17:00		Chamaya 40 Pavlov 20 Pankratova 15 Lahderanta 15	Atta 15 Oral blitz reports of young scientists (5min x 15)		Konopleva 15 Oral blitz reports of young scientists (5min x 15)	Bunkov 40 Kupriyanova 20 Mozzhukhlin 40	
17:00 – 17:30	Registration of participants	COFFEE BREAK			COFFEE BREAK		
17:30 – 19:00		Becher 15 Kulagina 20 Rameev 20 Ivanova 15 Grunin 20	POSTER SESSION I	POSTER SESSION II	Awarding Closing		
19:00 – 20:00		DINNER				DINNER	
20.00	Welcome	Cultural and sporting activities			CONFERENCE DINNER		